NONLINEAR LATTICE DYNAMICS IN HIGH–T_C SUPERCONDUCTORS

Francesco Piazza

Submitted for the Degree of
Doctor of Philosophy
at Heriot-Watt University
on completion of research in the
Department of Physics
March 2002.

Abstract

After 15 years since it was discovered, the microscopic mechanism of High–T_c superconductivity remains elusive. In particular, the role of lattice vibrations in the electronic coupling is still very debated. Many of the proposed models invoke unusual vibrational properties, such as nonlinearity in the interatomic potentials. In this thesis we present a combined experimental and theoretical study of lattice anharmonicities in cuprates.

We first introduce and describe our Extended X–Ray Absorption Spectroscopy (EXAFS) experiment. We then develop a novel data analysis technique, which enables us to measure directly the nonlinearity in the interatomic potentials of the copper-oxide planes, which constitute the basic structural unit of all cuprates. Finally, based on our experimental results, we introduce a simple dynamical model of the copper–oxide layers. We study this model both analytically and numerically, showing the emergence of anharmonic localised excitations known from nonlinear physics as discrete breathers. The general layout of the thesis is the following.

The first chapter is devoted to a review of the basic structural and physical properties of cuprates. In particular, we review and discuss the existing experimental data regarding the Cu–O interatomic potential in the CuO_2 planes. In the second chapter we introduce the basics of EXAFS spectroscopy. From a simple derivation of the main features of the theory underlying it, to a simple but complete discussion of the details of our experiment. The last three chapters are entirely dedicated to the original contribution to this thesis. First, we introduce and develop a pair distribution function based on quantum perturbation theory. It is designed to incorporate directly the parameters describing the interatomic potential of the Cu–O pair through a Taylor expansion. We thoroughly illustrate the properties of the distribution function and carefully examine its sensitivity to the potential parameter. For this purpose, we set up an easy and robust procedure based on the statistical F–test. In chapter four we present the data analysis of our experiment. We begin presenting the general fits of the whole spectra. Then we move on to a closer examination of the contribution from the Cu–O pair. and present a complete analysis of the Cu–O interatomic potential based on the pair distribution function developed in the previous chapter. The last chapter is entirely devoted to a detailed study of the lattice dynamics of the CuO_2 planes. As a start, we present a careful analytical and numerical analysis of the linear spectrum (phonon bands) based on a simple model with two force constants. This analysis provides the necessary background for the interpretation of the subsequent numerical experiments. Based on the experimental results discussed in the first part, we simulate a simple nonlinear model and show how it is possible to observe the spontaneous emergence of discrete breathers in a copper–oxide plane. We discuss the properties of such solutions and attempt a definition and a quantitative estimate of their lifetime, based on a simple non–linear stability analysis.

To Alissa: in loving memory of "Home Street"

$\pi\alpha\nu\tau\alpha\ \ \rho\varepsilon\tilde{\imath}$ ...

Acknowledgments

First and foremost, I wish to express here my gratitude to my friend and supervisor Dr Eitan Abraham. His help and guidance, delivered from the very beginning with great care and discretion, made the realisation of the present piece of work possible, besides turning me at the end of this great trip into a better scientist and man.

It is a pleasure to have a formal occasion here to thank again my former thesis supervisor and great friend Dr Luciano Cianchi. He never ceased to be active and caring part of my work, with precious suggestions and comments that largely contributed to the quality of the present work. Many thanks to the *guys* from Luciano's group as well, Dr Paolo Moretti, Dr Fabrizio Pieralli and Dr Franco Del Giallo, for their hospitality at I.R.O.E. during the last part of my work.

Both the experiments reported in this thesis and their data analysis would not have been possible without the expertise of Dr Paolo Ghigna, and his valuable help during my stay in Pavia learning EXAFS data analysis. I am also indebted to him for having provided the samples for our experiments. Many thanks to his nice wife Luisella as well, for their kind hospitality at their place in more than one occasion.

I am very proud to acknowledge here even a small contribution from a great expert of EXAFS, Prof. J. J. Rehr, for having provided me with the phase and amplitudes from the package `Feff` for the Cu–O shell. My warmest thanks to Dr S. Islam as well, for having shared with me some unpublished results of his regarding the Cu–O interatomic potential in $Ca_2CuO_2Cl_2$.

Finally, I would like to acknowledge financial support and allocation of beam time from the Daresbury Labs, beam time Award No 33211.

It is now the turn of my friends and relatives. It would be impossible to list and acknowledge here the tremendous amount of support that kept me up and going during these sometime difficult years. The ones who will not find themselves explicitly listed below, please apply for a free hand–shake.

My first friends form Edinburgh: the little sister and the great Toys, The Ale (ciao babbo), the Ginger one, the *bloody* greek and the little Czech. You have been my second family, and so you will be in the future, just a little bit more scattered around than it used to be. My brother, whom I used to miss the most being abroad - the man I am is unbelievably indebted to his bright mind and caring devotion. So he is and will be to my ever–green friends from my mental child–hood, Giovanni *the Globe* De Ninno and Duccio *tranquillity* Fanelli. I hope I will keep on owing you all much. My folks, of course. An unlimited reservoir of care, love and support. The only one you are allowed to take for granted... how peaceful.

Someone told once that there is a great woman behind every great man. I have been a fortunate and great man so far...

Contents

Chapter 1

Introduction

Since the discovery of high–T_c superconductivity in 1986 [1], several mechanisms leading to the formation of Cooper pairs have been proposed [2]. In particular, the role of the lattice in the microscopic mechanism of charge pairing has been widely investigated [4, 5, 6]. For example, it has been recently shown how induced stresses in the lattice at the microscopic level can dramatically enhance T_c [7]. However, many problems regarding the role of lattice dynamical properties in the mechanism for superconductivity have not been settled yet, and much work is still in progress in this field [3].

Vibrational anharmonicities: the CuO_2 planes and the apical ions

Many of the models proposed invoke unusual vibrational properties of the cuprates [8, 9]. In particular, one of the *hot* issues is vibrational anharmonicity [10, 11, 12, 13, 14]: is it an ubiquitous phenomenon in high–T_c superconductors? What is its role in the microscopic mechanism? These are the questions that the superconductivity community is trying to answer. Regarding the former problem, it is interesting to quote here recent results obtained by experimental and numerical lattice dynamics studies of the newly–discovered superconductor MgB_2. Clear evidence of a *giant* anharmonicity associated with the in–plane motion of the B ions has been given in recent reports [15, 16]. Such anomaly is described by a huge quartic term in the interatomic potential accounting for the motion of the B ions, whose dynamics turns out to be strongly coupled to the electronic degrees of freedom near the Fermi level. As a result, a 10 % enhancement of T_c with respect to the corresponding BCS value is obtained, in agreement with the experiments.

In this thesis, we shall focus on two important points regarding vibrational anharmonicity in high–T_c superconductivity, namely:

The copper–oxide planes It is well known that high–T_c superconductivity is a two–dimensional phenomenon, reflecting the basic layered lattice structure which is common to all cuprate families. In particular, the crucial role is played by the CuO_2 planes (also referred to as *copper–oxide* planes): this is where the mobile holes are injected as a result of doping, determining the metal–like conductivity of the doped compounds. This is where the (two–dimensional) supercurrents flow, and where the pairing mechanism occurs [17]. However, while the electronic properties of the copper–oxide sheets have been widely investigated [18], not many experimental data are available on the dynamics of the in–plane Cu–O pairs. Several systematic temperature–dependent studies performed on a number of different cuprates have provided evidence of vibrational anomalies occurring in the copper–oxide planes [23]. However, the nature and detailed characteristics of such anomalies are far from being clarified.

The apical ions It is now widely recognized that the ions lying at the apical sites (i.e. the nearest off–plane neighbours of the Cu ions in the copper–oxide planes) are involved in the microscopic mechanism which leads to the superconducting transition [19]. In addition, EXAFS studies have found evidence of vibrational anharmonicity at such site in YBCO, in the form of a double well potential [10, 11]. Accordingly, it has been speculated that the large amplitude vibration along c could lead to an enhanced electron–phonon coupling [13]. It is worth observing that a similar mechanism had been hypothesized a few years before by K. A. Müller [20].

Recently, high–T_c superconductivity has been discovered in a class of oxyhalides, such as Na–doped $Ca_2CuO_2Cl_2$ [21]. Their structure closely resembles that of the LSCO cuprate family. However, in such compounds the apical site is occupied by a halyde ions (Cl, F). This discovery was interpreted as a proof against the involvement of the apical *oxygens* in the mechanism for superconductivity, rather than a confirmation of the involvement of the apical *site*.

Vibrational anharmonicity: the experiments

The experimental techniques used to probe lattice dynamics properties of condensed–matter systems can be roughly divided in two categories: local and non–local probes. The latter category includes X–rays and neutron diffraction, while the two most important local techniques are Mössbauer and extended X–rays absorption spectroscopy (EXAFS). Such distinction is not artificial, in that it reflects the very nature of the physical probe. On one hand, Mössbauer measurements directly probe the motion of the Mössbauer–active atom in the sample. Analogously, EXAFS is sensitive to a limited region ($\approx 3 - 4$ Å) around the photoabsorber. On the other hand, X–rays and neutrons are diffracted by sets of crystallographic planes. As a consequence, the correlations between atomic motions play a critical role in the measured scattered intensities (diffuse temperature scattering [22]).

The same distinction shows in the literature among the results of different techniques. In fact, contradictory findings have been reported regarding the vibrational properties of different superconductors by different experimental techniques. One of such examples is the lattice dynamics of the Sn ion in the superconductor Nb_3Sn. Mössbauer studies reveal a large low–temperature anharmonicity at the Sn site [24], while X–rays diffraction measurements determine a much smaller mean square displacement. The dynamics of the Eu ion in the Eu-BCO superconductor provides another clear demonstration of such inconsistencies. Careful Mössbauer experiments have revealed the presence of a low–temperature anharmonic flat–bottomed potential at the Eu site, whose flat part is as large as ≈ 0.1 Å [12]. On the contrary, no evidence of such anomaly is found in neutron–diffraction experiments [25]. The same discrepancy

exists regarding the motion of apical ions: the above–cited EXAFS experiments (confirmed by Raman measurements [139]) reveal the presence of a double–well potential at the apical O site in YBCO, while again no anomalies are found by means of neutron diffraction [25].

As a result of the above facts, it is apparent that the important topic of vibrational anharmonicity in high–T_c superconductors calls for further experimental and theoretical work.

Vibrational anharmonicity: discrete breathers

It is well known that, by putting together spatial discreteness and nonlinearity, a number of intriguing features emerge in the dynamics of atomic lattices. It is of particular interest the phenomenon of *energy localisation*, reminiscent of the localisation in linear lattices with impurities. It is found that nonlinear homogeneous discrete lattices support a special class of time–periodic localised excitations, which have been named discrete breathers (DB)[1]. They can be either stationary or propagate at sub–sonic speeds with a very small energy degradation, and exist for a wide variety of potential energy functions in one, two and three dimensions. The frequency of their internal vibration lies outside the linear spectrum, in such a way that its harmonics do not resonate with any of the linear frequencies. These solutions have attracted a great deal of research among the condensed matter and dynamical systems communities [26], and are now intensively studied. In particular, much is understood in terms of existence criteria and linear stability of these solutions, while less is known about their physical relevance. Are discrete breathers excitations present and detectable in real systems? If so, what could be an order of magnitude for a breather's lifetime?

A very interesting case is muscovite mica, where a model based on the propagation of DB's has been proposed to explain the long–standing puzzle of the formation of *mysterious dark lines* in the natural crystals [27]. In this study, the authors conclude that the new kind of lattice excitations introduced to account for the dark lines are associated with *quasi–one–dimensional* (QOD) behaviour in the potassium sheets of the mica crystal. Therefore, they introduce QOD chains, associated with special symmetry directions of the lattice. They are such that no shear forces emerge against disturbances parallel to them.

The discovery of high–temperature superconductivity in layered cuprates raised the question of the possibility of quasi–one–dimensional behaviour in the copper–oxide layers. In a molecular dynamic study of $YBa_2Cu_3O_7$, $Y_2Ba_4Cu_6O_{13}$ and La_2CuO_4, it was claimed that the non–puckered CuO_2 planes indeed contain QOD Cu–O chains [28]. Also Y–Y QOD chains have been found. Therefore, it seems very interesting to study the energy localisation properties of copper–oxide lattices, including the DB mobility along QOD chains. In a recent study, mobile DB's have been found in a full–blown model of CuO_2 planes, which included both interparticle and on–site nonlinear potentials [29]. The localised excitations have been found to be robust and propagate along QOD chains in the copper–oxide sheets.

[1] Sometimes they are also called Intrinsic Localised Modes (ILM)

About this thesis

It is the aim of the present thesis to tackle all the above mentioned questions in one run. To do so, we chose to perform EXAFS experiments at the Cu–K edge in $Ca_2CuO_2Cl_2$. This will allow us to study the local neighborhood of the Cu ions. In particular, we will probe the dynamics of the Cu–O pairs lying in the copper–oxide sheets. For this purpose, we shall develop a general technique for constructing atomic pair distribution functions from model interatomic potentials. We shall then employ this formalism to attack the problem of vibrational anharmonicity in the CuO_2 planes by fitting the potential parameters directly to the raw experimental data. Furthermore, we will perform a thorough temperature–dependent analysis of the atomic Debye–Waller factors. This will allow us to speculate about the presence of vibrational anharmonicity at the apical sites.

After the analysis and discussion of the experimental results, we shall move on to a theoretical analysis of the lattice dynamics of the copper–oxide sheets. We will first develop a simple two–parameter model of the lattice dynamics of such two–dimensional lattices within the harmonic model. This will lead us to calculate and discuss in detail the phonon spectrum. Such results will prepare the ground for tackling the study of discrete breathers. We will discuss a simple nonlinear model, based on the experimental results reported in the first part of this work. We shall analyse the spontaneous emergence of breathers within the scheme of *energy relaxation* experiments, attempt an estimate of their lifetime and discuss the dynamical constraints on the quasi–one–dimensional propagation of such solutions along preferred directions in the planes.[2] Here is how the present work is organised:

Chap.1 The first chapter is devoted to a review of the basic structural and physical properties of cuprates. Particular attention will be paid to the above–cited family of oxyhalides. The chapter ends with a discussion of the existing experimental data regarding the Cu–O interatomic potential in the CuO_2 planes.

Chap.2 In this chapter we shall introduce the basics of EXAFS spectroscopy. From a simple derivation of the main features of the theory underlying it, to a simple but complete discussion of the details of our experiment.

Chap.3 The last three chapters are entirely dedicated to the original contribution to this thesis. Here we introduce and develop a pair distribution function based on quantum perturbation theory. It is designed to incorporate directly the parameters describing the interatomic potential of the given pair through its Taylor expansion. We shall thoroughly illustrate the properties of the distribution function and carefully examine its sensitivity to the potential parameter. For this purpose, we shall set up an easy and robust procedure based on the statistical F–test.

[2] It should be noted that QOD chains, as introduced for mica, are isolated from the rest of the lattice just by symmetry requirements. No prescription comes from their symmetry properties on the *dynamical* coupling of QOD chains with the neighbouring rows of atoms. Hence, isolation by symmetry of a QOD chain could be regarded as a necessary but not sufficient condition for the propagation of DB's in a lattice without lateral spread of energy. Therefore, we think that in a nonlinear dynamical model of CuO_2 planes it is important to focus on both the dynamics and symmetry constraints on QOD chains.

Chap.4 In this chapter we present the data analysis of our experiment. We begin presenting the general fits of the whole spectra, based on the simple harmonic model of lattice vibrations. We still can learn much from such analysis regarding the dynamics of the Cl ions, and we shall discuss these results in detail. Then we move on to a closer examination of the contribution from the Cu–O pair. In the last sections, we shall present an analysis of the Cu–O interatomic potential based on the pair distribution function developed in the previous chapter.

Chap.5 The last chapter is entirely devoted to a detailed study of the lattice dynamics of the CuO_2 planes. As a start, we will present a careful analysis of the linear spectrum (phonon bands) based on a simple model with two force constants. We shall discuss in detail two different (isotropic–force and anisotropic–force) models and also comment on the phonon eigenvectors. Results from numerical simulations are provided at the end of this first part to corroborate the analytical calculations. This analysis provides the necessary background for the interpretation of the subsequent numerical experiments. Based on the experimental results discussed in the first part, we will simulate a simple nonlinear model and show how it is possible to observe the spontaneous emergence of breathers in a copper–oxide plane. We will discuss the properties of such solutions and attempt a definition and a quantitative estimate of their lifetime. The chapter ends with a discussion of the dynamical constraints built in the model on the quasi–one–dimensional propagation for the given geometry of the CuO_2 lattice. The consequences on the lifetime of the breathers will also be examined.

Chapter 2

High–T_c superconductors

In this introductory chapter we shall describe the principal structural properties of high–T_c copper oxides, including a review of the models commonly used in the literature to describe their lattice dynamics. A brief review of the main physical properties of cuprates is reported in appendix A. Particular attention will be here devoted to the ancestor of the Cl–based oxide–halide superconductors, the compound $Ca_2CuO_2Cl_2$, whose vibrational properties are studied in this thesis. We end the chapter by providing a critical review of what is available in the literature regarding the interatomic potentials of CuO_2 planes in cuprates. This information will be the bench–mark for some of the experimental results reported in this thesis.

2.1 Structure and electronic properties of high–T_c superconductors

In spite of their complex lattice structures, it is possible to identify some general features in all families of high–T_c copper oxides (cuprates). Their structure is sketched in Fig. 2.1. All cuprates are layered materials which alternate $n \leq 3$ CuO_2 sheets[1] and *insulating* blocks. These are also called reservoir layers and are formed by oxides of various elements such as alkali metals (Ca, Sr, etc), metalloids (Tl, Bi, Hg, Pb), rare earths (La, Ce, Nd) or Cu itself. The number n of CuO_2 planes is fixed for each compound. If $n > 1$, the n CuO_2 layers are separated by planes of rare earths (Y, Eu, Er, etc.), or alkali metals (Ca, Sr, etc.) (Y blocks in Fig. 2.1).

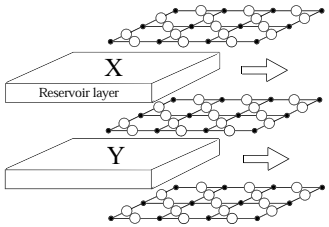

Figure 2.1: Schematic representation of the layered structure of cuprate superconductors.

The generic structure of all cuprates is a compound known as perovskite. Such structure is very common in nature and is characteristic of many natural and synthetic

[1]Indeed, some compounds with $n = 4$ are documented among all the alchemic attempts towards greater T_c's present in the literature, see Table I.

compounds, which exhibit a wide variety of physical and electric properties. This confirms the extreme versatility of such lattice structure and its tolerance against structural and stoichiometric manipulations. The cubic perovskite structure ABD_3 is represented in Fig. 2.2. The A and B ions are both metallic cations - with B usually a small transition metal. The D ions are usually non–metallic negative ions. More than 20 elements can lie at site A and more than 50 at site B. This explains the great number of possible existing combinations. Usually an O ion sits at site D, but also halogen ions (F, Cl, Br) can be found in that position. The B cation lies at the centre of an octahedron, whose vertices are occupied by D ions, while the A ion is surrounded by 12 D ions at a greater distance. It is clear from Fig. 2.2 (b) that the perovskite structure is formed by repeated sequences of alternating AD and BD_2 planes. In the copper–oxides, D=O and B=Cu. Hence, any cuprate structures can be obtained from the perovskite lattice by replacing the AD planes with some more complicated insulating blocks. In the case $n > 1$, some other insulating sheets will be present in between the CuO_2 sheets. As a result, the cuprate unit cell will be tetragonal with the c dimension greater than the a and b sides.

Two of the most known cuprate structures are shown in Fig. 2.3. These are the $RBa_2Cu_3O_{7-\delta}$ series (R=Y, Eu, Nb, Pr) and $La_{2-x}(Ba,Sr)_xCuO_4$, which was the first cuprate to exhibit high–T_c superconductivity [1] (see also appendix A).

The total coordination number of the Cu ions lying in the CuO_2 sheets depends on the number of adjacent CuO_2 layers. If $n = 1$, the Cu ion is octahedrically coordinated. The O ions above and below the plane belong to the reservoir layers and occupy the so-called *apical* position (Fig.2.4 (a)). If $n = 2$, each Cu is coordinated to five O ions in a pyramidal structure. In this case, there is only one apical oxygen (Fig.2.4 (b)). If $n = 3$, the Cu ions in the central CuO_2 layer are tetra–coordinated to its planar O neighbour (Fig.2.4 (c)), while the ones lying on the outer planes are coordinated

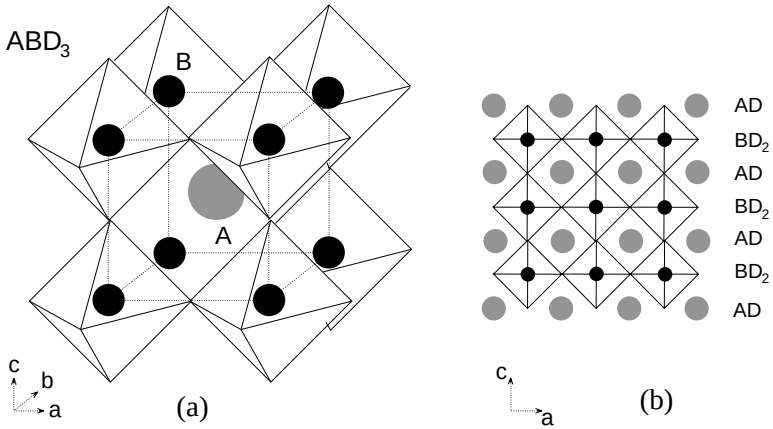

Figure 2.2: (a) The cubic structure of perovskite ABD_3. The D ions lying at the vertices of the octahedra are not indicated. (b) Scheme of the layered structure of the perovskite lattice.

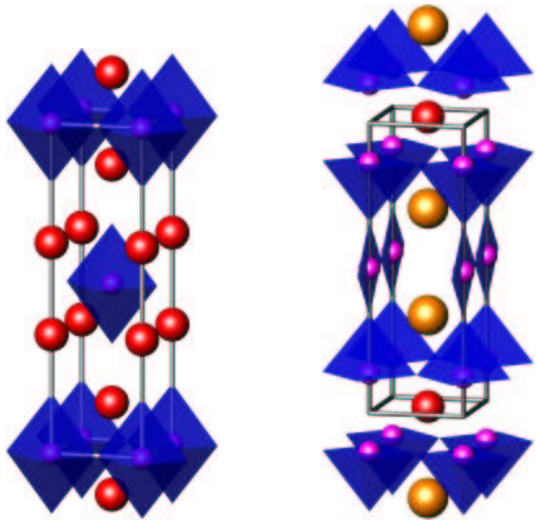

(a) (b)

Figure 2.3: (a) Unit cell of La_2CuO_4. The red atoms are lanthanum ions. Explicitly shown are the coordination octahedra around the copper ions. (b) Unit cell of $YBa2Cu3O_7$. Yellow and red atoms are Barium and Yttrium ions, respectively. Explicitly shown are the coordination pyramids of copper ions (magenta), and the Cu–O chains (vertical squares).

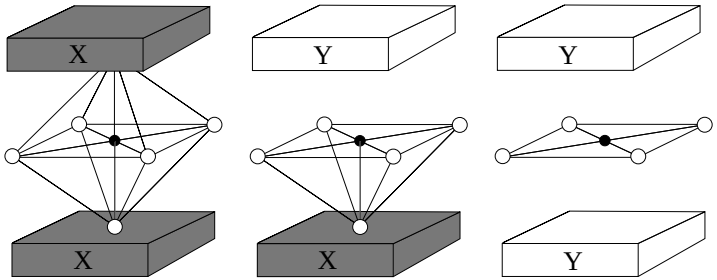

(a) (b) (c)

Figure 2.4: Coordination of the Cu ions (black circles) in the CuO_2 sheets with their O neighbours (white circles): (a) n=1: octahedrical; (b) n=2: pyramidal; (c) n=3 (internal plane): planar.

in a pyramid structure (Fig.2.4 (c)). The distance between each Cu ion and its four coplanar O neighbours is approximately 1.9 Å, which is shorter than the sum of the

respective ionic radii ($\approx 2.1\mathring{A}$). On the contrary, the distance between Cu ions and the apical oxygens ranges between 2.2 and 2.4 Å([31]). Therefore, we can conclude that the Cu–apical O bonds are essentially ionic in nature, while the planar bonds are mostly covalent.

The structure of the CuO_2 planes is sketched in Fig. 2.5. The electric field produced by all (apical and planar) neighbouring oxygen atoms splits the degenerate Cu d orbitals. For octahedrically coordinated copper atoms, the four d orbitals are split in two groups: the lowest energy set comprises the degenerate d_{xy}, $d_{xz}$and d_{yz}, while the $d_{x^2-y^2}$ and d_{z^2} orbitals have their energy increased. In the case of pyramidal coordination or for octahedrons elongated [2] along c, these two groups are split further, and the energy of the $d_{x^2-y^2}$ orbital is promoted the highest. The reason is that the $d_{x^2-y^2}$ orbital protrudes its lobes towards the lobes of the neighboring oxygen p orbitals farther than the other d orbitals (see section 6.4).

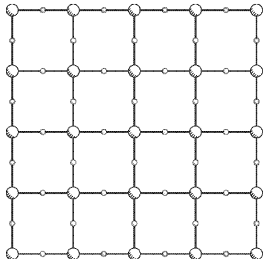

Figure 2.5: The CuO_2 structure. Smaller circles represent the oxygen atoms.

Each family of cuprates has an *ancestor* compound, which is an insulating antiferromagnet. In such compounds, the nominal charges of Cu and O are +2 and −2, respectively. Thus, the $d_{x^2-y^2}$ planar orbitals are half–filled, which means that there is one electronic hole at each Cu site. By performing band calculations (also in the simple tight–binding approach), one can show that the three bands originating from the Cu $d_{x^2-y^2}$ and O p_x, p_y orbitals are antibonding, non–bonding and bonding, respectively. Moreover, in respect of the cell neutrality, each lattice site contributes five electrons to fill these bands. Hence the upper anti–bonding band is half–filled. Ordinary band theory would then prescribe a metallic behaviour for the non–doped compounds, with electronic conduction taking place in the copper–oxide sheets. However, the mother–compounds are insulators. The reason for this is that the spins of holes at neighbouring sites are antiferromagnetically coupled through the diamagnetic O^{2-} lying in between them (superexchange interaction [32]). In this state, electronic conduction is strongly inhibited and one has the so–called Mott insulator [33]. In other words, the transfer of one electron from a Cu ion to its neighbour is prohibited, since overcoming the coulombic[3] potential energy barrier would cost more energy than that gained by the corresponding wavefunction spread [34]. The metallic–like conductivity of the doped compounds is determined by the additional holes that are injected in the CuO_2 sheets with doping.

[2]This effect is called Jahn–Teller effect. Actually, it was the suspect that this effect had to do with superconductivity that led Bednorz and Müller to the discovery of HTSC in the compound $La_{2-x}Sr_xCuO4$ [1].

[3]The Mott gap in the charge excitation spectrum is indeed set by the Coulomb interaction U or the charge transfer energy Δ (energy to remove an electron from the oxygen orbital and put it on the copper site), depending on which one is lower.

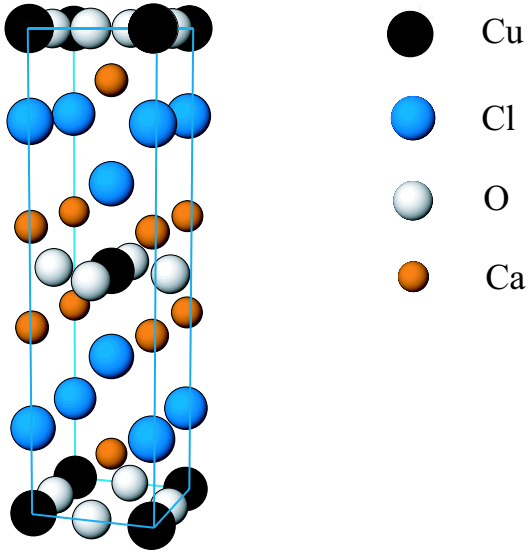

Figure 2.6: The tetragonal unit cell of $Ca_2CuO_2Cl_2$.

2.2 The family of Oxide–halides

The reservoir blocks do not participate directly in the superconductivity mechanism, which is in essence a two–dimensional phenomenon. However, these structural units provide the essential chemical control of the electronic requirements for superconductivity within the superconducting sheets, and the chemical make–up of these regions has a significant influence on T_c. The early years of synthetic research on high–T_c materials focused on the total or partial substitution of cations in the reservoir layers, and resulted in remarkable increases in the transition temperature. As the possibilities for devising and accomplishing novel syntheses in this way became increasingly exhausted, the researchers began to explore the options of anionic manipulations in cuprates. After the first questionable results,[4] there have now been major advances in the synthesis and characterisation of supeconductors containing anions other than the oxide ion O^{2-}. These materials are usually divided in two classes (see appendix A), containing respectively oxyanions ($(CO_3)^{2-}$, $(SO_4)^{2-}$, etc) and halide ions (F^-, Cl^-, etc). Particularly interesting are the two oxide–halide superconductors, $Sr_2CuO_2F_{2+\delta}$ and $(Ca,M)_2CuO_2Cl_2$ (M=Na, K) which have F or Cl ions in the apical position instead of O ions. They come from fluorination (chlorination) of Sr_2CuO_3 and Ca_2CuO_3, respectively. The structure of the latter compounds is closely related to that of La_2CuO_4 (see Fig. 2.3 (b)). In particular, one O^{2-} ion in the CuO_2 plane of La_2CuO_4 is missing such

[4]The first reports of superconductivity in fluorine–substituted Y–123, at $T_c = 155$ K [62] and $T_c = 148.5$ K [63] could not be reproduced.

that layers of CuO_6 octahedra are transformed into isolated parallel chains of CuO_4 squares. The process of fluorination (chlorination) replaces such ions with F (Cl) ions, which successively migrate to the apical position, leaving behind O ions again. The CuO_2 planes are then restored. However, due to the smaller ionic radius, the F ions (δ) also occupy interstitial positions between SrF layers. On the contrary, the bigger Cl ions just sit at the apical sites. As a consequence, in $(Ca,M)_2CuO_2Cl_2$ superconductivity is achieved by conventional doping of the material with (monovalent) cations. The structure of the non–doped compound $Ca_2CuO_2Cl_2$ is shown in Fig. 2.6.

Superconductivity in $(Ca,Na)_2CuO_2Cl_2$ was first reported in 1994 [21]. A maximum transition temperature of 26 K was measured, and strong indications were given that the superconducting carriers in this material are holes. First of all, the reason for this was that a highly oxidising atmosphere during the high–pressure doping with Na ions was always necessary. Secondly, it was the observed shortening of the a axis with increasing carrier concentration, which is in good agreement with the general trend for the hole–doped superconductors. These speculations were later confirmed by atomistic simulation studies [64]. Moreover, the fact that Cl ions sit just at the apical position and do not occupy interstitial positions has been confirmed by means of neutron–diffraction studies [53].

Very recently, the parent cuprate $Ca_2CuO_2Cl_2$ has been the object of a very interesting resonant inelastic X–ray scattering [5](RIXS) study [65]. For the first time, the Mott gap of such material has been directly probed, by monitoring the evolution along the high–symmetry directions in the BZ of a low–energy feature in the inelastic spectra. The experimental results were shown to be well explained in the framework of a $t'-t''-t'''-U$ Hubbard model. The study also concluded that the unoccupied Hubbard band has a different symmetry relative to the occupied band. This disparity between the occupied and unoccupied bands may indicate the direction for understanding the origin of the different behaviours of p–type and n–type cuprate superconductors.

To our knowledge, there are no experimental studies on the vibrational properties of the Cl–based oxide–halide superconductors. This observation alone would more than justify the EXAFS measurements which are in part reported in this thesis. Moreover, these studies on materials which lack apical O ions in favour of other species of anions are expected to clarify the role of the apical ions in the microscopic mechanism of superconductivity.

We end this section by reporting some structural data on the parent compound $Ca_2CuO_2Cl_2$ and the superconducting $(Ca,Na)_2CuO_2Cl_2$ in Table 2.1 [53].

2.3 Lattice dynamics of cuprates

The general interest in the high–T_c cuprates stimulated numerous experimental as well as theoretical investigations of the lattice–dynamical properties of these materials. On the experimental side, inelastic neutron scattering has given very detailed information

[5]RIXS spectroscopy is a powerful probe for electronic excitations in condensed matter, especially in strongly–correlated electron systems. In particular, an inelastically scattered photon can probe the full charge gap in a Mott insulator through the creation of a hole in the occupied band, thereby promoting an electron across the gap to the unoccupied band with a finite (tunable) momentum transferred into the system.

Ion	$Ca_2CuO_2Cl_2$	$(Ca,Na)_2CuO_2Cl_2$
Ca/Na	0.3958(1)	0.3959(3)
Cl	0.18298(6)	0.1820(1)
$a = b$ (Å)	3.8688(1)	3.8495(1)
c (Å)	15.0501(1)	15.1729(5)

Table 2.1: Cell dimensions and z coordinates of $(Ca,Na)_2CuO_2Cl_2$ and $Ca_2CuO_2Cl_2$. Ca and/or Na ions are at (0,0,z), Cu at (0,0,0), O at (0,1/2,0) and Cl at (0,0,z).

about the phonon in the whole Brillouin zone [66]. In addition, most of the zone–centre modes have been studied by Raman and infrared experiments [67]. On the theoretical side, the most rigorous *ab initio* methods are limited to the calculation of a few specific modes at high–symmetry points of the BZ because of computational complexities. Therefore, empirical models were developed for the calculation of the complete phonon dispersion relations and of the phonon density of states. First, these models are indispensable for the assignment of phonon peaks observed in inelastic neutron–scattering experiments. Second, the models provide some insight into the strength and nature of the interatomic forces. Last but not least, such models might help isolate anomalies in the phonon dispersion curves which are possibly due to strong electron–phonon coupling.

Models used in the early investigations of the phonon dispersion curves were more interpolation schemes, i.e. the parameters were just refined on the experimental data without imposing any further physical constraints (such as equilibrium lattice structure, elastic constants, etc.). At a later stage, attempts were made to reduce the number of parameters, keeping only those which lend themselves to an obvious physical interpretation. Very good agreement between model and experiment was achieved for several compounds [68], but there arose the problem of *transferability* of the model parameters from one compound to another. The first attempts to determine entirely transferable interatomic potentials suffered from the lack of broad data bases of lattice–dynamical properties [69]. Later attempts found more satisfactory results [70], in particular in concluding that a fully ionic model is not adequate for a comprehensive description of all cuprates, but remained isolated attempts. As a matter of fact, even at the present stage, the interest in such type of studies appears to have somewhat slowed down, and the problem of unexpectedly large differences between the systems investigated remains unsolved.

The coulombic type of interactions account for approximately 90 % of a typical crystal's lattice energy, and cuprates are no exception. Two types of models have been used to describe the coulombic interactions in cuprates. The rigid–ion model, which treats ions as point charges, and the polarisable–ion class of models which better accounts for the predominant ionicity of cuprates. Among the latter, the most used is the shell model [71], which parametrises the ionic polarisability in a very simple

fashion by using, at the same time, a comparatively small number of parameters. Thus every ion has a massless shell and a core, whose charges add up to the nominal valency of the ion (sometimes reduced by a factor of $90 - 95$ % to account for the screening effects). The shell and the core are coupled by a harmonic spring, which accounts for the ionic polarisability. Among the polarisable–ion class of models we also mention here the so–called distributed multipole model (DMM), introduced by Nozaki and Itoh to study the lattice dynamics of YBa2Cu_3O_7 [80]. They model the coulombic energy as multipole–multipole interactions, taking into account multipoles up to second order. They find that the monopole–monopole interactions amounts to about 97 % of the total coulombic energy, and only the quadrupole moments are effective higher–order moments to represent the structural anisotropy of YBa2Cu_3O_7.

The remaining interactions are usually written in the following fashion

$$V(r_{ij}) = A_{ij}\, e^{-r_{ij}/\rho_{ij}} - \sum_{n=6,8,\ldots} \frac{C_{ij}^{[n]}}{r_{ij}^{n}} \quad . \tag{2.1}$$

The function $A_{ij}\, e^{-r_{ij}/\rho_{ij}}$ is a *repulsive short–range* term. It represents the excluded–volume interactions from the overlap of the closed–shell ion wavefunctions. This is the main factor counteracting the coulombic term and determines the equilibrium lattice parameters for an ionic solid. The parameter ρ_{ij} gives a measure of the potentials *hardness*, which defines the radial shape of the ion wavefunctions and hence the rate at which repulsion falls off with separation. The parameter A_{ij} controls the amplitude of the repulsion at a given separation and is primarily dominated by the ionic radii. The remaining terms model the *dispersion* interactions of the ions. These terms are always attractive and are present due to the effect of perturbations in an ion's electron distribution on a neighbouring ion's electron distribution. The $C^{[6]}$ term is due to an instantaneous dipole–induced dipole interaction (Van der Waals) while the $C^{[8]}$ is due to a dipole–induced quadrupole interaction. The exponential plus $1/r^6$ term is usually referred to as *Buckingham* potential, and is usually present also if the ionic polarisability is accounted for within the shell model.

Although the nature of the Cu–O bonds in the copper–oxide layers is predominantly covalent, in the lattice–dynamical studies reported in the literature we have found that no specific potential energy function is used. Instead, the functional form 2.1 is extended, along with the ordinary coulomb interaction, to the Cu–O pairs as well. The only exceptions we have found are Refs. [72] and [73]. The first work introduces in YBCO for both the Cu–O pairs in the planes and in the chain networks a covalent potential of the Lippincot-Schröder type

$$V(r_{ij}) = -cD \exp\left[-\frac{(r_{ij} - r_o)^2}{2c\rho r_{ij}}\right] \quad , \tag{2.2}$$

along with ordinary Buckingham and coulomb potentials. The second work attempts a microscopically–based description of atomic interactions through an extension of the Vissher–Falicov potential [74]. This potential explicitly takes into account the exchange–correlation effects present in cuprates both because of their layered structure and low density of electrons. Such potential has the following form

$$V(r_{ij}) = \frac{e^2 Z_i Z_j}{4\pi\varepsilon_o \kappa}\left[\frac{1}{r_{ij}} - v_{el}\right] \quad , \tag{2.3}$$

where κ is the dielectric constant and v_{el} is the contribution from electron exchange–correlation interactions, which is given in a complicated integral form.

It is interesting to compare all the phenomenological potentials reported in the literature to describe the Cu–O pairs. A useful way to do this is to work out the corresponding nearest–neighbour force constants for the Cu–O pair.[6] Let V^R and V^C indicate the repulsive and Coulomb potentials, respectively, and r_{ij}^{α} ($\alpha = x,y,z$) be the equilibrium interparticle vectors relative to the (i,j) atomic pair. In the central–forces approximation, the expressions for the repulsive and Coulomb force constants are [75],

$$\mathcal{D}^R_{\alpha\beta}(i,j) = -\left[(A_{ij} - B_{ij})\frac{r_{ij}^{\alpha} r_{ij}^{\beta}}{r_{ij}^2} + \delta_{\alpha\beta} B_{ij}\right] \quad , \tag{2.4}$$

and

$$\mathcal{D}^C_{\alpha\beta}(i,j) = -\frac{Z_i Z_j e^2}{4\pi\epsilon_0}\left[\frac{\delta_{\alpha\beta} r_{ij}^2 - 3 r_{ij}^{\alpha} r_{ij}^{\beta}}{r_{ij}^5}\right] \quad , \tag{2.5}$$

respectively, where

$$A_{ij} = \frac{d^2 V^{SR}}{dr_{ij}^2} \qquad \text{and} \qquad B_{ij} = \frac{1}{r_{ij}}\frac{dV^{SR}}{dr_{ij}} \quad . \tag{2.6}$$

As an additional piece of information, it is customary to introduce a measure of *force anisotropy* from expressions (2.6) in the simple form

$$\chi_{ij} = B_{ij}/A_{ij} \quad . \tag{2.7}$$

We shall come back later on this point in Chapter 6, where we calculate the force–anisotropy parameter χ for a CuO_2 lattice by means of molecular orbital theory.

The total force constant is given by

$$\mathcal{D}^{RI}_{\alpha\beta}(i,j) = \mathcal{D}^R_{\alpha\beta}(i,j) + \mathcal{D}^C_{\alpha\beta}(i,j) \quad . \tag{2.8}$$

Expression (2.8) is fine for rigid–ion models, where the Coulomb potential energy is that of point charges. The task of working out the Coulomb force constants in the framework of a shell model is a more complicated task, since the ionic polarisabilities are to be taken into account. To get an estimate of the shell model correction to the rigid–ion force constants, we can follow the calculation reported in Ref. [75], performed for a diatomic lattice (see appendix B for the details).

We gather in Table 2.2 results for the Cu–O force constants and force–anisotropies derived from some of the model potentials appeared in the literature. The predictions of the shell model have been worked out by using the value $\beta = 8\pi/3$, characteristic of LO–modes in alkali–halides crystals. However, we observe that such results are little sensitive to small variations of β.

In principle, it is not known whether the potential parameters of the Cu–O pairs in the copper–oxide sheets are the same in the different families of cuprates. However,

[6] We remark that there is an intrinsic source of ambiguity in the simple procedure outlined below, stemming from the long–range nature of the Coulomb interactions. In fact, the potential parameters given in the literature are refined self–consistently for the motion of all atoms in the unit cell, while we are considering electrostatic interactions within the pair only.

Compound	k_2 (eV/Å^2)	B/A	Ref.
$YBa_2Cu_3O_{7-\delta}$	51.3	0.15	[72] ($\circ$)
$YBa_2Cu_3O_7$	68.3	0.15	[79] ($\circ$)
$YBa_2Cu_3O_7$	34.6	0.1	[81] ($\circ$)
CuO	23.0	0.19	[83] ($*$)
$Hg_2Ba2Ca_2Cu_3O_{8+\delta}$	24.6	0.15	[84] ($*$)
$Sr_2CuO_2F_{2+\delta}$	25.8	0.15	[85] ($*$)
$(La,Sr)_2CuO_4, Nd_2CuO_4, YBa_2Cu_3O_{6,7}$	31.7	0.14	[70] ($*$)
$Ca_CuO_2Cl_2$	26.2	0.15	[86] ($*$)

Table 2.2: Comparison of the Cu–O force constant calculated from different semi–empirical potentials with Eqs. (2.8) and (B.1). ($\circ$) = rigid ion model, ($*$)=shell model.

there is no particular reason to believe that the different reservoir blocks may cause strong changes in such parameters. One would also conclude so by looking at Table 2.2. We note that the predictions of the shell models are anyway much more consistent among each other than the ones of rigid–ion models. This is also confirmed by the direct phonon band calculations. We also observe that we expect the force constants reported in Table 2.2 to be slightly underestimated with respect to the *true* values, since we have only accounted for the nearest–neighbour Coulomb terms.

Chapter 3

Principles of EXAFS spectroscopy

3.1 Introduction

In this chapter we shall describe the principles of Extended X-ray Absorption Fine Structure (EXAFS) spectroscopy. This experimental technique is based on the selective absorption of X–rays by a particular atomic species in the sample under study. In particular, the characteristic modulations of the absorption coefficient (fine structure) carry important information on the lattice structural and dynamical properties of the region around the absorber. Despite the fact that such modulations were both experimentally [88] [89] and theoretically[90] [91] studied since the 20's, it is only in the 70's that the their utility has been recognized by the physicists [92]. The full rigorous explanation of the phenomenon, along with the availability of the new powerful synchrotron radiation sources, contributed in the last decades to making EXAFS one of the best known and used techniques of structural analysis in condensed matter physics.

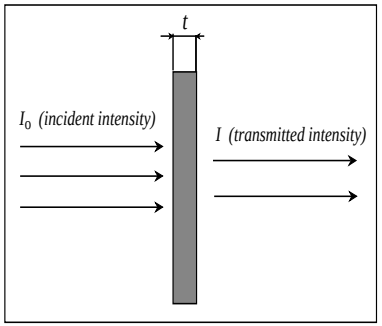

Figure 3.1: Scheme of an X–ray attenuation experiment.

3.2 X-ray absorption spectroscopy

The relevant X-rays in EXAFS spectroscopy have energies in the range 1 to 50 KeV approximately (wavelengths in the range 0.25 to 12.4 Å). This will be our reference interval in the following.

When a collimated beam of monochromatic radiation crosses a homogeneous slab

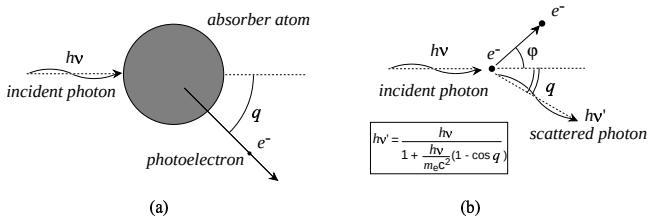

Figure 3.2: (a) Scheme of the photoelectric absorption process. The incident photon is absorbed and an electron ejected at an angle θ. The conservation of momentum is guaranteed by the atom recoil. (b) Compton scattering. the incident photon has energy $h\nu$, the scattered one $h\nu'$ while the scatterer electron is practically free (rest energy $m_e c^2 = 511$ keV)

of thickness d, its intensity is reduced according to the Lambert–Beer law

$$I = I_o e^{-\mu d} \quad , \tag{3.1}$$

where I_o is the intensity of the incident beam and I the intensity of the transmitted one (see Fig. 3.1). The coefficient μ is called *linear absorption coefficient*. It depends, besides the energy of the incident photons, on the sample density and the atomic species present in it. In the above energy interval, the attenuation is essentially due to two processes characteristic of the radiation–matter interaction:

1. The dominant effect is **photoelectric absorption** (Fig.3.2 (a)): a photon is absorbed, and a core electron is ejected (*ionisation*) or promoted in a bound state near the continuum (*excitation*).

2. The photon can also be simply *scattered*, either elastically (Rayleigh scattering) or inelastically (Compton scattering). The photon is elastically scattered by the core electrons, while it can exchange some energy with the outer electrons (Fig.3.2 (b)).

Both processes contribute to the attenuation of the incident beam. Depending on which process is dominant, it is possible to identify two groups of experimental techniques based on the use of X–rays:

- Absorption or emission **spectroscopy** $\Longrightarrow$ Probe for the electronic structure of the sample (e.g. XANES spectroscopy) or for the local short–range atomic order (EXAFS)
- Elastic **scattering** $\Longrightarrow$ Lattice structure and geometry of the sample
- Inelastic **scattering** $\Longrightarrow$ Electronic excitations (see Chapter 2)

Let us consider a material made of a single atomic species. According to the above considerations, the Lambert–Beer absorption coefficient can be expressed as the sum of two terms

$$\mu = \tau + \sigma$$

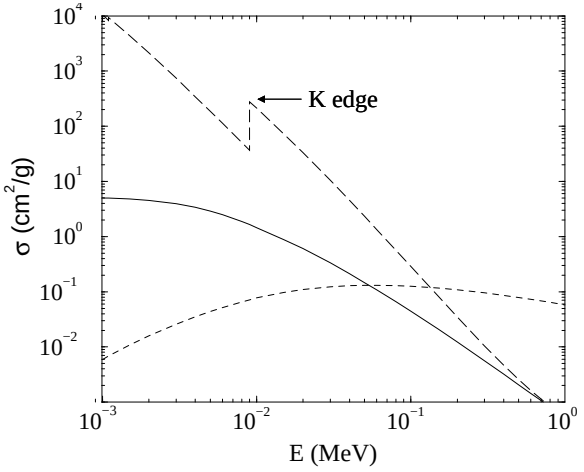

Figure 3.3: Partial cross sections for X–rays absorption by Copper [93]. The solid line is the contribution from Rayleigh scattering, the dashed line is the Compton cross section and the long–dashed line is the contribution from photoelectric absorption. Note the K–edge (8.9789 KeV).

where τ is the photoelectric absorption coefficient while $\sigma = \sigma_{el.} + \sigma_{Comp.}$ accounts for the scattering processes. The latter coefficients can be obtained by the corresponding electronic cross sections multiplied by the atomic number Z and the number of atoms per unit volume n. On the contrary, in the photoelectric absorption the cross section is necessarily atomic, since a photon cannot be absorbed by a single free electron without violating the energy–momentum conservation laws.[1]. For clarity, we show in Fig.3.3 the photoelectric absorption cross section along with the cross sections of the scattering processes in the case of copper. In general, for copper as for elements of low to medium atomic numbers, the photoelectric absorption is the dominant contribution to the total absorption coefficient in the range 1 to approximately $30 - 50$ KeV. The Compton scattering gets increasingly important at higher energies, and follow the so–called Klein–Nishina formula [94]. On the contrary, Rayleigh scattering becomes important at energies of a few KeV or for low Z atomic species.

In the energy interval relevant for X–rays absorption spectroscopy (XAS) the linear absorption coefficient is dominated by the photoelectric effect. Its trend vs energy displays the characteristic absorption edges, which correspond to the energy thresholds for the ejection of an electron from a core level. Above the threshold the absorption coefficient decreases approximately as Z^m/E^n, with $m \approx 4$ e $n \approx 3$ [95].

Edges are referred to in terms of the electronic core levels relative to the photoelectric transition. If the photoelectron comes from a $1s$ orbital, one has a K–edge. These are the highest in energy. In order of decreasing energies edges can be classified

[1]This is because of the finite rest mass of the electron

in the following fashion

edge	K	L_I	$L_I{}^I$	$L_I{}^{II}$	M_I	$\cdots$
level	$1s_{1/2}$	$2s_{1/2}$	$2p_{1/2}$	$2p_{3/2}$	$3s_{1/2}$	$\cdots$

The energy of a given edge increases with the atomic number Z. Hence, it uniquely identifies the absorbing atomic species.

Right above an absorption edge, it is possible to observe a fine structure (XAFS), characterised by damped oscillations superimposed to the power–law decrease of the absorption coefficient. For isolated atoms (noble gases, metallic vapours) it is confined to a region a few eV above the edge, and is due to electronic transitions towards unoccupied levels. For condensed–matter systems or molecular gases such oscillations extend up to a few KeV above the edge, and can be roughly divided in three different regions. The first $40 - 50$ eV above the edge are known as the near–edge structure (XANES). The next wider region is the extended fine structure (EXAFS), characterised by oscillations of decreasing amplitude. Depending on the temperature and the lattice structure of the sample, it can be even $2 - 3$ KeV wide. As we discuss it below, such oscillations contain information on the short–range lattice order. On the contrary, the peaks in the XANES region carry information on the electronic structure of the absorber atom and on the partial density of unoccupied states (and hence on its oxidation state).

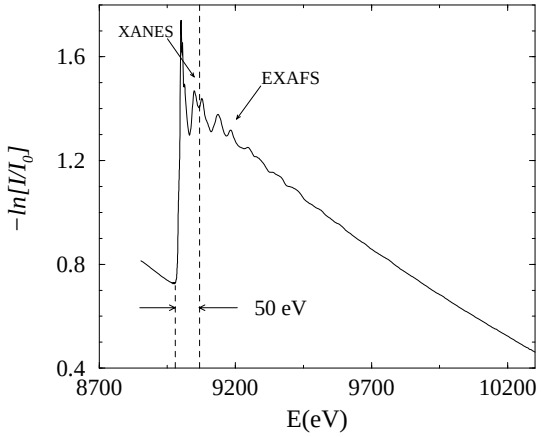

Figure 3.4: Fine structure of the Cu K–edge (8,079 eV) for a sample of $Ca_2CuCl_2O_2$ at T=10 K. Explicitly shown are the XANES and EXAFS regions (see text)

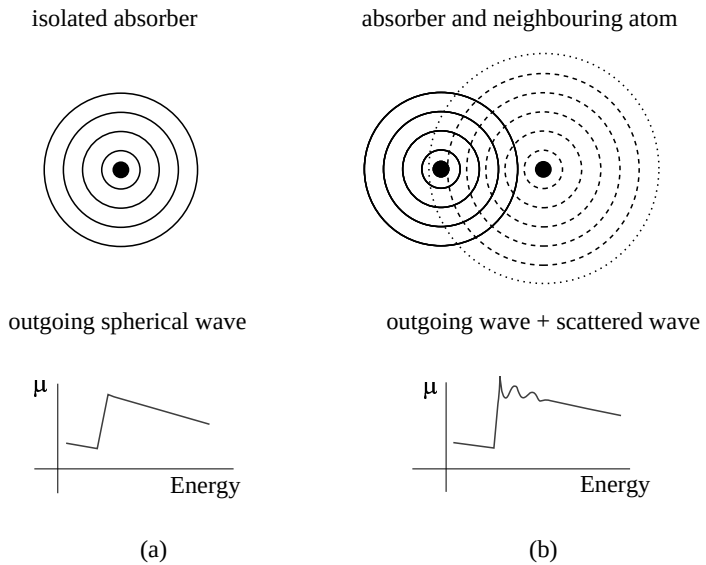

Figure 3.5: Scheme of the mechanism responsible for the EXAFS modulation of the absorption coefficient. (a) Isolated atom: the ejected photoelectron propagates undisturbed. (b) Non–isolated atom: the outgoing electron wave interferes with the waves backscattered from the neighbouring atoms.

3.3 The EXAFS mechanism

We shall here provide a qualitative description of the EXAFS modulation of the linear absorption coefficient.

The photoelectron extracted from a core level of energy E_o (threshold energy) upon absorption of a photon of energy $h\nu$ has a kinetic energy $K = h\nu - E_o$. Its quantum state is described by a spherical wavefunction whose wavelength is

$$\lambda = \frac{h}{p} = \frac{2\pi}{k}$$

where k is the modulus of the electron wavevector

$$k = \frac{1}{\hbar}\sqrt{2m[h\nu - E_o]} \quad . \tag{3.2}$$

If the absorber atom is isolated, the ejected electron propagates freely (Fig. 3.5 (a)) . On the contrary, if the absorber is surrounded by other atoms, the photoelectron is backscattered by its neighbouring atomic shells (Fig. 3.5 (b)). The interference between the outgoing wave and the backscattered waves can be either constructive or destructive, depending on the wavelength of the photoelectron and on the distances

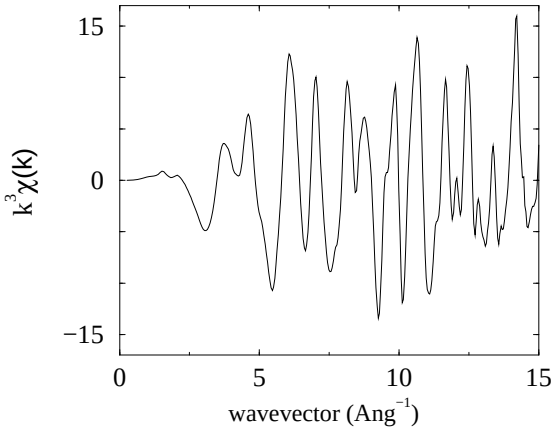

Figure 3.6: EXAFS signal relative to the spectrum shown in Fig. 3.4. The EXAFS signal $\chi(k)$ has been multiplied by k^3 in order to highlight the small–amplitude contributions in the high–k region.

of the backscattering centres from the absorber. On the other hand, the photoelectric absorption probability depends on the electron wavefunction at the absorber site. Hence, the absorption coefficient will be lower or greater depending on whether the interference of the outgoing and backscattered waves is, respectively, constructive or destructive.

In order to isolate the EXAFS oscillations, it is customary to introduce the non–dimensional function $\chi(k)$ (Fig. 3.6), conventionally expressed as a function of the wavevector k. It is defined as

$$\chi(k) = \frac{\mu - \mu_o}{\mu_o} \quad , \tag{3.3}$$

where μ_o is the absorption coefficient of the isolated atom. Typically the function $\chi(k)$ amounts to a fraction from 1 to 20% of the atomic absorption [95].

3.4 Simple derivation of the analytic expression of the EXAFS signal $\chi(\mathbf{k})$

It is possible to give a simple description of the EXAFS phenomenon within a semi–classical approximation, whereby the electromagnetic radiation is dealt with classically and we retain the full quantum treatment of matter.

Let us consider an X–ray beam of frequency ω incident on the sample. Let us assume that its intensity is small enough to allow for a perturbative approach of the radiation–matter interaction. The transition rate (transition probability per unit time) $W_{i\to f}$ from an initial state $|\Phi_i\rangle$ to a final state $|\Phi_f\rangle$ of the absorbing atom is described, to first order in the perturbation, by the well known Fermi golden rule

$$W_{i\to f} = \frac{2\pi}{\hbar} \mid \langle \Phi_i | H_{int} | \Phi_f \rangle \mid^2 \rho(E_f) \quad , \tag{3.4}$$

where H_{int} is the hamiltonian operator describing the interaction between the electromagnetic field and the absorber atom, while $\rho(E_f) = (dN/dE)_f$ is the density of final states. The operator H_{int} can be written as [96] [97]

$$H_{int} = \frac{e}{mc} \sum_j \vec{A}(\vec{r}_j) \cdot \vec{p}_j + \frac{e^2}{2mc^2} \sum_j \mid \vec{A}(\vec{r}_j) \mid^2 \quad , \tag{3.5}$$

where $\vec{r}_j$ is the position vector of the j–th electron in the atom, $\vec{p}_j = -i\hbar\vec{\nabla}_j$ the corresponding momentum operator, and $\vec{A}(\vec{r}_j)$ the vector potential describing the incident radiation. In the following, we shall neglect the quadratic term $\propto |\vec{A}|^2$ (*weak field approximation*). This approximation, along with the assumption of validity of the perturbative regime, amount to consider just single–photon emission and absorption processes, neglecting two–photon processes [97]. We can write

$$\vec{A}(\vec{r},t) = 2\vec{A}_o \cos(\vec{k}\cdot\vec{r} - \omega t) = \vec{A}_o [\, e^{i(\vec{k}\cdot\vec{r}-\omega t)} + e^{-i(\vec{k}\cdot\vec{r}-\omega t)}\,] \quad . \tag{3.6}$$

If we just consider the term $e^{i(\vec{k}\cdot\vec{r}-\omega t)}$, which accounts for absorption transitions, we get

$$W_{i\to f} = \frac{2\pi}{\hbar} \left(\frac{e}{mc}\right)^2 A_o^2 \mid \langle \Phi_i | \sum_j e^{i\vec{k}\cdot\vec{r}_j} \hat{\epsilon}\cdot\vec{p}_j | \Phi_f \rangle \mid^2 \rho(E_f) \quad , \tag{3.7}$$

where $\hat{\epsilon}$ is the polarisation unit vector of the vector potential. In order to proceed, we make two further simplifications

[1] **Single–electron approximation**: It amounts to assume that, as a consequence of the ejection of the core electron, all other $Z-1$ electrons (*passive* electrons) adiabatically follow the new potential created by the core hole. It takes $10^{-16} - 10^{-17}$ s for a core electron to leave the atom (considering a binding energy of the order of 10 eV). We can assume that this time is much less than the relaxation time of the other orbitals. As a consequence, we can reduce the formal treatment of EXAFS oscillations to the calculation of the matrix element in Eq. (3.7) between the initial state $|\phi_i\rangle$ and the final state $|\phi_f\rangle$ of the photoelectron only (*single–electron* approximation).

[2] **Electric dipole approximation**: It amounts to reject all terms in the expansion of $e^{i\vec{k}\cdot\vec{r}_j}$ but the zero–order term

$$e^{i\vec{k}\cdot\vec{r}_j} = 1 + i\vec{k}\cdot\vec{r}_j - (\vec{k}\cdot\vec{r}_j)^2/2! \ldots \simeq 1 \quad .$$

This approximation is legitimate whenever $\mid \vec{k}\cdot\vec{r}_j \mid^2 \ll 1$, i.e. for photon wavelengths much greater than the linear dimension of the system. More precisely, in the single–electron approximation the photon wavelength must be compared with the core orbital that is ionised. The dipole approximation amounts then to considering the electric field constant over such region. For the Cu K–edge (8,979 eV), which will be analysed here, since $R_o \simeq 0.0125$ Å(2), it is $(kR_o)^2 = [2\pi\nu/cR_o]^2 \approx 5\times10^{-3}$, and the zero–order approximation is more than justified.

[2]Approximate value calculated in the hydrogen model. However, this simple model is more than adequate for K photoelectrons.

Exploiting the two above approximations, Eq. (3.7) reduces to

$$W_{i\to f} = \frac{2\pi}{c}\,\alpha\,(A_o^2\omega^2) \mid \langle \phi_i | \vec{\epsilon}\cdot\vec{r} | \phi_f \rangle \mid^2 \rho(E_f) \quad , \tag{3.8}$$

where $\alpha = e^2/\hbar c \simeq 1/137$ is the fine–structure constant for electromagnetic interactions and $\vec{r}$ the position vector of the photoelectron. It is possible to express A_o^2 in terms of the photon density $n(\omega)$ (see e.g. [97]) as

$$A_o^2 = n(\omega) \left[\frac{2\pi\hbar}{\omega} c^2\right] \quad . \tag{3.9}$$

Furthermore, the total absorption cross section for photons of frequency ω is given by $\sigma = W_{i\to f}/n(\omega)c$. Hence, from Eq. (3.8) we get

$$\sigma_{phot}(\omega) = 4\hbar\omega\ \pi^2\,\alpha \mid \langle \phi_i | \vec{\epsilon}\cdot\vec{r} | \phi_f \rangle \mid^2 \rho(E_f) \quad . \tag{3.10}$$

We know that in the EXAFS region the absorption is dominated by the photoelectric effect. Hence, $\mu \simeq \tau$, i.e.

$$\mu = N_a \sigma_{phot}(\omega) = 4\hbar\omega\pi^2 N_a \alpha \mid \langle \phi_i | \vec{\epsilon}\cdot\vec{r} | \phi_f \rangle \mid^2 \rho(E_f) \tag{3.11}$$

where N_a is the number of absorber atoms per unit volume.

Let us now discuss the effect of the photoelectron backscattering on the absorption coefficient in the EXAFS region in the case of a $1s$ core hole (K–edge). Since the dipole selection rule prescribes $\Delta l = \pm 1$, the final state of the photoelectron will have p symmetry.

It is convenient to analyse separately the case of isolated absorber and multi-atomic system.

Isolated absorber The electron, ejected from the absorber, feels the Hartree–Fock potential due to the other electrons in a region of the order of the atomic dimension r_o, while it is free outside such region. Let k be its wavevector. The outgoing wave ϕ_f has the following form [98]

$$\phi_f(\vec{r}) = \begin{cases} \psi_o(\vec{r}) & r \le r_o \\ N_1 h_1^+(kr)\, e^{i\vartheta_1} Y_{1,m}(\theta,\phi) & r > r_o \end{cases} \quad . \tag{3.12}$$

For $r \le r_o$, the wavefunction is the one corresponding to the Hartree–Fock potential, while outside a sphere of radius r_o the wavefunction represents the appropriate solution for a free electron of kinetic energy $\hbar^2k^2/2m$. $N_{l=1}$ is a normalisation factor. The spherical harmonic $Y_{l,m}(\theta,\phi)$ describes the angular part of the wavefunction, while the radial dependence is accounted for by a spherical Hankel function $h_l^+(kr)$, which is the solution of the radial equation for the function $R(r)$ with zero potential in the case of angular momentum l

$$\frac{d^2R}{d\rho^2} + \frac{2}{\rho}\frac{dR}{d\rho} + \left(1 - \frac{l(l+1)}{\rho^2}\right) R = 0 \qquad (\rho = kr) \quad .$$

The phase shift δ_l is necessary in order to match at the boundary $r = r_o$ the free electron wavefunction and the wavefunction of the core electron.

For high enough energies ($kr \gg 1$), one can replace the Hankel function with its asymptotic behaviour. We can therefore write [95]

$$\phi_f(\vec{r}) = \frac{i}{2}\,\frac{e^{i(kr+\delta_1)}}{kr}\,Y_{1,m}(\theta,\phi) \quad . \tag{3.13}$$

However, $|\phi_i\rangle$ is an atomic state localised in a region of the order of the atomic dimensions. Consequently, we can suppose that only a region of such extension contributes to the overlap integral in $\langle\phi_i|\hat{\epsilon}\cdot\vec{r}|\phi_f\rangle$. Therefore, for isolated atoms we can conclude that

$$\mu_o \propto |\,\langle\phi_i|\hat{\epsilon}\cdot\vec{r}|\psi_o\rangle\,|^2 \tag{3.14}$$

Non–isolated absorber The derivation that we shall include in this thesis has been chosen because it is a simple one, but at the same time it underlines the main physical aspects of the phenomenon under study. The interested reader can find other more rigorous and complete derivations e.g. in refs. [99] [100] [101].

In the EXAFS region, the kinetic energy of the photoelectron is much greater than the interaction energy with the neighbouring atoms. Therefore, the scattering can be studied in the usual perturbative approach and the wavefunction of the final state can be written as

$$|\phi_f\rangle = |\phi_o\rangle + |\delta\phi_f\rangle$$

where $|\delta\phi_f\rangle$ denotes the backscattered component. In order to determine its contribution we adopt the following simplifications.

Muffin–tin approximation for the potential – According to this approximation, three spatial regions are introduced (Fig. 3.7). Region I: spherically symmetric potential around the absorber. Region II: constant potential in the interstitial region. Region III: non–overlapping spherically symmetric potentials centred on the backscatterer atoms. The spherical potentials of the absorber and backscatterer atoms are matched at the boundaries with the constant potential. Moreover, one also assumes that atoms of the same chemical species are described by the same spherical potentials.

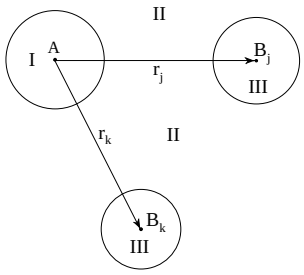

Figure 3.7: Scheme of the muffin–tin approximation. A is the absorber, while B_j and B_k are two neighbours that act as backscattering centres.

Isotropic sample [3] – In our experiments we employed linearly polarised radiation. Therefore, the dipole selection rules prescribe that the angular part of the final state of the ejected photoelectron is proportional to $Y_{1,0}(\theta,\phi)$. As a consequence, the probability that the electron is emitted within a given angle is proportional to $|Y_{1,0}(\theta,\phi)|^2 \propto \cos^2\theta$, where θ is the angle between the position vector of the electron and the polarisation vector of the electromagnetic field. As a consequence, the electron is emitted with the greatest probability along the field polarisation. In particular, the probability of emission along the direction of propagation

of photons vanishes. Hence, the absorption coefficient in ordered systems (as mono-crystals or oriented polycrystalline samples) depends on the direction of the polarisation vector with respect to the crystallographic axes.[4] On the contrary, in polycrystalline samples and amorphous materials all information is mediated over all possible directions of the polarisation vector with respect to the crystallographic axes. Hence, EXAFS provides information on average distances of the backscattering centres, but not information on the local symmetry of the absorber's neighborhoods. In the latter case, we can drop the angular part of the photoelectron wavefunction.

The scattering process can be described in the following fashion. In region II the radial part of the unperturbed wavefunction is described by the Hankel function $h_l^+(kr)$, which can be replaced by its asymptotic expansion in the EXAFS range of energies. Let us then imagine the spherical wave impinging on a neighbouring atom. The photoelectron energy is large, and therefore it interacts with the core electrons, while the interaction with the relatively free outer electrons can be neglected. We can thus approximate the photoelectron wavefunction with a plane wave in the small scattering region (*small atom approximation*). The backscattered spherical wave can be written as [103]

$$f_j(\alpha,k)\,\frac{e^{ikr'}}{r'} \quad ,$$

where r' is the distance from the scattering centre, α the scattering angle and $f_j(\alpha,k)$ the scattering amplitude.[5]. It is also necessary to match the outgoing wave with the backscattered wave in region I. Thus, we shall include in the latter the same phase factor $e^{i\delta_1}$. Therefore, being $r' = -\hat{r}_j\cdot(\vec{r}-\vec{r}_j)$, (with $\hat{r}_j = \vec{r}_j/r_j$), the total radial wavefunction in region II will be

$$\left[i\frac{e^{i(kr_j+\delta_1)}}{2kr_j}\right]\left\{f_j(\pi,k)\,\frac{e^{-ik\hat{r}_j\cdot(\vec{r}-\vec{r}_j)}}{|\,\hat{r}_j\cdot(\vec{r}-\vec{r}_j)\,|}\,e^{i\delta_1}\right\} \quad . \tag{3.15}$$

The term in square brackets is the amplitude of the outgoing wave incident on the backscatterer atom, at a distance r_j away from the absorber. Let $\psi_o(r)$ indicate the wavefunction relative to the isolated atom in region I. If we assume that the initial wavefunction is nonzero only in the vicinity of the nucleus (i.e. in a very limited region with $r \approx 0$), we can write the wavefunction of the final state in the following fashion [95]

$$\psi(r) = \psi_o(r) + \left\{i\frac{e^{2i(kr_j+\delta_1)}}{2kr_j^2}\,f_j(\pi,k)\right\}\psi_o(r) \qquad (r\approx 0) \quad . \tag{3.16}$$

[4] For example, if one of the absorber's neighbours lies along a direction orthogonal to the polarisation, it does not contribute to the backscattering of the photoelectron, since the emission probability along such direction vanishes.

[5] In general, the partial waves expansion gives

$$f(\alpha,k) = \frac{1}{k}\sum_{l=0}^{\infty}(2l+1)\,e^{i\delta_l}\sin\delta_l\,P_l(\cos\alpha) \quad ,$$

where δ_l is the phase change of the l–th component and $P_l(\cos\alpha)$ is the l–th order Legendre polynomial [98].

Inserting Eq. (3.16) in expression (3.11), and recalling Eq. (3.14), we get after some algebra

$$\chi(k) = \frac{\mu - \mu_o}{\mu_o} = \frac{|f_j(\pi,k)|}{kr_j^2} \sin[2kr_j + \varphi_j(k)] \quad . \tag{3.17}$$

In the derivation of Eq. (3.17), we have neglected $|\delta\psi|^2$, which is a small quantity and does not give rise to interference. Moreover, we have also introduced the *total phase shift* $\varphi_j(k) = 2\delta_1(k) + \vartheta_j(k)$, where $\vartheta_j(k)$ is the phase shift introduced by the complex backscattering amplitude $f_j(\pi,k) = |f_j(\pi,k)|\, e^{i\vartheta_j}$. In the general case of more than one backscattering centres, the calculations are complicated by multiple scattering (MS) effects (Fig.3.8). However, in many cases multiple scattering processes give a negligible contribution to the EXAFS signal. We shall comment further on that in the following. Neglecting MS contribution, the total EXAFS signal will be

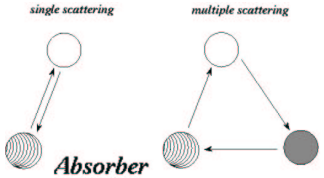

Figure 3.8: Single (SC) and multiple (MS) scattering processes. Arrows indicate the direction of motion of the photoelectron.

$$\chi(k) = \sum_j N_j \frac{|f_j(\pi,k)|}{kr_j^2} \sin(2kr_j + \varphi_j(k)) \quad , \tag{3.18}$$

where N_j is the number of atoms of the same species j at the same distance r_j from the absorber. These atoms form the j–th coordination shell, and the summation runs over all coordination shells.

3.5 Phenomenological corrections

In the derivation of Eq. (3.18) we have neglected some important phenomena concerning the environment of the photoelectron motion. The two most important factors to consider are: (1) multi-electronic excitations within the absorber atom and (2) inelastic processes and relaxation leading to a finite lifetime of the final state ϕ_f of the photoelectron. These are many–body effects, but can be incorporated in a phenomenological fashion in the simple theory of EXAFS.

- **Multi-electronic excitations**

As a matter of fact, the absorption of a photon with emission of a photoelectron is connected to a sudden variation of the potential felt by all other $Z-1$ electrons. In the large majority of cases, the relaxation of the passive electrons in the new potential proceeds smoothly without change of their quantum numbers. However, it may happen that such relaxation results in excitation (*shake–up*) or ionisation (*shake–off*) processes [104] [105] [106]. In these cases, a fraction of the energy made available by the absorption is lost by the photoelectron. Thus, its kinetic energy will be less than $\hbar\omega - E_o$. At any rate, the initial and final wavefunctions of the other $Z-1$ electrons are different. Thus, one cannot in principle consider just single–electron states in calculating the linear absorption coefficient. However, one can write [110]

$$\mu(\omega) = \mu_{el}(\omega) + \mu_{inel}(\omega)$$

where the two terms in the right-hand side refer to elastic and inelastic processes, respectively. Regarding elastic transitions, we know that the passive electrons adiabatically adapt to the new potential. As a consequence, $\mu_{el}(\omega)$ can be obtained from Eq. (3.8) by just replacing the matrix element present in it with

$$\langle \Phi_i^{Z-1} \phi_i | \vec{\epsilon} \cdot \vec{r} | \Phi_f^{Z-1} \phi_f \rangle \quad ,$$

where Φ^{Z-1} is the Slater determinant of the passive electrons' wavefunctions. We have seen that the time scales associated to the ejection of the photoelectron and the relaxation of the other electrons are markedly different. Hence, it is possible to separate the initial and final states ϕ_i and ϕ_f of the primary electron from the collective states Φ_i^{Z-1} and Φ_f^{Z-1}. As a result, the absorption coefficient in Eq. (3.11) acquires the multiplicative factor

$$S_o^2 = | \langle \Phi_i^{Z-1} | \Phi_f^{Z-1} \rangle |^2 < 1 \quad . \tag{3.19}$$

The S_o^2 factor is then the probability that the passive electrons, initially in state Φ_i^{Z-1}, end up in the relaxed state Φ_f^{Z-1}, characterised by the same set of quantum numbers. In other words, $1 - S_o^2$ is the probability that at least one of the passive electrons is excited and leaves its original level [107].

Inelastic processes mean change of the photoelectron wavevector, and therefore a shift in the contribution to $\chi(k)$. But, since the spectrum of multi-electronic excitations is rather broad, the corresponding contribution to the absorption is incoherent [108]. Hence they do not contribute to the interference phenomenon which originates the EXAFS modulation of the absorption coefficient. Thus, the overall effect is a reduction of the EXAFS oscillations amplitude [109]:

$$\chi(k) = \frac{\mu(\omega) - \mu_o(\omega)}{\mu_o(\omega)} = \frac{\mu_{el}(\omega) - \mu_{el}^o(\omega)}{\mu_o(\omega)|_{S_o^2=1}} = S_o^2 \left[\frac{\mu(\omega) - \mu_o(\omega)}{\mu_o(\omega)} \right]_{S_o^2=1} \quad ,$$

where the term in square brackets is the one given by Eq. (3.18).

The factor S_o^2 depends on the modulus of the wavevector k. However, it can be assumed constant in the EXAFS range of energy. Commonly, it is determined empirically in the range 0.7 to 0.9. Alternatively, it may be regarded as a free parameter in the fitting procedure of the EXAFS spectra.

- **Finite lifetime of the photoelectron**

As we know, the EXAFS signal is produced by the interference between the outgoing electron wave with the backscattered wave in the region of the absorber. Therefore, the wavefunction ψ_o in such region must not change much in the time interval taken by the photoelectron to come back to the absorber. In particular, the core hole must not decay too rapidly as a result of the electronic rearrangement. Furthermore, it is necessary that the photoelectron wavefunction does not loose coherence, in order for the backscattered wave $\delta\psi$ to keep its proportionality with the outgoing wave ψ_o. The main sources of incoherence are the interactions of the photoelectron with the outer electrons of the surrounding atoms.

Material	η	ξ
Elements	0.95	3.106
Inorganic	0.53	3.913
Organic	0.59	1.881
Adsorbed gas	0.80	– –

Table 3.1: Parameters of the universal curves for electron inelastic mean free path (λ in Å) as a function of photoelectron wavevector (k in Å^{-1}) [95].

The lifetime τ of the final state ϕ_f can be expressed as a function of the core hole lifetime τ_h and the photoelectron lifetime τ_e as [110]:

$$\frac{1}{\tau} = \frac{1}{\tau_h} + \frac{1}{\tau_e}$$

The lifetime τ_h is typically of the order $10^{-15} - 10^{-16} s$, and is essentially determined by two kinds of decays [111]: radiative decay (*fluorescence*), where the excess energy is emitted in the form of X–rays, and non–radiative decay (*Auger effect*), where such energy is used to eject one of the outer electrons. The lifetime τ_e is determined by inelastic scattering of the photoelectron and depends on its kinetic energy (and hence on the wavevector k). It corresponds to a mean free path (MFP) $\lambda_e = v\tau_e$ (v velocity of the photoelectron) typically in the range 5 to 15 Å [110].

If we indicate with $\lambda(k)$ the MFP corresponding to the total lifetime τ, we can account for a finite value of the latter in the EXAFS signal by inserting in expression (3.18) a damping factor of the form $\exp(-2r_j/\lambda(k))$. The inelastic MFP can be approximated by [112]

$$\lambda(k) = \frac{1}{\eta}\left[\left(\frac{\xi}{k}\right)^4 + k^n\right] \quad . \tag{3.20}$$

For $k > 5$ Å^{-1} (which is more or less where the XANES–EXAFS border is), Eq. (3.20) reduces to

$$\lambda(k) = \frac{k^n}{\eta} \quad . \tag{3.21}$$

In fact, there is a universal curve $\lambda(E_e)$ vs E_e for each type of material (element, inorganic or organic compounds, adsorbed gases etc.) of the form [95]

$$\lambda(E_e) = \frac{A}{E_e^2} + B\sqrt{E_e} \quad , \tag{3.22}$$

where E_e is the electron kinetic energy. For $E_e > 150$ eV it can be approximated by $\lambda(E_e) = B\sqrt{E_e}$. The values of η and ξ for the universal curves are tabulated in Table 3.1. In EXAFS data analysis it has been shown [112] that $n = 1$ and $n = 2$ give rise to about the same quality fit for data with $k > 5$ Å^{-1}.However, the latter generally yields values of λ in the range 2–17 Å^{-1}, which is more in line with that predicted from the universal curves for electron MFP. Parameter η can also be refined to best fit the EXAFS data, which is what we did in our data analysis.

Concluding, taking all the above discussed effects into account, expression (3.18) becomes

$$\chi(k) = S_o^2 \sum_j N_j \frac{|f_j(\pi,k)|}{kr_j^2} e^{-\frac{2r_j}{\lambda(k)}} \sin(2kr_j + \varphi_j(k)) \tag{3.23}$$

3.6 Effects of disorder on the EXAFS signal

Despite the corrections introduced in the previous section, expression (3.23) is still not applicable to practical data analysis in its present form. In fact, we still have to account for the effects of disorder. The main causes of disorder are listed here below.

1. Thermal disorder: it is due to the vibrational atomic motion, which increases with temperature. However, it is also present at $T = 0$, due to the zero–point energy.

2. Static disorder: it is associated with the slight variations of distance from the absorber of different atoms in the same coordination shell. These variations are not always resolved within instrumental accuracy.

3. Compositional disorder: it originates from the presence of atoms of different chemical species in the same coordination shell. In fact they are located at the same distance from the absorber, but their scattering amplitudes are different.

4. Site disorder: it is important when absorber atoms of the same species are present in the crystal at two different lattice sites in the unit cell. This is the case e.g. of copper ions in the RBCO series materials.

In this thesis we are interested in the lattice dynamics of copper–oxide planes in cuprates. Hence, we shall discuss in detail only the effects of thermal disorder.

3.6.1 Thermal disorder

Let us consider a single coordination shell, labeled by index s and whose distance from the absorber is R_s. Let N_s be its coordination number. The contribution to the EXAFS signal of this shell can be written as

$$\chi_s(k) = \frac{S_o^2}{k} N_s \, Im\left\{ f_s(\pi,k)\, e^{2i\delta_1}\, e^{2ikR_s}\, \frac{e^{-2R_s/\lambda}}{R_s^2} \right\} \quad . \tag{3.24}$$

However, the distance r between the absorber and each atom of the shell does not have a fixed value, but it varies in time because of the thermal motion. The flight time of the photoelectron is of the order $10^{-15} - 10^{-16}$ sec, and hence it is much smaller than the period of thermal lattice vibrations (of the order of $10^{-12} - 10^{-13}$ sec). This means that the photoelectron sees the lattice *frozen*. On the other hand, data collected in an EXAFS experiment are obtained from a large number of photoelectrons and over time intervals larger than the periods of lattice vibrations. Thus EXAFS is actually able to probe distributions of instantaneous distances.

Let us indicate with $g_s(r)\,dr$ the normalised probability that the distance of an atom in the the s–th shell from the absorber is in the interval $[r,r+dr]$. The function $g_s(r)\,dr$ is usually referred to as the pair distribution function. Hence, the EXAFS signal must be averaged over such distributions for the different shells. In particular, the contribution from the s–th shell will be

$$\chi_s(k) = \frac{S_o^2}{k} N_s \, Im \left\{ f_s(\pi,k)\, e^{2i\delta_1} \int_o^\infty g_s(r)\, \frac{e^{-2r/\lambda}}{r^2}\, e^{2ikr}\, dr \right\} \quad . \tag{3.25}$$

This expression shows that the EXAFS signal $\chi(k)$ is proportional to the Fourier transform of the so–called *effective distribution function*

$$G_s(r,\lambda) = g_s(r)\, \frac{e^{-2r/\lambda}}{r^2} \quad . \tag{3.26}$$

The moments of the effective distribution function have an interesting meaning in the so–called *cumulant method*. This procedure allows one to include some model–independent anharmonic contributions in the pair distribution $g(r)$, based on a series expansion of the effective distribution function $G(r)$.

The starting point is the Fourier transform of the effective distribution function $G(r,\lambda)$ (Eq. (3.26))

$$F(2k) = \int_o^\infty G(r,\lambda) e^{2ikr}\, dr \quad ,$$

called *characteristic function*. The cumulants C_n are defined as the coefficients that enter the MacLaurin expansion of the function $\ln[F(2k)]$ in the following fashion

$$\ln[F(2k)] = \sum_{n=0}^{\infty} \frac{(2ik)^n}{n!} C_n \quad . \tag{3.27}$$

If the convergence of the series (3.27) is fast, to reconstruct the characteristic function F one needs to know a limited number of cumulants. In this case one has

$$F(2k) = \exp\left\{ \sum_{n=0}^{\infty} \frac{(2ik)^n}{n!} C_n \right\} \quad . \tag{3.28}$$

The utility of this method is that the cumulants are related to the moments of the effective distribution. In particular, $C_0 = \ln[\int_0^\infty G(r,\lambda)dr]$ vanishes if G is normalised to unity. The first cumulant $C_1 = \langle r \rangle$ is the mean value of the interatomic distance, while $C_2 = \langle r^2 \rangle - \langle r \rangle^2$ is the variance of the effective distribution. The higher order cumulants C_3 and C_4 are related to the *skewness* (asymmetry) and *kurtosis* (deviation from a Gaussian), respectively, of the distribution [110]. If we assume that the distribution $g(r)$ does not deviate too much from its harmonic limit, one can prove that the single–shell formula of EXAFS for the s–th shell assumes the following form

$$\chi_s(k) = \frac{S_o^2 N_s |f_s(\pi,k)|}{k C_{1s}^2}\, \sin[2kC_{1s} - 4C_{3s}k^3/3 + \varphi_s(k)]\, e^{(-2C_{1s}/\lambda - 2C_{2s}k^2 + 2C_{4s}k^4/3)} \quad . \tag{3.29}$$

Eq. (3.29) shows that asymmetries in the distribution function [6] affect the phase of the EXAFS oscillations, while deviations from the Gaussian shape appear in changes of its amplitude. The amplitude factor corresponding to the second–order term in the cumulant expansion is nothing but the so–called Debye–Waller factor of the shell (see below).

In practice it is impossible to reconstruct the pair distribution function by inverse Fourier transform of the signal $\chi(k)$, because of the finite extension of the experimental spectrum. From one hand, the signal is severely damped at high values of k. Typically, for $k > 15-17$ Å^{-1} the signal–to–noise ratio is too small for the signal to be extracted with accuracy. On the other hand, for $k < 4-5$ Å^{-1} the signal cannot be used, since the effects of the final state lifetime are more marked for slow photoelectrons. Moreover, multiple scattering effects in the XANES region (large wavelength of the photoelectron) lead to a distortion of the signal. These difficulties are usually overcome by introducing some structural models and deriving the corresponding PDF, whose structural parameters will then be refined to best fit the EXAFS data. This is what we shall do in the next chapter, where we shall introduce our own structural model.

The simplest structural model one can introduce is represented by a Gaussian distribution

$$g(r) = \frac{1}{\sqrt{2\pi\sigma^2}} \exp\left[-\frac{(r-R)^2}{2\sigma^2} \right] \quad . \tag{3.30}$$

It is not difficult to see by direct integration of Eq. (3.25) that this simple model amounts to introduce in the EXAFS signal (3.23) the multiplicative factor

$$e^{-2k^2\sigma^2} \quad , \tag{3.31}$$

universally known as Debye–Waller (DW) factor. The variance σ^2 of the PDF is also known as mean square relative displacement (MSRD). To clarify its meaning, it is instructive to derive expression (3.31) again without introducing the PDF.

As we mentioned above, the photoelectrons probes instantaneous configurations of the shell distributions. However, the acquisition of the EXAFS spectra involves much larger time scales than those characteristic of atomic motions and a large number of photoelectrons. Hence, in order to correctly reproduce the effect of thermal disorder, it is necessary to take averages over all instantaneous configurations.

It is convenient to write the EXAFS signal (3.24) as a sum of the individual diatomic contributions as

$$\chi(k) = \sum_{j=1}^{N_j} \chi_j(k) = \sum_{j=1}^{N_j} S_o^2 \frac{|f_j(\pi,k)|}{k}\, Im \left\{ e^{i\varphi_j(k)}\, \frac{e^{-2r_j/\lambda}}{r_j^2} e^{2ikr_j} \right\} \quad , \tag{3.32}$$

[6] We should make clear that the cumulants entering Eq. (3.29) refer to the *effective* distribution $G(r)$, while one is interested in the shape of the *true* distribution $g(3)$, i.e. in the cumulants C_n^r. For the first cumulant one has [110, 138]

$$C_1 = C_1^r - \frac{2C_2^r}{C_1^r}\left(1 + \frac{C_1^r}{\lambda}\right) \quad .$$

Note that $C_1 < C_1^r$. This means that distances, as seen by EXAFS, are somewhat smaller than *true* distances. However, this effect is generally not within experimental reach. Usually, the differences $C_n - C_n^r$ for $n > 1$ can be neglected.

where r_j is the instantaneous distance between the absorber and its j–th neighbour (see Fig. 3.9). If we indicate with R_j the equilibrium distance, we have $\vec{r}_j = \vec{R}_j + (\vec{u}_j - \vec{u}_o)$, where $\vec{u}_j$ and $\vec{u}_o$ are the atomic displacements. If the latter are small, we can write $r_j \simeq [R_j + \hat{R}_j \cdot (\vec{u}_j - \vec{u}_o)]$, with $\hat{R}_j = \vec{R}_j / R_j$. Therefore, if we neglect the effect of thermal motion on the term accounting for the photoelectron mean free path, we get

$$\chi_j(k) = \chi_j^0(k) \langle e^{2ik\Delta_j} \rangle \tag{3.33}$$

where $\Delta_j = \hat{R}_j \cdot (\vec{u}_j - \vec{u}_o)$ and χ_j^0 is the static signal evaluated at the equilibrium distance R_j. The configurational average reads

$$\langle e^{2ik\Delta_j} \rangle = \frac{Tr\left[e^{-\beta H} e^{2ik\Delta_j}\right]}{Tr\left[e^{-\beta H}\right]} \quad ,$$

where $e^{-\beta H}$ is the density matrix ($\beta = 1/k_B T$). In general, such average cannot be computed exactly. However, whenever the harmonic approximation of lattice vibrations holds (i.e. in a solid for $T \ll \Theta_D$ = Debye temperature), we can use the known result [113]

$$\langle e^{2ik\Delta_j} \rangle = e^{-2k^2 \langle \Delta_j^2 \rangle} \quad ,$$

from which one re–obtain the expression of the DW factor as

$$\chi_j(k) = \chi_j^0(k)\ e^{-2\sigma^2 k^2} \quad ,$$

where

$$\sigma_j^2 = \langle \Delta_j^2 \rangle = \left\langle \left[\hat{R}_j \cdot (\vec{u}_j - \vec{u}_o)\right]^2 \right\rangle \tag{3.34}$$

is the MSRD along the line joining the absorber and its j–th neighbour. We see that the thermal broadening of atomic distance distributions as measured by EXAFS refers to the projected distance.

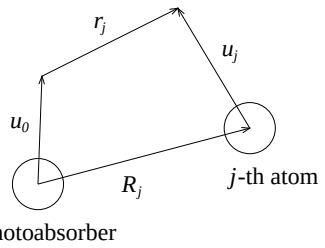

Figure 3.9: Equilibrium and instantaneous distances between the absorber and its j–th neighbour.

3.6.2 Static disorder

Static disorder is typically associated with the presence of N identical atoms at slightly different distances which cannot be resolved in different coordination shells. This problem is usually solved by introducing a PDF, whose mean represents an effective average distance, and whose standard deviation σ_{stat} accounts for the broadening introduced by the structural disorder. For example, let us assume that such distribution is Gaussian. Hence, it can be shown [95] that a system of m atoms at distance r_m and n atoms of the same species at distance r_n ($m + n = N$) is equivalent, for small disorder ($|r_m - r_n| \ll r_m, r_n$), to a coordination shell with occupation number N and mean distance

$$r_o = \frac{m r_m + n r_n}{m + n} \quad ,$$

provided that one introduces in the Debye–Waller factor the static variance

$$\sigma_{stat}^2 = \frac{mn}{(m+n)^2} |r_m - r_n|^2 \quad .$$

3.7 The standard formula of EXAFS: physical and structural parameters

If the Gaussian disorder is not too strong, the above considerations lead to the following expression for the contribution of the s–th coordination shell to the EXAFS signal

$$\boxed{\chi_s(k) = \frac{S_o^2 N_s |f_s(\pi, k)|}{k R_s^2}\ \sin[2kR_s + \varphi_s(k)]\, e^{-2R_s/\lambda}\ e^{-2\sigma^2 k^2}} \tag{3.35}$$

This expression is also known as the *standard formula of EXAFS*. Let us briefly summarise its characteristics.

The main point of formula (3.35) is its simple parametrisation, which enables one to use it directly in fitting the experimental spectra. If the *physical parameters* relative to the backscattering and multi-electronic processes are known, one can use formula (3.35) to directly refine the *structural parameters*. The latter are three for each coordination shell:

- The interatomic distance R_s, which determines the frequency of the EXAFS signal.
- The atomic MSRD σ_s^2. It enters the DW factor, and introduces a temperature–dependent damping of the EXAFS signal for high values of the photoelectron wavevector.
- The coordination number N_s, which defines the number of atoms in each coordination shell. It can also be kept fixed if it is known from other measurements, such as X–ray diffraction. This is our case.

The pre–requisite of determining the structural parameters is a satisfactory knowledge concerning the backscattering amplitude and total phase shift, which critically depend on the chemical species involved. They are usually evaluated according to either of the two following complementary procedures:

1. Phase shifts and amplitude are determined empirically from the EXAFS spectra of a reference sample, whose structure is known from other sources and where the lattice neighborhood of the absorber is similar to that of the sample under study. This procedure relies on the so–called principle of *chemical transferability* from a known to an unknown material.
2. Phase shifts and amplitude are calculated from theoretical models of the atomic potentials. Usually, these calculation are checked against the results obtained from samples of known structure.

It is important to stress that the standard formula of EXAFS is directly applicable to the excitation of an s state (K–, L_I–edges). In fact, if the photoelectron is ejected from, e.g., a p state, the final state can have either s or d symmetry according to the dipole selection rules. Thus, the signal must be weighted according to the corresponding transition probabilities [95][114]. Furthermore, we recall that the single–atom scattering and the plane–wave approximations must hold true. These assumptions are usually more than justified if one is interested in the first coordination shells only (multiple scattering contributions negligible due to the long paths involved). More critical are the spherical wave corrections to the outgoing wave incident on the backscatterer atom. In reality, the plane–wave approximation is only accurate at sufficiently large kr, which means high k (or energy) and/or large r. Hence, the plane–wave approximation may also be called *high–energy* or small–atom approximation. At lower energies the plane–wave approximation breaks down. This may cause errors in both the phase and, to a lesser extent, the amplitude of the calculated signal. This problem can be particularly troublesome for systems in which low–k data are important in the analysis. These include the case of light–atom scatterers, which scatter strongly only the low–energy electrons (rapid decay of the backscattering amplitude at high k). Unfortunately, among these is our case, where oxygen ions are characterised by a fast–decaying backscattering amplitude. In the present work, we shall not correct for these effect. However, we will cut away a certain fraction of the low–k data in our analysis, in order to minimise the effects of such errors. The exact curved–wave theory can be found in, e.g., refs. [115] and [116]. Unfortunately, this theory is quite complicated and difficult for practical data analysis. However, there is now available a simpler form of such theory, called *rapid curved–wave theory*, based on the historical work of Gurman, Binsted and Ross [117]. This formalism, has now been incorporated in the fitting program EXCURVE [118], which is made available as the standard fitting tool to the Daresbury (UK) labs users. Among our future objectives, is to devise a simple way to incorporate such theory in the standard formula of EXAFS for diatomic contributions from model potentials.

3.8 EXAFS: the experimental technique

This section is devoted to a brief description of the basics of an EXAFS experiment, from how the radiation is generated to the data acquisition. The details of the particular experimental setup made available to us at Daresbury labs are reported in the last section.

In an EXAFS experiment the linear absorption coefficient is measured as a function of the energy of the incident X–rays. Thus, one needs a source of *continuous* radiation. In order to do the energy scanning , it is then necessary to extract from the *white* radiation a monochromatic beam at selected energies, which is focused on the sample. Synchrotrons provide an excellent radiation source for an EXAFS experiment, both for the wide spectrum and the intensity, which is up to six orders of magnitude higher than that available by ordinary cathode tubes.

3.9 The radiation source

Synchrotron radiation is emitted by charged particles accelerated and kept moving in bunches in a storage ring. This is made of linear and curved tracts. In the linear sections there are the focusing systems and RF cavities, where and RF electric field in resonance with the syncrothron frequency accelerates the particles in order to compensate for the energy losses. In the curved tracts, the emission occurs and is directed outside the ring to the different beamlines.

In the relativistic regime $\beta = v_e/c \simeq 1$, the emission in highly directional, with an angular aperture $\theta \propto 1/\gamma$, where $\gamma = 1/\sqrt{1-\beta^2}$ [119][120]. In a synchrotron $\gamma = E/mc^2 \approx 10^4$, thus the emission cone is as narrow as $\approx 10^{-4}$ rad. This characteristic also determines the spectral composition of the radiation collected by an observer at rest. In fact, on will just observe the radiation emitted by the electrons along an arc $\approx 2\theta$. In a ring of radius $R = 100$ m, this means a time interval $\Delta t \approx 10^{-19}$ sec. Hence, the maximum frequency component ω_M in the synchrotron radiation is in the *hard* X–ray region (tens of KeV). Moreover, in such region the spectrum may be regarded as continuous,[7] since the frequency spacing $\Delta\omega \simeq \omega_o \ll \omega_M$.

3.10 The monochromator

The *white* beam, extracted from the storage ring, enters the *optical hutch* of the beam–line. Once there, the beam is passed through the monochromator, whose function is to extract the desired energy component E. This operation is accomplished by means of Bragg's diffraction of the X photons by a crystal, usually Si or Ge. The polychromatic beam impinges on one face of the crystal, and is reflected by a family of crystallographic planes of Miller indexes (h,k,l) according to the known formula (Fig. 3.10 (a))

$$2d_{hkl}\sin\theta = n\lambda = n\left(\frac{hc}{E}\right) \tag{3.36}$$

where d_{hkl} is the inter-planar distance, θ is the angle formed by the incident and diffracted beam with the crystallographic planes and n is the order of the reflection. Different energy components correspond to different angles. Hence, the energy scan can be performed by rotating the crystals around an angle normal to the beam and parallel to the Bragg planes. In order for the outcoming monochromatic radiation to be parallel to the incident one, monochromators are made of two parallel crystals (Fig. 3.10 (b)). The two crystals can be arranged in the *channel–cut* or *double–crystal* configurations. In the first case, the two reflecting faces are cut from a single crystal piece, while in the second arrangement the two reflecting planes can be rotated independently. The former type has the drawback that the outgoing beam leaves the monochromator at a distance $h = (D/\sin\theta)\sin 2\theta = 2D\cos\theta$ from the incident one. The second configuration, though more complicated and difficult to operate, allows one to avoid such problem, and is therefore widely used. Moreover, the latter arrangement is very

[7] The spectrum is discrete because the electron motion is periodic, and all frequencies are multiples of the fundamental frequency $\omega_o = c|e|B/mv_e$.

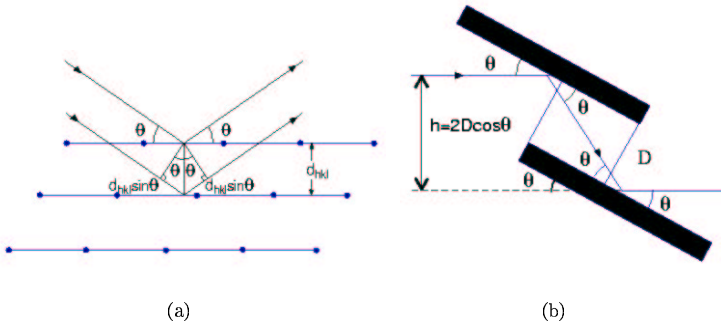

(a) (b)

Figure 3.10:

effective in solving the problem of *harmonics rejection*.[8]

The energy resolution $\Delta E/E$ of a typical monochromator depends on the width of the reflected intensity vs angle curve and on the angular width of the incident beam. By differentiating Braggs' law one gets $\Delta E/E = \Delta\lambda/\lambda = \Delta\theta \cot\theta_B$, where θ_B is Bragg's angle and $\Delta\theta$ is the convolution of Darwin's width with the divergence of the incident beam. Typically, $\Delta E/E \approx 10^{-4} - 10^{-5}$ [110].

3.11 Measuring the absorption coefficient

There are two commonly–used modes of X–rays absorption spectroscopy (XAS): *transmission*, where the X–ray beam intensity is measured both before and after the sample using ion chambers; and fluorescence, where the intensity of the X–ray beam is measured before the sample and the intensity of fluorescence signal emitted from the sample is measured using a solid state detector. We shall here describe the experimental setup of a transmission experiment (our case). For an extensive review of the various experimental arrangements and techniques the interested reader can see Ref. [121].

A typical setup of an EXAFS transmission experiment is shown in Fig. 3.11. The intensity of the monochromatic beam is measured before and after passing through the sample (intensities I_o and I, respectively) and the absorption coefficient is calculated and stored. The monochromator is then rotated (i.e. the energy increased) and the same measurement is repeated until the desired energy range has been spanned.

The ion chambers consist of two metallic plates with a 600 V potential difference between them, supplied by an Ortec 456 HT supply. The chambers are filled with inert gases, which are ionized by the X–ray photons. The current between the plates

[8] According to Bragg's law, the reflection of the principal wavelength λ is accompanied by reflection of its harmonics $\lambda/2, \lambda/3, \ldots, \lambda/n$. However, the reflected intensity vs angle curve (Rocking curve) is centred on Bragg's angle and has a characteristic width (Darwin's width) which is much larger for the principal wavelength than for its harmonics. Thus, by making Bragg's angles of the two crystals slightly different ($\approx 10^{-6}$ rad), one obtains the convolution of the corresponding two rocking curves for each harmonic. As a result, only the principal component survives.

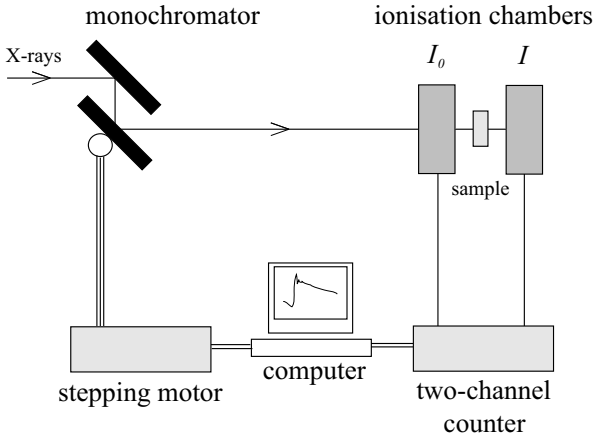

Figure 3.11:

is amplified and shown on the station rack upstairs in the hutch. This amplified signal is also simultaneously fed to a voltage–to–frequency converter and the digital output fed into a count register which feeds into the station computer. The ion chambers are operated in *current mode* [111], which means that the collected currents i_o and i (order of $10^{-10} - 10^{-8}$ A) are proportional to the corresponding beam intensity. It follows that

$$\frac{i_o}{i} = C\,\frac{I_o}{I} \quad , \tag{3.37}$$

where the constant C depends on the efficiency of the two chambers. The chambers characteristics (dimensions, type of gas and pressure) are chosen so that the first chamber absorbs about 20 % of the radiation, while the second absorbs all of the radiation left after the sample. This does not introduce any uncertainties in the measure of the absorption coefficient μ_c. In fact, if f is the fraction of radiation absorbed by the first chamber, the Lambert–Beer law gives

$$\mu_c d = \ln\frac{I_o e^{\mu d}}{(1-f)\,I_o} = \mu d + c \quad .$$

The constant c is eliminated when the atomic background is extracted from the spectrum to get the EXAFS signal $\chi(k)$.

3.12 Sample preparation

The measurements have been performed on non–oriented powder of $Ca_2CuO_2Cl_2$, prepared at The Chemical Physics Department of Pavia University. The $Ca_2CuO_2Cl_2$ crystals were crushed in a fine powder *in situ*, mixed with spectroscopic polyethylene

and then pressed in a small flat pellet by means of a 10 tons hydraulic press. The polyethylene powder acts as ligand and is transparent to X–rays. It is essential in order to obtain homogeneous samples.

Usually, one chooses the amount of material in the pellet in order to obtain an edge jump of order one at the absorption edge. If σ is the absorption cross section per unit mass, one has

$$\Delta\mu = |\mu_{post-edge} - \mu_{pre-edge}| = \rho_{Cu} \cdot \Delta\sigma = \rho \frac{A}{FW} \Delta\sigma \quad ,$$

where ρ is the mass density of the compound, $FW = 247.5$ is the formula weight and $A = 63.5$ is the atomic weight of copper. The total pre– and post–edge cross sections (which include all interactions of X–rays with the material) are 38.3 cm^2/g and 278 cm^2/g at the Cu K–edge [93]. If we express the density as $\rho = m/Sd$, S being the pellet surface (about 1 cm^2) and d the thickness, we can write

$$m = \frac{S}{\Delta\sigma} \frac{FW}{A} \Delta\mu d \quad . \tag{3.38}$$

By putting $\Delta\mu d = 1$ in Eq. (3.38), we obtain the required amount of the compound as $m \approx 16$ mg.

3.13 The experiment

The measurements have been carried out at the synchrotron radiation source of the Daresbury Laboratories, over five days in September 1999.

At the time of our experiment, our station was equipped with a novel water cooled, bent double crystal Si (2,2,2) monochromator. In such monochromator the crystals are bent in order to match the vertical dispersion of the source, hence eliminating the requirement of vertical defining slits to maintain the resolution. The first crystal is also water cooled for temperature stabilisation. The monochromator is followed by a toroidal mirror to focus the beam at the sample, thereby collecting a large solid angle and delivering it in a small spot (1×1 mm^2).

The ion chambers have been filled at optimal level for measurements at the copper K–edge, according to the provided charts. These indicate how large a partial pressure of the absorbing gas, and which gas to use for each element that is being studied. Thus, for copper the reference (I_o) ion chamber was filled with 63 mBar of Argon and filled up to atmospheric pressure (about 1000 mBar) with Helium, while the signal (I) ion chamber was filled with 452 mBar of Argon and then filled to atmospheric pressure with Helium.

The sample was mounted in a liquid–helium cryostat, which allowed coarse and fine tunings of the temperature by operating directly on the helium flow and/or on a small resistance inside the cryostat. The range of allowed temperatures is 4 K $< T <$ 300 K, with fluctuations of the order of 1 K. We took measurements at T =10, 20, 30, 40, 50, 60, 80 and 200 K. For each value of the temperature, we collected two spectra, which have then been averaged. This is a highly recommended practice in order to isolate possible fluctuations that would lead to systematic errors in the measurements. All the energy scans have been divided into different regions (3 or

4), each characterised by different acquisition times and energy spacing of the points. This is common practice, since different regions of the spectrum are characterised by different absorptions (essentially pre–edge and edge regions). Moreover, in the last part of the spectrum (order of 1000 eV above the edge) the EXAFS oscillations are severely damped and hence a fine scanning is pointless.

We also recorded spectra at the Cu K–edge in $EuBa_2Cu_3O_{6+x}$, for $x = 0.25, 0.38$ and 0.8 at temperatures T =10,80,85,90,95,100 and 200 K. Analysis of these data, among other things, is still in progress.

3.14 Conclusions

In this chapter we have developed on simple grounds the theory of the EXAFS modulation of the X–ray absorption coefficient. In particular, we have derived the analytic expression of the standard formula of single–shell EXAFS signals. Moreover, we have shown how to generalise the latter expression in the presence of thermal disorder by introducing a radial distribution function. In the next chapter we will tackle the problem of how to explicitly incorporate the dynamics of the neighbour–absorber pair in the corresponding distribution function.

Chapter 4

The Quantum–Mechanical Perturbative Pair Distribution Function

4.1 Introduction

In the preceding chapter, we have described how to introduce in the EXAFS formalism a function that accounts for the thermal broadening in the distribution of absorber–neighbour distances. We now turn to the following question: how do the details of the interatomic absorber–neighbour potential enter such a pair distribution? The classical approximation provides a simple answer to that question. Unfortunately, the validity of the classical regime is limited. As a consequence, physically interesting regions in terms of temperature might not be accessible to such a simple treatment for specific materials. In this chapter, we shall introduce a method that allows one to calculate a full quantum pair distribution function, which incorporates the potential parameters in a simple fashion. We shall carefully discuss the limits of our approach, and provide a clear working procedure to assess its sensitivity to the relevant parameters in terms of its capability of fitting a set of experimental data.

4.2 Interatomic potentials

In the usual Born–Oppenheimer approximation, the motions of electrons and nuclei are decoupled, because electrons are moving much faster than nuclei. The reason is, of course, the huge mass difference ($M_N/m_{el} \approx 10^4$). Therefore, the Schrödinger equation for the electrons depends parametrically on the position of nuclei. It may be written as

$$\mathcal{H}_{el}\Psi_{el}(\{\mathbf{r}\},\{\mathbf{R}\}) = U(\{\mathbf{R}\})\,\Psi_{el}(\{\mathbf{r}\},\{\mathbf{R}\}) \quad , \tag{4.1}$$

where $\{\mathbf{r}\}$ and $\{\mathbf{R}\}$ denote the electron and nuclei coordinate sets, respectively. Once solved, Eq. (4.1) provides the potential energy $U(\{\mathbf{R}\})$ that enters the Schrödinger equation for the nuclei. This is normally called *interatomic potential*. However, although very appealing, it is impossible to solve Eq. (4.1) for a system of N atoms. Therefore, one usually introduces a semi–empirical potential energy. This can either be an empirical function whose parameters are refined on a set of experimental data (e.g. atomistic simulations) or an analytical function derived from quantum–mechanical arguments (e.g. embedded atom method). The interested reader can find extensive bibliography in Ref. [123].

In general, the total energy of a system of N atoms with interactions described by an empirical function can be written in a many–body expansion in the following fashion

$$U(\mathbf{R}_1,\mathbf{R}_2,\ldots,\mathbf{R}_N) = \sum_i U_1(\mathbf{R}_i) + \sum_i \sum_{j\neq i} U_2(\mathbf{R}_i,\mathbf{R}_j) + \sum_i \sum_{j\neq i} \sum_{k\neq i} U_3(\mathbf{R}_i,\mathbf{R}_j,\mathbf{R}_k) + \ldots \quad , \tag{4.2}$$

The one–body term U_1 accounts for the energy due to external fields or boundary conditions (e.g. walls of a container). The two–body term U_2 describes the *effective* interaction of any pair of atoms as it was unaffected by the presence of the other atoms. Three–body and higher terms account for more complicated interactions, such as stretching, bending and torsion of bond angles.

As we mentioned in Chapter 3, the thermal damping of the EXAFS modulation of the absorption coefficient of a given atomic species is related to the distribution of distances between the absorber and its coordination shells. The pair distribution function, in turn, depends on the effective pair potentials describing the dynamics between the absorber and its neighbours. Hence, EXAFS spectroscopy provides a natural selective probe for the effective pair potentials. We stress that EXAFS naturally probes the effective *pair* potentials, since it is sensitive to the distribution of *projected* distances only.

The simplest way an effective pair–potential $V(r)$ may enter the distribution function $g(r)$ is through the classical configurational integral scheme

$$g(r,T) = \frac{e^{-V(r)/k_BT}}{\int_0^\infty e^{-V(r)/k_BT}\,dr} \quad . \tag{4.3}$$

However, the validity of expression (4.3) depends on the ratio $\mathcal{R}_Q = \hbar\omega/k_BT$, where ω is the frequency corresponding to the harmonic approximation of the function $V(r)$. When $\mathcal{R}_Q$ is of the order of one, the classical approximation breaks down and the the full quantum treatment is in order. In this case, the Schrödinger equation of the system has to be solved and the energy levels and wavefunctions of the pair computed explicitly. The usual quantum mechanical treatment of two–body Hamiltonians applies: first the centre–of–mass Hamiltonian is separated from the one that describes the relative motion. The Schrödinger equation resulting from the latter is then solved. Let $\psi_n(r)$ and E_n be the eigenfunctions and eigenvalues, respectively, of the relative–motion

Hamiltonian. The relative coordinate is $r = |\mathbf{x}_1 - \mathbf{x}_2|$. The quantum–mechanical analogue of expression (4.3) is

$$g(r,T) = \frac{\sum_n |\psi_n(r)|^2 e^{-E_n/k_BT}}{\sum_n e^{-E_n/k_BT}} \quad . \tag{4.4}$$

formula (4.4) has been used in Ref. [10] to study the interatomic potential of the Cu–O(4) (planar copper–apical oxygen) pair in the YBCO superconductor. The procedure is the following: one first introduces a model potential which is characterised by a set of parameters $\{\lambda\}$. Then a numerical routine is set up, which solves the radial Schrödinger equation for a particular choice of the set $\{\lambda\}$, builds the radial distribution function (4.4) and calculates the EXAFS signal $\chi(k,\{\lambda\})$. This routine is then incorporated in the fitting program that refines the free parameters $\{\lambda\}$ on a set of experimental data through ordinary χ^2 minimisation.

The above–outlined procedure has the advantage that it can be applied to arbitrary potentials (e.g. double–well potentials). However, a more concise and handy procedure of calculating expression (4.4) in a closed form independently of the fitting cycle would be welcome. This task can be accomplished in a relatively simple way by resorting to ordinary time–independent quantum perturbation theory, provided the Taylor series of the interatomic potential is taken as the the analytical expression of the potential. By doing so, one can calculate in a closed form the quantum–mechanical distribution function retaining, for instance, just the first three non–zero coefficients of the Taylor expansion as free parameters. In principle, after refining the latter on the experimental EXAFS signal, one can fit any four–parameter potentials on the results (the fourth condition coming from the requirement that the potential has the minimum at the correct value of the interparticle distance r). In this way, different analytical expressions of the potential function may be directly tested against the experimental data.

4.3 The Quantum–Mechanical Perturbative Pair Distribution

In this section we describe how to calculate the above, which we will refer to in the following as the pair distribution function, for a pair of atoms in a crystal starting from the Taylor expansion of a given model potential, without the need to specify its analytical expression. Let $V(r)$ be the potential. We can write its Taylor expansion in the following fashion

$$V(r) = \frac{1}{2}k_2(r-r_0)^2 + \frac{1}{3}k_3(r-r_0)^3 + \frac{1}{4}k_4(r-r_0)^4 + \mathcal{O}(|r-r_0|^5) \quad , \tag{4.5}$$

where

$$k_m = \frac{1}{(m-1)!}\left(\frac{d^m V(r)}{dr^m}\right)_{r=r_0} \quad ,$$

r_0 being the equilibrium interparticle distance, given by

$$\left(\frac{dV(r)}{dr}\right)_{r=r_0} = 0 \quad .$$

We see that the harmonic approximation of $V(r)$ gives rise to a Gaussian distribution, and hence it results in a correction to the amplitude of the EXAFS signal $\chi(k)$ given by the corresponding Debye–Waller factor $e^{-2\sigma^2k^2}$. On the other hand, the third and fourth order terms in the Taylor expansion represent the first– and second–order corrections to the phase and amplitude, respectively [124].
The Schrödinger equation of the pair reads

$$-i\hbar\frac{\partial\Psi}{\partial t} = \mathcal{H}\,\Psi \quad , \tag{4.6}$$

where the Hamiltonian of the system can be written as

$$\mathcal{H} = \mathcal{K}_1 + \mathcal{K}_2 + V + U_G \quad ,$$

$\mathcal{K}_i$ being the kinetic energy of the i–th atom, and U_G a potential function for the centre of mass of the pair. We can follow the ordinary procedure to separate the two–body Schrödinger equation by introducing the relative and centre–of–mass coordinates. Let us denote with $\mathbf{x}_i$ the Cartesian coordinate vector (x_i, y_i, z_i). We introduce the centre of mass position and momentum variables $\mathbf{X}$ and $\mathbf{P}$ and the relative coordinates $\mathbf{r}$ and $\mathbf{q}$ in the following fashion

$$\begin{aligned} \mathbf{X} &= \frac{m_1\mathbf{x}_1 + m_2\mathbf{x}_2}{m_1+m_2}, & \mathbf{P} &= m_1\dot{\mathbf{x}}_1 + m_2\dot{\mathbf{x}}_2, \\ \mathbf{r} &= \mathbf{x}_1 - \mathbf{x}_2, & \mathbf{q} &= m_2\dot{\mathbf{x}}_1 - m_1\dot{\mathbf{x}}_2 \quad . \end{aligned}$$

By rewriting equation (4.6) we are led to an equivalent equation which is separable by letting

$$\Psi(\mathbf{x}_1,\mathbf{x}_2) = \psi_G(\mathbf{X})\psi(\mathbf{r}) \quad .$$

If the mean action of the crystal on the centre of mass of the pair can be neglected, the centre of mass wavefunction ψ_G obeys the simple free–particle Schrödinger equation. [1]
If we introduce spherical coordinates, the time–independent equation for the relative motion reads

$$-\frac{\hbar^2}{2\mu}\left[\frac{1}{r^2}\frac{\partial}{\partial r}\left(r^2\frac{\partial\psi}{\partial r}\right) + \frac{1}{r^2\sin\theta}\frac{\partial}{\partial\theta}\left(\sin\theta\frac{\partial\psi}{\partial\theta}\right) + \frac{1}{r^2\sin^2\theta}\frac{\partial^2\psi}{\partial\phi^2}\right] + V(r)\psi = E\psi \quad , \tag{4.7}$$

where $\mu = m_1m_2/(m_1+m_2)$ is the reduced mass of the pair. Equation (4.7) is in turn separable by letting

$$\psi(\mathbf{r}) = R(r)Y_l^m(\theta,\phi) \quad .$$

We are then led to an "angular" equation

$$-\left[\frac{1}{\sin\theta}\frac{\partial}{\partial\theta}\left(\sin\theta\frac{\partial}{\partial\theta}\right) + \frac{1}{\sin^2\theta}\frac{\partial^2}{\partial\phi^2}\right]Y_l^m = l(l+1)\,Y_l^m \quad ,$$

where for the spherical harmonics

$$Y_l^m(\theta,\phi), \quad l = 0,1,\ldots, \quad m = -l, -l+1, \ldots, +l$$

[1] This assumption amounts to assume that the total momentum of the pair is conserved.

the following differential equation holds

$$-i\frac{\partial Y_l^m}{\partial \phi} = m Y_l^m \quad .$$

The spherical harmonics can be expressed in the following fashion

$$Y_l^m(\theta,\phi) = \begin{cases} (-1)^m \sqrt{\dfrac{2l+1}{4\pi}\dfrac{(l-m)!}{(l+m)!}}\, P_l^m(\cos\theta) e^{im\phi} & \text{for } m \geq 0, \\ (-1)^{|m|} Y_l^{|m|*}(\theta,\phi) & \text{for } m < 0, \end{cases} \tag{4.8}$$

where $P_l^m(\cos\theta)$ are the Legendre polynomials, defined by

$$P_l^m(\cos\theta) = (1-\cos^2\theta)^{m/2}\frac{d^m}{d(\cos\theta)^m}P_l(\cos\theta)$$
$$P_l(\cos\theta) = \frac{(-1)^l}{2^l l!}\frac{d^l(1-\cos^2\theta)^l}{d(\cos\theta)^l} \quad .$$

In order to solve the radial equation, let us define

$$u(r) = rR(r) \quad .$$

As a consequence, the radial equation reduces to a one-dimensional equivalent problem, i.e.

$$-\frac{\hbar^2}{2\mu}\frac{d^2u}{dr^2} + \left[V(r) + \frac{l(l+1)\hbar^2}{2\mu r^2}\right]u = Eu \quad , \tag{4.9}$$

with the condition $u(r)|_{r=0} = 0$. We require the wavefunction of the pair to have spherical symmetry, since we do not want the pair distribution function to depend on the bond orientation in the crystal. We therefore set $l = 0$ hereafter. Recalling the expression of the potential function (4.5), equation (4.9) reads

$$-\frac{\hbar^2}{2\mu}\frac{d^2u}{dr^2} + \left[\frac{1}{2}k_2(r-r_0)^2 + V_1(r)\right]u = Eu \quad , \tag{4.10}$$

where we have explicitly written the harmonic term of the Taylor series and included the cubic and quartic terms in the function $V_1(r)$,

$$V_1(r) = \frac{1}{3}k_3(r-r_0)^3 + \frac{1}{4}k_4(r-r_0)^4 \quad . \tag{4.11}$$

In the spirit of ordinary time–independent perturbation theory, we consider the harmonic Hamiltonian as the unperturbed problem and the potential V_1 as the perturbation.

It is useful to re–write the time–independent radial Schrödinger equation in the formalism of creation and annihilation operators, whereby the eigenfunctions are no longer expressed in the coordinate representation but in the representation of occupation numbers (henceforth the n–representation). The unperturbed problem is defined by the Hamiltonian

$$\mathcal{H}_0 = \hbar\omega\left(\hat{N} + \frac{1}{2}\right) \quad , \tag{4.12}$$

whose eigenvalues $E_n^{(0)}$ are given by

$$\mathcal{H}_0|n\rangle = E_n^{(0)}|n\rangle = \hbar\omega\left(n + \frac{1}{2}\right)|n\rangle \quad n = 0,1,2,\ldots \quad ,$$

where $\omega = \sqrt{k_2/\mu}$. The operator $\hat{N} = \hat{a}^\dagger\hat{a}$ is the number operator, while $\hat{a}^\dagger$ and $\hat{a}$ are the creation and annihilation operators, respectively. In the n–representation the coordinate operator $\hat{r}$ is given by

$$\hat{r} = \frac{x_0}{\sqrt{2}}\left(\hat{a} + \hat{a}^\dagger\right) \quad , \tag{4.13}$$

where $x_0 = \sqrt{\hbar/\mu\omega}$. Recalling the well known commutation relations between creation and annihilation operators

$$[\hat{a},\hat{a}^\dagger] = 1, \quad [\hat{a},\hat{a}] = [\hat{a}^\dagger,\hat{a}^\dagger] = 0 \quad ,$$

it is straightforward to write down the expression of the perturbation potential (4.11) in the n–representation

$$\begin{aligned}\mathcal{V} =& \hbar\omega\,\Lambda_3[\hat{a}^{\dagger 3} + \hat{a}^3 + 3n\hat{a}^\dagger + 3(n+1)\hat{a}] + \\ & \hbar\omega\,\Lambda_4[\hat{a}^{\dagger 4} + \hat{a}^4 + 2(2n-1)\hat{a}^{\dagger 2} + 2(2n+3)\hat{a}^2 + 3(n+1)^2 + 3n^2] \quad ,\end{aligned}$$

where

$$\Lambda_m = \frac{1}{2^{m/2}m}\left(\frac{k_m x_0^m}{\hbar\omega}\right) \quad . \tag{4.14}$$

It is useful to have the explicit expressions of the coefficient Λ_3 and Λ_4 in terms of the expansion coefficients k_m ($m = 2,3,4$) and the reduced mass of the pair. If we measure masses in units of 10^{-26} Kg, lengths in Å and energies in eV (thus k_m is measured in eV/Å^m), we have

$$\Lambda_m = c_m\left[\frac{k_m}{(k_2^{m+2}\mu^{m-2})^{1/4}}\right] \quad , \tag{4.15}$$

where $c_3 = 0.0189$ and $c_4 = 0.0016$.

We shall use perturbation theory to calculate the eigenvalues and eigenvectors of the Hamiltonian $\mathcal{H}_0 + \mathcal{V}_1$.

4.3.1 The perturbed energy eigenvalues

Within the framework of ordinary time–independent perturbation theory the corrections to the unperturbed non–degenerate energy levels are given by

$$\Delta E_n = \langle n|\mathcal{V}|n\rangle + \sum_{k\neq n}\frac{|\mathcal{V}_{nk}|^2}{E_n^{(0)} - E_k^{(0)}} + \mathcal{O}(|(\mathcal{V}/E_n^{(0)}|^3) \tag{4.16}$$

up to second order. The matrix elements of the perturbation Hamiltonian $\mathcal{V}$ are given by

$$\begin{aligned}|\mathcal{V}_{nk}|^2 &= \langle n|\mathcal{V}|k\rangle\langle n|\mathcal{V}|k\rangle^* \\ &= \langle n|\mathcal{V}|k\rangle\langle k|\mathcal{V}^\dagger|n\rangle \\ &= \langle n|\mathcal{V}|k\rangle\langle k|\mathcal{V}|n\rangle \quad ,\end{aligned}$$

the last step following from the property of hermiticity of the operator $\mathcal{V}$, $\mathcal{V} = \mathcal{V}^\dagger$. Recalling expression (4.14) and the definition of creation and annihilation operators, [2] we can easily evaluate the matrix elements $\langle k|\mathcal{V}|n\rangle$. Let us define the four–dimensional vector β as

$$\beta(\sigma) = \Lambda_3[\delta_{\sigma,1} + \delta_{\sigma,3}] + \Lambda_4[\delta_{\sigma,2} + \delta_{\sigma,4}] \quad , \tag{4.17}$$

where $\delta_{i,j}$ is the Kronecker integer delta function. We have

$$\langle k|\mathcal{V}|n\rangle = \langle n|\mathcal{V}|k\rangle = \sum_{\sigma=1}^{4} \beta(\sigma)\left[\gamma_n^+(\sigma)\delta_{k,n+\sigma} + \gamma_n^-(\sigma)\delta_{k,n-\sigma}\right] \quad , \tag{4.18}$$

where we have explicitly used the hermiticity of $\mathcal{V}$, and defined

$$\gamma_n^+(\sigma) = \sqrt{\frac{(n+\sigma)!}{n!}}\alpha^+(n,\sigma)$$

$$\gamma_n^-(\sigma) = \begin{cases} \sqrt{\dfrac{n!}{(n-\sigma)!}}\alpha^-(n,\sigma) & n \geq \sigma \\ 0 & \text{otherwise} \end{cases} .$$

σ	$\alpha^+(n,\sigma)$	$\alpha^-(n,\sigma)$
1	$3(n+1)$	$3n$
2	$2(2n+3)$	$2(2n-1)$
3	1	1
4	1	1

Table 4.1:

The coefficient $\alpha(n,\sigma)$ are reported in Table 4.1. We note that the coefficients γ_n and $\alpha(n,\sigma)$ satisfy to the following relations

$$\gamma_{n-\sigma}^+(\sigma) = \gamma_n^- \qquad \alpha^+(n-\sigma,\sigma) = \alpha^-(n,\sigma)$$
$$\gamma_{n+\sigma}^-(\sigma) = \gamma_n^+ \qquad \alpha^-(n+\sigma,\sigma) = \alpha^+(n,\sigma) \quad .$$

first–order corrections We have to calculate the expectation values of $\mathcal{V}$ using the states $|n\rangle$. We note that the only first–order corrections arise from the terms containing an equal number of creation and annihilation operators. Hence, only the fourth–order term will contribute. We easily obtain

$$\Delta E_n^{(1)} = \langle n|\mathcal{V}|n = 3\Lambda_4(2n^2+2n+1) \quad . \tag{4.19}$$

second–order corrections We have to calculate

$$\Delta E_n^{[2]} = \sum_{k\neq n} \frac{|\mathcal{V}_{nk}|^2}{E_n^{(0)} - E_k^{(0)}} = \sum_{k\neq n} \frac{\langle n|\mathcal{V}|k\rangle\langle k|\mathcal{V}|n\rangle}{E_n^{(0)} - E_k^{(0)}} =$$
$$\sum_{\sigma,\sigma'=1}^{4}\sum_{k\neq n} \beta(\sigma)\beta(\sigma')\frac{\left[\gamma_n^+(\sigma)\delta_{k,n+\sigma} + \gamma_n^-(\sigma)\delta_{k,n-\sigma}\right]\left[\gamma_k^+(\sigma')\delta_{n,k+\sigma'} + \gamma_k^-(\sigma')\delta_{n,k-\sigma'}\right]}{n-k} \quad ,$$

where we have made use of equality (4.17) in the second step. It is not difficult to realise that, in evaluating the product in equation (4.20), the only terms that contribute are the cross products, because of the selection rules imposed by the Kronecker delta's. As an example let us consider the factor $\gamma_n^+(\sigma)\gamma_k^+(\sigma')\delta_{k,n+\sigma}\delta_{n,k+\sigma'}$. The selection rule

[2] i.e. $a|n\rangle = \sqrt{n}|n-1\rangle$ and $a^\dagger|n\rangle = \sqrt{n+1}|n+1\rangle$.

prescribes $k = n+\sigma = n-\sigma'$, i.e. $\sigma+\sigma' = 0$, which is not possible being σ and σ' positive integers. Similar considerations lead to exclude the $\gamma^-\gamma^-$ term. Hence, we obtain

$$\Delta E_n^{(2)} = \sum_{\sigma=1}^{4}\beta(\sigma)^2\left[-\frac{\gamma_n^+(\sigma)\gamma_{n+\sigma}^-(\sigma)}{\sigma} + \frac{\gamma_n^-(\sigma)\gamma_{n-\sigma}^+(\sigma)}{\sigma}\right]$$
$$= \sum_{\sigma=1}^{4}\frac{\beta(\sigma)^2}{\sigma}\left[(\gamma_n^-(\sigma))^2 - (\gamma_n^+(\sigma))^2\right] \quad ,$$

where we have used the relations (4.19) in the last step.

Finally, let us summarise the results obtained for the corrections to the energy levels

$$\boxed{\begin{aligned} E_n &= E_n^{(0)} + \Delta E_n^{(1)} + \Delta E_n^{(2)} \\ &= E_n^{(0)} + 3\Lambda_4(2n^2+2n+1) + \sum_{\sigma=1}^{4}\frac{\beta(\sigma)^2}{\sigma}\left[(\gamma_n^-(\sigma))^2 - (\gamma_n^+(\sigma))^2\right] \quad . \end{aligned}}$$

4.3.2 The perturbed energy eigenstates

In this section we shall calculate the corrections to the unperturbed states $|n\rangle$ up to second order.

First order correction The first–order correction to the unperturbed states are defined as

$$|n^{(1)}\rangle = \sum_{k\neq n}|k\rangle\frac{\langle k|\mathcal{V}|n\rangle}{E_n^{(0)} - E_k^{(0)}} \quad . \tag{4.20}$$

Recalling equation (4.18), we easily obtain

$$|n^{(1)}\rangle = \sum_{\sigma=1}^{4}\frac{\beta(\sigma)}{\sigma}\left[\gamma_n^-(\sigma)|n-\sigma\rangle - \gamma_n^+(\sigma)|n+\sigma\rangle\right] \quad . \tag{4.21}$$

Second order corrections The second–order contribution to the perturbed wavefunction is given by

$$|n^{(2)}\rangle = \sum_{m,k\neq n}\frac{\langle m|\mathcal{V}|k\rangle\langle k|\mathcal{V}|n\rangle}{\left[E_n^{(0)} - E_k^{(0)}\right]\left[E_n^{(0)} - E_m^{(0)}\right]}|m\rangle +$$
$$-\sum_{m\neq n}\frac{\langle n|\mathcal{V}|n\rangle\langle m|\mathcal{V}|n\rangle}{\left[E_n^{(0)} - E_m^{(0)}\right]^2}|m\rangle - \frac{1}{2}|n\rangle\sum_{m\neq n}\frac{|\langle m|\mathcal{V}|n\rangle|^2}{\left[E_n^{(0)} - E_m^{(0)}\right]^2} \quad .$$

The last term has been been introduced to guarantee that the perturbed wavefunctions are normalised up to second order. The calculation is not difficult, however it is rather lengthy. It is all based on evaluating the summations over the eigenvalue indexes

by taking into account the multiple selection rules contained in the expression of the matrix elements (4.18). Here, we just report the final expression

$$
\begin{aligned}
|n^{(2)}\rangle = & \sum_{\sigma,\sigma'=1}^{4} \frac{\beta(\sigma)\beta(\sigma')}{\sigma(\sigma+\sigma')} \left[\gamma_n^+(\sigma)\gamma_{n+\sigma}^+(\sigma')|n+(\sigma+\sigma')\rangle + \gamma_n^-(\sigma)\gamma_{n-\sigma}^-(\sigma')|n-(\sigma+\sigma')\rangle\right] \\
& - \sum_{\sigma\neq\sigma'=1}^{4} \frac{\beta(\sigma)\beta(\sigma')}{\sigma(\sigma'-\sigma)} \left[\gamma_n^+(\sigma)\gamma_{n+\sigma}^-(\sigma')|n-(\sigma'-\sigma)\rangle + \gamma_n^-(\sigma)\gamma_{n-\sigma}^+(\sigma')|n+(\sigma'-\sigma)\rangle\right] \\
& - \Delta E_n^{(1)} \sum_{\sigma=1}^{4} \frac{\beta(\sigma)}{\sigma^2} \left[\gamma_n^+(\sigma)|n+\sigma\rangle + \gamma_n^-(\sigma)|n-\sigma\rangle\right] \\
& - \frac{1}{2}|n\rangle \sum_{\sigma=1}^{4} \frac{\beta^2(\sigma)}{\sigma^2} \left[(\gamma_n^+(\sigma))^2 + (\gamma_n^-(\sigma))^2\right] \quad .
\end{aligned}
$$

Note that the requirement $m \neq n$ in summations (4.22), translated on indexes σ, σ' in equation (4.22), turns out to apply in the second summation only. In fact, this requirement is automatically fulfilled in the first sum due to the selection rules.

4.3.3 The Pair Distribution Function

In order to calculate the pair distribution function, let us come back to the coordinate representation. We have for the unperturbed states

$$u_n^{(0)}(r) = \langle r|n\rangle = \frac{1}{\sqrt{2^n n!\sqrt{\pi}}} e^{-r^2/2} H_n(r) \tag{4.22}$$

where $H_n(r)$ is the n–degree Hermite polynomial, defined as

$$H_n(r) = \sum_{k=0}^{[n/2]} \frac{(-1)^k \sqrt{n!}}{k!(n-2k)!} (2r)^{n-2k} \quad . \tag{4.23}$$

Similarly, we define

$$u_n^{(1)}(r) = \langle r|n^{(1)}\rangle \quad \text{and} \quad u_n^{(2)}(r) = \langle r|n^{(2)}\rangle \quad . \tag{4.24}$$

We can then use formula (4.4) together with the results from the previous paragraphs for the perturbed energy eigenvalues and eigenvectors. Since the wavefunctions are real, we can write

$$g(r,T) = \frac{\sum_{n=0}^{n_{max}} [u_n^{(0)}(r) + u_n^{(1)}(r) + u_n^{(2)}(r)]^2 e^{-[E_n^{(0)} + \Delta E_n^{(1)} + \Delta E_n^{(2)}]/k_B T}}{\sum_{n=0}^{n_{max}} e^{-[E_n^{(0)} + \Delta E_n^{(1)} + \Delta E_n^{(2)}]/k_B T}} \quad . \tag{4.25}$$

We have explicitly indicated the truncation of the summations as the integer n_{max}. In the computations this integer has always been fixed by requiring that the corresponding

normalised Boltzmann factor z_{nmax}/Z (Z being the partition function) was negligible up to some specified tolerance $tol = 10^{-M}$, i.e.

$$z_{nmax} = e^{-[E_{n_{max}}^{(0)} + \Delta E_{n_{max}}^{(1)} + \Delta E_{n_{max}}^{(2)}]/k_B T} \leq tol \quad . \tag{4.26}$$

This condition fixes the number of levels which are included in the perturbative series (4.25). Of course, the energy of the highest level included must be small compared to the potential well depth V_o. If we express energies in eV and temperature in Kelvin, from Equation (4.26) we get

$$2M\,T \times 10^{-4} < V_o \quad . \tag{4.27}$$

Typically for cuprates, V_o is of the order of 10 eV (see Chapter 2). Thus, requiring for example $M = 6$, we see that condition (4.27) is well satisfied up to temperatures of the order of 100 K. It is instructive to report examples of the whole set of perturbed levels for different choices of the harmonic constant k_2 and temperature T. The small nonlinear corrections to the energy levels will not appreciably affect the validity criteria deduced in the harmonic model. Therefore, we can temporarily consider $k_3 = k_4 = 0$.

An example of a typical output from a run of the program that calculates the pair distribution function is reported in Tables 4.2 and 4.3. We see that, in order to

n	E (eV)	z - T=80 K z - T=140 K z - T=200 K
0	0.0280	0.96E+00.99E+00.10E+01
1	0.0839	0.38E-010.96E-020.30E-03
2	0.1398	0.15E-020.94E-04.91E-07
3	0.1958	0.57E-04.91E-06.27E-10
4	0.2517	0.22E-05 0.89E-080.83E-14

Table 4.2: Energy levels and normalised Boltzmann factors as output from the program that computes the pair distribution function. Parameters are $k_2 = 10$ eV/Å^2, $k_3 = k_4 = 0$, $\mu = 2.13 \times 10^{-26}$ Kg, $n_{max} = 4$.

fulfill condition (4.26) for the Cu–O pair, the number of levels that must be included in the perturbative series does not exceed 4 for temperatures as high as T=200 K and elastic constants as low as 2 eV/Å^2. Moreover, it is apparent that the highest level that contributes appreciably to the perturbative expansion is low enough on the energy scale set by the well depth.

For what concerns the extension of our approach to other atomic species, it is important to observe that such self–consistency pre–analysis regarding levels and Boltzmann weighting is very sensitive to the value of the reduced mass μ.

As a general remark when a perturbative treatment is in use, one wants to monitor the validity of the perturbative approximation. We therefore introduce a parameter which gives a measure of the relative strengths of the perturbed and unperturbed energies, i.e.

$$
\begin{aligned}
\mathcal{R}_E &= \frac{2V_1(\sqrt{\langle (r-r_0)^2\rangle_T})}{k_2\langle (r-r_0)^2\rangle_T} \\
&= \frac{1}{k_2}\left[\frac{2}{3}k_3\sqrt{\langle (r-r_0)^2\rangle_T} + \frac{1}{2}k_4\langle (r-r_0)^2\rangle_T\right] \quad .
\end{aligned}
$$

	k_2=2 eV/Å^2		k_2=10 eV/Å^2	
n	E (eV)	z	E (eV)	z
0	0.0125	0.77E+00	0.028	0.96E+00
1	0.0375	0.18E+00	0.0839	0.38E-01
2	0.0625	0.42E-01	0.1398	0.15E-02
3	0.0876	0.99E-02	0.1958	0.57E-04
4	0.1126	0.23E-02	0.2517	0.22E-05
5	0.1376	0.54E-03	0.3077	0.87E-07
6	0.1626	0.13E-03	0.3636	0.34E-08
7	0.1876	0.30E-04	0.4195	0.13E-09
8	0.2126	0.70E-05	0.4755	0.52E-11

Table 4.3: Energy levels and normalised Boltzmann factors as output from the program that computes the pair distribution function. Parameters are $T = 80$ K, $k_3 = k_4 = 0$, $\mu = 2.13 \times 10^{-26}$ Kg, $n_{max} = 8$.

This parameter has always been checked in all the calculations of the pair distribution function, in order to prevent it from exceeding a critical value where our perturbative approach would break down. We fix at $\mathcal{R}_E \approx 0.1$, the self–consistency threshold of our perturbative calculation. The mean square value $\langle (r - r_0)^2 \rangle_T$ is defined as

$$\langle (r - r_0)^2 \rangle_T = \frac{1}{\mathcal{A}_g} \int (r - r_0)^2 g(r,T)\, dr \quad , \tag{4.28}$$

where $\mathcal{A}_g = \int g(r)\, dr$.

It is also important to observe that our approach in calculating the pair distribution function is meaningful so long as the quantum treatment of the two–body problem holds. The ratio $\mathcal{R}_Q = \hbar\omega / k_B T$ provides a good qualitative estimate of such condition. Here $\omega = \sqrt{k_2/\mu}$ is the frequency corresponding to the harmonic approximation in the power expansion of the potential $V_1(r)$. If $\mathcal{R}_Q$ is of order one, the quantum energy scale is comparable with the thermal one, and the system requires the full quantum description. On the contrary, if $\mathcal{R}_Q < 1$, the quantum levels are densely spaced on the thermal energy scale, and the classical approximation of the system holds. In Fig. 4.1 we plot $\mathcal{R}_Q$ as a function of k_2 in the interval [10,70] eV/Å^2, with the reduced mass of the Cu–O pair $\mu = 2.1355 \times 10^{-26}$ Kg. We show two curves, at the temperatures $T = 80$ and 200 K. The range chosen for the harmonic force constant k_2 corresponds to the variability range obtained from different lattice dynamic studies reported in the literature (see Chapter 2). As it shows, $\mathcal{R}_Q$ is of order one for temperatures up to $T = 200$ K and higher in the whole k_2 range.

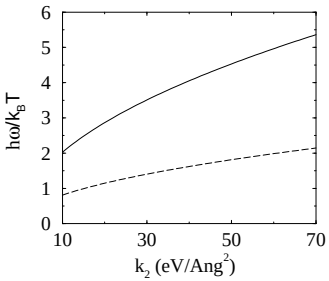

Figure 4.1: Plot of the ratio $\mathcal{R}_Q = \hbar\omega/k_B T$ vs k_2 for $T = 80$ K (solid line) and $T = 200$ K.(dashed line).

We shall now present a few examples of calculations of the pair distribution function, in order to better illustrate the specific effects of changing the relevant parameters. In Fig. 4.2 we illustrate the effect of changing the harmonic constant k_2, for a purely harmonic potential ($k_3 = k_4 = 0$) at $T = 200$ K. As it shows, increasing k_2 makes the radial distribution narrower and more peaked [3]. It is easy to understand

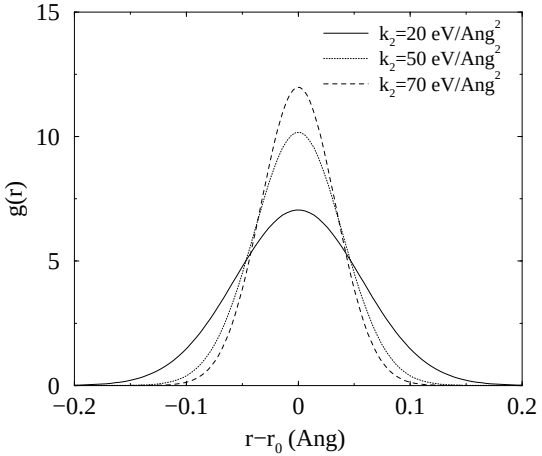

Figure 4.2: Plot of the pair distribution function as calculated from formula (4.25) for three different values of k_2. Parameters are: $k_3 = k_4 = 0$, $T = 200$ K, $m = 2.135 \times 10^{-26}$ Kg, $n_{max} = 9, 6, 4$ and $\mathcal{R}_Q = 1.15, 1.81, 2.29$ at $k_2 = 20, 50$ and 70 eV/Å^2, respectively.

the reason and make this observation more quantitative if we note that the variance of the harmonic distribution function coincides with the prediction of a simple Einstein model of frequency $\omega_E = \sqrt{k_2/\mu}$. Within such model, the mean square displacement is $\langle (r - r_0)^2 \rangle = (\hbar/2\mu\omega_E) \coth(\hbar\omega_E / 2k_B T)$ [125], where ω_E is the frequency associated with the quantum oscillator which describes each atom in the crystal. In the low temperature limit ($\hbar\omega > k_B T$)

$$\sigma^2 = \langle (r - r_0)^2 \rangle \approx \frac{\hbar}{2\mu\omega_E} \propto \frac{1}{\sqrt{k_2}} \quad .$$

On the contrary, at high temperatures ($\hbar\omega < k_B T$) the classical regime is recovered

$$\sigma^2 = \langle (r - r_0)^2 \rangle \approx \frac{k_B T}{\mu\omega_E^2} \propto \frac{1}{k_2} \quad .$$

We see that the function $\sigma^2(k_2)$, which controls the height and width of the distribution $g(r)$, is a power law with temperature–dependent exponent lying in the interval [-1,-0.5]. To complete this discussion, we plot in Fig. 4.3 the calculated variance of the pure–harmonic PQP–PDF as a function of the parameter k_2 (symbols) together with power–law best fits.

[3] We stress that all the plotted distributions are normalised to one

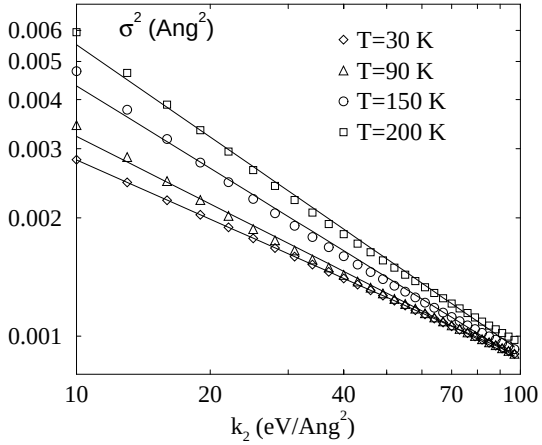

Figure 4.3: Symbols: log–log plot of the variance σ^2 of the pair distribution function as a function of k_2 for $T = 30, 90, 150$ and 200 K. Shown as solid lines are power–law best fits of the kind $y = ax^{-b}$; $b = 0.5, 0.57, 0.7$ and 0.78 in order of increasing temperature. The other parameters are: $k_3 = k_4 = 0$, $n_{max} = 20$ and $m = 2.13 \times 10^{-26}$ Kg.

Let us illustrate the dependence of the distribution function on the other two parameters k_3 and k_4. We shall here present results for two different atomic pairs: Ag–I pair ($\mu = 9.74 \times 10^{-26}$ Kg) and Cu–O pair ($\mu = 2.13 \times 10^{-26}$ Kg). We are here also reporting pair distribution functions for Ag–I since we shall use a spectrum taken at the Ag K–edge in AgI as a reference for testing our fitting procedure (see Chapter 5).

The parameter k_3 is responsible for the axial asymmetry of the potential well $V(r)$ with respect to its equilibrium position r_0. Hence, we expect this parameter to influence the degree of *skewness* of the pair distribution function, i.e. the asymmetry of the two halves with respect to an axis passing through the maximum. In Fig. 4.4 we plot the pair distribution for the pure–harmonic (k_3=0) and asymmetric potential. As it shows, the effect on the distribution of a negative k_3 (repulsive core in the potential stronger than the attractive part) leads to a positive–skewed distribution. We stress that the effect of changing k_3 on the pair distribution function is weaker the greater is k_2 at a fixed temperature. This can be simply understood by recalling the expression of the perturbation parameter Λ_3 formula (4.15). We see that, if one fixes the relative magnitude of k_3 and k_2, still Λ_3 decreases with increasing k_2 as $k_2^{-1/4}$. The same phenomenon occurs for the other potential parameter k_4. From formula (4.15) we see that Λ_4 decreases even more rapidly ($k_2^{-1/2}$) with increasing k_2, once the ratio k_4/k_2 has been fixed. As a consequence, to see the effect of a change in k_4, one must deal with small enough k_2 values. In Fig. 4.5 we plot the PQP–PDF for two different potentials with $k_2 = 5$ eV/Å^2, k_3=0 and $k_4 = 0, 20$ eV/Å^4. We see that changes k_4 control how much the PQP–PDF deviates from the pure Gaussian shape ($k_4 = 0$). Of course, the PQP–PDF is modified in a symmetric fashion. Finally, we give an example of the dependence of the pair distribution function on the temperature. In Fig. 4.6 we plot the

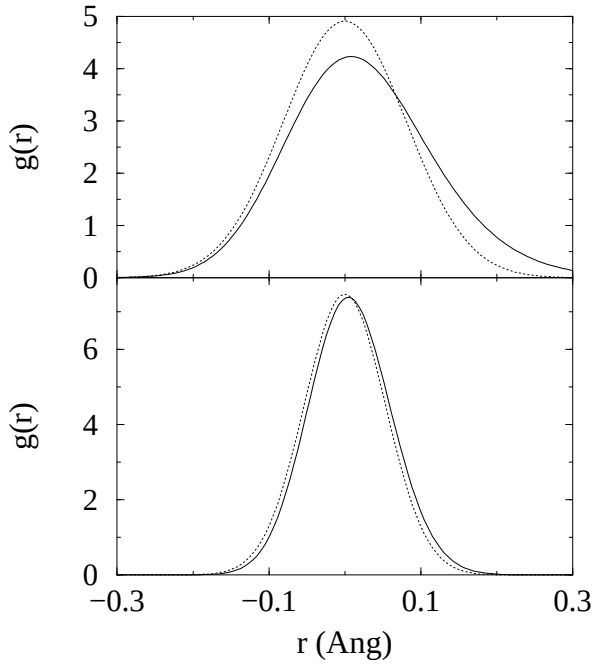

Figure 4.4: Plot of the pair distribution function as calculated from formula (4.25) for $k_3 = k_4 = 0$ (dotted lines) and $k_3 \neq 0, k_4 = 0$ (solid lines). Upper panel: $k_2 = 2$ eV/Å^2, $k_3 = -5$ eV/Å^3, $\mu = 9.74 \times 10^{-26}$ Kg. Lower panel: $k_2 = 10$ eV/Å^2, $k_3 = -25$ eV/Å^3, $\mu = 2.13 \times 10^{-26}$ Kg Other parameters are: $T = 140$ K, $\mathcal{R}_Q = 0.52(1.16)$ and $\mathcal{R}_E = 0.16(0.09)$, $n_{max} = 8(4)$ for $k_2 = 2(10)$ eV/Å^2.

distribution function at three different temperatures. We note that the temperature sensitivity of the distribution function tends to decrease as the temperature increases. We also observe that the quantum hypothesis breaks down for $k_2 \approx 2$ eV/Å^2 at $T \approx 200$ K ($\mathcal{R}_Q \ll 1$), while for $k_2 \approx 10$ eV/Å^2 the quantum treatment holds up to temperatures as high as $T \approx 300$ K.

4.4 Sensitivity of the pair distribution function to the potential anharmonicity.

In this chapter, we described how to calculate the pair distribution function and provided a few examples as to how it changes upon changing the relevant parameters of the pair potential energy, namely k_2, k_3, k_4. In the next chapter, we shall be using the pair distribution function to calculate model EXAFS signals and compare them

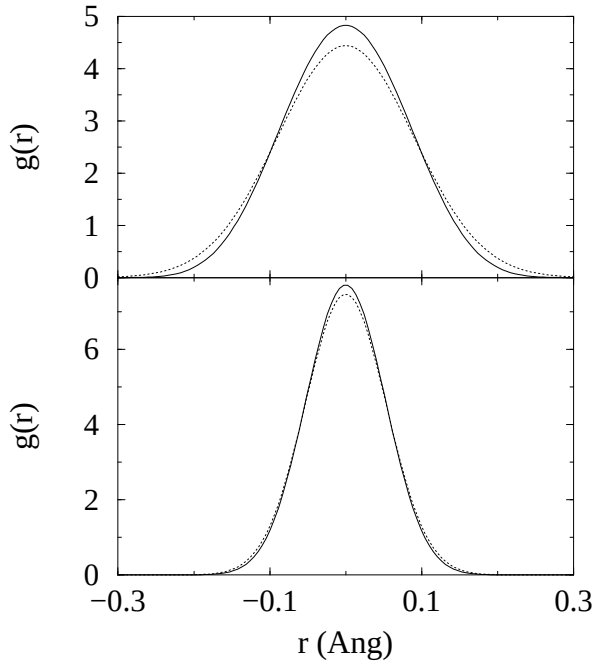

Figure 4.5: Plot of the pair distribution function as calculated from formula (4.25) for $k_3 = k_4 = 0$ (dotted lines) and $k_3 = 0, k_4 \neq 0$ (solid lines). Upper panel: $k_2 = 2$ eV/Å^2, $k_4 = 35$ eV/Å^4, $\mu = 9.74 \times 10^{-26}$ Kg. Lower panel: $k_2 = 10$ eV/Å^2, $k_4 = 200$ eV/Å^4, $\mu = 2.13 \times 10^{-26}$ Kg Other parameters are: $T = 140$ K, $\mathcal{R}_Q = 0.52(1.16)$ and $\mathcal{R}_E = 0.06(0.03)$, $n_{max} = 8(4)$ for $k_2 = 2(10)$ eV/Å^2.

with experimental spectra. In particular, we will refine the potential parameters k_2, k_3 and k_4 to best fit the experimental data. Moreover, we recall that k_3 and k_4 describe a perturbative Hamiltonian, and therefore we must make sure that the perturbative limit holds. Hence, it is clear that a quantitative assessment of the sensitivity of the distribution function on the important parameters is in order. Indeed, a first inspection at Figures 4.4 and 4.5 would seem to indicate that there is little sensitivity on k_3 and k_4. This is not the case. Or, better, it is not the case in certain regions of the parameter space spanned by the other parameters, namely k_2 and T. In this section, we shall introduce a simple procedure to assess the sensitivity of the pair distribution function, based on the so–called F–test [126]. The F–test is a very useful tool when one is interested in determining which of two different models, and to what extent, is more accurate in describing some experimental data which are being fitted with the maximum–likelihood method [127]. Such a situation typically arises in EXAFS spectroscopy when it is to be decided whether a spectrum needs the introduction of an

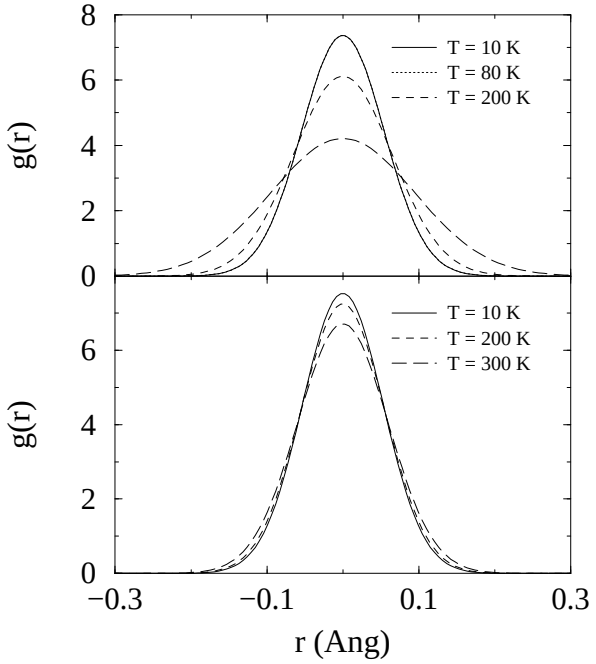

Figure 4.6: Plot of the pair distribution function as calculated from formula (4.25) for three different temperatures. Upper panel: $k_2 = 2$ eV/Å^2, $k_3 = 0$ eV/Å^3, $k_4 = 0$ eV/Å^4, $\mu = 9.74 \times 10^{-26}$ Kg, $n_{max} = 6$. $\mathcal{R}_Q = 3.39, 0.42$, and 0.17, respectively. Lower panel: $k_2 = 10$ eV/Å^2, $k_3 = 0$ eV/Å^3, $k_4 = 0$ eV/Å^4, $\mu = 2.13 \times 10^{-26}$ Kg, $n_{max} = 6$. $\mathcal{R}_Q = 16.2, 2.03$ and 0.54, respectively.

additional shell to be fitted (some physical information still present in the data) or the improvement achievable by incrementing the number of free parameters is statistically meaningless [128]. In our case, we are interested in assessing the sensitivity of the pair distribution function in capturing real physical information regarding potential anharmonicities. We shall do this separately for the following two cases

(a) Fitting directly the pair distribution function to a peak in the experimental Fourier transform of the EXAFS signal. This fit is carried out in the r (distance) space (as opposed to the k space), and therefore it does not involve any numerical integration (instead required to calculate $\chi(k)$). Although the characteristics of the experimental peaks cannot be directly translated into information regarding the interatomic potential, it is usually assumed that any anharmonicities show up in the same fashion in the Fourier transform of the experimental EXAFS signal and in the pair distribution function. This procedure is then suitable for detecting the presence of nonlinearities, but not to measure them.

(b) Fitting the model EXAFS signal calculated by means of Eq. (3.25) to the experimental signal (fit carried out in k space). The parameters that describe the pair distribution function describe the *true* interatomic potential as seen by EXAFS (see Chapter 3).

We are interested in applying the sensitivity test to both cases in order to ascertain whether, and possibly to what extent, some information and accuracy is lost through the numerical integration in the distance space that yields $\chi(k)$. We anticipate here the result, as we found that no appreciable loss of accuracy is observed to appear as a consequence of the numerical integration.

4.4.1 Least–square fitting and the F–test

Let us suppose that we are fitting N experimental data points (k_i, χ_i^{exp}), $i = 1, \ldots, N$, to a model that has M adjustable parameters a_j, $j = 1, \ldots, M$. The model predicts a functional relationship between the measured independent and dependent variables

$$\chi(k) = \chi(k; a_1, \ldots, a_M) \quad ,$$

where the dependence on the parameters is indicated explicitly on the right-hand side. In the spirit of the maximum–likelihood [4] method, we want to minimise a fit index (or residual function) of the kind

$$\mathcal{F} = \sum_{i=1}^{N} [\chi_i^{exp} - \chi^{the}(k_i; a_1, \ldots, a_M)]^2 \, w_i \tag{4.29}$$

where the w_i are some weight functions. In general, if the standard deviations σ_i of the experimental data are known independently, the correct choice would be

$$w_i = \frac{1}{\sigma_i^2} \quad .$$

However, depending on the particular algorithm used to actually perform the fit, some weighting functions are preferred. We shall discuss again this point in Chapter 5.

A general theorem in statistics states that the minimum of the residual function $\mathcal{F}_{min}$ is distributed as a χ^2 distribution with $\nu_1 = N-(M+1)$ degrees of freedom [129]. [5] Let us assume we want to compare an harmonic model potential (fit with M parameters) to a potential obtained by perturbing it with some anharmonicity (fit with $M+1$

[4] It is customary to refer to maximum likelihood, referring to the probability of occurrence of different sets of free parameters. Here we assume that there is just one model, the correct one, and a statistical universe of parameter sets that are drawn from it. Thus, if the measurement errors are independent and normally distributed, maximising with respect to the different parameter sets is equivalent do minimise a least–square indicator of the form (4.29).

[5] This result strictly holds when (i) the measurement errors are normally distributed, and either (ii) the model is linear in its parameters or (iii) the sample size is large enough that the uncertainties in the fitted parameters do not extend outside a region in which the model could be replaced by a suitable linearised model. Fits in EXAFS are usually at the limit of validity of condition (iii). However, all the statistical analysis that stems from this basic theorem is routinely applied in EXAFS data analysis (see e.g. [130]).

parameters), and we want to assess whether this last model *significantly* improves the fit (given the automatic improvement following the introduction of any additional free parameter). In other words, we are asking whether we are capturing a real physical feature in the experimental data. Let us consider the ratio of the normalised minima of the two corresponding fit indexes

$$F = \frac{\mathcal{F}_{min}(M)/\nu_1}{\mathcal{F}_{min}(M+1)/\nu_2} \quad , \tag{4.30}$$

where $\nu_2 = [N-(M+2)]$ and we have explicitly indicated the number of free parameters in either case. It can be shown that, as a consequence of the above theorem, such ratio follows an F_{ν_1,ν_2} distribution, whose density function is

$$\mathcal{D}_{\nu_1,\nu_2}(F)dF = \frac{\Gamma[(\nu_1+\nu_2)/2][(\nu_1/\nu_2)F]^{\nu_1/2-1}dF}{\Gamma(\nu_1/2)\Gamma(\nu_2/2)[(\nu_1/\nu_2)F+1]^{(\nu_1+\nu_2)/2}} \quad . \tag{4.31}$$

In particular, if both the harmonic and anharmonic models were appropriate to explaining all of the signal, one would expect the function

$$f = \nu_2 \left(\frac{\mathcal{F}_{min}(M)}{\mathcal{F}_{min}(M+1)} - 1 \right) \tag{4.32}$$

to follow an F_{1,ν_2} distribution. The F–test is then conducted as follows.

1. Based on some estimate of the experimental standard deviation, we generate an *artificial* experimental data set from the anharmonic model by just adding some Gaussian noise.

2. The two residuals $\mathcal{F}_h$ and $\mathcal{F}_a$ (h and a for the harmonic and anharmonic models, respectively) are calculated and the value of f obtained.

3. We can now fix our preferred confidence level c and compare f with F^c_{1,ν_2}. Here c is the percentage probability of obtaining a reduction $\mathcal{F}_{harm} - \mathcal{F}_{anh}$ as large as actually observed, when the added anharmonicity is not physically meaningful. The corresponding value F^c_{1,ν_2} of the stochastic variable F is defined as

$$c = 1 - \int_0^{F^c_{1,\nu_2}} \mathcal{D}_{1,\nu_2}(F)\, dF \quad .$$

We shall call such confidence level the *rejection probability*, which expresses the probability that the harmonic and anharmonic model are equivalent, that is, if $c = 1$ the two models are by all means indistinguishable, while if $c = 0$ there is virtually no probability that the harmonic one could explain the data instead of the anharmonic one. Here we chose to present our results regarding the sensitivity of the pair distribution function on the potential anharmonicities in two different ways.

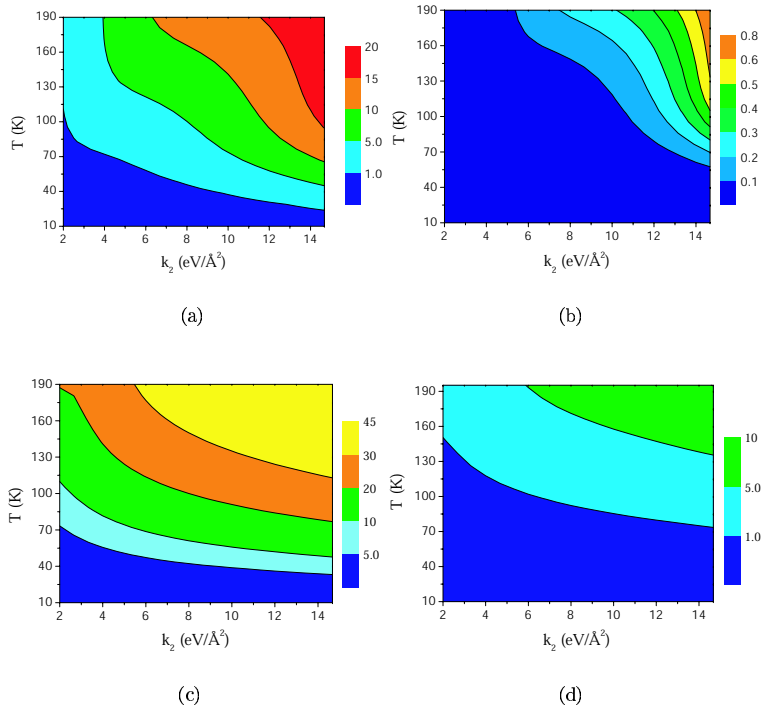

Figure 4.7: Case (a): sensitivity in the distance space. Fixed–anharmonicity phase–diagrams of the pair distribution function in the form of contour maps of the rejection probability (%). Different colors are associated with regions bounded by constant rejection probabilities as from the corresponding legends. Upper frames: Ag–I pair, $\mu = 9.74 \times 10^{-26}$ and (a) $|k_3| = |k_4| = |k_2|$ (b) $|k_3| = 2.1 \times |k_2|$, $|k_4| = 2.53 \times |k_2|$. Lower frames: Cu–O pair, $\mu = 2.13 \times 10^{-26}$ and (a) $|k_3| = |k_4| = |k_2|/2$ (b) $|k_3| = |k_4| = |k_2|$.

$k_2 - T$ phase diagrams We fix the anharmonic term in the potential energy as a fixed fraction [6] of the harmonic energy. We then sweep a certain region in the (k_2, T) space, calculate f and the corresponding rejection probability at each point. Such a table is then presented in the form of a contour map, which identifies regions in the (k_2, T) plane where the fixed anharmonicity in the potential shows at different confidence levels in the pair distribution function. Examples of such diagrams are presented in Fig. 4.7 for case (a). The standard deviation used to generate the artificial experimental set

[6] We shall refer to the *magnitude* of the anharmonic coefficients $|k_i|$ $(i = 3,4)$ as energies per unit weighted displacement.

has been fixed to

$$\sigma = \sigma_{T=10}\sqrt{\frac{T}{10}} \quad , \tag{4.33}$$

where $\sigma_{T=10} = 0.035$ is the experimental standard deviation corresponding to the best fit of the $T = 10$ K Cu–O peak in the Fourier transform of the experimental EXAFS signal from the Cu K–edge spectrum of $Ca_2CuO_2Cl_2$ (see Chapter 5). Case (a) and (b) turn out to be equivalent, which means that not much information is lost in the integration over distance. The number of points N has been fixed to 20, which is what is usually available for a typical peak in ordinary EXAFS data. The number of free parameters is $M = 2$.

In all the phase diagrams the anharmonicity is rather weak. Nevertheless, we see that our pair distribution function is quite sensitive (low rejection probabilities) to even weak anharmonicities over a large portion of the (k_2, T) space. These phase diagrams need only the reduced mass of the pair to be known, and can be constructed fairly easily for specific anharmonicities in the potential. For example, one can easily foresee whether our method is going to be sensitive to a certain anharmonicity at a given temperature and in a given interval of elastic constants.

Such phase diagrams, although very instructive, are calculated by fixing, for each value of k_2, the anharmonic constants k_3 and k_4 according to the same specific prescription. Hence, they do not allow one to separate the specific contribution to rejection probabilities of the cubic and quartic anharmonicities. This task can be accomplished by letting one of the cubic and quartic terms in the potential energy vary while keeping the other at zero.

Single–parameter sensitivity curves An other useful approach to obtain some sensitivity reference curves is to fix a point in the (k_2, T) space and let just one of the anharmonic force constants k_3 and k_4 vary at a time, while keeping the other at zero. By doing this, one can immediately estimate the anharmonicity threshold corresponding to the fixed confidence level, that is the lowest detectable anharmonicity in the potential at such a confidence level. We report here examples of such reference curves for case (a) (fit in the r space) in Fig. 4.8. The 5 % confidence level is explicitly shown. Parameters N and M are here 20 and 2 again, respectively. Note that in this case the choice $M = 2$ has a somewhat different meaning, since we are now fixing one of the two anharmonic force constant at zero in each case. Thus, this can also be regarded as an additional constraint. However, it is seen that by setting $M = 2$ or $M = 1$ does not appreciably affect the sensitivity reference curves.

Reference curves for case (b) (fit in the k space) are reported in Fig. 4.9. Here $N = 100$ and $M = 5$ for Ag–I and $M = 4$ for Cu–O (see Chapter 5). We note that the increase in the number of points makes the transition from the zero–sensitivity regime (100 % rejection probability) to the specific acceptance level much sharper. As a matter of fact, this makes even clearer the identification of the threshold anharmonicity. A k–dependent standard deviation has been adopted here in order to generate the artificial experimental data set, namely

$$\sigma(k) = \sigma_o \left(\frac{k_o}{k}\right)^3 \sqrt{\frac{T}{77}} \quad , \tag{4.34}$$

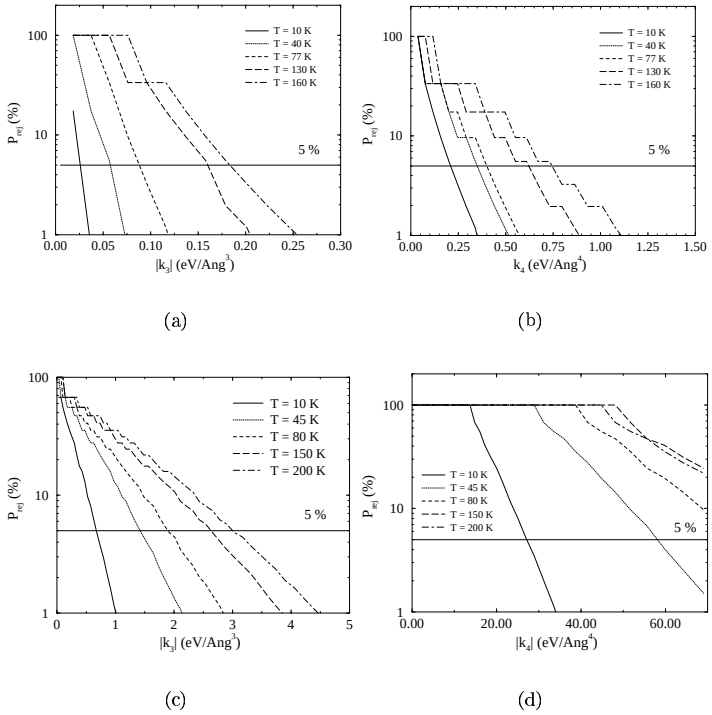

Figure 4.8: Case (a): Rejection probability as a function of the potential anharmonicity calculated at different temperatures in the case of fixed elastic constant. Upper frames: Ag–I pair, $\mu = 9.74 \times 10^{-26}$ and $k_2 = 1.83$ eV/Å^2. Lower frames: Cu–O pair, $\mu = 2.13 \times 10^{-26}$ and $k_2 = 10$ eV/Å^2.

where $\sigma_o = 0.041$ and $k_o = 12.7$ Å^{-1}. Expression (4.34) is the result of a fit performed on the the residuals from the EXAFS best fit of a $T = 77$ K Ag K–edge spectrum from AgI (see Chapter 5).

As a general feature, we recover the observation that the sensitivity to the anharmonic parameter k_4 gets worse on increasing the elastic constant k_2. This feature is also shared by the cubic constant, but to a lesser extent. We conclude that quartic nonlinearities in the potential are at the sensitivity limits of a perturbative treatment. In particular, a careful analysis of confidence domains is in required.

When varying the anharmonicity parameters, it is important to monitor the perturbative approximation. In Fig. 4.10, we report surface plots of $\mathcal{R}_E$ as a function of k_3 and k_4 in the parameter regions that have been taken into consideration in the preceding discussion. As it shows, the perturbative approximation is valid to a very good extent in the whole portions of the (k_3,k_4) plane which are relevant to the sensitivity

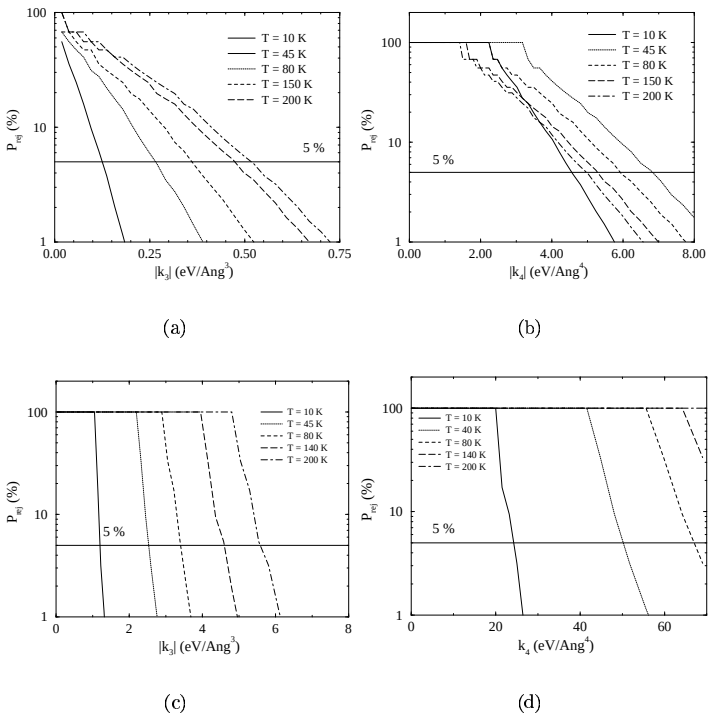

Figure 4.9: Case (b): Rejection probability as a function of the potential anharmonicity calculated at different temperatures in the case of fixed elastic constant. Upper frames: Ag–I pair, $\mu = 9.74 \times 10^{-26}$ and $k_2 = 1.83$ eV/Å^2. Lower frames: Cu–O pair, $\mu = 2.13 \times 10^{-26}$ and $k_2 = 10$ eV/Å^2.

assessment procedure, up to the higher temperatures considered.

4.5 Conclusions

In this chapter we have introduced a quantum pair distribution function, based on non–degenerate quantum perturbation theory. This function is directly parametrised by the first non–zero expansion coefficients in the Taylor series of the effective interatomic potential of the considered pair. We have shown how this function depends on the relevant potential parameters and on temperature. Moreover, we have discussed the limits of validity of our results. Namely, the constraints imposed by the perturbative treatment, and sensibility of the quantum regime as opposed to the ordinary classical treatment of pair distribution functions from model potentials. Finally, we discussed

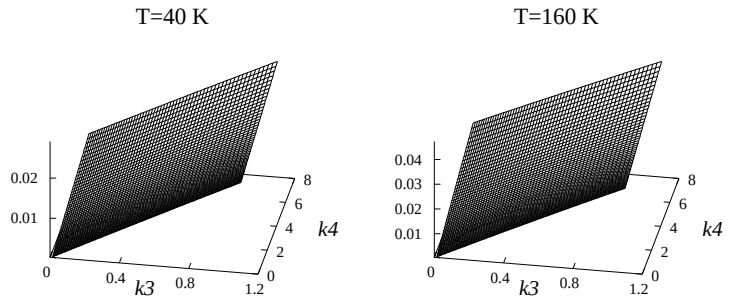

(a)

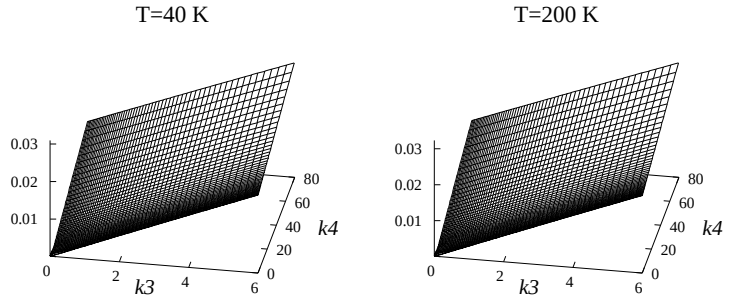

(b)

Figure 4.10: Surface plots of the perturbative index $\mathcal{R}_E$, defined in Eq. (4.28). (a): Ag–I pair, $\mu = 9.74 \times 10^{-26}$ and $k_2 = 1.83$ eV/Å^2. (b): Cu–O pair, $\mu = 2.13 \times 10^{-26}$ and $k_2 = 10$ eV/Å^2. Units for k_3 and k_4 are eV/Å^3 and eV/Å^4, respectively.

the problem of the sensitivity of the pair distribution function on the anharmonic parameters of the potential. In order to quantitatively assess such sensitivity, we developed a standard procedure based on the F–test. This procedure can be applied before analysing the data, whenever one is interested in using our method to extract from the EXAFS spectrum the information regarding interatomic potentials.

Chapter 5

Data analysis

5.1 Introduction

The details of both the theoretical and experimental frameworks of an EXAFS experiment have been described in Chapter 3, while our theoretical approach to the fitting of single–shell signals has been introduced and discussed in Chapter 4. This chapter is devoted to a complete analysis of our experimental data.

In the first half of this chapter we report a temperature–dependent study of the whole $Ca_2CuO_2Cl_2$ EXAFS spectra, performed by means of the comprehensive package GNXAS [131]. In the second half, we shall concentrate on the applications of the theory developed in Chapter 4 to the study of the Cu–O shell.

5.2 GNXAS analysis of the spectra

In this section we describe the analysis of the spectra which we carried out by means of the package GNXAS. The utility of such analysis is twofold. First, this procedure allows a very reliable extraction of the EXAFS signal $\chi(k)$ from the experimental spectra. This will allow us to accurately analyse the Cu–O peak in the Fourier transform of $\chi(k)$ and draw conclusions on the anharmonicity associated with the relative motion of the Cu–O pair. Second, an overall analysis of the whole spectrum up to the third coordination shell will enable us to discuss the lattice vibrations in the unit cell from a unified point of view. This is particularly important for a discussion of the correlations among atomic motions.

5.2.1 Preliminary analysis of the experimental spectra

The spectra collected during the measurements contain the absorption coefficient as a function of energy. In principle, one should expect an exact correspondence between the threshold energies of different spectra collected at different temperatures on the

same sample in the same experimental conditions. In practice, however, the alignment condition might not be fulfilled due to thermal instabilities of the monochromator. Therefore, the very first thing to do is to align the spectra. In general, one arbitrarily chooses a reference spectrum and shifts all other spectra to match the same reference peak (usually the most pronounced one).

As already mentioned in Chapter 3, the EXAFS oscillations in a crystalline material are superimposed to other contributions to the photoelectric absorption. They are generally referred to as *background* and include, besides the absorption of the isolated atom, absorption by atomic species other than the photoabsorber plus spurious contributions depending on the details of the experimental setup. In most data analysis schemes, these contributions are subtracted once for all at the beginning of the data analysis to obtain the EXAFS signal $\chi(k)$. In our case, the procedure followed by the package GNXAS has the advantage to interactively fit and subtract the background contribution while fitting the EXAFS signal. The refinement of the spline parameters describing the background absorption is performed until they are no longer correlated with the structural parameters which describe the EXAFS signal.

5.2.2 The GNXAS program

The GNXAS package is a very up–to–date and fully–featured EXAFS analysis tools, based on a multiple–scattering expansion of the absorption coefficient [132, 133, 134]. The data analysis procedure can be divided in two steps:

1. *ab initio* calculation of multiple–scattering model signals for a model structure around the absorber, hereafter *the cluster*;

2. refinement of the background and EXAFS parameters via the fitting of the total model signal to the experimental spectrum.

The first step is dealt with by the set of cascade programs CRYMOL, PHAGEN, GNPEAK and GNXAS. The program that actually performs the fit is called FITHEO. We give here a brief description of the individual programs that make up the package.
1 The Cartesian coordinates of the atoms in the coordination shells deemed important for the analysis are inputted to the program CRYMOL. Usually, they are known from crystallographic experiments. The program then builds all the so–called mini–clusters, one for each neighbour. These data are then used by the program GNXAS to compute the muffin–tin potentials at each site. With reference to Fig. 2.6, we included in the cluster the following coordination shells:

1. Planar O ions ($R \approx 1.93$ Å). Coordination number $N_s = 4$.

2. Apical Cl ions ($R \approx 2.75$ Å). Coordination number $N_s = 2$

3. Ca ions ($R \approx 3.18$ Å). Coordination number $N_s = 4$.

2 The program PHAGEN calculates the atomic potentials and all the phase shifts.
3 The next step is to determine all the possible n–body configurations that include the absorber atom, each associated to a peak in the generalised n–body distribution functions g_n. This is done by the program GNPEAK, that finds all the 2–,3– and 4–body

configurations around the absorber. A 2–body configuration is completely described by specifying the distance and the nature of the atomic species. A 3–body triangular configuration requires the assignment of two sides of the triangle (conventionally the two shortest ones) and the corresponding angle. Analogously, a 4–body configuration is described by 3 sides and 2 angles, whose choice depends on the topology of the configuration [135].

4 The program GNPEAK also determines the scattering paths associated with each configuration. All these data are then inputted to the program GNXAS that calculates the EXAFS signals γ^n associated with every n–body configuration. To clarify this strategy, let us consider the simple case of an absorber and one neighbour. The EXAFS signal is

$$\chi(k) = \gamma^{(2)}_{(0,i)}(k) = \chi_2^{(0i0)} + \chi_4^{(0i0i0)} + \dots \quad , \tag{5.1}$$

where $\chi_2^{(0i0)}$ corresponds to the single scattering $0 \to i \to 0$ while the generic $\chi_{2n}^{(\dots)}$ is associated with scattering paths where the photoelectron undergoes n consecutive scatterings form the i–th neighbour. Usually, the calculation is truncated at $\chi_2^{(0i0)}$ and $\chi_4^{(0i0i0)}$. This is because the scattering length is $2nR_{0i}$ (where R_{0i} is the distance between the absorber and its i–th neighbour) and the finite lifetime of the photoelectron strongly reduces the contribution of higher order scattering processes. For a three–atom (0, i and j) system the total signal is

$$\chi(k) = \gamma^{(2)}_{(0,i)}(k) + \gamma^{(2)}_{(0,j)}(k) + \gamma^{(3)}_{(0,i,j)}(k) \quad , \tag{5.2}$$

where $\gamma^{(3)}_{(0,i,j)}$ is associated with multiple–scattering paths of the kind $0 \to i \to j \to 0$, $0 \to j \to i \to 0$, $0 \to i \to j \to i \to 0$, $0 \to j \to i \to j \to 0$, $0 \to i \to 0 \to j \to 0$, etc. [132]. Note that $\gamma^{(3)}_{(0,i,j)}$ does not include the scattering paths involving two atoms only: these are already included in $\gamma^{(2)}_{(0,i)}$ and $\gamma^{(2)}_{(0,j)}$.

5 The final fitting procedure is performed by the program FITHEO. This program builds the model signal $\mu_{exp}(E_i)$ (E_i = kinetic energy at the i–th data point) by putting together the oscillations described by the different $\gamma^{(n)}$'s into a signal $\chi(k_i)$. It then adds the contribution of the background and compares the result with the experimental absorption coefficient $\mu_{exp}(E_i)$. The index i runs on the experimental points, and the wavevector k_i is given by

$$k_i = \sqrt{\frac{2m}{\hbar^2}(E_i - E_o)} \quad , \tag{5.3}$$

where E_o is the threshold energy.

The background is made of a pre–edge component $\mu^*(E_i)$, which is approximately linear, and a post–edge component $\mu_{spl}(E_i)$, which describes the non–oscillating part of the absorption coefficient above the edge. These two contributions are illustrated in Fig. 5.1: they are due to the absorption of atomic species different from that of the absorber present in the crystal, other possible neighbouring edges, and in general to the attenuation in the upstream ion–chamber and to the efficiency of the detectors.

If we indicate with $\mu_o(E_i)$ the contribution to absorption of the isolated photoabsorber, we have

$$\mu_o(E_i) = \mu_{spl}(E_i) - \mu^*(E_i) \quad .$$

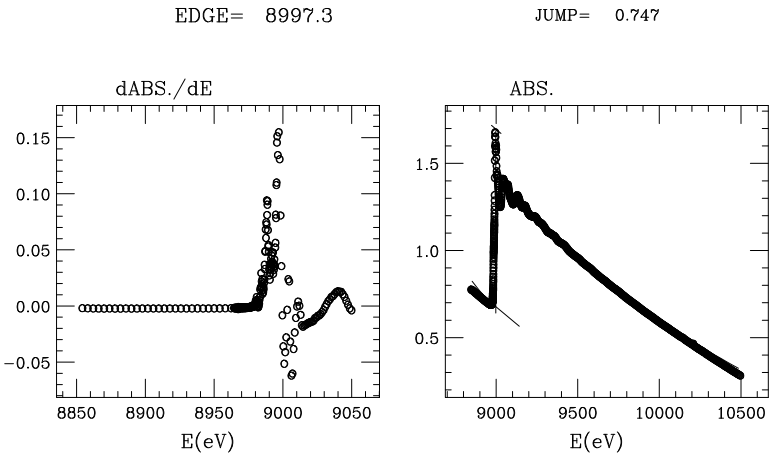

Figure 5.1: Cu K–edge EXAFS spectrum of $Ca_2CuO_2Cl_2$, T = 200 K. Left panel: numerical derivative of the experimental spectrum in the edge region. Right panel: Absorption coefficient $\mu(E)$ along with the pre–edge background $\mu^*(E)$ and the post–edge background $\mu_{spl}(E)$ as output from the program FITHEO.

On the other hand, the model EXAFS signal is defined as [135]

$$\chi_{th}(k_i) \equiv [(\mu_{th} - \mu^*) - \mu_o]/\mu_o \quad .$$

Therefore, we have

$$\mu_{th}(E_i) = \mu_{spl}(E_i) + \mu_o(E_i) \cdot S_o^2 \cdot \chi_{th}(E_i - E_o)$$

The pre–edge background is determined by fitting a straight line to the experimental absorption in the pre–edge region, and considering its continuation in the post–edge region. The post–edge background is determined by fitting a set of splines (usually 3 or 4) to the experimental absorption above the edge. This is intended to reproduce the signal–less trend of the EXAFS oscillations.

The comparison between μ_{exp} and μ_{th} is performed by FITHEO by defining a residual function of the form

$$R(\{\lambda\}) = \sum_{i=1}^{N} w_i \left[\mu_{exp}(E_i) - \mu_{th}(E_i;\, \lambda_1,\, \lambda_2,\, \dots\, \lambda_p)\right]^2 \quad , \tag{5.4}$$

where $\{\lambda\} = (\lambda_1,\, \lambda_2, \dots\, \lambda_p)$ is the set of p free parameters while the index i runs over the number N of experimental data points; w_i is the weight associated to each data point. If the errors in the measured data points are normally distributed the weight functions are inversely proportional to the experimental variances. In the GNXAS the weight functions are chosen as

$$w_i = \frac{N}{N-p} \frac{k_i^n}{\sum_i [\mu^2_{exp}(E_i) k_i^n]} \quad .$$

The choice $n = 0$ amounts to giving the same weight to all data points. By changing the exponent n one can assign a greater weight to high–k data points. It is customary to choose $k = 3$, as we did.

The core of the program FITHEO is the subroutine MINUIT, from the CERN FORTRAN library [136]. This minimisation routine employs a variety of different minimisation algorithms and gives the opportunity to set the interval of variation of the free parameters. In particular, one can hold a number of parameters fixed during the minimisation, from the beginning of the procedure or starting from a certain point. This flexibility proves particularly useful in investigating the sensitivity of the residual function on individual parameters. Finally, the computed minimum of the residual function can be checked by looking at contour maps in the parameters space, obtained by fixing all parameters but two at their best–fit value. This is the standard procedure to estimate confidence intervals for the floating parameters without neglecting correlations among different parameters (see section 5.3 for more details).

5.2.3 The free parameters

The structural model in the harmonic approximation is described, for each coordination shell s, by a mean distance R_s, a mean square relative displacement σ_s^2 and a coordination number N_s, which gives the number of atoms in the same shell. In crystals, the coordination numbers are often known from crystallographic data and do not need to be included in the fitting parameters.

The present theory of X–ray absorption contains some other physical quantities in the calculation of the cross–section that have no direct structural meaning. The nature of these quantities is mainly related to the description of the interaction of the photoelectron with deep and valence electrons. The introduction of phenomenological quantities describing the inelastic processes, the core–hole lifetime and many–electron effects is in any case necessary to obtain a good fit of the experimental spectra. The finite energy resolution of the experimental spectra has to be also taken into account in the calculation of the model signal. The difference between the theoretical and the experimental energy scale ΔE_o has to be refined too. In standard situations, only S_o^2 (amplitude correction factor) and ΔE_o (calibration of the energy scale) should be used as floating parameters.

The GNXAS strategy for multiple–scattering calculations is based on the use of an accurate complex energy–dependent self–energy function which automatically accounts for the inelastic mean–free–path of the excited photoelectron. This also avoids the introduction of a large number of parameters. In this case, it is assumed that the inelastic losses are correctly reproduced by the model potential and no refinement of the mean–free–path curve is performed. In our case, a complex potential is used from the beginning and the correct core–hole energy width has been already considered. Hence we do not need a MINUIT parameter accounting for the core–hole lifetime.

The experimental resolution depends on the experimental set–up used for the measurement under consideration. A single parameter $\sigma_{\rm res}$ defining the standard deviation (half–width) of the energy resolution function is used and refined around the estimated value.

Another important parameter is the S_o^2 reduction factor, accounting for effective

many–body corrections to the one–electron cross–section (see Chapter 3). Unfortunately, the multiple–scattering theory does not give a precise value for the amplitude of the principal transition, and scattered values are found in the literature. It is well known that the overall amplitude factor S_o^2 must lie in the interval 0.8-1, approximately constant as a function of the energy. Moreover, the intrinsic uncertainty in the threshold shape of the atomic cross–section also affects the actual intensity of the structural signal. Due to these sources of uncertainty in the overall amplitude of the structural signal, the program FITHEO allows one to float an amplitude reduction factor S_o^2, which does not depend on the energy, in a convenient region.

Another MINUIT parameter to be defined in FITHEO is the difference between the energy scales of the experiment and of the calculation (ΔE_o). This parameter enters the model signal in the energy–to–wavevector conversion (see Eq. (5.3)). The uncertainty of this parameter is due to many practical and theoretical reasons. In fact, for example, it is well known that experimental spectra recorded in different international facilities show tiny differences in the energy calibration and, on the other hand, that it is difficult to define a precise Fermi energy for the multiple–scattering calculations performed in the muffin–tin scheme. In particular, the zero of the theoretical energy scale is usually assigned to the muffin–tin interstitial potential energy level, a quantity that is generally difficult to relate precisely to the Fermi energy. Following these arguments, FITHEO is able to vary the ΔE_o parameter in the EXAFS region. The value of ΔE_o is usually in a range of 4-5 eV around the edge energy previously determined.[1] It has to be noted that the high–energy region, which is usually considered in the fitting procedure, is less sensitive to tiny variations of the ΔE_0 parameter.

The Cu K–edge EXAFS spectra in $Ca_2CuO_2Cl_2$ (and in all other cuprates) present a distinctive feature, which has to be taken into account. It is a multiple scattering contribution of the form $0 \to i \to 0+ \to i \to 0$, where 0 is the absorber Cu ion, i is its neighbour planar oxygen and 0+ is the Cu ion lying in the adjacent unit cell. This contribution is associated with a high–amplitude signal, since the atomic configuration is almost collinear (the backscattering functions $f(k,\theta)$ have a maximum at $\theta = \pi$), and will correspond to a mean distance approximately twice as much as the one describing the first shell. The fitting parameters associated with such a contribution are in principle the bond and angle variances and the bond–bond and bond–angle correlations contained in the symmetric covariance matrix

$$\mathcal{C} = \begin{pmatrix} \sigma^2_{R_1} & \rho^2_{R_1R_2} & \rho^2_{R_1\theta} \\ - & \sigma^2_{R_2} & \rho^2_{R_2\theta} \\ - & - & \sigma^2_{\theta} \end{pmatrix} \qquad (5.5)$$

where

$$\rho_{ij} = \frac{\sigma^2_{ij}}{\sqrt{\sigma^2_i \sigma^2_j}} \qquad \text{with} \quad i,j = R_1, R_2, \theta \quad \text{and} \quad i \neq j \quad .$$

The bond–bond and bond–angle correlations ρ_{ij} are non–dimensional and are defined in the range [-1,1]. Our case is simpler since the two distances R_1 and R_2 are the same.

[1] The program FITHEO calculates the estimated threshold energy as the maximum of the derivative of the experimental spectrum in the edge region (see left panel in Fig. 5.1)

We also found that a single correlation parameter was enough to obtain a satisfactory fit of the spectra. Thus, the three–parameters covariance matrix for the Cu–O–Cu peak can be written as

$$\mathcal{C} = \begin{pmatrix} \sigma_{\rm O}^2 & \rho^2 & \rho^2 \\ - & \sigma_{\rm O}^2 & \rho^2 \\ - & - & \sigma_\theta^2 \end{pmatrix} \tag{5.6}$$

where $\sigma_{\rm O}^2$ is the same fitting parameter used to describe the broadening of the Cu–O 2–body peak.

The total number of floating parameters in our fits is thus $p = 11$. We note that there exists a maximum number of parameters p_{max} that one is allowed to float in order to describe a given set of experimental points. In the case of EXAFS, it has been proved that [137]

$$p_{max} = \frac{2\,\Delta R \Delta k}{\pi} + 2 \quad , \tag{5.7}$$

where ΔR is a measure of the spherical region around the absorber described by our structural model ($\Delta R \approx 3$ Å= mean distance of the third and last shell included), while Δk is the extension in k–space of the interval where significant EXAFS oscillations are found. In the low–k region the limit comes from the exclusion of the XANES region (see Chapter 3) whilst in the high–k region the constraints are essentially due to the thermal damping of the signal and to the noise. We have $\Delta k \approx 11$ Å^{-1}. Eq. (5.7) then gives $p_{max} \approx 23$.

5.2.4 Results of the fits

We shall here briefly comment on the *global* results of the analysis performed with the GNXAS tools and then move to a more accurate analysis of the first shell contribution, namely the planar O ions. By global results we mean here the predictions of a model which takes into account all the coordination shells simultaneously. This approach has many advantages; among others, it allows a comparative analysis of the inter–parameter correlations. This is a delicate point in a multi–parameter non–linear fit, for a superficial analysis of the interdependencies among parameters can lead to wrong results. These problems mainly affect small–amplitude contributions to the EXAFS signal, and all signals with similar frequencies.

One of the shortcomings of such global analysis is that the structural model associated with every shell must be relatively simple. This requirement also comes from the fact that the number of parameters, which one is allowed to float meaningfully, is limited by the number of data points. Accordingly, it is very risky to introduce anharmonicity in the description of complicated EXAFS spectra (many coordination shells, multiple scattering contributions etc.) without actually introducing spurious uncontrolled information in the results. In particular, the cumulant expansion including the 3rd– and 4th–order terms can always be used for the g_2 , g_3 and g_4 peaks. However, the series is slowly convergent and can be useful only for very small deviations from the Gaussian approximation. Moreover, the reconstruction of the $g(r)$ shape is not always possible for a given set of cumulants. In particular, large statistical errors in the values of the higher–order cumulants generally lead to unacceptable uncertainties in the shape

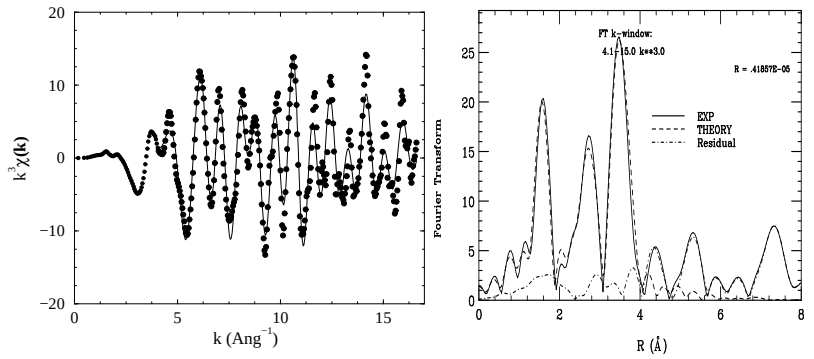

Figure 5.2: Cu K–edge EXAFS of $Ca_2CuO_2Cl_2$, $T = 80$ K. (a) Total model signal $\chi(k)$ (solid line) and experimental signal (filled circles). (b) Modulus of the Fourier transform.

of the distribution function. Therefore, the use of the cumulant expansion is generally not recommended[135]. However, the cumulant method (see Chapter 3) can still be used to reveal a *tendency* towards anharmonic behaviour in a given contribution to the total EXAFS (given peak in the Fourier transform), without actually demanding such indication to be quantitative. Of course, the perturbation introduced by anharmonic parameters has to be monitored and showed not to dramatically change the landscape of the residual function in $\{\lambda\}$–space.

In Figures 5.2 and 5.3 we show the quality of the fits carried out with the GNXAS package for two representative temperatures. We both show the total EXAFS signal and the modulus of the Fourier transform. The latter kind of plot is very useful for different reasons. In particular, the shape of each peak (associated to a different shell or multiple scattering contribution) is related to the structural properties of the shell itself. As we mentioned in Chapter 4, this allows one to look for the presence of anharmonicities directly in the peak shape. Although no direct quantitative information can be deduced in this way, this analysis can point the way for further investigations

We see three major peaks in the Fourier transform. Indeed they are four: the first three correspond to the three 2–body signals of the first three shells, while the fourth represent the contribution of the Cu–O–Cu multiple scattering. The second and third peaks are not distinguishable, not even at the lowest temperature ($T = 10$ K). This is essentially because of the high value of the mean square relative displacement of the second shell (namely, Cl ions). In fact, the height of a peak in the EXAFS Fourier transform is inversely proportional to the mean square displacement of the atoms lying in the corresponding shell [92]. We shall come back to this point in the following. The situation is sketched for clarity in Fig. 5.4, where we plot the theoretical γ signals corresponding to the best–fit value of the parameters along with their individual Fourier transforms at $T = 200$ K.

We found that all peaks could be reasonably reproduced by the harmonic model, with the exception of the contribution of the Ca shell. In this case we found that the

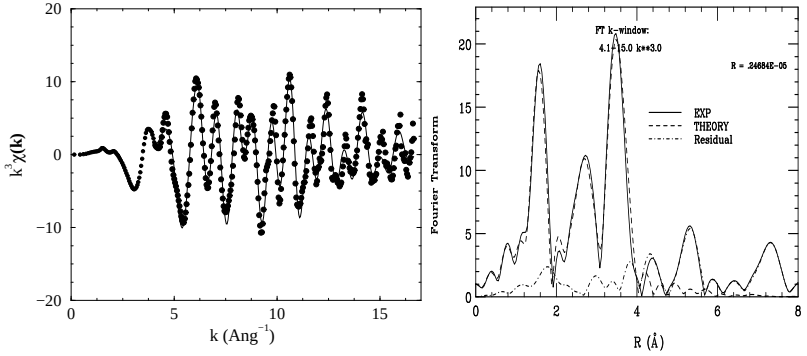

(a) (b)

Figure 5.3: Cu K–edge EXAFS of $Ca_2CuO_2Cl_2$, $T = 200$ K. (a) Total model signal $\chi(k)$ (solid line) and experimental signal (filled circles). (b) Modulus of the Fourier transform.

introduction of a non–zero third–order cumulant was necessary in order to significantly improve the quality of the whole fit. The measured valued of $C_{3,Ca}$ was found to be approximately constant over the whole temperature range ([10-200] K). The non–dimensional value of $C_{3,Ca}$ (normalised to one) turned out to be 0.9 ± 0.1. This is a very high value and cannot be quantitatively trusted as such. However, we must accept the indication that the harmonic model is not able to explain the dynamics of the Ca ions. Four contour sections in the parameter space are shown in Fig. 5.5 to illustrate the goodness of fit in the presence of the third cumulant $C_{3,Ca}$. This results certainly prompts a more accurate analysis of the Ca shell signal alone.

Another important result comes from a comparative analysis of the mean square displacements of the first three shells. The best–fit values are reported in Table 5.1 along with the best–fit values of the non–dimensional correlation parameter describing the Cu–O–Cu collinear multiple–scattering signal (see expression (5.6)). We see that the mean square displacements of Cl ions are much larger than those of the other ions. In particular, one order of magnitude larger than the mean square displacements of O ions. A partial explanation for this observation is possibly related to the covalent nature of the Cu–O bonds, compared with the looser, mainly ionic, Cu–Cl bonds. The same effect can be seen directly in R space in Fig. 5.4. However, it is intriguing to recall that low–temperature anharmonicity has been already found in the dynamics of the apical oxygens in YBCO [10, 11] and PrBCO [139]. In particular, a double–well potential was found for the Cu–apical-O pair both by EXAFS and Raman spectroscopies. In fact, the motivation for the choice of the experiment described in this thesis was originally to study the dynamics of apical ions in superconducting compounds where the apical site is not occupied by oxygen ions. Of course, with the structural model allowed by the GNXAS fitting routines we cannot discriminate between a single–minimum and a double–minimum potential. However, we observe that the lack of such resolution

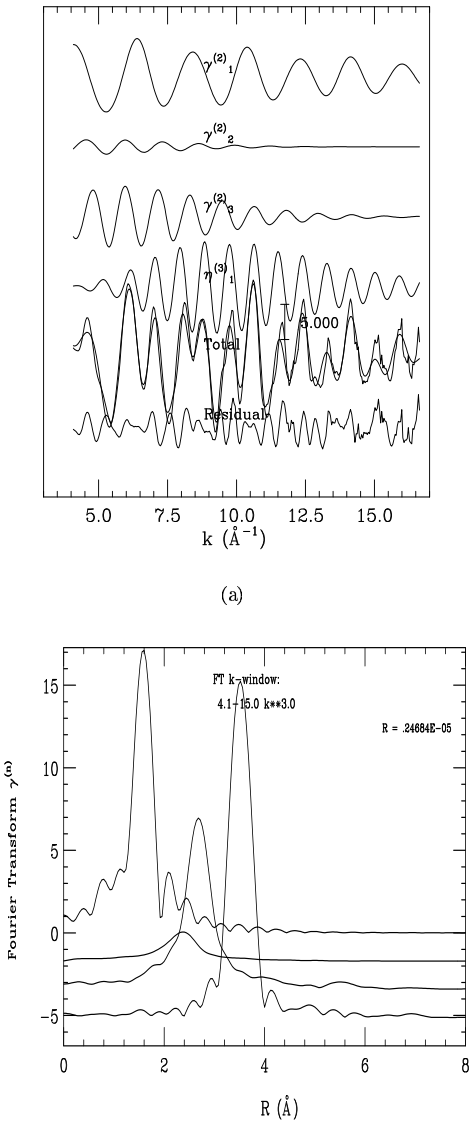

(a)

(b)

Figure 5.4: Cu K–edge EXAFS of $Ca_2CuO_2Cl_2$, $T = 200$ K. (a) best–fit γ signals and total EXAFS signal. (b) Fourier transform of the individual best–fit γ signals.

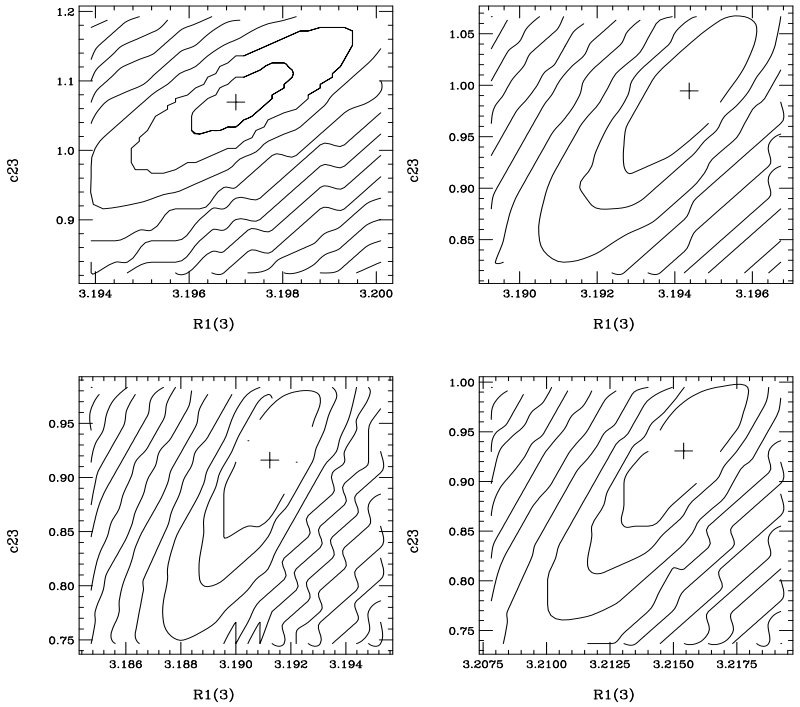

Figure 5.5: Cu K–edge EXAFS of $Ca_2CuO_2Cl_2$. Contour maps of sections of the residual function minimum (best fit) in the $(C_{3,Ca}, R_{Ca})$ space. A plus indicates the best–fit pair while the inner contour delimitates the 95 %–confidence region. From top to bottom and from left to right: $T = 20$ K, $T = 30$ K, $T = 50$ K and $T = 200$ K,

would most probably appear in the case of a double–well potential as anomalously large fluctuations in the mean distance. We then speculate that the Cl ions are described by an anharmonic flat–bottomed potential, whose details cannot be resolved within the present theory. This, if confirmed by other measurements (we think here of Raman spectroscopy as the ideal candidate), would be an important result. First, because it would mean that the apical ions are associated with anomalous vibrational properties irrespective of their nature. Second, because such anomalies would probably not be associated with the doping of the materials.[2] Alternatively, we might conjecture that the possible low temperature anharmonicity associated with the apical ions is a result of the doping against a pre–existing lattice instability in the non–doped compounds. It is clear that further experimental work is needed in order to properly assess the nature of

[2]We recall here that we are reporting EXAFS measurements on the non–doped oxy–halide $Ca_2CuO_2Cl_2$, ancestor of the Na–doped superconducting compound. (see Chapter 2).

T (K)	σ^2_O (Å^2)	σ^2_{Cl} (Å^2)	σ^2_{Ca} (Å^2)	ρ
10	0.00092(3)	0.0087(5)	0.0062(1)	0.74(5)
20	0.00112(3)	0.009(1)	0.0066(2)	0.47(4)
30	0.00125(3)	0.0091(6)	0.0066(1)	0.32(5)
40	0.00127(3)	0.0079(7)	0.0066(1)	0.25(3)
50	0.00130(2)	0.0098(7)	0.0068(1)	0.29(4)
60	0.00130(7)	0.0099(7)	0.0068(1)	0.30(7)
80	0.00132(7)	0.0097(6)	0.0071(1)	0.31(8)
200	0.00183(9)	0.0140(2)	0.0097(3)	0.32(7)

Table 5.1: Cu K–edge EXAFS of $Ca_2CuO_2Cl_2$. Measured mean square relative displacements of the first three coordination shells. The figures in brackets denote experimental errors (on the last digit) corresponding to a 95 % confidence level. The entries in the last column are the measured values of the non–dimensional correlation ρ describing the Cu–O–Cu multiple–scattering peak (see Eq. (5.6)).

such vibrational instability. In particular, EXAFS and Raman spectra of the Na–doped compounds are welcome in order to get a complete picture of the phenomenon.

5.3 Analysis of the oxygen peak

In this section we shall present a more detailed analysis of the oxygen peak. In particular, we will study its shape and attempt a quantitative measure of its deviations from the Gaussian shape. Let us first list the results obtained with the GNXAS tools.

(1) The contribution of the O ions is associated with small mean square displacements (high and narrow peaks in the EXAFS Fourier transform). This is one indication of the tight nature of the covalent Cu–O bond. At this level of analysis it is impossible to determine quantitatively whether this peak departs from the Gaussian shape.

(2) We observe a high (negative) correlation between the mean square displacement of the O ions and the non–dimensional correlation parameter ρ describing the Cu–O–Cu multiple–scattering peak. This is shown in Fig. 5.6 in the form of contour maps of the residual function in the (σ^2_O, ρ) space. In particular, it is interesting to note that the correlation describing the Cu–O–Cu peak displays a substantial increase for temperatures approximately below the measured transition temperature of the Na–doped compound (see Fig. 5.7). The measured correlation trend suggests an increase of order in the CuO_2

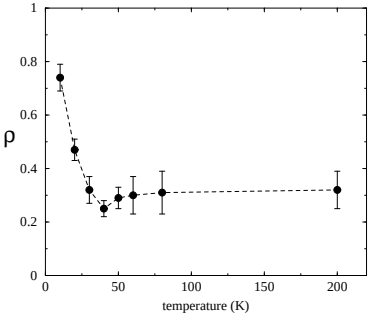

Figure 5.7: Cu K–edge EXAFS of $Ca_2CuO_2Cl_2$. Correlation describing the Cu – O –Cu multiple scattering signal.

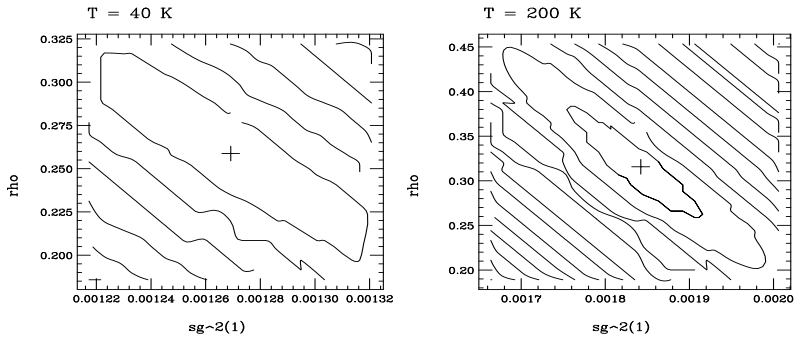

Figure 5.6: Cu K–edge EXAFS of $Ca_2CuO_2Cl_2$. Contour maps of sections of the residual function minimum (best fit) in the (σ_O^2, ρ) space. A plus indicates the best–fit pair while the inner contour delimitates the 95 %–confidence region.

planes for temperatures $T < T_c$. Towards greater values of the temperature, the superconducting transition seems to mark a crossover to a different state of correlation between atomic motions in the copper–oxide sheets, characterised by an almost constant value of the correlation. We recall that ρ describes both the bond–bond and bond–angle correlations of the Cu–O–Cu multiple scattering signal. However, we found no significant deviations from the ideal $\theta = 180^0$ geometry, nor anomalous behaviour of the angle standard deviation at low temperatures. We conclude that the behaviour of ρ is largely dominated by the bond–bond correlations. We observe that the same measurement in the Na–doped superconducting material would add an important piece of information to the present speculations.

5.3.1 Analysis with the quantum perturbative pair distribution

We have already stressed that the shape of a peak in the EXAFS Fourier transform carries important information on the dynamics of the ions lying in the corresponding shell. However, this information is difficult to capture in the framework of a global analysis of the EXAFS signal, such as that performed with the GNXAS tools. We shall discuss here an alternative analysis of the O peak, based on the quantum perturbative pair distribution worked out in Chapter 4. We fitted the experimental peak directly with the distribution function. This approach does not allow us to assign a specific meaning to the floating anharmonic parameters entering the distribution function (namely k_3 and k_4). However, even slight deviations from the Gaussian shape can be detected with this procedure. More important, a statistical analysis of the significance of such variations can be carried out, based on the F–test (see Chapter 4). We anticipate here the results: significant low–temperature anharmonicity of the quartic type (flat–bottomed–like potential) is found at very low temperatures. Such deviations from the Gaussian shape disappear soon with increasing temperatures, and the Gaussian shape is recovered. We stress that the spline fitting of the post–edge EXAFS

signal (used for the background extraction) has been performed according to exactly the same procedure for all analysed temperatures. This ensures that the comparison of the experimental peaks at different temperatures is a meaningful operation. The fits were performed by means of the Nag FORTRAN routine E04UNF [140]. This routine is a very flexible and stable tool, designed to minimise an arbitrary smooth sum of squares function subject to constraints (which may include simple bounds on the variables, linear constraints and smooth nonlinear constraints) using a sequential quadratic programming [141]. The residual function that we minimised is

$$\mathcal{R} = \sum_{i=1}^{N} w_i [g_i - g(R_i; k_2, k_4)]^2 \quad . \tag{5.8}$$

where the weight functions have been set to the optimal value $w_i = 10 \; \forall \; i$ in order to obtain $\mathcal{R}_{min}$ of order unity.

The problem of revealing a *true* nonlinear component in the Cu–O potential is equivalent to assessing the statistical significance of the improvement in the fits performed with the anharmonic distribution with respect to those carried out with a Gaussian distributions. However, it is very difficult to quantify such improvement from direct inspection of the best–fit distributions, due to the small differences of the anharmonic and Gaussian functions (see Chapter 4). To solve the problem, the F–test can be invoked. Let us clearly state the problem.

In the harmonic model, we are fitting a set of N experimental points (the peak) within a theory with $p = 1$ (the harmonic constant k_2) floating parameters. We now add two more parameters, namely the cubic and quartic constants k_3 and k_4. We then ask: what is a significant reduction in the residual function? More precisely: If a new parameter is added to a fit within the present theory, what improvement in the residual function should we seek in order to have a specified confidence level in the results? The significance test then takes the form that the fit with the anharmonic distribution is to be accepted if (see Chapter 4)

$$\left(\frac{\mathcal{R}^h_{min} - \mathcal{R}^{anh}_{min}}{\mathcal{R}^{anh}_{min}} \right) n_d > F^c_{1,n_d} \quad , \tag{5.9}$$

where $n_d = N - (p+1)$ is the number of degrees of freedom and the superscripts h and anh indicate the values of the residual $\mathcal{R}_{min}$ within the harmonic and anharmonic models, respectively. We are interested in the statistical significance of the fit improvement obtained after introducing one anharmonic parameter at one time. This procedure is meaningful since the k_3 and k_4 parameters are uncorrelated (see Chapter 4). The value of the F–distribution $F^c_{n_1,n_2}$ for $n_1 = 1$ and $n_2 = 12$ (corresponding to $N = 14$ data points) at the 95 % and 99 % confidence levels are

$$F^{0.05}_{1,12} = 4.747 \qquad \text{and} \qquad F^{0.01}_{1,12} = 9.33 \quad .$$

Eq. 5.9 prescribes then that the anharmonic fit is to be accepted with 95 % confidence if

$$\frac{\mathcal{R}^h_{min}}{\mathcal{R}^{anh}_{min}} > 1.39 \tag{5.10}$$

and with 99 % confidence if

$$\frac{\mathcal{R}^h_{min}}{\mathcal{R}^{anh}_{min}} > 1.78 \quad . \tag{5.11}$$

Furthermore, the above arguments can be reversed to calculate the rejection probability c corresponding to a given ratio $\mathcal{R}^h_{min}/\mathcal{R}^{anh}_{min}$. In this case, the following equation has to be solved with respect to the variable c

$$\left(\frac{\mathcal{R}^h_{min}}{\mathcal{R}^{anh}_{min}} - 1\right) n_d = F^c_{p,n_d} \quad , \tag{5.12}$$

with $p = 1$ and $n_d = 12$. The results of our fits are reported in Table 5.2. We found that no significant improvement in the fits could be obtained by introducing a cubic nonlinearity in the model potential. On the contrary, a significant large low–temperature anharmonicity of the quartic type was found at temperatures $T < 40$ K. Such nonlinearity significantly shows also at larger temperatures, although it is not as large as it is at low temperatures. This finding is particularly interesting, since the onset of such a nonlinearity in the potential roughly matches the onset of superconductivity in the Na–doped compound.

The analysis of the quartic anharmonicity in the potential can be made quantitative by calculating the fourth–order cumulant (see Chapter 3) according to the formula [142]

$$C_4 = \langle (r - \langle r \rangle)^4 \rangle - 3[\langle (r - \langle r \rangle)^2 \rangle]^2 \quad , \tag{5.13}$$

where the 4th– and 2nd–order moments can be calculated directly from the best–fit normalised distribution $g(r)$ as

$$\langle (r - \langle r \rangle)^4 \rangle = \int_{-\infty}^{+\infty} r^4 g(r) dr \qquad \text{and} \qquad \langle (r - \langle r \rangle)^2 \rangle = \int_{-\infty}^{+\infty} r^2 g(r) dr$$

It can be shown that the expression (5.13) identically vanishes in the harmonic limit. This is because, in the limit of a Gaussian distribution, the fourth–order moment $m_4 = \langle (r - \langle r \rangle)^4 \rangle$ is exactly $m_4 = 3m_2$, where m_2 is the second–order moment. In fact, the non–dimensional parameter

$$\kappa = m_4/m_2^2 - 3 \quad , \tag{5.14}$$

known as *kurtosis*, is used in the context of the theory of probability to measure the deviation of a given distribution from a Gaussian. Therefore, we can use both formula (5.13) and (5.14) to provide an independent (quantitative) check to analyse the experimentally measured nonlinearities.

The experimental values of C_4 and κ are reported in the last two columns of Table 5.2. We see that the measured distribution displays a marked *leptokurtik* ($\kappa > 0$) behaviour for $T < 40$, i.e. a marked peak of the distribution around the mean and rather *thick* tails. Conversely, at temperatures $T \geq 40$ K the kurtosis changes sign and becomes small and practically constant. This indicates smaller deviations from the Gaussian shape towards a flatter top and thinner tails. We conclude that the Cu–O potential displays a significant low–temperature anharmonicity up to $T = 40$ K. In particular, in such a temperature range it shows a characteristic flat bottle–like bottom

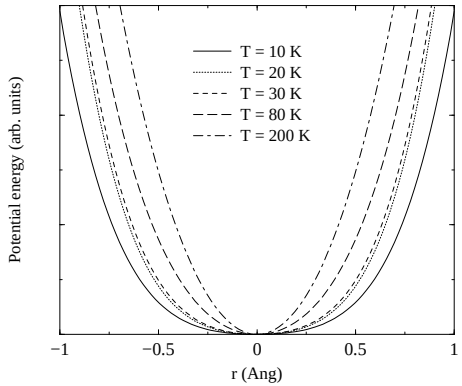

Figure 5.8: Cu–O interatomic potential at different temperatures as calculated from the fits of the experimental O peak in the EXAFS Fourier transform.

(see Fig. 5.8). We recall that a similar potential has also been revealed at the Eu site in Eu–BCO by means of Mössbauer spectroscopy [12]. We stress that the measured anharmonicities fall in the domain of validity of the perturbative approximation, being $\mathcal{R}_E \approx 0.12$ for the largest measured nonlinearity (see Chapter 4, Eq.(4.28) for the definition of .$\mathcal{R}_E$).

Let us finish this section by providing an estimate of the errors associated with the above–listed best–fit values of the peak parameters. As already mentioned in Chapter 4, there exists a general theorem that states that the minimum of the residual function $\mathcal{R}_{min}$ follows a χ^2 distribution with $N - (M + 1)$ degrees of freedom. Here N is the dimension of the experimental data set and M is the number of floating parameters $\lambda_1, \lambda_2, \ldots, \lambda_M$. This result holds under not very restrictive assumptions and is usually accepted in the context of optimisation with maximum–likelihood indicators [127]. An important corollary of such theorem provides the basis for the error analysis. Let us suppose that only ν parameters are varied, while the other $M - \nu$ are held fixed at their best–fit value. In this case the function

$$\Delta\mathcal{R} = \mathcal{R}(\lambda_1, \lambda_2, \ldots, \lambda_\nu) - \mathcal{R}_{min} \tag{5.15}$$

follows a χ^2 distribution with ν degrees of freedom. If $\nu = 1$ this result provides the error on the selected parameter in the form of *confidence intervals* through the simple condition

$$\Delta\mathcal{R}(\lambda) = [\chi^2]^c_{\nu=1} \quad , \tag{5.16}$$

where $[\chi^2]^c_{\nu=1}$ is the value of the χ^2 variable corresponding to the required confidence level (i.e. rejection probability) c for $\nu = 1$ degrees of freedom. This would be a safe procedure to estimate the errors on all floating parameters if there were no correlations among them. Unfortunately, this is not the case in complicated multi–parameter fits as those of EXAFS spectra. In such cases a more refined analysis is in order, one that allows to estimate confidence *regions* of more than one parameter jointly. This analysis

T (K)	k_2 (eV/Å^2)	k_4 (eVÅ^4)	$\mathcal{R}^h_{min}/\mathcal{R}^{anh}_{min}$	c (%)	C_4 (Å^4)	κ
10	0.125	-				
	0.058	0.47	1.78	0.2	0.0036	3.96
20	0.13	-				
	0.075	0.59	2.69	0.07	0.0029	3.16
30	0.145	-				
	0.11	0.7	2.05	0.4	0.0005	0.81
40	0.146	-				
	0.127	0.301	1.12	25	-0.0001	-0.17
50	0.19	-				
	0.16	0.51	1.43	4	-0.0001	-0.19
60	0.23	-				
	0.19	0.6	1.46	4	-0.0001	-0.19
80	0.31	-				
	0.29	0.49	1.16	19	-0.0001	-0.15
200	0.58	-				
	0.56	0.25	1.03	56	-0.00007	-0.07

Table 5.2: Analysis of the oxygen peak with the quantum distribution function. The entries in the column labeled $\mathcal{R}^h_{min}/\mathcal{R}^{anh}_{min}$ are to be compared with the expressions (5.10) and (5.11). The rejection probabilities are listed in the column labeled c. In the last column, the values of the measured kurtosis have been set to zero if less than 0.1.

ν	50 %	70 %	90 %	95 %	99 %
1	0.46	1.07	2.70	3.84	6.63
2	1.39	2.41	4.61	5.99	9.21

Table 5.3: Values of $[\chi^2]^c_\nu$ for $\nu = 1, 2$ and five different confidence levels c.

is usually performed for $\nu = 2$ by constructing the so–called *confidence ellipses*

$$\Delta\mathcal{R}(\lambda_1, \lambda_2) = [\chi^2]^c_{\nu=2} \quad . \tag{5.17}$$

A few values of $[\chi^2]^c_\nu$ are reported in Table 5.3 for $\nu = 1, 2$ and a few confidence levels. The errors on individual parameters are estimated from the two–dimensional confidence regions by *projecting* the ellipsis on the parameter axes. In case of no correlation the ellipses (5.17) degenerate into circumferences, whilst a high degree of correlation manifests itself by distorting the ellipsis boundaries.

As an example of the above considerations, we calculated the confidence ellipses (5.17) for our fits of the Cu–O peak (5.8). These are shown in Fig. 5.9 (b) for the $T = 20$ K peak. The high degree of correlation between k_2 and k_4 is apparent. In Fig. 5.9 (a) we show two sections of the form (5.16), obtained by letting one parameter vary while keeping the other at its best–fit value. It is clear that an error estimate based on confidence intervals leads in this case to a substantial underestimation of the errors associated with the two floating parameters. If the shape of the two–dimensional contour is not taken into account, the error estimate is

$$\frac{\Delta k_2}{k_2} \approx 2.3\% \qquad \frac{\Delta k_4}{k_4} \approx 2.1\%$$

at the 90 % confidence level, while the full analysis of the joint variations yields

$$\frac{\Delta k_2}{k_2} \approx 3\% \qquad \frac{\Delta k_4}{k_4} \approx 8.5\%$$

at the same level of confidence. In practice, we found that relative errors of ≈ 5 % and ≈ 10 % on $\Delta k_2/k_2$ and $\Delta k_4/k_4$, respectively, well account for the uncertainties associated with the fits of the Cu–O peak at all the examined temperatures.

5.4 Fitting the Cu–O single–shell EXAFS with the QPDF

The rest of this Chapter is dedicated to the application of the quantum perturbative distribution function developed in Chapter 4 to the fit of the Cu–O EXAFS signal. Unfortunately, it is well known that the task of extracting single–shell signals from the complete EXAFS is a very complicated one. Usually, Fourier filtering techniques are used. The main problem with this approach, however, is that the filtered EXAFS signal undergoes unpredictable distortions by means of this procedure, both in its amplitude and phase. As a consequence, the fitting algorithm must be a very reliable one. Moreover, in order not to accept unphysical results as true, the physical grounds underlying the choice of the floating parameters must be settled on a firm basis. Therefore, in our case, it is desirable to test the fitting procedure based on the quantum perturbative distribution function in a well–studied case.

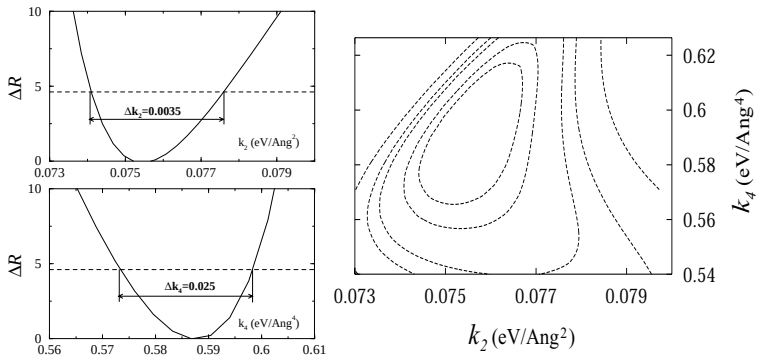

Figure 5.9: Analysis of the minimum shape for the fit of the Cu–O peak at $T = 20$ K. (a) Sections of the function $\Delta\mathcal{R}$. The dashed line at $\Delta\mathcal{R} = 4.61$ marks the 90 % confidence level for $\nu = 2$. (b) Contours of $\Delta\mathcal{R}$ at (from centre): $c = 50$ %, 70 %, 90 %, 95 %, 99 %.

T(K)	k_2 (eV/Å^2)	k_3 (eV/Å^3)	k_4 (eV/Å^4)
300	2.37(1)	-5.0(1)	0.1(0.3)
600	2.75(1)	-5.3(1)	0.04(0.21)

Table 5.4: Potential parameters as measured in Ref. [147].

5.4.1 Ag K–edge EXAFS of AgI: a case study

Silver iodide (AgI) is known for being a highly–anharmonic material [144, 145, 146]. In particular, the classical expression(4.3), Chap. 4, of the pair distribution function has been recently used in Ref. [147] to measure the first three coefficients of the Taylor expansion of the Ag–I potential. Two spectra have been analysed in that piece of work, at $T = 300$ K and $T = 600$ K. The corresponding results for the potential parameters are reported in Table 5.4 (second and third lines) for a Taylor expansion of the form (4.5), Chap. 4. The experiment finds no trace of fourth–order anharmonicity (see the reported errors in Table 5.4, third column).

In this section we will analyse an Ag K–edge EXAFS spectrum[3] collected at $T = 77$ K by means of our quantum perturbative distribution function. It is not difficult to foresee that such temperature lies in the range of validity of quantum mechanics. In fact, substituting a value of the order $k_2 \approx 2$ eV/Å^2 in the the expression $\mathcal{R}_Q = \hbar\omega/k_B T$, yields $\mathcal{R}_Q \approx 0.5$. Hence, we can be sure that a limited number of energy levels is required to construct the whole pair distribution $g(r)$ according to our perturbative treatment (see Fig. 5.12 (b)).

The EXAFS signal $\chi(k)$ is constructed as described in Chapter 3 according to the

[3]Courtesy of Dr P. Ghigna, Pavia University.

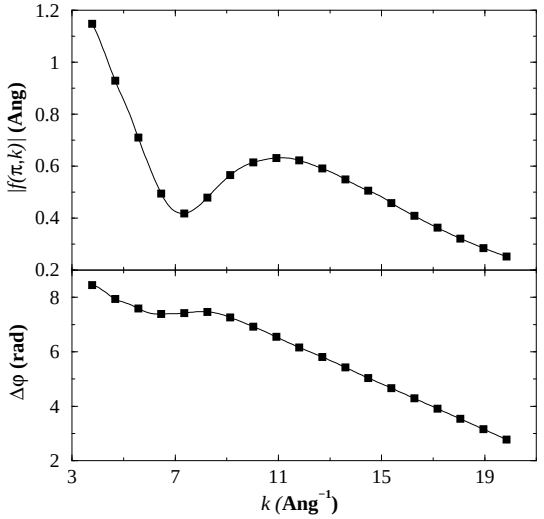

Figure 5.10: Upper frame: backscattering amplitude $|f_I(\pi, k)|$ of the I ions. Lower frame: total phase shift $\Delta\varphi$. The symbols are the data points from Ref. [95], the solid line is a cubic spline interpolation from our built–in routine.

following expression

$$\chi(k) = \frac{S_o^2}{k} N_I \, Im\left\{ f_I(\pi,k)\, e^{2i\delta_{Ag}} \int_0^\infty g(r)\, \frac{e^{-2r/\lambda(k)}}{r^2}\, e^{2ikr}\, dr \right\} \quad , \tag{5.18}$$

where $N_I = 4$ is the coordination number of the I ions, δ_{Ag} is the central atom phase shift[4] and $f_I(\pi, k) = |f_I(\pi, k)| \exp(i\phi_I)$ is the complex backscattering amplitude of the I ions. The total phase shift $\Delta\varphi$ is given by

$$\Delta\varphi = 2\delta_{Ag} + \phi_I - \pi \quad , \tag{5.19}$$

where the last term must be added for K edges [95]. Both the backscattering amplitude and phase shift were taken from the tables reported in Ref. [95] in the form of a set of data points from theoretical calculations performed at certain values of the wavevector k. We then incorporated in the main fitting code a routine that calculates a cubic spline approximation of both amplitude and phase curves at any point in k space corresponding to a given value of the (floating) energy shift ΔE_o. These are shown in Fig. 5.10.

The mean free path $\lambda(k)$ is parametrised as described in Chapter 3 as

$$\lambda(k) = \frac{1}{\eta}\left[\left(\frac{\xi}{k}\right)^4 + k^n\right] \quad , \tag{5.20}$$

[4]Recall from Chapter 3 that this phase shift has to be counted twice, since the photoelectron experiences a phase shift at the photoabsorber site both as it is ejected and as it comes back after interacting with the backscattering atoms.

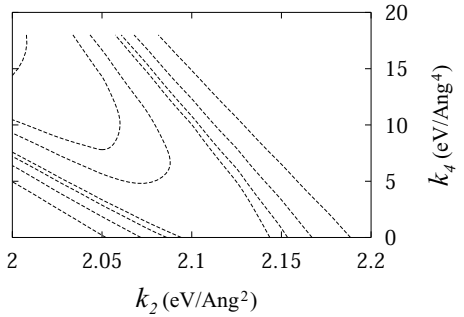

Figure 5.11: Contour levels of the function $\Delta\mathcal{R} = \mathcal{R}(k_2, k_4) - \mathcal{R}_{min}$ for the minimum corresponding to the harmonic model. The contours correspond, from left to right, to $\Delta\mathcal{R} = -9.21, -4.61, -2.41, 1.39, 2.41, 4.61$ and 9.21 (see Table 5.3).

model	k_2 (eV/Å^2)	k_3 (eV/Å^3)	k_4 (eV/Å^4)	η (Å^{-2})	R (Å)	ΔE_0 (eV)	$\mathcal{R}_{min}$
harm.	2.11	0.0	0.0	0.84	2.86	-48.4	41.0
anhh.	1.86	-7.65	48.8	0.82	2.87	-42.9	31.5

Table 5.5: Best–fit values of the parameters describing the Ag–I potential.

with $\xi = 0$ (the fit is done for $k > 5$ Å^{-1}) and $n = 1$.

The quality of a representative fit obtained with formula (5.18) is shown in Fig. 5.12. The agreement of the experimental data with the model is excellent. We also show a fit of the squared residuals (k–dependent variance) obtained with the law

$$\sigma^2(k) = \sigma^2_{exp}\left[\frac{k_0}{k}\right]^3 \quad , \tag{5.21}$$

with $\sigma^2_{exp} = 0.0016$ and $k_0 = 12.7$ Å^{-1}. This simple power law is usually found to well approximate the experimental k–dependent variance, the exponent corresponding to the k–weighting used in the fit (this was indeed 3 in our fits) [135]. The value σ_{exp} is a good estimate of the experimental standard deviation.

We followed the same approach described for the Cu–O peak fit: (1) the first fit with the harmonic model will give us a certain value for the minimum of the residual function $\mathcal{R}_{min}$; (2) we then allow for an anharmonic potential and look for a significant lowering of $\mathcal{R}_{min}$. The best–fit values of the fitting parameters are reported in Table 5.5 in both cases. We get

$$\frac{\mathcal{R}^h_{min}}{\mathcal{R}^{anh}_{min}} \approx 1.3 \quad .$$

In order to estimate the significance of such reduction we can determine the rejection probability c by solving Eq. (5.12) with $p = 2$ and $n_d = N - (p+1) = 150 - (6+1) = 143$. The result is c of the order of 10^{-10}! The reader can further convince himself that the anharmonicity is crucial in order to explain the experimental data

by looking at the contour levels of the function $\Delta\mathcal{R} = \mathcal{R}(k_2, k_4) - \mathcal{R}_{min}$, relative to the minimum obtained within the harmonic model (Fig. 5.11). The presence of a significant (corresponding to 99 % confidence) region of negative values away from the computed minimum explains the dramatic improvement of the fit upon introducing the nonlinearities in the potential. Our results also confirm that the measured nonlinearity in the Ag–I potential can still be described by a perturbative treatment, being $\mathcal{R}_E \approx 0.13$.

The uncertainties associated with the best–fit values of the floating parameters can be estimated according to the above–mentioned argument by taking the projections of confidence contours on the parameter axes. A choice of four such diagrams for the parameter pairs (k_2, k_4), (k_2, η),(k_3, k_4), and (k_3, R) are shown in Fig. 5.13. Such plots are very useful also for estimating the correlation existing among the different parameters. For example, it is clear than the most important correlation that rules the amplitude of the EXAFS signal is that between k_2 and η. Moreover, as is to be expected in a perturbative model, the parameters corresponding to the perturbative part of the potential are less correlated with the rest of the parameters. From a comprehensive

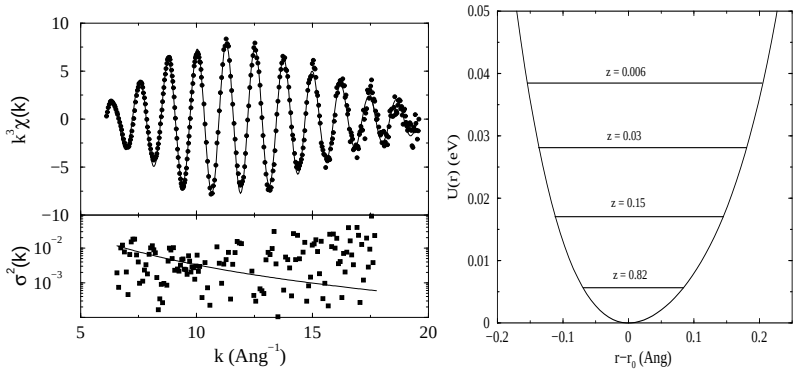

(a) (b)

Figure 5.12: (a) Upper frame: Ag K–edge EXAFS signal at $T = 77$ K (symbols) and fit obtained with the quantum perturbative distribution. Lower frame: residuals (symbols) and fit with the law (5.21) (solid line). (b). Ag–I potential as measured from the fit of the EXAFS signal. Also shown are the harmonic levels used to build the perturbative distribution, along with the corresponding normalised Boltzmann factors $z = \exp(-E_n/k_BT)/Z_p$ (Z_p partition function).

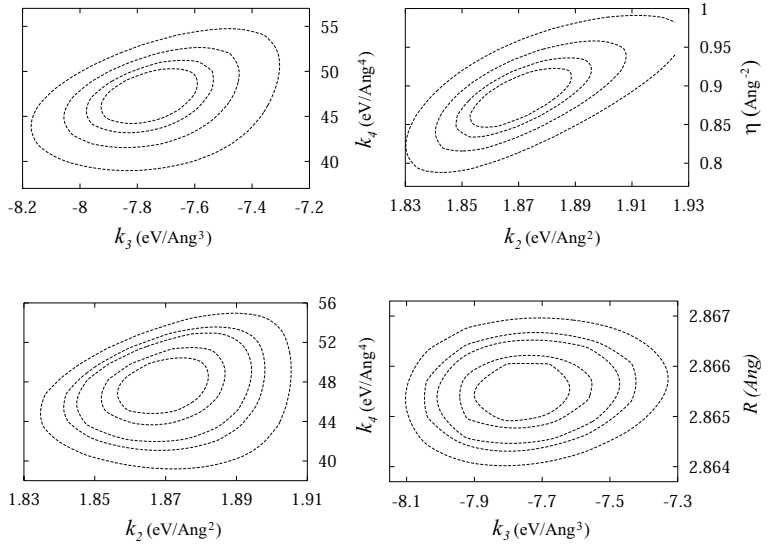

Figure 5.13: Contour levels of the of the function $\Delta\mathcal{R} = \mathcal{R}(\lambda_1, \lambda_2) - \mathcal{R}_{min}$ for the minimum corresponding to the anharmonic model. Four combinations of floating parameters pairs $\{\lambda_1, \lambda_2\}$ are shown. Contours correspond to $c(\Delta\mathcal{R}) = 50\%, 70\%, 90\%, (95\%)$ and 99 %

comparison of the plots shown in Fig 5.13, we get to the 99 % confidence level

$$\begin{aligned} \frac{\Delta k_2}{k_2} &\approx 3\% \qquad \frac{\Delta k_3}{k_3} \approx 5\% \\ \frac{\Delta k_4}{k_4} &\approx 15\% \qquad \frac{\Delta \eta}{\eta} \approx 10\% \\ \frac{\Delta R}{R} &\approx 0.5\% \quad . \end{aligned} \tag{5.22}$$

By similar arguments, it is possible to show that $\Delta(\Delta E_0)/\Delta E_0 \approx 3\%$ to the same confidence level.

5.4.2 The Cu–O EXAFS from GNXAS

The only way to isolate the single–shell Cu–O EXAFS signal from the measured spectra is through a Fourier filtering technique. Some window function is applied to the Fourier transform of the spectra in the region corresponding to the Cu–O peak. The filtered data are then back-transformed in k–space in order to obtain the single–shell EXAFS. However, this procedure introduces uncontrolled distortions in the signal amplitude and phase and is thus usually not recommended, especially in the case of complicated multi–atom signals like our data. Let us then start with something easier.

A good deal of information can be obtained by performing a temperature–dependent analysis of the single–shell best–fit Cu–O EXAFS signals as calculated in the GNXAS analysis. At first glance, fitting a best–fit data set may be regarded as a useless operation. However, we are now using an independent fitting routine, based on an explicit quantum treatment of the Cu–O pair motion. Hence, some details of the Cu–O pair potential, as incorporated in the quantum pair distribution, can be extracted from the GNXAS best–fit Cu–O signals. And at the same time, an independent check of the validity of our procedure can be obtained. Unfortunately, the Cu–O lattice model embedded in the GNXAS fitting scheme is harmonic. Thus, we only can measure a temperature–dependent harmonic potential at this stage.

The Cu–O EXAFS signal $\chi(k)$ is constructed according to the following expression

$$\chi(k) = \frac{S_o^2}{k} N_{\rm Ox}\, Im\left\{ f_{\rm Ox}(\pi, k)\, e^{2i\delta_{\rm Cu}} \int_0^\infty g(r)\, \frac{e^{-2r/\lambda(k)}}{r^2}\, e^{2ikr}\, dr \right\} \quad , \tag{5.23}$$

where $N_{\rm Ox} = 4$ is the coordination number of the oxygen ions lying in the CuO_2 planes, $\delta_{\rm Cu}$ is the central atom phase shift and $f_{\rm Ox}(\pi, k) = |f_{\rm Ox}(\pi, k)| \exp(i\phi_{\rm Ox})$ is the complex backscattering amplitude of the O ions. The total phase shift $\Delta\varphi$ is given for the Cu K–edge by a formula analogous to equation (5.19)

Both the backscattering amplitude and phase shift were calculated by using the program `Feff` [148] and again cubic–spline fitting routines were incorporated in the main fitting program for calculating both the amplitude and phase data sets at any given point in k–space. Both the original `Feff` amplitude and phase data and their cubic–spline approximations are shown in Fig. 5.14. The mean free path $\lambda(k)$ is again parametrised as described in equation (5.20). We found that a model with $\xi = 0$ (this is reasonable since the fit is done for $k > 4$ Å^{-1}) and $n = 1$ was enough in order to reproduce the experimental data.

The results of the present fits are reported in Table 5.6. According to our formalism, the Cu–O pair potential is well characterised by a temperature–independent harmonic constant $k_2 \approx 27 \pm 3$ eV/Å^2 up to $T = 80$ K. This result is in excellent agreement with the estimates from the literature reported in Chapter 2 (see Chapter 2).

We observe that the slightly greater values of k_2 at $T = 10$ K and $T = 20$ K are consistent with the quartic low–temperature anharmonicity found in the Cu–O peak analysis. Moreover, we find that the electron mean free path does not change throughout the considered range of temperatures. Our results reveal a significant softening of the Cu–O potential at $T = 200$ K. We note that there is no particular reason why our treatment should fail in this case. We are thus led to accept this result as significant. Experimental data at greater temperatures would be necessary in order to confirm and enlighten this finding. A typical fit is reported here in Fig. 5.15. As it shows, the agreement between the complicated theory embedded in GNXAS and our simple treatment with an harmonic quantum distribution Function is good.

An other example of the quality of the present fits is shown in the parameter space in Fig. 5.16. We plot there four different contour plots of the function $\Delta\mathcal{R} = \mathcal{R}(\lambda_1, \lambda_2) - \mathcal{R}_{min}$, for two different choices of the parameters (λ_1, λ_2): $(\lambda_1, \lambda_2) = (k_2, \eta)$ and $(\lambda_1, \lambda_2) = (R, \Delta E_0)$. In both cases, the substantial degree of correlation existing between the two pairs of parameters is evident.

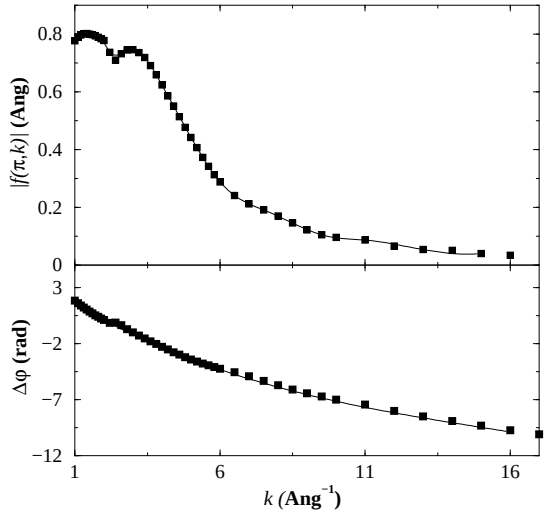

Figure 5.14: Upper frame: backscattering amplitude $|f_{\rm Ox}(\pi,k)|$ of the O ions. Lower frame: total phase shift $\Delta\varphi$. The symbols are the data points from the program `Feff`, the solid line is a cubic spline interpolation from our built–in routine for a given mesh in k–space.

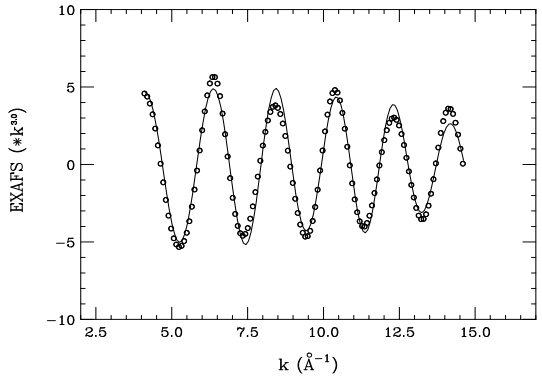

Figure 5.15: Fit of the Cu–O single–shell EXAFS signal at $T = 30$ K. Symbols are the Cu–O EXAFS signal as calculated with GNXAS. The solid line is the fit obtained with a simple harmonic quantum distribution function.

5.4.3 The Cu–O Fourier–filtered EXAFS

We shall now present the results of the analysis performed on the Fourier–filtered Cu–O EXAFS signal. The procedure to obtain the single–shell $\chi(k)$ is simple: first a smooth

T (K)	k_2 (eV/Å^2)	η (Å^{-2})	ΔE_0 (eV)	R (Å)
10	30(3)	0.64(3)	-11.6	1.915(1)
20	31(3)	0.65(3)	-10.7	1.918(1)
30	26(3)	0.65(3)	-10.8	1.918(1)
40	26(3)	0.65(3)	-10.8	1.918(1)
50	25(3)	0.65(3)	-10.9	1.918(1)
60	25(2)	0.66(3)	-11.0	1.918(1)
80	24(2)	0.65(3)	-10.6	1.919(2)
200	15(2)	0.63(3)	-10.6	1.921(2)

Table 5.6: Best–fit values of the parameters describing the Cu–O single–shell EXAFS signal as calculated with GNXAS. Errors in brackets correspond to a rejection probability $c = 99\%$.

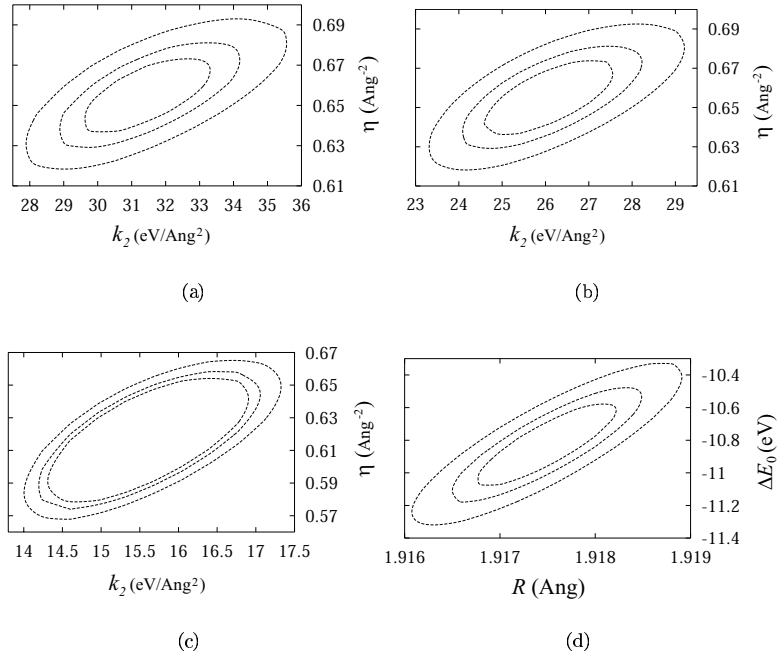

Figure 5.16: Fit of the Cu–O single–shell GNXAS best–fit signal. Contour maps of sections of the function $\Delta\mathcal{R} = \mathcal{R}(\lambda_1,\lambda_2) - \mathcal{R}_{min}$ in the $(\lambda_1,\lambda_2) = (k_2,\eta)$–space at: (a) $T = 20$, (b) $T = 30$ K, (c) $T = 200$ K. (d) Contour maps in the $(\lambda_1,\lambda_2) = (R,\Delta E_0)$–space at $T = 30$ K. Contours correspond to $c(\Delta\mathcal{R}) = 70\%, 95\%$ and 99 %.

window function is used to isolate the Cu–O peak in the Fourier transform $\tilde{\chi}(R)$ of the total EXAFS signal (see e.g. Fig. 5.3 (b) and 5.2 (b)) in a given interval $[R_1, R_2]$. We chose $R_1 = 1.35$ Å and $R_2 = 1.85$ Å. A standard routinely–used window function is the Hanning function

$$w(R) = \frac{1}{2}\left[1 - \cos\left(2\pi \frac{R - R_1}{R_2 - R_1}\right)\right] \quad . \tag{5.24}$$

It is clear that this window smoothly sets the data to zero ($w(R) = 0$) at the ends of the filtering interval $R = R_1$ and $R = R_2$. The filtered data are then back-transformed again in k–space

$$\chi_{FF}(k) = \frac{1}{2\pi}\int_{-\infty}^{+\infty} w(R)\tilde{\chi}(R)e^{-2ikR}dR \tag{5.25}$$

The data set $\chi_{FF}(k)$ can now be fitted with the full anharmonic quantum distribution

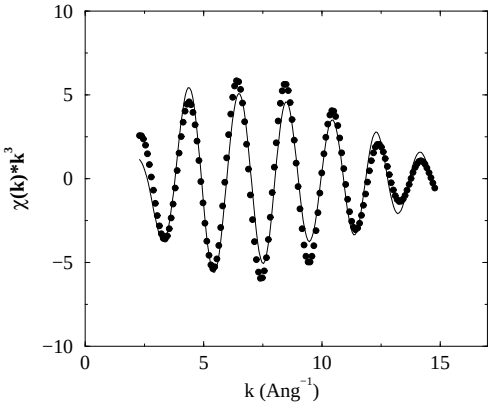

Figure 5.17: Fit of the Cu–O single–shell Fourier–filtered EXAFS signal at $T = 10$ K. Symbols are the experimental points (formula (5.25)). The solid line is the fit obtained with the anharmonic Quantum Distribution Function.

function as described in the previous section. We report here the analysis of the Fourier–filtered Cu–O EXAFS signals at $T = 10$ K. The quality of the fit is illustrated in Fig. 5.17. The results of the analysis with the harmonic and anharmonic models are summarised in Table 5.7. The reduction of the residual minimum $\mathcal{R}_{min}$ resulting from the introduction of anharmonicity in the potential corresponds, according to the usual F–test, to a rejection probability $c \approx 18\%$. The anharmonic model is in this case at the verge of statistical significance. This was expected, since the sensitivity of the model $\chi(k)$ on the anharmonic parameters is somewhat intrinsically reduced with respect to that of the corresponding $g(r)$ (see Chapter 4). This is also clear from direct inspection of the contour maps of the function $\Delta\mathcal{R}$ in the (k_2, k_4)–subspace (Fig. 5.18). However, it is interesting to note that the measured kurtosis of the distribution function as calculated according to Eq. (5.14) from the best–fit values of k_2 and k_4 is $\kappa = 3.1$, in

model	k_2 (eV/Å^2)	k_3 (eV/Å^3)	k_4 (eV/Å^4)	η (Å^{-2})	R (Å)	ΔE_0 (eV)	$\mathcal{R}_{min}$
harm.	7.5	-	-	0.46	1.918	-0.25	26.3
anhh.	6.5	-49.7	98.8	0.43	1.918	-0.25	26.0

Table 5.7: Best–fit values of the parameters describing the Cu–O potential as from fit of the Fourier–filtered EXAFS signal at $T = 10$ K.

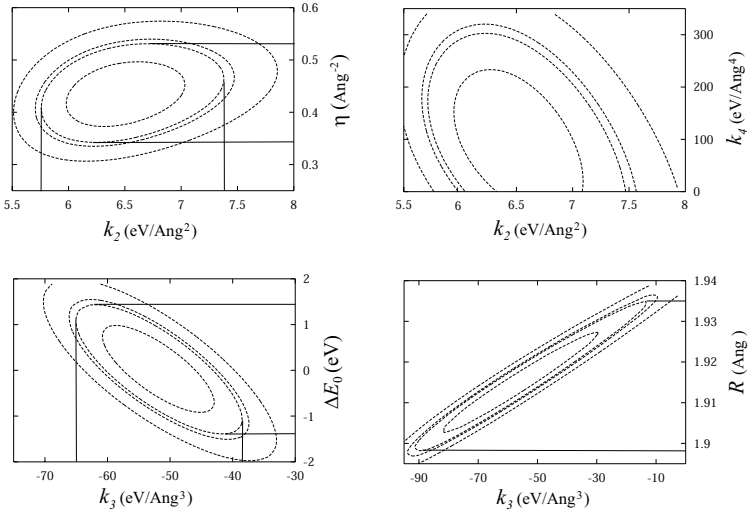

Figure 5.18: Fit of the Fourier–filtered Cu–O EXAFS signal at $T = 10$ K. Contour levels of the function $\Delta\mathcal{R} = \mathcal{R}(\lambda_1, \lambda_2) - \mathcal{R}_{min}$ for the minimum corresponding to the anharmonic model in four different (λ_1, λ_2)–subspaces. Contours correspond to rejection probabilities $c = 70\%, 90\%, 95\%$ and 99%. The projections of the 90%–confidence regions on the parameter axes are drawn for clarity.

agreement with the value found in the analysis of the Cu–O peak shape (section 5.3). Moreover, the influence on the significance test of spurious contributions to the signal amplitude and phase introduced by the Fourier–filtering machinery cannot be made quantitative. This problem is made clear by the emergence of a large k_3 contribution in the fitted anharmonic model, which might probably reflect a spurious phase lag coming from the filtering process. Unfortunately, the above–highlighted problems are peculiar of the analysis of any Fourier–filtered spectrum, irrespective of the details of the filtering procedure. Concluding, a temperature–dependent analysis of this kind of the complete set of data will be affected by the same sources of uncertainty, and will not be reported here.

5.5 Conclusions

In this chapter we have reported the analysis of the data collected during our EXAFS experiment. Some of the results discussed here will be used in the next Chapter to quantitatively investigate non–linear excitations in CuO_2 planes.

The spectra have been first analysed within the harmonic model by means of the package GNXAS. Such analysis has highlighted large–amplitude vibrations of the apical ions, in agreement with the general conjectures on anharmonicity associated with the ions at the apical site. This important result prompts, among other things, for an EXAFS investigation of the superconducting Na–doped compound.

We have then performed an accurate temperature–dependent analysis of the experimental Cu–O peak by means of the quantum perturbative distribution function developed in Chapter 4. We have found that the Cu–O potential is characterised by a low–temperature anharmonicity of the quadratic–plus–quartic type up to $T = 40$ K. Although this analysis could not give a quantitative estimate of the Cu–O potential parameters, we have calculated the peak kurtosis, which can be regarded as an independent quantitative measure of the potential anharmonicity

The last part of this chapter has been devoted to the application of the quantum perturbative distribution function to the single–shell Cu-O EXAFS signal. In order to test the quantum perturbative distribution function we first have examined an Ag K–edge EXAFS spectrum of AgI, which is known for being a highly–anharmonic material. We found that our procedure is very robust and gives reliable results. In particular, the best–fit values of the Ag–I potential are in good agreement with the literature.

Then, we have analysed the best-fit GNXAS Cu–O single–shell EXAFS signal with an harmonic distribution. This procedure has allowed us to determine an accurate temperature–independent value of the harmonic constant of the Cu–O potential. We find excellent agreement with the data extracted form the literature (see Table 2.2).

The chapter ends with an attempt of fitting a Fourier–filtered Cu–O EXAFS signal with our distribution function. Despite the large source of errors introduced by the filtering process, the filtered signal still contains the full dynamical information on the Cu–O potential. We find that the best–fit value of the harmonic constant is not in agreement with the correct estimate. However, we find that a quantitative measure of the potential anharmonicity revealed in the spectrum is in good agreement with the kurtosis of the corresponding peak in the EXAFS Fourier transform.

Chapter 6

Lattice dynamics of the CuO_2 planes

6.1 Introduction

In this chapter we shall discuss some of the possible implications of our experimental results reported in chapter 5 in the copper–oxide lattice dynamics.

We start off by introducing a simple model for the lattice dynamics of harmonic copper–oxide planes. We shall calculate the phonon bands and the eigenvectors of the dynamical matrix and illustrate our analytical results with the aid of computer simulations. We shall then introduce the important issue of energy localisation in anharmonic lattices and study the case of CuO_2–like structures. We will discuss the results of numerical simulations of a simple nonlinear scalar model and settle them in the broader context of the interplay between force anisotropy and energy localisation. Finally, we will attempt to provide a realistic estimate of the force–anisotropy parameter of our model based on molecular orbital calculations.

6.2 Dispersion relations of the CuO_2 planes

The CuO_2 planes are 2D lattices with a basis (sometimes called *decorated* lattices), therefore we need three integers to specify the position of each atom. Let us indicate the atomic displacements with

$$u_\alpha(i_x, i_y; \sigma) \qquad \alpha = x, y, \quad \sigma = 1, 2, 3 \quad , \tag{6.1}$$

d where i_x and i_y denote the position of the lattice sites (i.e. the ones occupied by the copper ions) and σ is the basis index. For the sake of simplicity, we shall use in the following a unified index i instead of the pair (i_x, i_y), except when explicitly indicated. The atomic arrangement is reported in Fig. 6.1.

Within the framework of the harmonic approximation the equations of motion read

$$m(\sigma)\ddot{u}_\alpha(i,\sigma) = \sum_\beta \sum_{j,\sigma'}^{N(i,\sigma)} \mathcal{D}_{\alpha\beta}(j,\sigma'; i,\sigma)\left[u_\beta(j,\sigma') - u_\alpha(i,\sigma)\right] \quad , \tag{6.2}$$

where $m(\sigma)$ is the mass of the σ–th atomic species, $N(i,\sigma)$ is the number of neighbours of atom (i,σ) which we wish to include in the equations, and $\mathcal{D}_{\alpha\beta}(j,\sigma';i,\sigma)$ denote the coupling force constants. Here we just consider nearest–neighbour interactions, i.e.

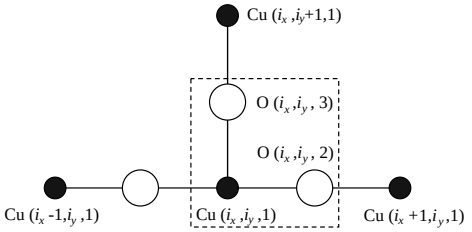

Figure 6.1: The CUO_2 plane unit cell. Black circles denote Cu ions, white circles O ions. The portion of the lattice within the dotted rectangle is the lattice basis: $\sigma = 1$ Cu ions, $\sigma = 2$ O neighbours along x, $\sigma = 3$ O neighbours along y.

$$N(i,1) = 4$$
$$N(i,2) = N(i,3) = 2 \quad .$$

The number and the magnitude of the non–zero force constants depend on the symmetry of the lattice. Let us consider the force exerted on a copper ion due to a unit displacement of its neighbour O(2). It will be described by the four force constants (we drop the index i for the moment)

$\mathcal{D}_{xx}(2;1)$ ..... *force on* Cu *along* x *due to a displ. of* O(2) *along* x
$\mathcal{D}_{xy}(2;1)$ ..... *force on* Cu *along* x *due to a displ. of* O(2) *along* y
$\mathcal{D}_{yx}(2;1)$ ..... *force on* Cu *along* y *due to a displ. of* O(2) *along* x
$\mathcal{D}_{yy}(2;1)$ ..... *force on* Cu *along* y *due to a displ. of* O(2) *along* y .

Since the two ions lie on a reflection plane of the lattice, the two force constants $\mathcal{D}_{xy}$ and $\mathcal{D}_{yx}$ vanish identically, [1] since otherwise, by symmetry, a reversal of the O(2) ion displacement could not produce a reversal of the force on the Cu(1) ion, as required by the expression introduced to describe interatomic forces. We are then left with the two constants

$$\mathcal{D}_{xx}(2;1) = \alpha$$
$$\mathcal{D}_{yy}(2;1) = \beta \quad .$$

The constant α represents the force acting on a copper ion along x due to a unit displacement of its neighbouring O(2) ion along x. Similarly, β accounts for the coupling of the displacements along y. Moreover, the CuO_2 lattice is invariant with respect to 4–fold rotations[2]. This means that

$$\mathcal{D}_{xx}(3;1) = \mathcal{D}_{yy}(2;1) = \beta$$
$$\mathcal{D}_{yy}(3;1) = \mathcal{D}_{xx}(2;1) = \alpha \quad .$$

The third principle of dynamics completes the picture by giving the remaining non–zero force constants

$$\mathcal{D}_{xx}(1;3) = \mathcal{D}_{xx}(3;1) = \beta$$
$$\mathcal{D}_{yy}(3;1) = \mathcal{D}_{yy}(1;3) = \alpha \quad .$$

We gather all the force constant in tables 6.1 and 6.2.

$O(i_x,i_y;2)$	$\mathcal{D}_{xx}$	$\mathcal{D}_{xy}$	$\mathcal{D}_{yy}$	$\mathcal{D}_{yx}$	$O(i_x,i_y;3)$	$\mathcal{D}_{xx}$	$\mathcal{D}_{xy}$	$\mathcal{D}_{yy}$	$\mathcal{D}_{yx}$
$Cu(i_x,i_y)$	α	0	β	0	$Cu(i_x,i_y)$	β	0	α	0
$Cu(i_x+1,i_y)$	α	0	β	0	$Cu(i_x,i_y+1)$	β	0	α	0

Table 6.1: Force constants for the $O(\sigma)$ ions. The entries in the columns labeled $O(i_x,i_y;\sigma)$ represent the corresponding two nearest–neighbour Cu ions.

$Cu(i_x,i_y)$	$\mathcal{D}_{xx}$	$\mathcal{D}_{xy}$	$\mathcal{D}_{yy}$	$\mathcal{D}_{yx}$
$O(i_x,i_y;2)$	α	0	β	0
$O(i_x,i_y;3)$	β	0	α	0
$O(i_x-1,i_y;2)$	α	0	β	0
$O(i_x,i_y-1;3)$	β	0	α	0

Table 6.2: Force constants for the Cu ions. The entries in the column labeled $Cu(i_x,i_y)$ represent the corresponding four nearest–neighbour $O(\sigma)$ ions.

It is clear that the relative magnitude of the force constants α and β will strongly influence the shape of the phonon bands and gaps. Let us here introduce the force–anisotropy parameter [149], which we define as

$$\chi = \frac{\beta}{\alpha} \quad . \tag{6.3}$$

We shall see later on in this section that in the general case there exists a critical value of the force–anisotropy parameter χ below which there exists a secondary gap which separates the four optical bands in two pairs. We stress that the structure of the gap(s) is of fundamental importance in studying the vibrational properties of the CuO_2 lattice. This is true in particular in studying the localised solutions which arise if one introduces nonlinearities in the equations of motion (see next section). We shall later on discuss how it is possible to get a qualitative but reliable estimate of the force anisotropy χ through the theory of molecular orbitals.

6.2.1 The isotropic case

It is useful to discuss into detail the isotropic ($\chi = 1$) lattice. In fact, in this case it is possible to cast the dispersion relations in a simple self–explanatory analytic form.

[1] Of course, this is strictly true only at first order in the atomic displacements (linear forces).

[2] This is not strictly true for the superconducting orthorombic phase of cuprates. But the differences of the lattice parameters are tiny and we can assume that they do not appreciably affect the shape of the interatomic potential minima in the harmonic approximation.

The equations of motion (6.2) take the following form

$$\begin{aligned}
\ddot{u}_\alpha(i_x,i_y;1) &= \frac{\alpha}{M}[u_\alpha(i_x,i_y;2) + u_\alpha(i_x,i_y;3) + u_\alpha(i_x-1,i_y;2) + u_\alpha(i_x,i_y-1;3) \\
&\qquad - 4u_\alpha(i_x,i_y;1)] \\
\ddot{u}_\alpha(i_x,i_y;2) &= \frac{\alpha}{m}[u_\alpha(i_x,i_y;1) + u_\alpha(i_x+1,i_y;1) - 2u_\alpha(i_x,i_y;2)] \\
\ddot{u}_\alpha(i_x,i_y;3) &= \frac{\alpha}{m}[u_\alpha(i_x,i_y;1) + u_\alpha(i_x,i_y+1;1) - 2u_\alpha(i_x,i_y;3)] \quad ,
\end{aligned}$$

where $M = m(1)$ and $m = m(2) = m(3)$ ($M > m$). We look for plane–wave solutions of the form

$$\vec{u}(i,\sigma) = \vec{u}(\sigma)\exp\{i[\vec{q}\cdot\vec{r}(i_x,i_y;\sigma) - \omega(q_x,q_y)t]\} \quad , \tag{6.4}$$

where $\vec{r}(i_x,i_y;\sigma)$ is the position vector of atom $(i_x,i_y;\sigma)$ with respect to a fixed origin. Substituting (6.4) in equations (6.4) we get two degenerate homogeneous systems of equations in the variables $u_\alpha(1), u_\alpha(2)$ and $u_\alpha(3)$ for the spatial directions $\alpha = x,y$. We already know that in the isotropic case the six phonon bands are pairwise degenerate. Dropping the spatial index from the displacements, we have

$$\begin{aligned}
&\left(\frac{4\alpha}{M} - \omega^2\right)u(1) - \frac{2\alpha}{M}\cos\left(\frac{q_x}{2}\right)u(2) - \frac{2\alpha}{M}\cos\left(\frac{q_y}{2}\right)u(3) = 0 \\
&-\frac{2\alpha}{m}\cos\left(\frac{q_x}{2}\right)u(1) + \left(\frac{2\alpha}{m} - \omega^2\right)u(2) = 0 \\
&-\frac{2\alpha}{m}\cos\left(\frac{q_y}{2}\right)u(1) + \left(\frac{2\alpha}{m} - \omega^2\right)u(3) = 0 \quad .
\end{aligned}$$

The wavevectors q_α are measured in units of $1/a$, a being the lattice spacing, i.e. the equilibrium distance between copper ions lying on adjacent lattice sites. The three degenerate dispersion relations are obtained by requiring that the determinant of (6.5) vanishes. We get

$$\begin{aligned}
\omega_\pm(q_x,q_y) &= \frac{\omega_0}{\sqrt{2}}\sqrt{\frac{2+\delta}{1+\delta}}\sqrt{1 \pm \sqrt{1 - \frac{4\delta}{(2+\delta)^2}\left[2 - \cos^2\left(\frac{q_x}{2}\right) - \cos^2\left(\frac{q_y}{2}\right)\right]}} \\
\omega_{DL} &= \omega_0\sqrt{\frac{\delta}{1+\delta}} \quad ,
\end{aligned} \tag{6.5}$$

where we have introduced the mass ratio parameter $\delta = M/m$ ($\delta = 4$ in the CuO_2 planes) and defined $\omega_o = \sqrt{2\alpha/\mu}$, μ being the reduced mass of the copper–oxygen pair

$$\mu = \frac{Mm}{M+m} = m\left(\frac{\delta}{1+\delta}\right) \quad . \tag{6.6}$$

The two degenerate acoustic branches are described by the function $\omega_-(q_x,q_y)$, while the four pairwise degenerate optical branches appear in the form of the functions $\omega_+(q_x,q_y)$ and the dispersion–less ω_{DL}.

The gap

The gap of forbidden frequencies between the optical and acoustic bands is obtained as

$$\Delta\omega_G = \min_{q\in BZ}\{\omega_+(q_x,q_y)\} - \max_{q\in BZ}\{\omega_-(q_x,q_y)\}$$

In the simple case $\chi = 1$ the band extremes correspond to the four corners of the two–dimensional Brillouin zone (BZ), namely $(q_x = \pm\pi, q_y = \pm\pi)$. The flat solution ω_{DL} turns out to coincide with the minimum frequency of the optical band $\omega_+(\pm\pi,\pm\pi)$ for $\delta > 2$ and with the maximum frequency of the acoustic band $\omega_-(\pm\pi,\pm\pi)$ for $\delta < 2$. The gap $\Delta\omega_G(\delta)$ vanishes for $\delta = 2$, and is given by the following expression

$$\Delta\omega_G(\delta) = \frac{|\sqrt{\delta} - \sqrt{2}|}{\sqrt{1+\delta}} \quad . \tag{6.7}$$

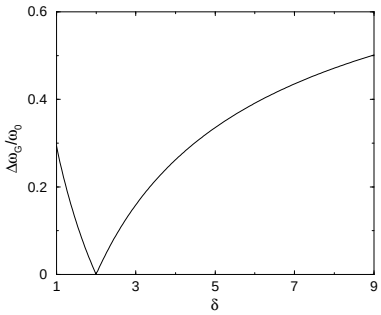

Figure 6.2: Plot of the gap function $\Delta\omega_G(\delta)$.

The gap function is shown in units of ω_o in Fig. 6.2. In Fig. 6.3 we show two sections of the phonon bands along two different directions in the q space within the Brillouin zone, for $\delta = 1.1$ and for $\delta = 4$. Notice the flat band ω_{DL} jumping from the top of the acoustic band to the bottom of the optical band as the mass ratio parameter δ is increased across the critical value of 2 to the value $\delta = 4$, characteristic of the CuO_2 planes. In Fig. 6.4 and 6.5 we report tridimensional plots of the phonon bands for the case $\delta = 2$ (vanishing gap) and $\delta = 4$ (CuO_2 planes).

The eigenvectors

We shall now calculate the expressions of the coefficient ratios $u(1)/u(2)$ and $u(1)/u(3)$ as functions of the wavevector (q_x, q_y). Let us introduce the following short–hand notation

$$C_\alpha = \cos\left(\frac{q_\alpha}{2}\right), \quad \alpha = x, y$$
$$C^2 = C_x^2 + C_y^2$$

We can recast the dispersion relations (6.5) in the following form

$$\omega_\pm^2 = \frac{\omega_0^2}{2}\frac{2+\delta}{1+\delta}\left(1 \pm \sqrt{\Delta(q_x,q_y)}\right) \quad , \tag{6.8}$$

where $\Delta(q_x,q_y) = 1 - 4\delta(2-C^2)/(2+\delta)^2$. It is convenient to rewrite homogeneous system (6.5) in matrix form by introducing the matrix $\mathcal{A}$ and the column vector $u = (u(1), u(2), u(3))$ in the form $\mathcal{A}(\omega)u = 0$. We then have to solve the system $\mathcal{A}_\pm u = 0$, where $\mathcal{A}_\pm = \mathcal{A}(\omega = \omega_\pm)$. The elements of matrix $\mathcal{A}_\pm$ can be cast in a simple form by expressing M and m in terms of the mass ratio parameter δ and the reduced mass μ. We have

$$\mathcal{A}_\pm u = \begin{pmatrix} \gamma_\pm & -2C_x & -2C_y \\ -2\delta C_x & 2(\delta+2)+\gamma_\pm & 0 \\ -2\delta C_y & 0 & 2(\delta+2)+\gamma_\pm \end{pmatrix} \begin{pmatrix} u(1) \\ u(2) \\ u(3) \end{pmatrix} = 0 \quad , \tag{6.9}$$

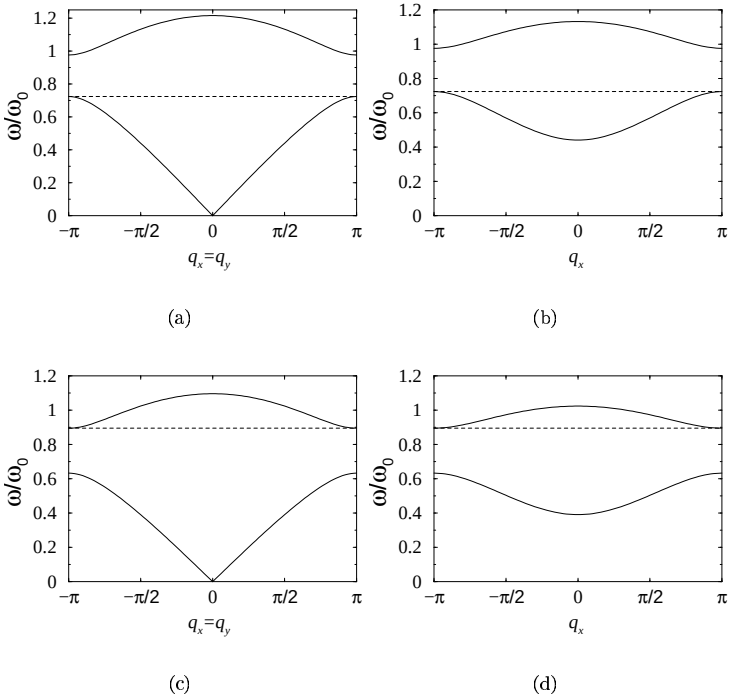

Figure 6.3: Sections of the phonon bands in CuO_2 planes in the isotropic case $\chi = 1$. (a) $\delta = 1.1$, $q_x = q_y$, (b) $\delta = 1.1$, $q_y = \pi$, (c) $\delta = 4$, $q_x = q_y$, (d) $\delta = 4$, $q_y = \pi$.

where $\gamma_\pm = 4 - (2+\delta)[1 \pm \sqrt{\Delta}]$. It is not difficult to see that, multiplying the second equation of system (6.9) by C_y and the third one by C_x and then subtracting them, we obtain

$$\frac{u(2)}{u(3)} = \frac{C_x}{C_y} \quad . \tag{6.10}$$

Substituting result (6.10) in the first equation gives finally

$$\begin{aligned} \frac{u(1)}{u(2)} &= \frac{2}{\gamma_\pm}\left(\frac{C^2}{C_x}\right) \\ \frac{u(1)}{u(3)} &= \frac{2}{\gamma_\pm}\left(\frac{C^2}{C_y}\right) \quad . \end{aligned} \tag{6.11}$$

Let us calculate explicitly expressions (6.11) for the ratios of the heavy–to–light amplitudes along specific symmetry directions within the Brillouin zone.

Centre of the BZ ($q_x = 0, q_y = 0$) We have

$$\lim_{q_\alpha \to 0} \frac{2}{\gamma_\pm} \left(\frac{C^2}{C_\alpha} \right) = \frac{4}{4 - (2+\delta)(1 \pm 1)} = \begin{cases} 1 & \text{acoustic branch} \\ -\frac{2}{\delta} & \text{optical branch} \end{cases} . \tag{6.12}$$

This is the expected result. At low q in the acoustic branch all the atoms, heavy and light, move together in long wavelength ordinary sound waves. On the contrary, in the optical branch in the same domain we get the usual long wavelength optical mode, all heavy atoms moving together in one direction while all light atoms go in the opposite direction. The ratio of the heavy–to–light displacements is inversely proportional to the ratio of the heavy mass to twice the light one, to keep the centre of mass at rest for $q = 0$.

Corners of the BZ ($q_x = \pm\pi, q_y = \pm\pi$) We can calculate the limit of the coefficient ratios along the bisector line $q_x = q_y$. We have

$$\lim_{q_\alpha \to \pm\pi} \frac{2}{\gamma_\pm} \left(\frac{C^2}{C_\alpha} \right) = \lim_{q_\alpha \to \pm\pi} \frac{4 \cos\left(\frac{q_\alpha}{2}\right)}{4 - [(2+\delta) \pm |2-\delta|]} = \begin{cases} \text{ac. branch} & \begin{cases} 0_+ & \delta < 2 \\ 1 & \delta = 2 \\ +\infty & \delta > 2 \end{cases} \\ \text{opt. branch} & \begin{cases} -\infty & \delta < 2 \\ -1 & \delta = 2 \\ 0_- & \delta > 2 \end{cases} \end{cases} . \tag{6.13}$$

For $\delta > 2$, we recover the customary trend of the heavy–to–light ratios in diatomic lattices, whereby at large q only the heavy atoms oscillate in the acoustic branch while

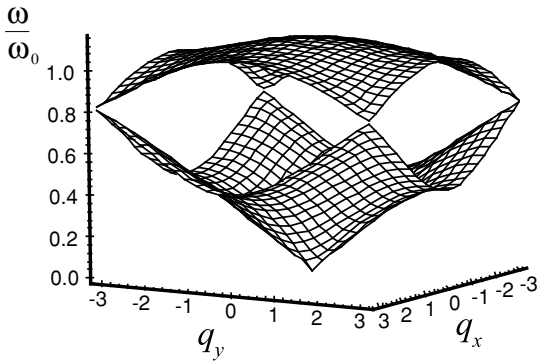

Figure 6.4: Tridimensional plot of the CuO_2 phonon bands in the isotropic case $\chi = 1$ for $\delta = 2$.

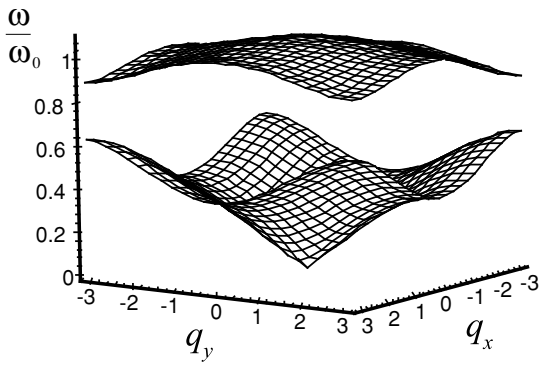

Figure 6.5: Tridimensional plot of the CuO_2 phonon bands in the isotropic case $\chi = 1$ for $\delta = 4$.

the light ones stand still ($u(2), u(3) \to 0$). On the contrary, in the optical branch only the light atoms oscillate while the heavy ones stand still ($u(1) \to 0$). For $\delta < 2$, the latter trends swap with each other. At the critical value $\delta = 2$ the ratios (6.11) keep their ($q_x = 0, q_y = 0$) value (1 and -1 in the acoustic and optical branches, respectively) all the way from the centre to the corners of the BZ.

The trends of the ratios of the heavy–to–light amplitudes (6.11) are sketched in Fig. 6.6 for $\delta = 1.1$ and $\delta = 4$ along two different directions within the BZ.

6.2.2 The general case

In this section we study the general case of anisotropic coupling, $\chi = \beta/\alpha < 1$. In this case, the six bands are no longer pairwise degenerate and we have to solve the full homogeneous system of six equations in the six unknown variables $u_\alpha(i_x, i_y; \sigma)$, with

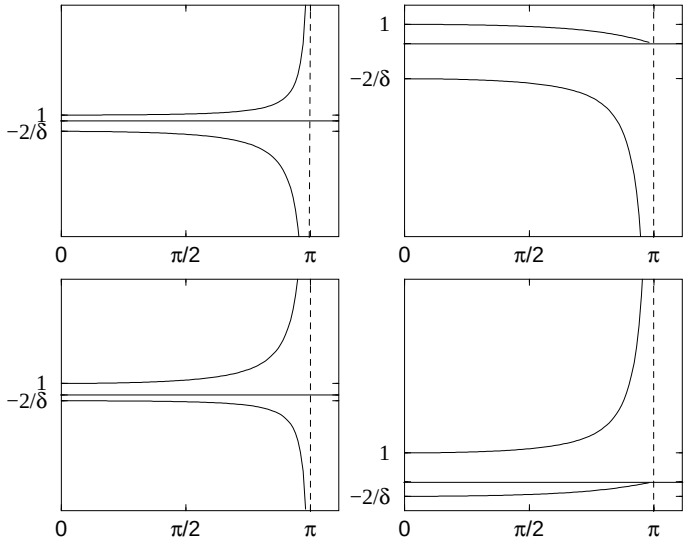

Figure 6.6: Sections of the ratios of the heavy–to–light amplitudes (6.11) along specific symmetry directions within the BZ. Upper left panel: direction $(q_x, q_y = 0)$, $\delta = 1.1$. Upper right panel: direction $(q_x = q_y)$, $\delta = 1.1$. Lower left panel: direction $(q_x, q_y = 0)$, $\delta = 4$. Lower right panel: direction $(q_x = q_y)$, $\delta = 4$.

$\sigma = 1,2,3$ and $\alpha = x,y$. The latter reads

$$\begin{aligned}
\ddot{u}_x(i_x,i_y;1) &= \frac{\alpha}{M}[u_x(i_x,i_y;2) + u_x(i_x-1,i_y;2)] + \frac{\beta}{M}[u_x(i_x,i_y;3) + u_x(i_x,i_y-1;3)] \\
&\quad - \frac{2(\alpha+\beta)}{M}u_x(i_x,i_y;1) \\
\ddot{u}_y(i_x,i_y;1) &= \frac{\beta}{M}[u_y(i_x,i_y;2) + u_y(i_x-1,i_y;2)] + \frac{\alpha}{M}[u_y(i_x,i_y;3) + u_y(i_x,i_y-1;3)] \\
&\quad - \frac{2(\alpha+\beta)}{M}u_y(i_x,i_y;1) \\
\ddot{u}_x(i_x,i_y;2) &= \frac{\alpha}{m}[u_x(i_x,i_y;1) + u_x(i_x+1,i_y;1) - 2u_x(i_x,i_y;2)] \\
\ddot{u}_y(i_x,i_y;2) &= \frac{\beta}{m}[u_y(i_x,i_y;1) + u_y(i_x+1,i_y;1) - 2u_y(i_x,i_y;2)] \\
\ddot{u}_x(i_x,i_y;3) &= \frac{\beta}{m}[u_x(i_x,i_y;1) + u_x(i_x,i_y+1;1) - 2u_x(i_x,i_y;3)] \\
\ddot{u}_y(i_x,i_y;3) &= \frac{\alpha}{m}[u_y(i_x,i_y;1) + u_y(i_x,i_y+1;1) - 2u_y(i_x,i_y;3)] \quad .
\end{aligned} \tag{6.14}$$

If we substitute a plane–wave solution of the form (6.4) in equations (6.14) we obtain the following system

$$[\Omega - \omega^2\mathcal{I}]u = 0 \quad ,$$

where $u = (u_x(1), u_y(1), u_x(2), u_y(2), u_x(3), u_y(3))$ and we indicate with $\mathcal{I}$ the 6x6 identity matrix. The coefficient matrix Ω is given by

$$\begin{pmatrix}
\frac{2(\alpha+\beta)}{M} & 0 & -\frac{2\alpha}{M}C_x & 0 & -\frac{2\beta}{M}C_y & 0 \\
0 & \frac{2(\alpha+\beta)}{M} & 0 & -\frac{2\beta}{M}C_x & 0 & -\frac{2\alpha}{M}C_y \\
-\frac{2\alpha}{m}C_x & 0 & \frac{2\alpha}{m} & 0 & 0 & 0 \\
0 & -\frac{2\beta}{m}C_x & 0 & \frac{2\beta}{m} & 0 & 0 \\
-\frac{2\beta}{m}C_y & 0 & 0 & 0 & \frac{2\beta}{m} & 0 \\
0 & -\frac{2\alpha}{m}C_y & 0 & 0 & 0 & \frac{2\alpha}{m}
\end{pmatrix} \quad , \tag{6.15}$$

As usual, the equation for the dispersion relations is

$$\det[\Omega - \omega^2\mathcal{I}] = 0 \quad . \tag{6.16}$$

By developing the determinant (6.16), we get the following two cubic equations for ω^2

$$\begin{aligned}
\omega^6 - a\,\omega^4 + b_{x,y}\,\omega^2 - c_{x,y} &= 0 \\
\omega^6 - a\,\omega^4 + b_{y,x}\,\omega^2 - c_{y,x} &= 0 \quad ,
\end{aligned} \tag{6.17}$$

where we measure the frequency in units of $\omega_0 = \sqrt{2\alpha/\mu}$, and

$$\begin{aligned}
a &= 1 + \chi \\
b_{x,y} &= \frac{\delta\chi}{(1+\delta)^2}\left[\delta + 2 + \frac{1}{\chi}\sin^2\left(\frac{q_x}{2}\right) + \chi\sin^2\left(\frac{q_y}{2}\right)\right] \\
c_{x,y} &= \frac{\delta^2\chi}{(1+\delta)^3}\left[\sin^2\left(\frac{q_x}{2}\right) + \chi\sin^2\left(\frac{q_y}{2}\right)\right] \quad ,
\end{aligned} \tag{6.18}$$

After some lengthy algebra we obtain the six solutions to the cubic equations Equations (6.17) in the following fashion

$$\begin{aligned}
\omega_1^2(q_x,q_y) &= \frac{a}{3} + \xi_{x,y}^{1/3} - \eta_{x,y} \\
\omega_2^2(q_x,q_y) &= \frac{a}{3} - \frac{1}{2}\left[\xi_{x,y}^{1/3} - \eta_{x,y}\right] + i\frac{\sqrt{3}}{2}\left[\xi_{x,y}^{1/3} + \eta_{x,y}\right] \\
\omega_3^2(q_x,q_y) &= \frac{a}{3} - \frac{1}{2}\left[\xi_{x,y}^{1/3} - \eta_{x,y}\right] - i\frac{\sqrt{3}}{2}\left[\xi_{x,y}^{1/3} + \eta_{x,y}\right] \\
\omega_4^2(q_x,q_y) &= \frac{a}{3} + \xi_{y,x}^{1/3} - \eta_{y,x} \\
\omega_5^2(q_x,q_y) &= \frac{a}{3} - \frac{1}{2}\left[\xi_{y,x}^{1/3} - \eta_{y,x}\right] + i\frac{\sqrt{3}}{2}\left[\xi_{y,x}^{1/3} + \eta_{y,x}\right] \\
\omega_6^2(q_x,q_y) &= \frac{a}{3} - \frac{1}{2}\left[\xi_{y,x}^{1/3} - \eta_{y,x}\right] - i\frac{\sqrt{3}}{2}\left[\xi_{y,x}^{1/3} + \eta_{y,x}\right] \quad ,
\end{aligned} \tag{6.19}$$

where

$$\begin{aligned}
\xi_{x,y} &= \frac{a^3}{27} - \frac{ab_{x,y}}{6} + \frac{c_{x,y}}{2} + \frac{\sqrt{\mu_{x,y}}}{18} \\
\eta_{x,y} &= \frac{3b_{x,y} - a^2}{9\xi_{x,y}^{1/3}} \\
\mu_{x,y} &= 12b_{x,y}^3 - 9a^2b_{x,y}^2 - 54ab_{x,y}c_{x,y} + 81c_{x,y}^2 + 12a^3c_{x,y} \quad .
\end{aligned} \tag{6.20}$$

The six solutions (6.19) represent six non–degenerate bands: two acoustic (ω_2, ω_5) and four optical ones. It is possible to establish a pairwise correspondence between them and the three bands characteristic of the isotropic problem ($\chi = 1$), as the force anisotropy parameter χ is lowered from 1. In particular, the two optical bands ω_1 and ω_4, which originate from the flat band $\omega = \omega_{DL}$, turn out to detach from the edges of the other two sets of bands. This means that for $\chi < 1$ an additional gap of forbidden frequencies opens up above the gap obtained as the separation between the maximum acoustic and minimum optical frequencies. We will refer to the latter as Gap1, while the former will be Gap2. We can give a definition of the two gaps as

$$\begin{aligned} \text{Gap1}(\delta,\chi) &= \min_{q\in BZ}\{\omega_{3,6}(q_x,q_y)\} - \max_{q\in BZ}\{\omega_{2,5} - (q_x,q_y)\} \\ \text{Gap2}(\delta,\chi) &= \min_{q\in BZ}\{\omega_{1,4}(q_x,q_y)\} - \max_{q\in BZ}\{\omega_{3,6} - (q_x,q_y)\} \quad . \end{aligned} \tag{6.21}$$

Therefore, in the general case $\chi < 1$ there are two gaps to take into account. This scenario is sketched in Fig. 6.7, where we plot as 3D surfaces the functions $\omega_1(q_x,q_y), \omega_3(q_x,q_y)$ and $\omega_5(q_x,q_y)$ for $\chi = 0.5$ (the other three bands are simply obtained from these by a rotation of $\pi/2$). The two gaps are explicitly highlighted. Gap2 is also illustrated in Fig. 6.8 for the same choice of parameters. In Fig. 6.9 we show all the 6 bands,

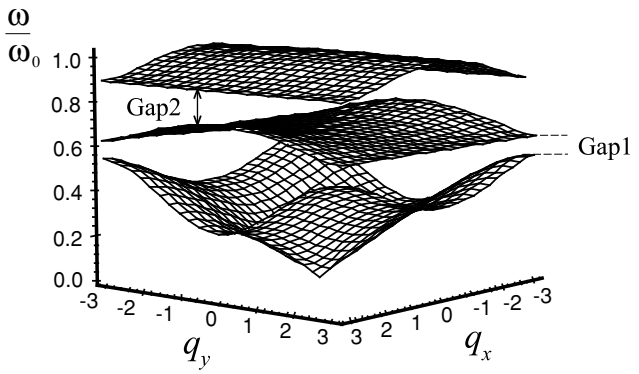

Figure 6.7: One acoustic (ω_5) and two optical bands (ω_1, ω_3) for $\chi = 0.5$ and $\delta = 4$. The lower optical band ω_3 originates from the dispersion–less band ω_{DL} as χ is lowered from 1. The two gaps are clearly exhibited.

calculated for $\chi = 0.6$, not on the same scale. In this way, their characteristic shapes are better illustrated. Another view of the six bands is given in Fig. 6.10, where we show two sections of the bands along two different directions within the BZ. Note that the bands are pairwise degenerate along the diagonals of the BZ. This is obvious, since the six bands can be pairwise obtained from each other by four–fold rotations. Let us now discuss in some detail the behaviour of the additional gap as a function of the force anisotropy parameter. Increasing χ from zero, the two pairs of optical bands move towards each other. The function Gap2(δ,χ) as defined in Eq. (6.21) stays nonzero up to a critical value χ_c, which depends on the mass ratio parameter. This effect is shown in Fig. 6.11 (a), where we plot the difference $\omega_4(0,\pi) - \omega_6(0,\pi)$ vs χ for

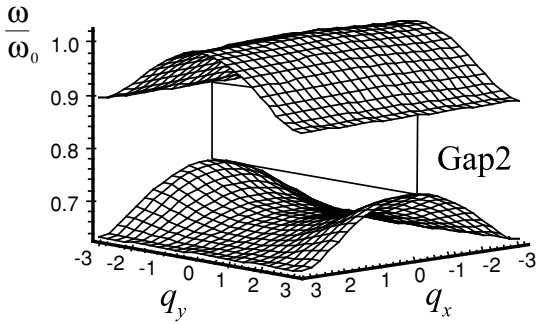

Figure 6.8: Optical bands ω_4 and ω_6 and Gap2 for $\chi = 0.5$ and $\delta = 4$.

$\delta = 4$. In this case, the critical point is $\chi_c \approx 0.75$. Increasing χ further than χ_c, the difference between the two bands increases. They move again away from each other in this direction, but Gap2 is still zero. As a matter of fact, the four optical bands mingle for $\chi > \chi_c$ in a complicate fashion. This behaviour is shown in Fig. 6.11 (b), where we plot the bands ω_4 and ω_6 for $\chi = 0.9$. When $\chi = 1$ the two upper optical bands ω_1 and ω_4 degenerate into the optical band of Fig. 6.4 and 6.5, while the two lower ones ω_3 and ω_6 collapse onto the flat ω_{DL}.

Finally, let us comment on the function Gap1(δ,χ). We know that in the isotropic case it vanishes for $\delta < 2$. If χ is decreased from 1, the critical value increases from 2. Moreover, the nodes of the function $\omega_3(q_x,q_y) - \omega_2(q_x,q_y)$ move along the borders of the Brillouin zone away from the corners.

6.2.3 Numerical simulations

In this section we illustrate the analytical calculations performed in the previous sections by numerically integrating Eqns (6.14) and calculating power spectra of the atomic vibrations. We note that system (6.14), can be split in two equivalent subsystems, each of them corresponding to a given spatial direction α. As already pointed out, the two corresponding linear spectra can be obtained from each other by four–fold rotations in q–space. Therefore, we can confine ourselves to a scalar model with one degree of freedom per atom.

We have numerically integrated Eqns (6.14) with free–end boundary conditions. We fixed the number of lattice sites to $N = 10$ (300 atoms in total). The initial velocities have been set to zero for all particles, while their initial displacements have been drawn from a set of Gaussian deviates of fixed standard deviation $\sigma = \sqrt{2\epsilon_0}$, where $\epsilon_0 = E(0)/N$ is the energy density of the system. This is the customary procedure in simulating the dynamics of nonlinear lattices at thermal equilibrium, where the spectra of the *nonlinear* excitations are energy–dependent. In particular, this is an efficient way to partition the energy evenly among the linear modes. We obtained the spectrum by performing ordinary discrete Fourier transforms(DFT's) on various time series $\{u(t_m)\}$ $(m = 0, 1, \ldots, N-1)$, corresponding to different choices of the parameters χ and δ, for

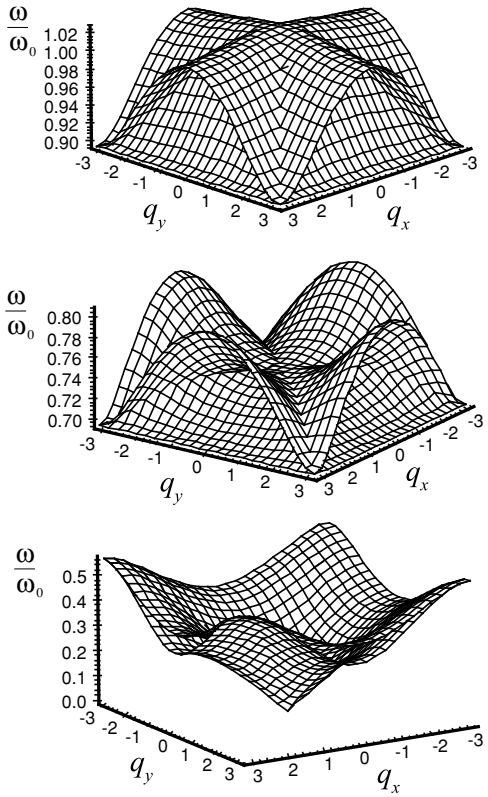

Figure 6.9: The six bands for $\chi = 0.6$ and $\delta = 4$. Upper frame: ω_1, ω_4. Central frame: ω_3, ω_6 (these correspond to the two flat degenerate bands ω_{DL} of the isotropic case) Lower frame: ω_2, ω_5.

ions of both mass M and m (Cu and O for $\delta = 4$, respectively). A window function $w(t)$ has also been included in the Fourier transform in order to select the time interval to be transformed. In fact, we found that the ordinary square function was inappropriate in this case, since no care could be taken to set the sharp cutoffs at small values of u. We therefore chose the Hanning function

$$w(t_m) = \frac{1}{2}\left[1 - \cos\left(2\pi \frac{t_m}{\Delta T}\right)\right] \quad , \tag{6.22}$$

where $\Delta T = (t_{m+1} - t_m)N$ is the sampling time interval. It is clear that $w(t_m) = 0$ at $m = 0$ and $N - 1$. We applied the window to approximately the first and the last 10 % of the data, while keeping $w(t_m) = 1$ for the remaining data set. It is clear that this window smoothly sets the data to zero ($w(t_m) = 0$) at $m = 0$ and $N - 1$.

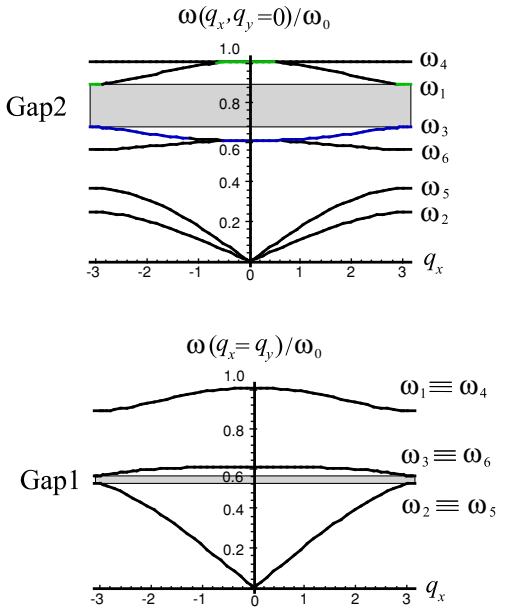

Figure 6.10: Sections of six bands along the directions $(q_x, q_y = 0)$ and $(q_x, q_y = q_x)$ for $\chi = 0.5$ and $\delta = 4$. The two gaps are explicitly indicated as shaded regions.

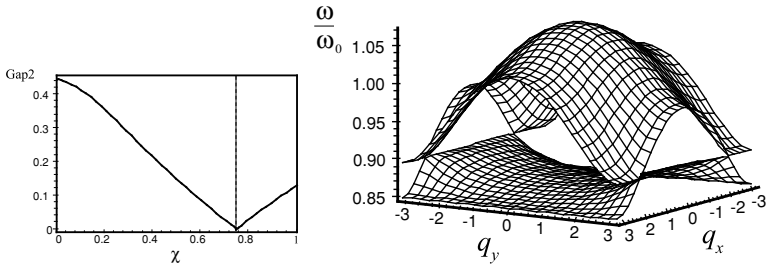

(a) (b)

Figure 6.11: (a) Difference $\omega_4(0,\pi) - \omega_6(0,\pi)$ as a function of the force anisotropy parameter for the CuO $_2$ planes ($\delta = 4$). (b) Optical bands ω_4 and ω_6 for $\chi = 0.9$ and $\delta = 4$.

Typical spectra obtained in the isotropic system for ions of both mass M and m are shown in Fig. 6.12 for $\delta = 2$ and $\delta = 4$. We also marked the bounds of the calculated spectrum (equation 6.5) explicitly as vertical lines. Notice the absence of

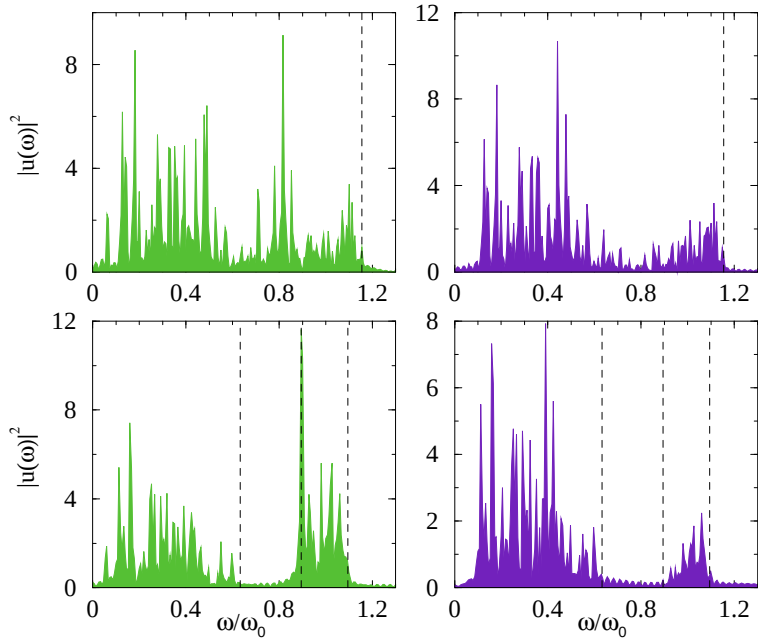

Figure 6.12: Power spectra in the harmonic isotropic CuO_2–like lattice. Upper left: $\delta = 2$, light ion, upper right: $\delta = 2$, heavy ion. The vertical dashed line marks the upper frequency of the calculated spectrum $\omega_+(0,0)$. Lower left: $\delta = 4$, O ion, lower right: $\delta = 4$, Cu ion. The vertical dashed lines mark the bounds of the calculated spectrum: $\omega_-(\pm\pi,\pm\pi)$, $\omega_+(\pm\pi,\pm\pi)$ and $\omega_+(0,0)$

a gap of forbidden frequencies for $\delta < 2$. Typical spectra obtained in the anisotropic CuO_2 lattice are shown in Fig. 6.13 ($\delta = 4$) for $\chi = 0.5, 0.9$. Again, we also marked the bounds of the calculated spectrum explicitly as vertical lines. Notice the absence of the secondary gap (Gap2) for $\chi = 0.9$.

6.3 Energy localisation in the CuO_2 planes

As we mentioned in the introduction, a very interesting aspect of discrete nonlinear systems is the phenomenon of energy localisation. In ref. [29], a vector model is introduced for CuO_2 planes and the role of QOD chains as privileged tracks for moving localised vibrations is brought forward. However, the implications of the model on the dynamics constraints on QOD chains are not fully discussed there in connection with the existence and stability of such solutions. We shall here show, by adding some simple nonlinearity to our anisotropic model of CuO_2 planes, how one can directly investigate the role of such constraints on energy localisation. In our simple model,

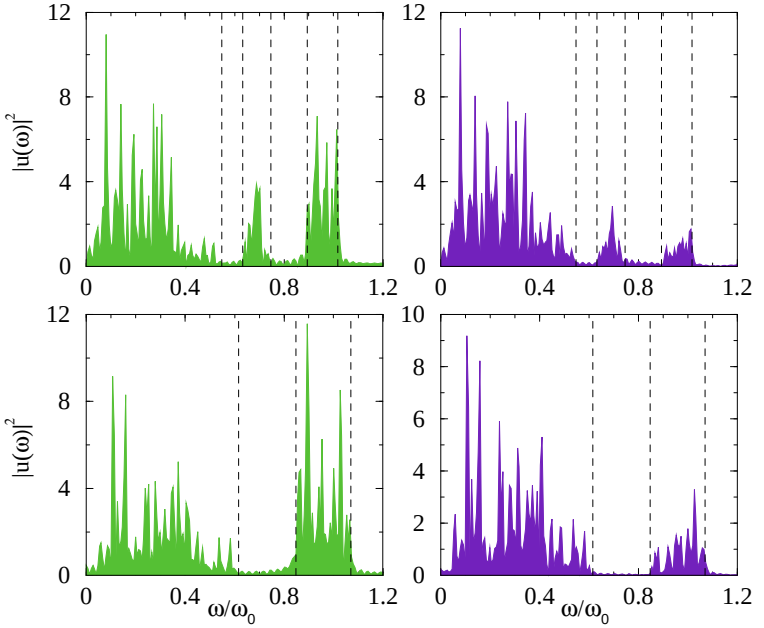

Figure 6.13: Power spectra in the harmonic anisotropic CuO_2 lattice ($\delta = 4$). Upper left: $\chi = 0.5$, O ion, upper right: $\chi = 0.5$, Cu ion. Lower left: $\chi = 0.9$, O ion, lower right: $\chi = 0.9$, Cu ion. The vertical dashed lines mark the bounds of the calculated spectrum.

dynamics constraints on QOD directions in the plane are described by the parameter χ. We showed how the linear spectrum crucially depends on the values of χ and δ. On the other hand, the properties of localised vibrations in nonlinear lattices depend on the details of the linear spectrum (no resonances with phonons). In addition, one can conjecture that different coupling strengths among adjacent atomic rows result in different rates of lateral energy spread, and hence affect the lifetime of DB's. In principle, the very existence of localised solutions could be confined to specific domains in the (δ, χ) plane.

We have found that the literature devoted to the study of localised vibrations in 2D and 3D lattices often lacks a detailed discussion of the model–dependent dynamics constraints which one introduces in the problem. It is worth elucidating this point with an example (the interested reader will find the details of our arguments in appendix C). The easiest choice of a vector model in more than one dimension is the central–force scheme. In this case, if the function V describes the interparticle potential energy,[3]

[3] In general, the total potential energy of N atoms in a lattice can be expanded as a sum of many–body terms. The two–body terms (pair potentials) do not take properly into account the angle–dependent interactions (see chapter 4). However, it is worthwhile to investigate models with two–body terms only, which still are able to take into account the geometry of bonds.

one writes for the energy of the pair (1,2):

$$V(1,2) = V(|\mathbf{r}_1| - |\mathbf{r}_2|) \quad ,$$

where $\mathbf{r}_i$ is the position vector of atom i. A simple calculation shows that the *scalar limit*[4] of the central force scheme is an anisotropic scalar model with χ of the order of $\chi_r = (u/d)^2 \ll 1$, u being of the order of atomic displacements and d the lattice spacing. A value $u \approx 0.1\,d$ in a solid is characteristic of the melting transition (Lindemann criterion [164]), therefore (u/d) can at most be of the order of a few hundredths. Thus, the model *intrinsically* allows for directions with the property that the restoring action against in–chain displacements will not let much energy be transmitted to adjacent chains. This means *intrinsic* little lateral spread of energy. Should one have chosen a coupling of the form

$$V(1,2) = V(|\mathbf{r}_1 - \mathbf{r}_2|) \quad ,$$

the limit would have been the scalar isotropic model ($\chi = 1$), i.e. maximum coupling among adjacent chains. We shall see in section 6.4 that a realistic value of χ lies between χ_r and 1, and is intimately connected to the nature and geometry of the atomic bonding. Therefore, if one wants to retain the two–body approximation of the lattice energy in such case, either of the two vector models discussed above must be modified to match a more realistic value of χ. Our results strongly suggest that such corrections can prove very important when studying the localisation properties of nonlinear CuO_2–like lattices.

6.3.1 Relaxation dynamics

A very efficient way to study DB's in a lattice is through a numerical experiment of relaxation dynamics. This technique has been recently applied to the study of energy localisation in different nonlinear lattices [153, 154, 155, 156]. In our work, this method has been employed for the first time to the study of the dynamics constraints of QOD chains in CuO_2 planes. To do this, we combined such technique with a simple nonlinear stability analysis of DB's. In summary, we performed the following experiments.

The system is first of all prepared in a thermalised state. Then the lattice is put in contact with a zero–temperature bath which slowly extracts energy to the reservoirs (Stage 1). The actions of such baths is accounted for by damping terms in the equations of motion of the edge atomic chains. As a result, breathers generated by local energy fluctuations are left behind and stabilised by the action of the baths, which effectively sweep all the linear vibrations away. [5] Then, in order to investigate the breather stability, we isolated the system again from the thermal baths and switched on some thermal noise (stage 2).

There are several ways to prepare a system in a thermalised state: one can perform a standard fixed–temperature canonical simulation, e.g. within the Nosé scheme [151]. Alternatively, one can implement the isokinetic algorithm [152] or a standard Langevin dynamics based on the fluctuation–dissipation theorem. More simply, we let the system

[4] By *scalar limit* we mean the projection of the model on a given crystal direction

[5] In practice, we have superimposed to the initial momentum distribution a little *artificial* amplitude fluctuation at some site. In the majority of cases, this lets us control where the DB would develop.

perform a microcanonical transient starting from a Gaussian distribution of momenta for particles with zero initial displacements. The momenta correspond to a fixed energy density $E(0)/N$. Of course, there exist many accurate methods to obtain exact breather solutions in nonlinear lattices [157]. On the contrary, relaxation experiments provide a *natural* way of localising energy in the form of DB's out of thermal fluctuations. One important consequence is that, among the different breather solutions allowed by a dynamical system, one is directly confronted with the *easiest* to be spontaneously produced[6]. In the framework of a relaxation experiment, we could not apply the standard technique of linear stability of periodic solutions (Floquet analysis [157]). In fact, one needs a very accurate solution for this analysis to work. Hence, we opted for a *nonlinear* stability analysis, where the stability is observed *directly* against the strength of some added noise. We employed a standard *white* Gaussian noise, with standard deviation of the momentum distribution $\sigma_N = \sqrt{\epsilon_N}$. The noise energy density ϵ_N controls the noise strength.

The type of nonlinearity to adopt in our numerical simulations is suggested directly by our experiment. In Chapter 5 we provided evidence for a low–temperature anharmonicity of the Cu–O pair dynamics. In particular, we found that the form of the potential energy could be described by a large quartic component (see section 5.3). We then chose here the simple quadratic plus quartic function

$$V(u_i, u_j) = \frac{1}{2}[u_i - u_j]^2 + \frac{1}{4}[u_i - u_j]^4 \quad . \tag{6.23}$$

The potential function (6.23) is called FPU potential from the original work by Fermi, Pasta and Ulam [159], and has been a matter of extensive study in the dynamical systems community [160, 161]. The 1D FPU diatomic system has been studied in ref [162]. In particular, both intrinsic gap modes (IGM's) and modes above the top of the optical band were *constructed* in the framework of the *mass anti–continuum limit*. We might expect to recover analogous results in the limit $\chi \to 0$.

Stage 1 We can write the total potential energy of the lattice as

$$V(\{u\}) = \sum_{i,j} \alpha[V(u(i_x,i_y;2),u(i_x,i_y;1)) + \chi V(u(i_x,i_y;3),u(i_x,i_y;1)) + V(u(i_x+1,i_y;1),u(i_x,i_y;2)) + \chi V(u(i_x,i_y+1;1),u(i_x,i_y;3))] \quad . \tag{6.24}$$

[6] This is an additional *free* piece of information. Particularly important in this respect are systems with a complicated linear spectrum as CuO_2–like lattices. In these systems the frequencies of localised vibrations can lie both in the gaps (modes sometimes referred to as intrinsic gap modes (IGM's)) [158], or above the top of the optical band(s), depending on the system parameters (as δ, χ) and potential functions.

The forces are obtained by taking the gradient of Eq. (6.24) and adding the coupling of the lattice at its edges with the $T = 0$ thermal baths. We can write

$$
\begin{aligned}
M\ddot{u}(i_x, i_y; 1) &= -\frac{\partial V(\{u\})}{\partial u(i_x, i_y; 1)} - \sum_{m,n} \Gamma^{j_x, j_y}_{i_x, i_y} \dot{u}(j_x, j_y; 1) \\
m\ddot{u}(i_x, i_y; 2) &= -\frac{\partial V(\{u\})}{\partial u(i_x, i_y; 2)} - \sum_{j_x, j_y} \Gamma^{j_x, j_y}_{i_x, i_y} \dot{u}(j_x, j_y; 2) \\
m\ddot{u}(i_x, i_y; 3) &= -\frac{\partial V(\{u\})}{\partial u(i_x, i_y; 2)} - \sum_{j_x, j_y} \Gamma^{j_x, j_y}_{i_x, i_y} \dot{u}(j_x, j_y; 3) \quad ,
\end{aligned}
$$

where $\Gamma^{m,n}_{i,j}$ is the damping tensor, which selects the atoms directly connected to the zero–temperature thermal bath. These are all the atoms of the edge rows ($i_y = 0, N-1, i_x = 0, 1, \ldots, N-1$) and columns ($i_x = 0, N-1, i_y = 0, 1, \ldots, N-1$). [7]

The outcome of a typical relaxation experiment is shown in Fig. 6.14 as a series of successive snapshots of the lattice site energies $e(i_x, i_y; \sigma)$. These are defined as

$$
\begin{aligned}
e(i_x, i_y; 1) = \frac{1}{2} M\dot{u}(i_x, i_y; 1) + \alpha[V(u(i_x, i_y; 2), u(i_x, i_y; 1)) + \chi V(u(i_x, i_y; 3), u(i_x, i_y; 1)) + \\
V(u(i_x, i_y; 1), u(i_x - 1, i_y; 2)) + \chi V(u(i_x, i_y; 1), u(i_x, i_y - 1; 3))] \\
e(i_x, i_y; 2) = \frac{1}{2} m\dot{u}(i_x, i_y; 2) + \alpha[V(u(i_x + 1, i_y; 1), u(i_x, i_y; 2)) + V(u(i_x, i_y; 1), u(i_x, i_y; 2))] \\
e(i_x, i_y; 3) = \frac{1}{2} m\dot{u}(i_x, i_y; 2) + \beta[V(u(i_x, i_y + 1; 1), u(i_x, i_y; 3)) + V(u(i_x, i_y; 1), u(i_x, i_y; 3))] \quad .
\end{aligned}
\tag{6.25}
$$

The process that leads to localisation is very clear. Two big energy fluctuations in the thermalised lattice at $t = 0$ give rise to high–amplitude vibrations of O(3) ions (at sites (5,8) and (9,3)). The power spectrum of the oscillations of these two ions reveals that a number of nonlinear frequencies above the optical bands are present at this stage of the time evolution (see upper left panel in Fig. 6.15 (a) and (b)), along with linear frequencies. As time goes by, the reservoirs sweep more and more radiation away from the lattice, stabilizing the breathers. This process can be followed directly in the ω–space, observing all the frequencies but the nonlinear ones disappear from the power spectrum (other frames in Fig. 6.15 (a) and (b)). As a side result, we find that the breathers that emerge spontaneously are those with their frequency lying above the optical bands. As a matter of fact, during our extensive numerical simulations, we never observed an IGM develop spontaneously in the CuO_2 lattice It is very easy to *construct* one, though, for example in the framework of the so–called rotating–wave approximation (RWA) [161]. We shall not report further on this side–problem here.

[7] Γ can be written as

$$
\Gamma^{j_x, j_y}_{i_x, i_y} = \gamma[g_{i_x, j_x}\delta_{i_y, j_y} + \delta_{i_x, j_x} g_{i_y, j_y} - g_{i_x, j_x} g_{i_y, j_y}] \quad ,
$$

where γ is the coupling strength, $g_{i_x, j_x} = \delta_{i_x, j_x}[\delta_{j_x, 0} + \delta_{j_x, N-1}]$, and δ is the usual Kronecker function.

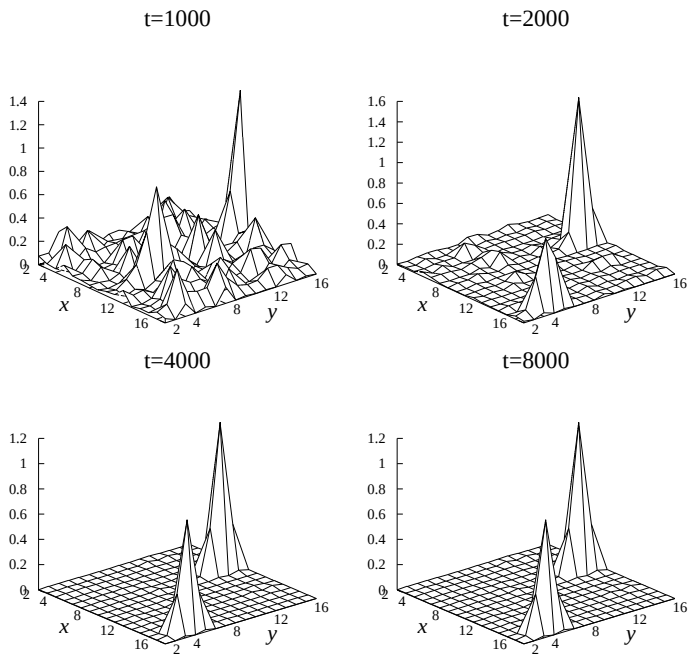

Figure 6.14: Relaxation dynamics in the CuO_2 lattice with FPU potential. The evolution of the system is shown as snapshots of the site energies. Parameters are: $\chi = 1$, $\delta = 4$, $E(0)/N = 1$ and $\gamma = 0.005$.

Stage 2 We want now to investigate the stability of the localised solutions that have spontaneously developed in the lattice. In particular, we follow the evolution of a breather at site $(N/2, N/2; 2)$. To do so, we switch off the damping and add some Gaussian thermal noise. We have considered three realisations of the noise, $\epsilon_N = \sigma_N^2/2 = 0.002, 0.005$ and 0.01. In order to monitor the time evolution of the localised solutions, it is useful to introduce the so–called *localisation parameter*. It is defined as

$$
\mathcal{L} = 3N \frac{\sum_{i_x, i_y = 0}^{N-1} \sum_{\sigma=1}^{3} e(i_x, i_y; \sigma)^2}{\left[\sum_{i_x, i_y = 0}^{N-1} \sum_{\sigma=1}^{3} e(i_x, i_y; \sigma) \right]^2} \quad , \tag{6.26}
$$

where $e(i_x, i_y; \sigma)$ are the site energies, defined in Eq. (6.25). According to its definition, the fewer sites the energies is localized onto, the closer $\mathcal{L}$ is to $3N$. On the other hand,

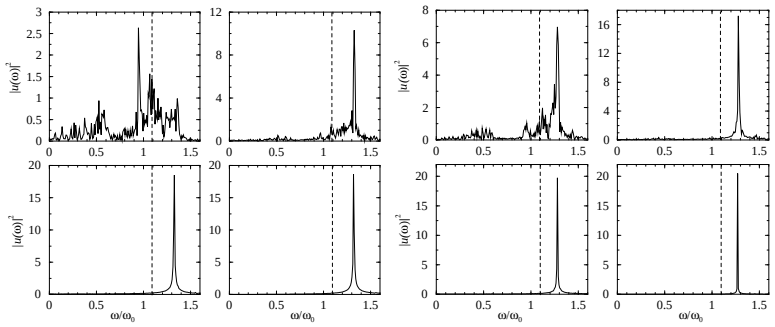

Figure 6.15: Relaxation dynamics in the CuO_2 lattice with FPU potential. (a) Power spectrum of the oscillations of O(5,8;3). (b) Power spectrum of the oscillations of O(9,3;3). Each subfigure shows four spectra relative to four successive time windows. From upper left to lower right: $\Delta T = [1000, 1500]$, $\Delta T = [1500, 2000]$, $\Delta T = [3500, 4000]$, $\Delta T = [7500, 8000]$. Other parameters as in Fig. 6.14.

.

the more evenly the energy is spread on all the atoms, the closer $\mathcal{L}$ is to a constant of order 1. For instance, in the latter case $\mathcal{L}$ for the FPU potential in 1D lies within the interval [7/4, 19/9], the two extremes being the energy–independent values of the harmonic and pure quartic potentials, respectively [160].

In Fig. 6.16 we plot the time evolution of the breather energy for increasing noise strength and $\chi = 0.1, 0.5, 1$. What the figures tell appears counterintuitive. In fact, we were surprised to observe the longest lifetimes in the lattices with intermediate values of force anisotropy. This effect is evident in Fig. 6.17 (a), where we plot $\mathcal{L}$ vs time for the largest noise strength $\epsilon_N = 0.01$. The *death* of the breather is easily identified (black arrows) for $\chi = 1$ and $\chi = 0.1$. On the contrary, the energy remains to a good extent localised in the same time span for $\chi = 0.5$. Surface plots of the lattice site energies are plotted in Fig. 6.17 (b) at times immediately prior to the energy spread out ($\chi = 0.1$ and $\chi = 1$). It is also instructive to observe the breather collapse in the ω space. In Fig. 6.18 we follow the nonlinear frequency of the breather as it interacts with the phonon frequencies. It is clear that an increasing population of the optic modes is associated with the energy spread out. The reason for this is that the first harmonics of such modes possess enough energy for the resonance with the breather frequency to be effective. On the contrary, acoustic modes do not interfere with the breather (see panel (ϵ_B, χ)=(0.01,0.5) in particular). One would expect that the breather lifetime would be a monotonic decreasing function of χ, since it is natural to associate greater decay rates of the breather energy to greater coupling between adjacent chains. However, we found that low values of χ are also associated to fast decays of the energy. We also observed that at low values of χ the breather is no longer stationary – it moves and it

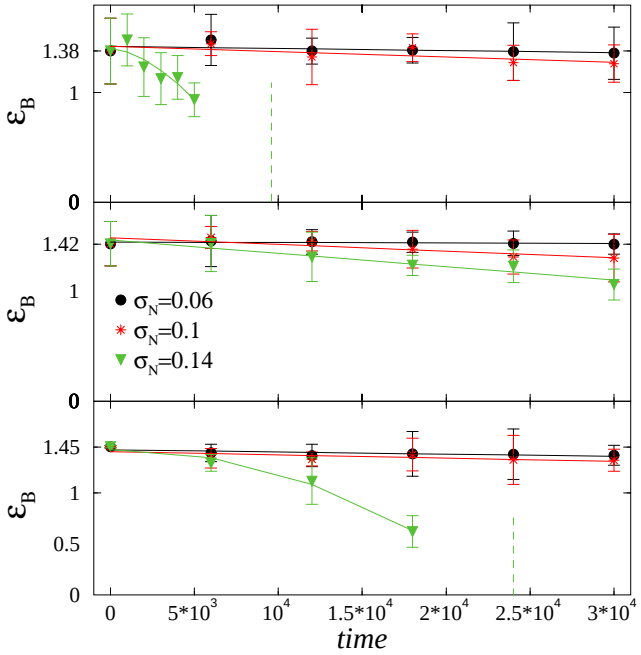

Figure 6.16: Breather energy vs time for $\epsilon_N = 0.002, 0.005, 0.01$ and linear fits. The solid lines for $e_N = 0.01$ are guides to the eye. Upper panel: $\chi = 1$, central panel: $\chi = 0.5$, lower panel: $\chi = 0.1$. The vertical dashed lines mark the times of the observed collapse.

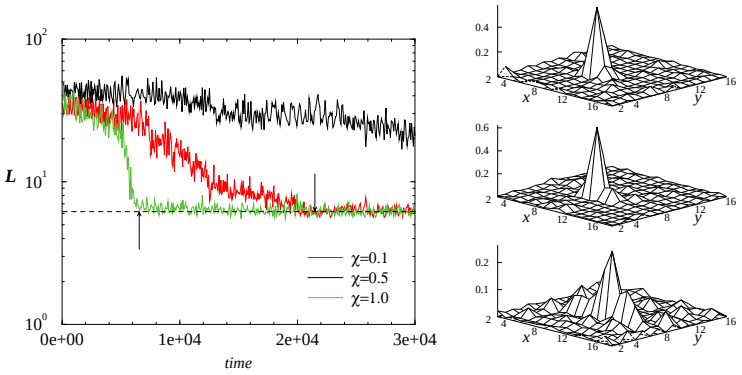

Figure 6.17: (a) Localisation parameter $\mathcal{L}$ vs time for $e_N = 0.01$ and $\chi = 0.1, 0.5, 1$. The arrows indicate the breather collapse. (b) Site energies. From above: $\chi = 1$ at $t = 5*10^3$, $\chi = 0.5$ at $t = 3*10^4$, $\chi = 0.1$ at $t = 1.2*10^4$.

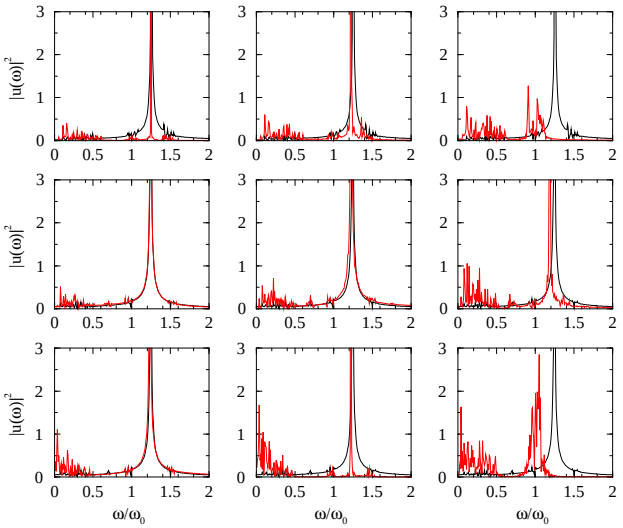

Figure 6.18: Power spectra of the time series $u_m(N/2, N/2; 2)$. From above: column index, $\epsilon_N = 0.002, 0.005, 0.01$. Row index, $\chi = 1, 0.5, 0.1$. Black lines, power spectra at $t = 0$. Red lines, power spectra at $t = 3*10^4$.

can even split in two moving breathers. It is important to stress that the decrease of the breather energy upon lowering χ further than some critical value χ_c is associated

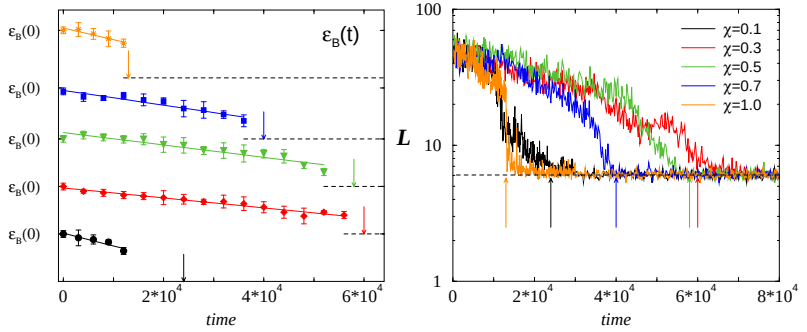

Figure 6.19: (a) Breather energy vs time and linear regressions for $\epsilon_N = 0.008$. From below: $\chi = 0.1, 0, 3, 0, 5, 0, 7, 1$. The arrows mark the time of the breather collapse. The graphs have been shifted along the y–axis for the sake of clarity. (b) Localisation parameter $\mathcal{L}$ vs time. The arrows mark the definitive disappearance of the breather.

to the *unpinning* of the breather[8]. Actually, it has already been observed in 1D and monoatomic isotropic 2D FPU lattices that breathers spontaneously emerging in the relaxation process are, respectively, moving and stationary [155, 165]. The reason for this is not known.

The issue of breather mobility is still a very controversial one [166, 167]. In particular, no proof of existence has been given yet for moving breathers, only indirect numerical observations reported in 1D FPU systems [166]. The only examples of moving localised excitations in 2D systems published so far can be found in Refs. [27] and [29]. In principle there exists a systematic approach for obtaining moving breathers in lattices, based on a generic feature shown by stationary breathers [168]. First, stationary breathers can be computed to any degree of accuracy [157]. Then, their stability can be monitored in terms of the system parameters. In wide regions of the parameters space, these stationary breathers undergo a bifurcation which enables them to be highly mobile.

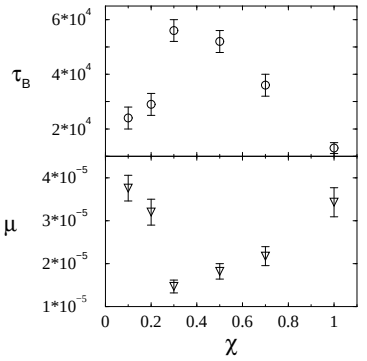

Figure 6.20: Upper panel: breather lifetime τ_B as observed. Errors reflect the uncertainty of identifying a proper collapse of the breather. Lower panel: slope μ of the breather energy decay vs χ as from fits shown in Fig. 6.19. Errors as from standard χ^2 errors on fitting parameters.

[8] our results indicate $\chi_c \approx 0.3$, see further on in this section

This is probably what happens in our simulations, upon lowering χ. However, in the presence of noise the breather mobility is still associated to a quick spread of its energy over the whole lattice.

Our observations strongly suggest that breather mobility in more than one dimension is deeply intertwined with its (nonlinear) stability through the lateral energy spread rate. In particular, our results strongly prompt for an accurate *linear* stability analysis of stationary localised solutions in terms of the parameter χ. This will certainly be matter of our future research.

To conclude this section, we attempt to give a quantitative estimate of the breather lifetime as a function of χ. For such analysis, we need a value of ϵ_N not so small that the breather decay takes place on too wide a time span, nor so big that the collapse is too quick to follow with accuracy. We chose $\epsilon_N = 0.008$. We then performed simulations with $\chi = 0.1, 0.3, 0.5, 0.7$ and 1. In Fig. 6.19 we plot the breather energy and $\mathcal{L}$ vs time. It is evident that intermediate values of χ ($0.3 < \chi < 0.7$) are associated with greater lifetimes. On the contrary, in the isotropic and strongly anisotropic lattices ($\chi = 1, 0.1$) the breather collapse is quicker (orange and black lines in Fig. 6.19 (b)). In particular, the decay process is more gradual in the latter case. This feature reflects the fact that the breather is set in motion by the noise. These effects were very well reproduced in our simulations for a wide choice of noise strengths.

It is possible to define a semi–quantitative breather lifetime τ_B by looking in parallel at the trend of $\mathcal{L}$ and at successive snapshots of the site energies during the time evolution. In Fig. 6.19, the times at which the breathers completely disappeared are indicated with arrows. They are plotted in the upper panel of Fig. 6.20. t is also instructive to look at the decay rate of the breather energy. We found that, for moderate values of ϵ_N, the trend of ε_B is to a good extent linear in time for all values of χ, $\varepsilon_B(t) = \varepsilon_B(0) - \mu(\chi)t$ (see also Fig. 6.16). In the lower panel of Fig. 6.20 we plot the slope of the breather energy decay curve vs χ as obtained from the linear regression for $\epsilon_N = 0.008$. The fits are plotted in Fig. 6.19 (a). This heuristic analysis confirms the instability associated to high and low values of the force anisotropy parameter χ.

Can we obtain quantitative results if we introduce physical units? Unfortunately, there is no physical scale of energy associated with a quadratic plus quartic potential. In fact, one can adjust the energy by just rescaling the displacements. Hence, a bounded potential like the Morse, Lennard–Jones or Born–Meyer–Coulomb functions (just to mention the commonest ones) must be introduced. There is some literature devoted to study breathers in lattices with *realistic* potentials [169]. It is interesting to note that, with such potential functions, breathers are found only in systems with a gap in their linear spectrum. These are constructed numerically within the framework of the RWA approximation [163]. In particular, it is argued that breathers do not *exist* above the top of the optical band [170]. We have performed numerous relaxation experiments in CuO_2 planes within our anisotropic scalar model with Morse and Lennard–Jones potentials. We found that no gap breathers spontaneously emerge out of the relaxation process for any of the different choices of parameters exploited. This, if confirmed by more rigorous proofs, would mean that gap breathers in systems with bounded potentials are likely to have little *thermodynamic* relevance. In ref. [29], the energy of a breather traveling in a CuO_2 plane within a realistic model is estimated in the interval $[0.01, 0.5]$ eV. However, the authors do not comment on the frequency of its internal vibration

with respect to the linear spectrum of their model.

Furthermore, in a realistic system there exist a *physical* limit to the energies that can be explored. Among other constraints, we might mention the Lindemann criterion, according to which atomic displacements greater than approximately 10 % of the lattice spacing are unphysical [164]. On the other hand, it is known that breathers in 2D and 3D lattices can be excited only for energies above a certain threshold, which depends on the nonlinearity degree in the potential energy [171]. Therefore, it might happen that one would need so enormous energies to excite a breather in a lattice that it would end up living in a melted solid! These issues should all be carefully taken into account when setting up and studying a realistic lattice model.

In our simple example, one can nonetheless set up a physical scale for times, which just depends on the value of the harmonic constant k_2. The non–dimensional time units $\tilde{t}$ corresponding to the choice (6.23) are given by

$$\tilde{t} = \frac{\omega_0}{\sqrt{2}} t = \frac{t}{3.6 \times 10^{-14}/\sqrt{k_2}}$$

where the harmonic constant k_2 is expressed in eV/Å^2. In Chapter 5 we have found from our experiment $k_2 = 27 \pm 3$ eV/Å^2. Therefore, the non–dimensional time unit of our simulations is of the order of $6.9 \pm 0.4 \times 10^{-15}$ sec (where we have used the reduced mass of the Cu–O pair, $\mu_{\mathrm{Cu-O}} \approx 2.13 \times 10^{-26}$ Kg). Therefore, lifetimes of the order of 10^4 would correspond to a few tenths of nanoseconds. These must be compared with the typical phonon periods in a solid, which are of the order of the inverse of the Debye frequency ω_D. For high–T_c materials of the RBCO family, $\omega_D \approx 400$ K [172], which means $2\pi/\omega_D \approx 10^{-13}$ sec.

It is natural to ask at this stage of the discussion what is a *reasonable* estimate of the parameter χ in a realistic model of the CuO_2 lattice. We shall try to answer this question in the last section of this chapter.

6.4 Estimate of the force-anisotropy parameter

What could be a reasonable value of χ? Before answering this question it is instructive to see how to obtain a rough estimate of at least an upper bound for χ by using the results of elasticity measurements. If it were possible to perform elasticity measurements on a perfectly two–dimensional CuO_2 plane, we could calculate χ as the ratio C_{xyxy}/C_{xxxx} between the shear and normal moduli of elasticity. In a three–dimensional solid, these elastic coefficients are labeled C_{11} and C_{66}. Of course, the latter coefficients describe the bulk elastic properties of the cuprate lattices. However, we can conjecture that the reservoir blocks which separate the copper–oxide sheets are well described by isotropic elastic constants at least for in–plane displacements, the errors resulting in an overestimate of the response to shear stress. This assumption is legitimated by the rather close–packed atomic arrangement and the dominant ionic nature of the bonding [150]. If this assumption is correct, the contribution of the reservoir layers to the measured C_{66} and C_{11} would be approximately the same, making the anisotropy left in their ratio an upper bound for χ. In the literature, the ratio C_{66}/C_{11} is found to fluctuate between 0.3 and 0.4 [172]. Let us now come to our estimate.

The atomic bonds between Cu and O ions in the CuO_2 planes are predominantly of covalent type (see chapter 2), while the bonds with the more distant atoms in the neighbouring planes along z are ionic. Therefore, the in–plane restoring forces are mainly determined by the distortion of the planar molecular orbitals. We can take advantage of this information to investigate the role of the bonds' nature and geometry on interatomic forces by directly looking at the energies of the bonding molecular orbitals (MO's). For this purpose, we made use of the computer program CACAO (Computer–Aided Composition of Atomic Orbitals) [173]. This code is based on the program SIMCON [174], and is equipped with a suitable graphical interface, that provides a very intuitive tool to examine the MO's of a given atomic cluster. The calculations are performed in the usual scheme of the linear composition of atomic orbitals (LCAO). We shall not enter here the details of such calculations. The interested reader can find exhaustive references in [173] and [174]. The idea is very simple. We build a molecular cluster with the local structure of CuO_2 planes, and then study the variation of energy of the filled orbitals as the position of a selected atom is varied from equilibrium. By summing the contributions of all relevant orbitals we obtain a potential well, whose curvature in the harmonic approximation gives a measure of the force constant involved. By repeating the same numerical experiment for displacements along x and along y of the same *probe* atom, we can provide an estimate of the relative magnitude of the corresponding force constants.

The major difficulty in implementing this simple argument is in isolating the contribution of relevant orbitals to the total energy. We shall see, by comparing clusters of different sizes, that the finite–size effects show in an unpredictable fashion in the variation of the total energy. Therefore, it is necessary to follow the energy changes of single orbitals isolated on pure physical grounds. In other words, we have to get rid of all those orbitals that do not describe the lattice *bulk* of the cluster.

Let us consider the atomic cluster shown in Fig. 6.21 (a) (cluster 1). It is built around a central copper ion and includes other 8 copper ions and 14 oxygens. We make it a closed–shell cluster by saturating the charges left over by the oxygens including 10 hydrogens. These are not shown in the figure. The probe atom is the one indicated by the arrow. Let us consider a generic potential energy function associated with the displacements of the probe atom along the x and y directions. Let us assume a functional form of the simple kind $V(u_i) = k_i u_i^2$ $(i = x, y)$. It is not difficult to see that the force anisotropy parameter χ is just the *experimental* ratio k_y/k_x, measured in the MO simulation. To see that, it is enough to write down explicitly the expressions of the forces on the probe atom when all its neighbours are at rest (see equations 6.2):

$$\begin{aligned} F_x &= -k_x u_x = -2\alpha u_x \\ F_y &= -k_y u_y = -2\beta u_y \quad . \end{aligned} \tag{6.27}$$

Hence $\chi = \beta/\alpha = k_y/k_x$.

The first question one could raise is how the TOTAL energy changes upon displacing the probe atom[9]. We show such changes in the right panel of Fig. 6.21 (a). It is clear that in this case $k_x < k_y$. In fact, the ratio k_x/k_y turns out to be about 0.375,

[9]Here the total energy includes the total *binding* energy and the work needed to bring together the atoms from infinity to form the cluster

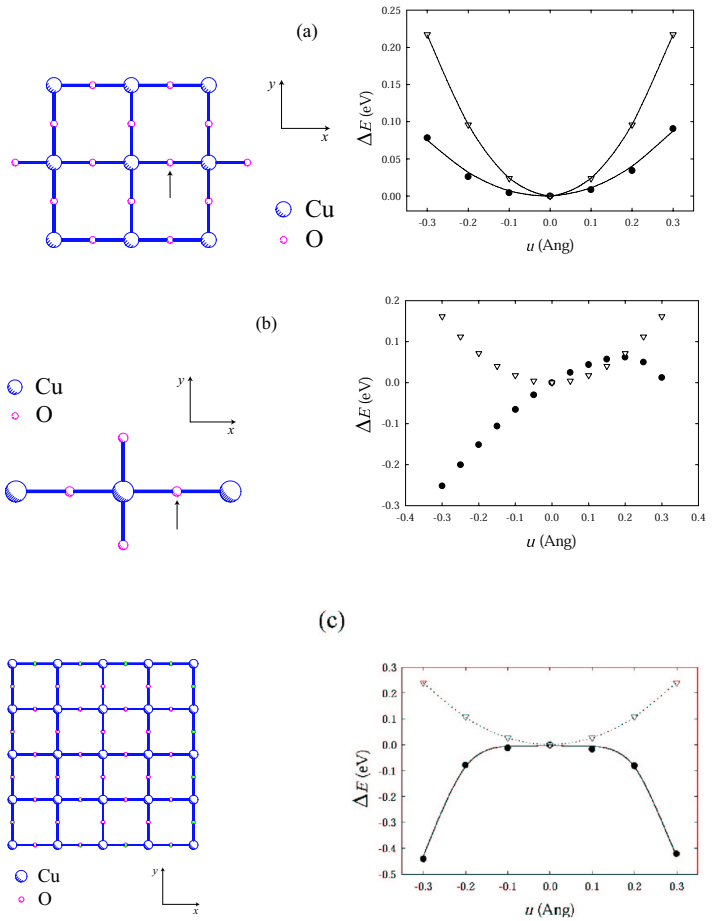

Figure 6.21: From above: left panels: clusters 1 2 and 3. The arrow indicates the probe atom. Right panels: Total energy vs displacement of the probe atom. Black circles correspond to displacements along x, white triangles to displacements along y.

which means $\chi \approx 2.67$. This result is clearly counterintuitive, since one would expect that the longitudinal coupling would always be stronger than the parallel one. In fact, we shall find out that this result is an artifact due to the finiteness of the cluster. In particular, the total energy displays a clear instability against displacements of the probe atom along x. One can easily realise that by making the cluster smaller and repeating the same measurement. Let us consider the cluster in Fig. 6.21 (b) (cluster

2). It is built of 3 copper ions, 4 oxygens and 2 hydrogens (not shown). The total energy curves are reported in the right panel. It is apparent that displacements along x do not even give rise to a restoring force. This is clearly unphysical. We must conclude that the total energy is unstable against displacements of the probe atom in the x direction. We checked that in other neutral clusters of different sizes and always found unphysical results. Among others, we chose to show cluster 3 (Fig. 6.21 (c)). The instability associated with the displacement of the probe atom along x is evident.

The solution is then to isolate the contribution to the total energy of the orbitals which are relevant for the bulk lattice dynamics. The energy of such a selected subset of orbitals must give rise to restoring forces against displacements of the probe atom in any directions of the plane. We also expect $k_y/k_x < 1$. We found that such MO's can be gathered in three groups. In the framework of the usual LCAO approximation their composition is (see Fig. 6.1 for atom referencing):

Gr1 • $d_{x^2-y^2}$ orbitals of Cu ions, p_x orbitals of O(2) ions and p_y orbitals of O(3) ions

Gr2 • d_{xy} orbitals of Cu ions p_y orbitals of O(2) ions and p_x orbitals of O(3) ions

Gr3 • d_{xz} (d_{yz}) orbitals of Cu ions and p_z orbitals of O(2) (O(3)) ions

They are all reported for clusters 1 and 2 in appendix D, where we also show the energy changes of each of them for both displacements along x and y.

6.4.1 Analysis of cluster 1

It is very instructive to analyse separately the contributions of the three groups of orbitals listed above. In Fig. 6.22, we plot the potential energy wells measured for the three groups versus displacements along x and along y. A few comments are in order.

About the fits. If we did the same numerical experiment on an infinite cluster, we should get to a good extent parabolic wells, at least for small enough displacements of the probe atom. However, we are dealing with finite clusters, where the symmetries of the true infinite lattice will never be perfectly reproduced. Nevertheless, after grouping MO's energies, we always got well defined wells with minima very close to the equilibrium configuration. Therefore, a sensible measure of group–specific k_x and k_y could be performed. This is clearly a self–consistency check for our grouping criteria. As a consequence, rather than fitting asymmetric curves with 3rd or 4th order polynomials, we did the following. Split the asymmetric curve in the $u < 0$ and $u > 0$ branches. By reflecting a copy of each branch on the opposite side of the u axis we get two parabolas. By fitting these two parabolas we identify the interval $[k_{min}, k_{max}]$. This interval is the most likely one to contain the *true* value of the force constant.

We found that Gr2 orbitals produce the strongest restoring force against displacements along x, while they react weakly against displacements along y (see Fig. 6.22). Gr1 orbitals do the opposite. This is possibly because σ–like MO's are tighter to distort than π–like MO's. On the contrary, it is easier to stretch a σ bond than a π bond. Gr3 orbitals display an original behaviour. In fact, we found that the equilibrium configuration of the clusters is a saddle point (see Fig. 6.22) in the changes of Gr3 energies. In particular, no restoring force develops against displacements of the probe atom along y. This effect could be a spurious one, due to the limited number of atoms

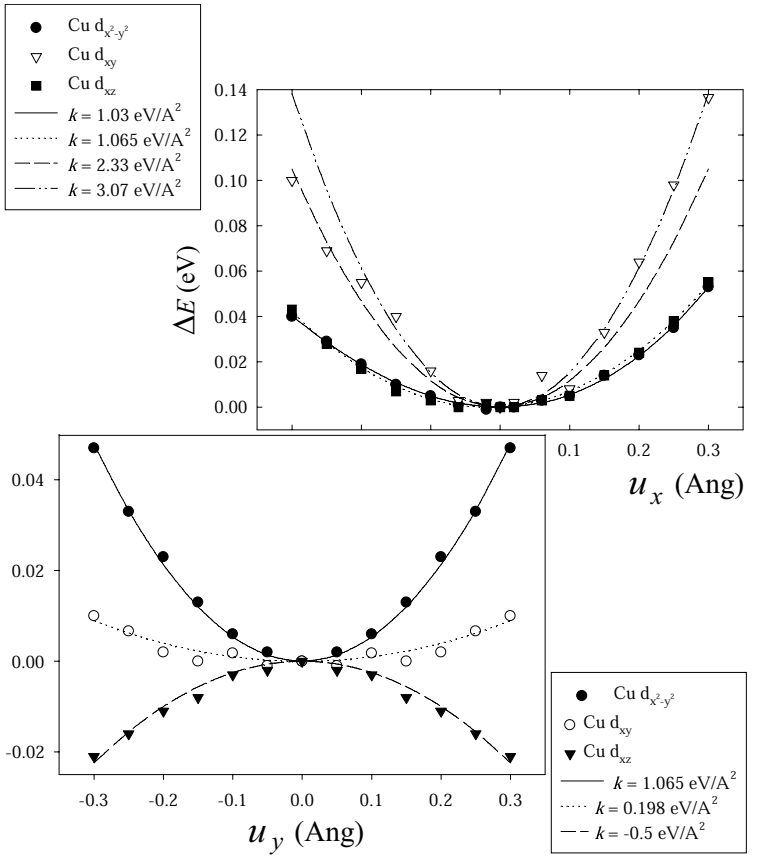

Figure 6.22: Cluster 1. Energy variations of the three selected groups of orbitals Gr1, Gr2 and Gr3 (symbols) and best fits. Upper panel: energy changes vs displacements along x. Lower panel: energy changes vs displacements along y

included in the clusters. Hence, a more accurate analysis would be in order. Here we just make two points. First, this effect is present in both clusters 1 and 2 (see below). Second, it is no surprise that there is an instability (or more generally *soft* coupling) for displacements along y. After all, this is the direction where we expect the weakest reaction. The changes in the total energies of Gr1, Gr2 and Gr3 orbitals are reported in Fig. 6.23. By performing the double–parabolas analysis described above, we get the following reference interval for the force anisotropy parameter

$$[\chi_{min}, \chi_{max}] = \left[\frac{k_{y,min}}{k_x}, \frac{k_{y,max}}{k_x}\right] \approx [0.15, 0.2] \quad . \tag{6.28}$$

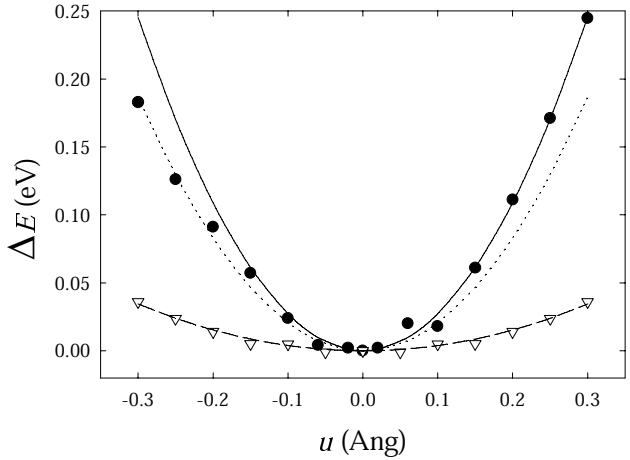

Figure 6.23: Cluster 1. Total energy variations of the relevant orbitals Gr1+Gr2+Gr3 (symbols) and best fits. Black circles: energy changes vs displacements along x. White triangles: energy changes vs displacements along y

This is an important result of this chapter. In particular, we find out that the CuO_2 planes are indeed described by the two–gap scenario (see Fig. 6.11 (a)). Moreover, we estimate the second gap between the two pairs of optical bands to be ≈ 0.35 of the frequency ω_0. We also note that the range (6.28) is in excellent agreement with the values derived in Chapter 2 from the Cu–O potentials reported in the literature (see Table 2.2).

6.4.2 Analysis of cluster 2

We end this chapter by discussing the results relative to cluster 2. Our analysis have made clear that the relative strengths of the restoring actions associated with different groups of MO's closely follow those of cluster 1. In Fig. 6.24 we compare the energies of the planar (Gr1+Gr2) and perpendicular–to–plane (Gr3) orbitals. We note that again the response of the Gr3 orbitals identifies an unstable saddle point. Moreover, the well associated with the planar contribution is more markedly asymmetric. This is obviously a consequence of the marked asymmetry of cluster 2 with respect to motion along x of the probe atom. It obviously experiences a greater repulsion moving towards the central Cu ion, than it gets repelled by its right-hand Cu neighbour (which, in turn, lacks its O(2) neighbour). This makes the curvature of the steepest branch of the measured potential energy a more reliable estimate of the associated force constant. The total energy of the cluster is also shown in Fig. 6.24. From these curves we measure $\chi_{min} = 0.28$. We also note that Coulomb interactions are less screened out in cluster 2 than in cluster 1. This might account for the slight discrepancy left with the results of cluster 1.

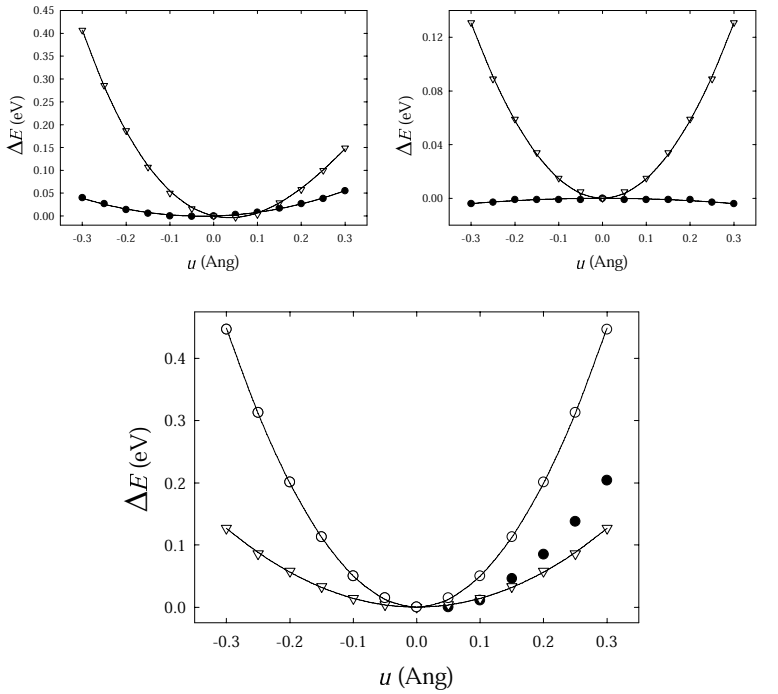

Figure 6.24: Cluster 2. Upper panel: energy variations of the Gr1+Gr2 orbitals (white triangles) and Gr3 orbitals (black circles). Solid lines are guides to the eye. Left: displacements along x, right: displacements along y. Total energy variations of the relevant orbitals Gr1+Gr2+Gr3 (symbols) and best fits. Black circles: energy change vs displacements along x (white circles: parabola corresponding to the steepest part of the curve). White triangles: energy change vs displacements along y

6.5 Conclusions

In this chapter, we introduced a simple scalar anisotropic model of the lattice dynamics of CuO_2 planes. We calculated the phonon bands and provided the exact analytical expressions for both the anisotropic and isotropic systems. The linear spectrum may be of extreme utility for all interested in studying Discrete Breathers in nonlinear CuO_2 planes (us included). Moreover, we described a numerical experiment which shows how the force anisotropy parameter χ may crucially influence the very existence and stability of nonlinear localised vibrations in such systems. In particular, we were able to combine such numerical results with the experimental results discussed in Chapter 5 to estimate the lifetime of localised excitations in CuO_2 lattices. We find from our simulations $\tau_B \approx 1$ to 3 nanoseconds, very large lifetimes on the scale of the typical

phonon periods.

Finally, we attempted to give a quantitative estimate of χ based on the theory of molecular orbitals in a reduced CuO_2 cluster. As a result, we located the *true* value of χ in the vicinity of 0.2, in excellent agreement with the estimates from the data available in the literature.

Summarising, from the results discussed for both the linear and nonlinear systems, we argued that CuO_2 planes are indeed described by the two–gaps scenario of the phonon band structure. Furthermore, such value of χ identifies in our model a critical point in terms of the breather stability. This conclusion definitely calls for more accurate investigations of the stability of localised solutions in CuO_2 lattices in terms of χ.

Appendix A

General physical properties of cuprates

In this appendix we gather some reference information regarding general physical features of cuprates. We also include an up–to–date table reporting the most important cuprate superconductors, along with their T_c, and citations of reference chemical and structural studies.[1]

Within each family, the various materials have identical reservoir layers and differ by the number n of CuO_2 adjacent sheets. The transition temperature increases with increasing n up to $n \leq 3$. However, a number of planes greater than three strongly affects in the majority of cases the structural stability of the compounds. Hence, the transition temperature also depends on the number of adjacent CuO_2 planes, besides the chemical composition of the reservoir blocks and the doping level.

In all p–type materials, superconductivity follows from hole injection in the CuO_2 planes upon doping. It is well known that the charge carriers in the superconducting state are pairs of fermions, with charge $2e$ (*Cooper pairs*). A common feature of all cuprates is the small size of such pairs, if compared with the Cooper pairs in ordinary metallic superconductors. Moreover, cuprates are strongly anisotropic materials. This feature is also reflected in their physical properties, and in the dimension of the Cooper pairs in particular. A measure of such dimension is the so–called *coherence length* ξ, which can be defined in two different ways [42]. According to the definition introduced by Pippard, it measures the non–local character of the superconductivity phenomenon. In practice, the current at some point in space is not only determined by the electric field at that point, but also by the contribution of the electric field from an extended region all around. The dimensions of that region are measured by ξ. Instead, in the Ginzburg–Landau (GL) theory, ξ accounts for the spatial extent of appreciable variations of the order parameter ψ. This, in turn, may be interpreted as an effective probability density (square modulus of the wavefunction) for the gas of pairs condensed in the superconducting state.[2] However, the two definitions agree in the vicinity of $T = 0$

In cuprates, ξ is about two orders of magnitude lower[3] than in ordinary superconductors, where it ranges in the interval 500–10000 Å. At $T \ll T_c$ ($T \to 0$) it is [37]:

$$\xi_c \simeq 2 - 5\,\text{Å} \qquad \text{along } c$$
$$\xi_{ab} \simeq 10 - 30\,\text{Å} \qquad \text{on the } ab\text{–plane} \quad .$$

We see that the coherence length is indeed strongly anisotropic. In particular, ξ_c is of the order of the lattice spacings and much smaller than ξ_{ab}. This means that the Cooper pairs in cuprates have a distinctive two-dimensional character.

Another important parameter is the *penetration depth* λ_p. For moderate intensities of applied magnetic fields, superconductors are perfect diamagnets. They expel the magnetic flux except for a small skin layer where the magnetic field penetrates with exponentially decreasing intensity. The depth of such penetration layer is defined by the London equation [37]:

$$\nabla^2_{\mathbf{r}}\mathbf{B} = \frac{1}{\lambda_p^2}\mathbf{B} \quad .$$

In cuprates $\lambda_p(T = 0)$ ranges between 10^3 and 10^4Å [37][59], and is also strongly anisotropic ($\lambda_p^c > \lambda_p^{ab}$). As a consequence, magnetic fields *can* penetrate in depth in these materials. Actually, being $\xi \ll \lambda_p$, cuprates are classified as *extreme type II superconductors*. This means that they are characterised by two different critical fields H_{c1} and H_{c2}, with $H_{c2} \gg H_{c1}$. For magnetic fields lower than H_{c1}, the material behaves as a perfect diamagnet. For intermediate values, the field partially penetrates in the form of vortexes of superconductive currents flowing around a core region of normal phase (*mixed state* [37]). Finally, for $H > H_{c2}$ the field penetrates completely and the material turns normal. For cuprates, H_{c1} is of the order of hundreds of Gauss, while H_{c2} is in general greater than 100 Tesla (1T=10^4 Gauss)[37].

Let us now discuss the *energy gap* 2Δ, which is the minimum energy required to create an elementary excitation in the superconducting state. At $T = 0$, it exactly equals the binding energy of a Cooper pair. It also is an anisotropic function. In particular, in cuprates it is [60]

$$2\Delta_c(0)/k_BT_c \approx 3.5 \qquad \text{and} \qquad 2\Delta_{ab}(0)/k_BT_c \approx 8 \quad .$$

The value predicted by the BCS theory is $2\Delta(0)/k_BT_c = 3.52$. However, since T_c is in cuprates much higher than in ordinary superconductors, the binding energy of the Cooper pairs must also be large. Consequently, the attractive interaction responsible for the pairing in cuprates must be very intense by comparison.

The transport properties of cuprates in the normal state show many differences with ordinary metals, besides the anisotropy related to their lattice structure. In particular, the resistivity in the *ab*–plane varies linearly with temperature and is from 2 to 4 order of magnitude lower than the resistivity along *c*. The latter usually displays the distinctive behaviour of the resistivity in semiconductors, i.e. it decreases with increasing temperature [61].

[1] The compound $Ca_{14-x}Sr_xCu_{24}O_{41}$ is the latest one to be have been synthetised (1996) among the listed ones. It aroused great interest, since the electronic conduction in this material takes place in the Cu_2O_3 planes instead of the CuO_2 planes [40] [41].

[2] According to the GL definition, ξ decreases as the temperature is reduced, while the Pippard coherence length is independent of the temperature [42].

[3] We refer here to the GL definition, since determination of ξ according to Pippard is more complex and delicate [58].

High–T_c Superconductors

Formula	T_c(K)	n	observations	Ref.
$La_{2-x}Sr_xCuO_4$	38	1	La(n=1); 214	[35][36][37]
$La_{2-x}Sr_xCaCu_2O_6$	60	2	La(n=2)	[35][37]
$La_2CuO_4F_\delta$	40	1	fluorinated,p–type	[38]
$Nd_{2-x}Ce_xCuO_4$	30	1	Nd(n=1); T'	[36][37]
$Nd_{2-x-y}Sr_xCe_yCuO_4$	28	1	T*	[36]
$Nd_2CuO_{4-x}F_x$	27	1	fluorinated, n–type	[39]
$YBa_2Cu_3O_7$	92	2	YBCO, Y123	[35][36][37]
$YBa_2Cu_4O_8$	81	2	Y124	[35][36][37]
$Y_2Ba_4Cu_7O_{14}$	40	2	Y247	[35][36][37]
$EuBa_2Cu_3O_7$	90	2	EBCO	[35][36][37]
$TlBa_2CuO_5$	50	1	1–Tl(n=1); Tl1201	[35][36][37]
$TlBa_2CaCu_2O_7$	80	2	1–Tl(n=2); Tl1212	[35][36][37]
$TlBa_2Ca_2Cu_3O_9$	110	3	1–Tl(n=3); Tl1223	[35][36][37]
$Tl_2Ba_2CuO_6$	80	1	2–Tl(n=1); Tl2201	[35][36][37]
$Tl_2Ba_2CaCu_2O_8$	108	2	2–Tl(n=2); Tl2212	[35][36][37]
$Tl_2Ba_2Ca_2Cu_3O_{10}$	125	3	2–Tl(n=3); Tl2223	[35][36][37]
$Bi_2Sr_2CuO_6$	20	1	2–Bi(n=1); Bi2201	[35][36][37]
$Bi_2Sr_2CaCu_2O_8$	85	2	2–Bi(n=2); Bi2212	[35][36][37]
$Bi_2Sr_2Ca_2Cu_3O_{10}$	110	3	2–Bi(n=3); Bi2223	[35][36][37]
$HgBa_2CuO_{4+\delta}$	94	1	1–Hg(n=1); Hg1201	[36]
$HgBa_2CaCu_2O_{6+\delta}$	125	2	1–Hg(n=2); Hg1212	[36]
$HgBa_2Ca_2Cu_3O_{8+\delta}$	135	3	1–Hg(n=3); Hg1223	[36]
$Pb_2Sr_2Y_{1-x}Ca_xCu_3O_{8+\delta}$	80	2	– – – –	[35]
$Sr_{2-x}Ba_xCu_{1+y}(CO_3)_{1-y}O_{2+2y+\delta}$ (highest T_c at x=1.1, $y \approx$0.1)	<40	–	carbocuprates	[36]
$[(CO_3)_{1-x}(NO_3)_x]Sr_2CuO_y$	50	1	carbocuprates	[36]
$[(CO_3)_{1-x}(NO_3)_x]Sr_2(Ca,Sr)Cu_2O_y$	105	2	carbocuprates	[36]
$[(CO_3)_{1-x}(NO_3)_x]Sr_2(Ca,Sr)_2Cu_3O_y$	115	3	carbocuprates	[36]
$Ca_{13.6}Sr_{0.4}Cu_{24}O_{41}$	12	–	– – – –	[40][41]

Table I – High–T_c superconductors (continued)

Formula	T_c(K)	n	observations	Ref.
$YSr_2Cu_{2.5}(CO_3)_{0.5}O_{5.5}$	66	2	oxyanions subst.	[43][44][45]
$(Y,Sr,Ca)Sr_2Cu_{2.8}(MO_4)_{0.2}$	< 78	2	oxyanions subst., M=S, P	[46][47][48]
$(Cu,C)Ba_2Ca_3CuO_4O_{11+\delta}$	117	4	$T_c = 136$ K at $P = 21$ GPa	[49][50][51]
$(Tl_{0.5},C_{0.5})(BaSr)_2CuO_y$	70	1	$(CO_3)^{2-} \rightarrow$ Tl1201	[52]
$(Ca,Na)_2CuO_2Cl_2$	26	1	oxide–halide superconductors	[21][53]
$(Ca,Na)_2CaCu_2O_4Cl_2$	49	2	oxide–halide superconductors	[54]
$Sr_2CuO_2F_{2.3}$	46	1	oxide–halide superconductors	[55][56]
$Sr_2CaCu_2O_4F_{2+\delta}$	99	2	oxide–halide superconductors	[57]
$Sr_2Ca_2Cu_3O_6F_{2+\delta}$	111	3	oxide–halide superconductors	[57]

Appendix B

Force constants in the shell model

In this appendix we report the formulae derived by Bruesh [75] for the calculation of the force constants within the shell model of interatomic potentials. We recall that in the shell model every ion has a mass–less shell and a core, whose charges add up to the nominal valence of the ion. The shell and the core are coupled by an harmonic spring, which accounts for the ionic polarisability.

Let y_i and x_i $(i = 1, 2)$ indicate the shell and core charges, respectively, of two neighbouring ions. Let $\mathcal{D} = \mathcal{D}^R + \mathcal{D}^C$ be the force constant describing the interaction between the mass–less shells, and k_i and m_i $(i = 1, 2)$ the stiffness of the core–shell springs and core masses, respectively. The *effective* shell–model force constant can then be expressed as

$$\mathcal{D}^{SM} = \mathcal{D}^* + \beta \frac{[Z^*]^2 \kappa}{V_a} \quad , \tag{B.1}$$

with,

$$\mathcal{D}^* = \frac{k_1 k_2 \mathcal{D}}{k_1 k_2 + (k_1 + k_2)\mathcal{D}}$$

$$Z^* = \frac{m_2|Z_1| + m_1|Z_2|}{m_1 + m_2}$$

$$\kappa = \frac{1}{1 - \beta\alpha^*/V_a} \quad ,$$

where V_a indicates the volume of the unit cell and

$$\alpha^* = \frac{y_1^2}{k_1} + \frac{y_2^2}{k_2} - \frac{\left[\dfrac{y_1}{k_1} - \dfrac{y_2}{k_2}\right]^2}{\dfrac{1}{\mathcal{D}} + \dfrac{1}{k_1} + \dfrac{1}{k_2}} \quad .$$

The constant β appearing in expression (B.2) relates the *effective* electric field E^* to the polarisation P in absence of an external field according to the simple law $E^* = \beta P$.

Appendix C

About vector models of interatomic coupling in lattices

The total energy of a lattice can be regarded as a sum of different many–body terms. The two–body terms do not take into account properly the angular energies, related to stretching, bending and torsional energies. Hence, many–body terms may be introduced when the equilibrium configuration of the lattice is manifestly the result of oriented bonding between atoms (a typical example is the diamond structure, e.g., in Si). However, in some cases, a two–body model can be modified by adding proper angular terms. By doing this, the computational advantages originated by pair interactions only are preserved, but angular energies are included. In this appendix, we shall discuss what kind of angular interactions are intrinsically contained in the *central–force* and *Euclidean–distance* schemes of two–body interactions.

Usually interatomic forces in a lattice are modeled within the framework of the central–force approximation [150]. This means that the forces between neighbouring atoms are assumed to act along the unit vector of the equilibrium distance between the particles.

C.1 Force models

Let us consider a d–dimensional lattice of N atoms. With respect to an arbitrary origin, fixed onto a particular reference atom, all atoms are identified by a lattice vector. If the lattice is described by a N_σ–atom basis at each lattice site ($N_\sigma > 1$), these vectors are labeled by a set of $d+1$ integers. For the sake of simplicity, in the following we will use single integers instead of $(d+1)$–plets of integers.

We shall first exploit the small–amplitude approximation of lattice vibrations and get explicit expressions of the central and angular forces.

Central forces Central forces are defined as pair forces acting along the line joining

two atoms. Let us consider atoms i and j. Let $\mathbf{r}_0(i,j)$ be the vector joining the equilibrium positions of the particles and $\mathbf{r}(i,j)$ the vector joining their displaced positions (see Fig. C.1). The following identity holds

$$\mathbf{r}(i,j) - \mathbf{r}_0(i,j) = \mathbf{u}(i) - \mathbf{u}(j), \qquad \text{(C.1)}$$

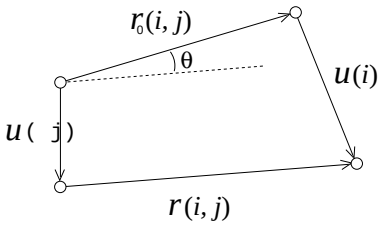

Figure C.1:

where $\mathbf{u}(i)$ and $\mathbf{u}(j)$ denote the displacement vectors of atoms i and j respectively. We assume the latter to be much smaller than the equilibrium interatomic distance $d = |\mathbf{r}_0(i,j)|$. Thus, even in the displaced positions the restoring forces may be assumed to be in the direction $\mathbf{s}(i,j) = \mathbf{r}_0(i,j)/d$. We want now to calculate the force $\mathbf{F}_j(i)$ on atom j due to its neighbour i. Within the harmonic approximation this force will be proportional to the net increase in the interatomic distance, that is

$$\mathbf{F}^c_j(i) = \alpha(|\mathbf{r}(i,j)| - d),$$

where α is the harmonic force constant. From Eq. (C.1) we get

$$\begin{aligned} |\mathbf{r}(i,j)| - d &= |\mathbf{u}(i) - \mathbf{u}(j) + \mathbf{r}_0(i,j)| - d \\ &= \sqrt{d^2 + |\mathbf{u}(i) - \mathbf{u}(j)|^2 + 2\,\mathbf{r}_0(i,j)\cdot(\mathbf{u}(i) - \mathbf{u}(j))} - d \\ &\simeq \mathbf{s}(i,j)\cdot(\mathbf{u}(i) - \mathbf{u}(j)) \quad , \end{aligned} \qquad \text{(C.2)}$$

and hence

$$\mathbf{F}^c_j(i) = \alpha \sum_{\beta=1}^{N_d} s^\beta(i,j)\left[u^\beta(i) - u^\beta(j)\right]\mathbf{s}(i,j) \quad , \qquad \text{(C.3)}$$

where N_d is the dimension of the coordinate space. To obtain the net force on atom j, it is enough to sum over all its neighbours whose interaction we want to include in the model. Usually, the nearest and next–nearest neighbouring atomic shells are enough. Thus, indicating with $\mathcal{N}_i$ the number of active neighbours of atom i we may write:

$$\mathbf{F}^c_j = \sum_{i=1}^{\mathcal{N}_j} \mathbf{F}^c_j(i) = \alpha \sum_{i=1}^{\mathcal{N}_j}\sum_{\beta=1}^{N_d} s^\beta(i,j)\left[u^\beta(i) - u^\beta(j)\right]\mathbf{s}(i,j). \qquad \text{(C.4)}$$

Angular forces Angular forces may be thought of as interactions arising in more than one dimension due to the deformation of bond angles. A very simple example is provided by the two–dimensional monoatomic square lattice, where longitudinal degrees of freedom along adjacent chains are coupled together by angular forces. On the contrary, longitudinal degrees of freedom along the same chain are obviously coupled by central forces. In the small–amplitude approximation, the central forces are *pure* central forces. This means that angular interactions vanish exactly, as it is not difficult to see by writing down Eq. (C.4) for the simple 2D square lattice (adjacent chains in the 2D square lattice are longitudinally exactly uncoupled). On the contrary, the general expression of central forces, which we shall derive further on, accounts for a small residual angular coupling between particles.

If θ denotes the angle which the line joining the displaced positions of atoms i and j makes with the line joining the equilibrium positions (see Fig. C.1), then

$$\begin{aligned}|\theta| \simeq |\sin\theta| &= \frac{|\mathbf{r}(i,j) \wedge \mathbf{r}_0(i,j)|}{|\mathbf{r}(i,j)|\,|\mathbf{r}_0(i,j)|} \\ &= \frac{|[(\mathbf{u}(i) - \mathbf{u}(j)) + \mathbf{r}_0(i,j)] \wedge \mathbf{r}_0(i,j)|}{d\,r(i,j)} \\ &= \frac{|[\mathbf{u}(i) - \mathbf{u}(j)] \wedge \mathbf{r}_0(i,j)|}{d\,r(i,j)} \\ &\simeq \frac{[|\mathbf{u}(i) - \mathbf{u}(j)] \wedge \mathbf{s}(i,j)|}{d}.\end{aligned}$$

Usually, a simple Hooke's law is assumed as a start to introduce the angular interactions. The restoring force will then be proportional to θ and we may therefore write

$$\mathbf{F}_j^a(i) = \beta[\mathbf{s}(i,j) \wedge (\mathbf{u}(i) - \mathbf{u}(j))] \wedge \mathbf{s}(i,j). \tag{C.5}$$

The triple vector product ensures that the restoring force will be perpendicular to the line joining the atoms. If we now use the vector identity

$$(\mathbf{a} \wedge \mathbf{b}) \wedge \mathbf{c} = \mathbf{b}(\mathbf{c} \cdot \mathbf{a}) - \mathbf{a}(\mathbf{c} \cdot \mathbf{b}),$$

we obtain

$$\mathbf{F}_j^a(i) = \beta \left[[\mathbf{u}(i) - \mathbf{u}(j)] - \sum_{\beta=1}^{N_d} s^\beta(i,j) \left[u^\beta(i) - u^\beta(j)\right] \mathbf{s}(i,j) \right]. \tag{C.6}$$

Again, the net angular force on atom j will be the sum over all the active neighbours $\mathcal{N}_j$

$$\mathbf{F}_j^a = -\beta \sum_{i=1}^{\mathcal{N}_j} \sum_{\beta=1}^{N_d} s^\beta(i,j) \left[u^\beta(i) - u^\beta(j)\right] \mathbf{s}(i,j) + \beta \sum_{i=1}^{\mathcal{N}_j} [\mathbf{u}(i) - \mathbf{u}(j)]. \tag{C.7}$$

We can now combine Eq. (C.4) and Eq. (C.7) to get the total central plus angular force on atom j due to its neighbours. We therefore get

$$\begin{aligned}\mathbf{F}_j &= \mathbf{F}_j^c + \mathbf{F}_j^a \\ &= \alpha \left\{ \chi \sum_{i=1}^{\mathcal{N}_j} [\mathbf{u}(i) - \mathbf{u}(j)] + (1-\chi) \sum_{i=1}^{\mathcal{N}_j} \sum_{\beta=1}^{N_d} s^\beta(i,j) \left[u^\beta(i) - u^\beta(j)\right] \mathbf{s}(i,j) \right\},\end{aligned}$$

where we have explicitly indicated the force anisotropy parameter $\chi = \beta/\alpha$. It is worthwhile to note that the central force strength appears weakened by a factor $1 - \chi$ as a result of the introduction of angular forces.

C.2 General expression of interatomic forces

In this section we introduce the general expression of central forces for arbitrary interatomic potential functions. We show that we recover the formula derived in the previous paragraph for small displacements. However, we also show that the general expression allow for a small angular component of the interactions.

The first step is to introduce the total lattice potential energy, which is a function of all the atomic coordinates. In the limit of two-body interactions only, the total energy is given by a sum of pair atomic interactions. Then one has to calculate the forces by taking the gradient of the lattice potential energy with respect to the atomic coordinates. In principle this function couples the degrees of freedom of each particle with all the degrees of freedom of all the other particles in the lattice. This is because of the long–range Coulombic potentials. In practice, such interactions are screened, and fade rapidly away with distance. As a consequence, it is customary to choose a distance cutoff in calculating the interactions. Again, this is done by allowing for a maximum number of interacting neighbours $\mathcal{N}_j$ (in principle a different number for each distinct atom in the lattice basis), which in the majority of the cases takes into account up to the next–nearest neigbouring atomic shells.

The central–force approximation amounts to assume that the function $V(x)$ describing the potential energy between any pair of atoms (i,j) depend on the difference between their instantaneous and equilibrium interparticle distances, i.e.

$$V(i,j) = V(r(i,j) - r_0(i,j)), \tag{C.8}$$

where $r(i,j)$ and $r_0(i,j)$ are respectively the actual and equilibrium distance between atom i and j. They are given in terms of their Cartesian coordinates by

$$\begin{aligned}r(i,j) &= \sqrt{\sum_{\alpha=1}^{N_d} [x^\alpha(i) - x^\alpha(j)]^2} \\ r_0(i,j) &= \sqrt{\sum_{\alpha=1}^{N_d} [x_0^\alpha(i) - x_0^\alpha(j)]^2}.\end{aligned} \tag{C.9}$$

We shall henceforth refer to model (C.8) as the r–model. The total N–particle lattice potential energy is

$$V_T = \frac{1}{2} \sum_{i=1}^{N} \sum_{j=1}^{\mathcal{N}_i} V(r(i,j) - r_0(i,j)). \tag{C.10}$$

The forces will be given by the gradient of this expression. Hence, the force on atom k along direction α due to its $\mathcal{N}_k$ neighbours will be

$$F_k^\alpha = \sum_{j=1}^{\mathcal{N}_k} \left[\frac{x^\alpha(j) - x^\alpha(k)}{r(j,k)} \right] \left(\frac{dV(x)}{dx} \right)_{x = r(jk) - r_0(jk)}. \tag{C.11}$$

Let us see what expression (C.11) looks like if we make the same assumptions as we did in the previous subsection. Namely, harmonic restoring forces and small

displacements. [1]. The first of this assumptions amounts to take

$$V(i,j) = \frac{1}{2}\alpha[r(i,j) - r_0(i,j)]^2 \quad , \tag{C.12}$$

where α is

$$\alpha = \left(\frac{d^2V(x)}{dr^2}\right)_{x=x_0} \quad . \tag{C.13}$$

Inserting expression (C.12) in Eq. (C.11), we get

$$F_k^\alpha = \alpha \sum_{j=1}^{\mathcal{N}_k} \left[\frac{x^\alpha(j) - x^\alpha(k)}{r(j,k)}\right][r(j,k) - r_0(j,k)]. \tag{C.14}$$

Recalling Eq. (C.2), the latter expression becomes

$$F_k^\alpha \simeq \alpha \sum_{j=1}^{\mathcal{N}_k} \left[\frac{r(j,k)^\alpha}{r(j,k)}\right] \mathbf{s}(j,k) \cdot [\mathbf{u}(j) - \mathbf{u}(k)]. \tag{C.15}$$

As in the previous section, small displacements mean that we can assume the restoring force to be in the unperturbed direction $\mathbf{s}(i,j)$. Consequently, we are finally led to Eq. (C.4) again

$$F_k^\alpha \simeq \alpha \sum_{j=1}^{\mathcal{N}_k} s(j,k)^\alpha \mathbf{s}(j,k) \cdot [\mathbf{u}(j) - \mathbf{u}(k)].$$

We see that, in the small amplitude approximation, the coordinate dependence expressed by definition (C.8) means identically vanishing angular forces. The latter result amounts to keep just the order 0 in u/d (i.e. the ratio of the *displacement* and the equilibrium interparticle distances) in the angular interactions. We can therefore say that, for general potential energy functions, model (C.8) introduces pure central forces only at order 0 in u/d. The first angular correction that arises if the atomic displacements are large enough is of second order. This is again well illustrated in the simple case of the monoatomic 2D square lattice (see fig C.2 (a)). We want to calculate the force on atom i in the x direction due to a displacement u of its lower neighbour j in the same direction (we take $u(i) = 0$). We have

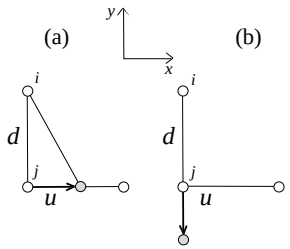

Figure C.2:

$$r(j,i) = \sqrt{d^2 + u^2} \approx d\left[1 + \frac{u^2}{2d^2}\right] \quad ,$$

while $r_0(i,j) = d$. Inserting these expressions in Eq. (C.14), we get

$$F_i^x(j) = \alpha u \left(\frac{u^2}{2d^2}\right) \quad .$$

[1] This point can be slightly confusing: in fact, the harmonic approximation is indeed the truncation of the Taylor series of the potential energy function to the second order, which one usually makes when the displacements are small. However, here the two are considered as disjoint approximations to elucidate their specificities.

On the other hand, the force on atom i in the y direction due to a displacement u of the same neighbour j along y is simply $F_i^y(j) = \alpha u$. Hence, angular forces in the harmonic approximation are characterised by an effective force constant of the form

$$\beta = \alpha\left(\frac{u^2}{2d^2}\right) \ll \alpha$$

We conclude that adopting model (C.8) in a molecular dynamics study amounts to practically neglecting angular forces. The latter have to be *forcibly* included in the model, e.g. in the harmonic approximation, as from formula (C.8), if the bonding nature and geometry in the lattice requires so.

We shall now discuss another way of introducing interatomic forces in lattices, which is based on the definition of Euclidean distance. In this model (henceforth the u–model)

$$V(i,j) = V(|\mathbf{r}(i,j) - \mathbf{r}_0(i,j)|) = V(|\mathbf{u}(i) - \mathbf{u}(j)|), \tag{C.16}$$

where $V(r)$ is the potential energy function. The total lattice potential energy is

$$U_T = \frac{1}{2}\sum_{i=1}^{N}\sum_{j=1}^{\mathcal{N}_i} V(|\mathbf{u}(i) - \mathbf{u}(j)|) \quad , \tag{C.17}$$

where again the long–range interactions are truncated and their action replaced by an effective number of neighbours $\mathcal{N}_i$. The forces will be given by the gradient of expression (C.17). Hence, the force on atom k along direction α due to its $\mathcal{N}_k$ neighbours will be in this case

$$F_k^\alpha = \sum_{j=1}^{\mathcal{N}_k}\left[\frac{u^\alpha(j) - u^\alpha(k)}{u(j,k)}\right]\left(\frac{dV(x)}{dx}\right)_{x=u(j,k)} \quad , \tag{C.18}$$

where

$$u(j,k) = |\mathbf{u}(j,k)| = \sqrt{\sum_{\alpha=1}^{N_d}[u^\alpha(j) - u^\alpha(k)]^2} \quad .$$

We are now interested in separating the central and angular contributions in expression (C.18). As for the r–model, we shall do so by exploiting the harmonic approximation. In this case we have

$$V(i,j) = \frac{1}{2}\alpha\, u(i,j)^2 \quad , \tag{C.19}$$

where again $\alpha = (d^2V(x)/dr^2)_{x=x_0}$. Inserting expression (C.19) in Eq. (C.18), we get

$$F_k^\alpha = \alpha \sum_{j=1}^{\mathcal{N}_k}[u^\alpha(j) - u^\alpha(k)] \tag{C.20}$$

If we compare Eq. (C.20) with the general expression (C.8), we see that the harmonic limit of the u model corresponds to *isotropic* coupling ($\chi = 1$), i.e. the strength of angular coupling *inherently* equals the central force constant. This is exactly the opposite result than that obtained in the r–model, where the angular forces are *inherently* strongly suppressed. In this case, it is still possible to retain the two–body approximation of the lattice energy provided one introduces an additional angular term in order to decrease χ.

Appendix D

Molecular Orbitals of CuO_2 clusters

In this appendix we show a number of pictures of the MO's that have been analysed for the calculations reported in chapter 6. The MO's surfaces correspond to a wavefunction value which is 0.06 the value in the origin. Red and blue surfaces denote positive and negative lobes, respectively. The relative magnitude of the different atomic orbitals correspond to different coefficients in the MO expansion. The clusters are in their equilibrium configurations.

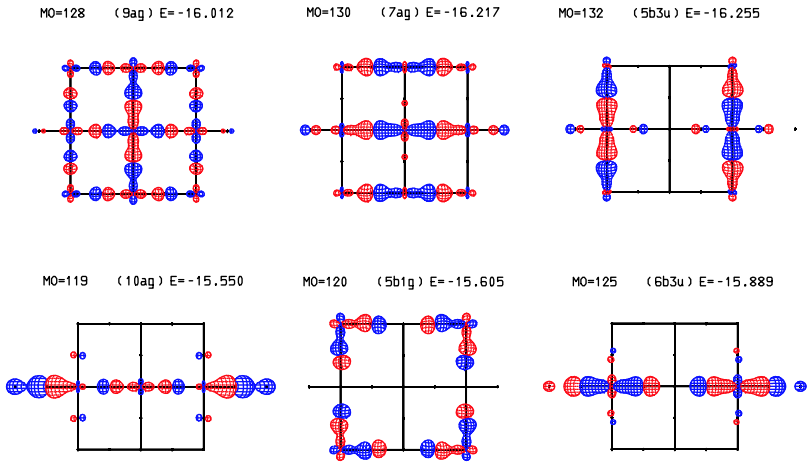

Figure D.1: Cluster No 1. MO's involving Cu $d_{x^2-y^2}$ orbitals (Gr1).

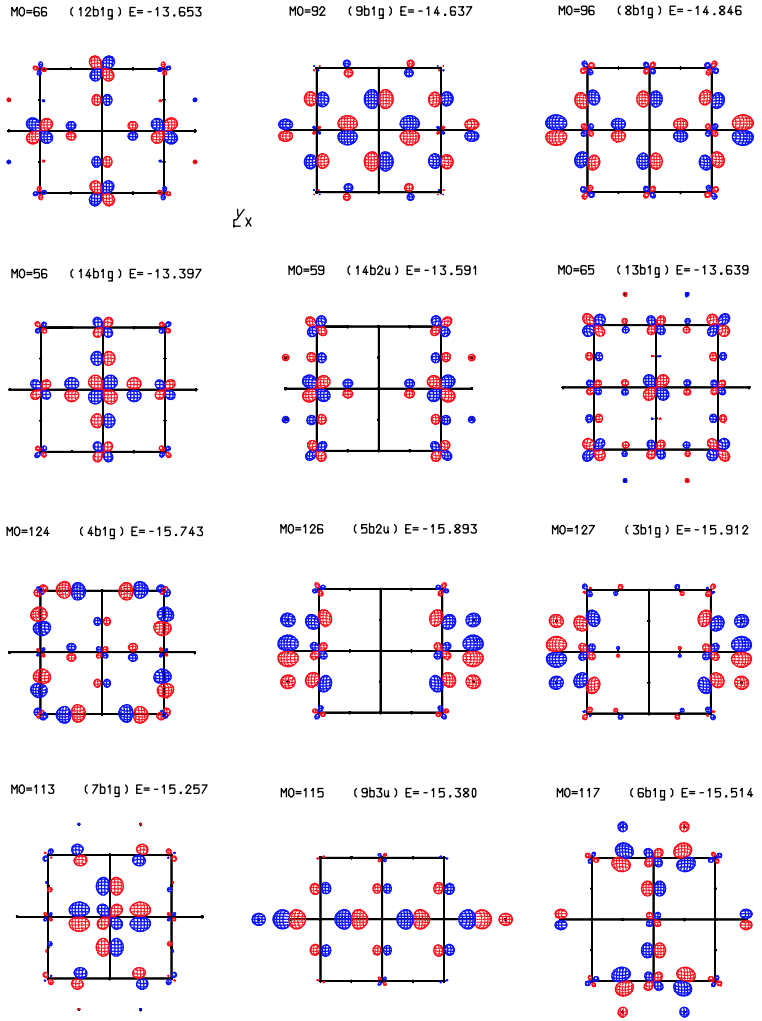

Figure D.2: Cluster No 1. MO's involving Cu d_{xy} orbitals (Gr2).

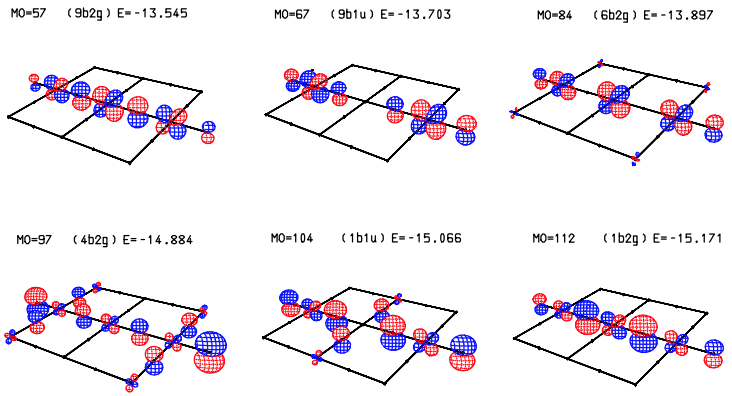

Figure D.3: Cluster No 1. MO's involving Cu d_{xz} orbitals (Gr3). MO's involving Cu d_{yz} orbitals can be obtained from these by a rotation of $\pi/2$.

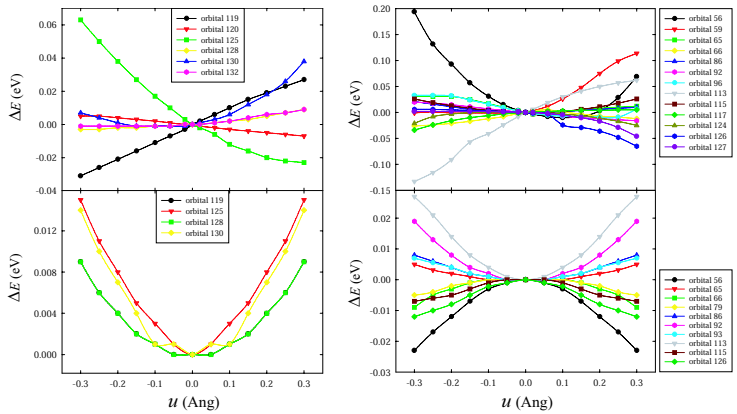

Figure D.4: Cluster No 1. Energy variations of planar orbitals. (a) Gr1 orbitals. (b) Gr2 orbitals. Upper panel: displacements along x. Lower panel: displacements along y.

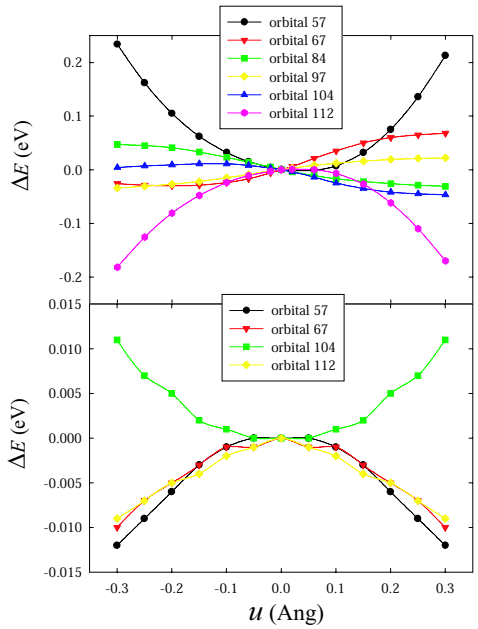

Figure D.5: Cluster No 1. Energy variations of perpendicular–to–plane (Gr3) orbitals. Upper panel: displacements along x. Lower panel: displacements along y.

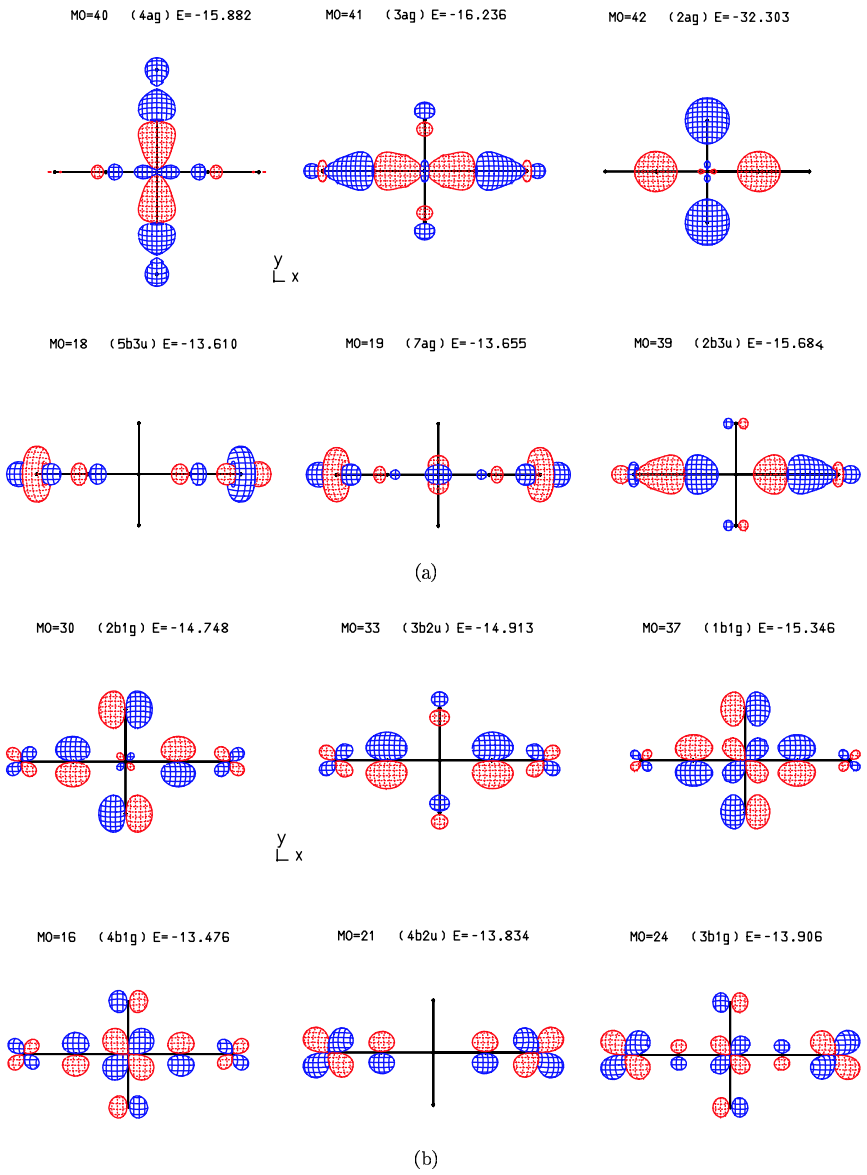

Figure D.6: Cluster No 2. (a) MO's involving Cu $d_{x^2-y^2}$ orbitals (Gr1). (b) MO's involving Cu d_{xy} orbitals (Gr2).

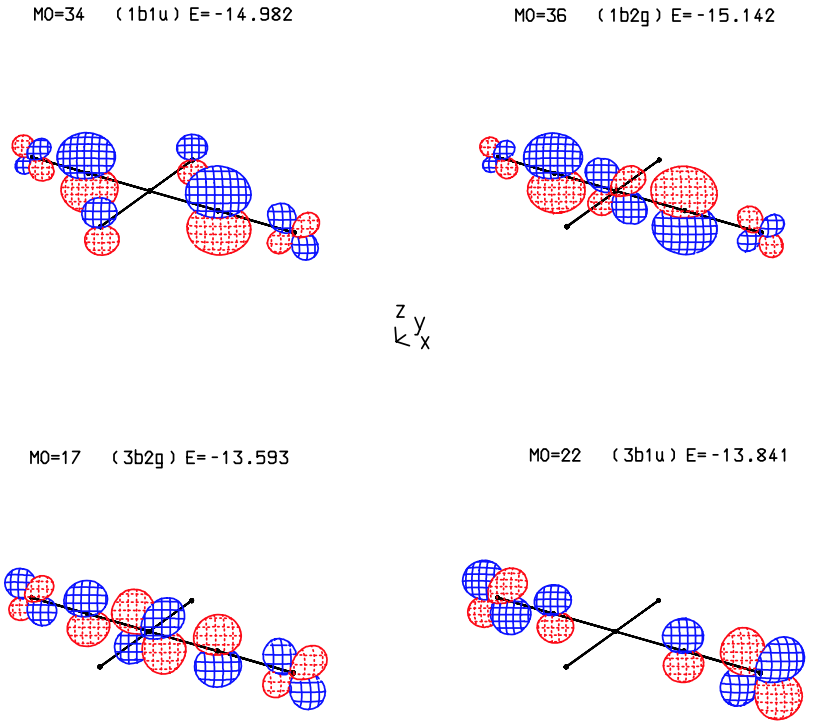

Figure D.7: Cluster No 2. MO's involving Cu d_{xz} orbitals (Gr3). MO's involving Cu d_{yz} orbitals can be obtained from these by a rotation of $\pi/2$.

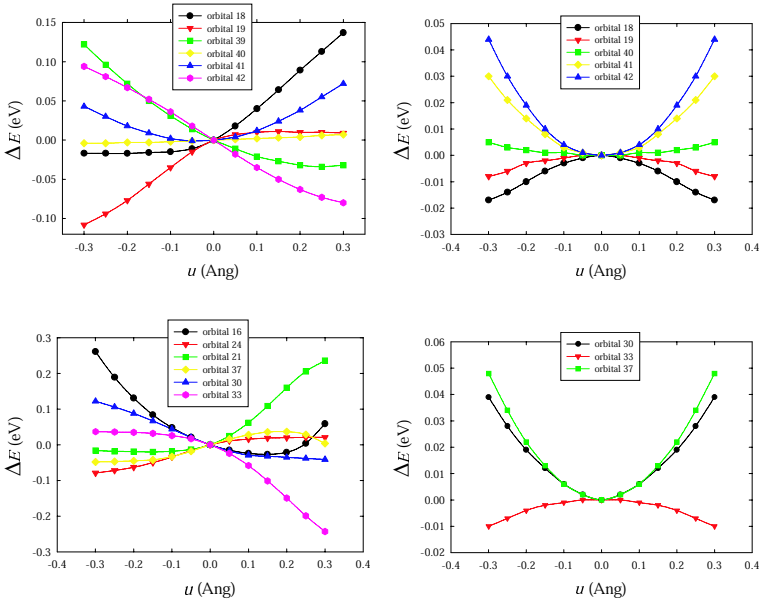

Figure D.8: Cluster No 2. Energy variations of planar orbitals. (a) Gr1 orbitals, displacements along x. (b) Gr1 orbitals, displacements along y. (c) Gr2 orbitals, displacements along x. (d) Gr2 orbitals, displacements along y

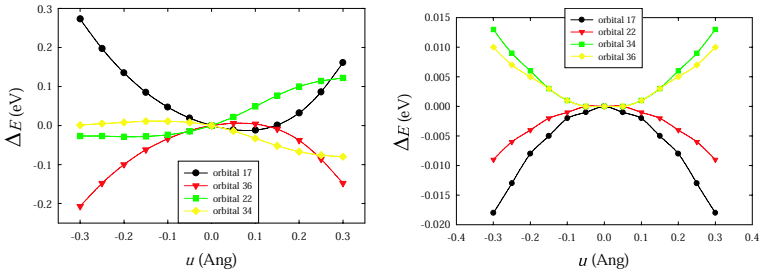

Figure D.9: Cluster No 2. Energy variations of perpendicular–to–plane (Gr3) orbitals. (a) displacements along x. (b) displacements along y

Bibliography

[1] J. G. Bednorz and K. A. Müller, *Z. Phys. B*, **64**, 189 (1986).

[2] P. W. Anderson, *The Theory of Superconductivity in the High–T_c Cuprates*, Princeton Series in Physics, Princeton University Press, Princeton, New Jersey (1997).

High Temperature Superconductivity. Models and Measurements, ed. by M. Acquarone, World Scientific, Singapore (1996).

N. M. Plakida, *High-Temperature Superconductivity: Experiment and Theory*, Springer–Verlag, Berlin (1995).

[3] J. Orenstein and A. J. Millis, *Science*, **288**, 468 (2000).

[4] M. L. Kulic, *Phys. Rep.*, **338**, 1–264 (2000).

[5] Proceedings of the Workshop on *Lattice Effects in High–T_c Superconductors*, edited by Y. Bar–Yam, T. Egami, J. Mustre de Leon, A. R. Bishop, World Scientific, Singapore, 1992.

[6] Proceedings of the Conference on *Stripes, Lattice Instabilities and High–T_c Superconductivity*, edited by A. Bianconi and N. L. Saini, *J. Supercond*, **10** No.4, (1997).

[7] J.–P.. Locquet, *Nature*, **394**, 453 (1998).

[8] Proceedings of the International Workshop on *Anharmonic properties of High–T_c Cuprates*, edited by D. Mihailović, G. Ruani, E. Kaldis and K. A. Müller, World Scientific (1995).

[9] F. Piazza *et al.*, *J. Superc.*, **14**, 675 (2001).

[10] J. Mustre de Leon, S. D. Conradson, I. Batistić and A. R. Bishop, *Phys. Rev. Lett.*, **65**, 1675 (1990).

[11] J. Mustre de Leon, S. D. Conradson, I. Batistić, A. R. Bishop, I. D. Raistrick, M. C. Aronson and F.H. Garzon, *Phys. Rev. B*, **45**, 2447 (1992).

J. Mustre de Leon, S. D. Conradson, I. Batistić and A. R. Bishop, *Phys. Rev. B*, **44**, 2422 (1991).

[12] L. Cianchi, F. Del Giallo, F. Lucchi and G. Spina, *Hyper. Int.*, **3** ,4 (2001).

M. Capaccioli, L. Cianchi, F. Del Giallo, F. Picralli and G. Spina, *J. Phys. Cond. Matt.*, **7** No 12, (1995).

[13] L. Cianchi, P. Moretti and F. Piazza, *Phys. Lett. A*, **246**, 451 (1998).

[14] A. Bianconi *et al.*,' *Phys. Rev. B*, **54**, 4310 (1996).
A. Bussmann–Holder and A. R. Bishop, *Phys. Rev. B*, **56**, 5297 (1997).
F. Cordero *et al.*,' *Phys. Rev. B*, **59**, 12078 (1999).
R. P. Sharma *et al.*, *Nature*, **404**, 736 (2000).
A. Bussmann–Holder *et al.*, *J. Phys. Cond. Matt.*, **13**, L169 (2001).

[15] T. Yildirim *et al.*,' *Phys. Rev. Lett.*, **87**, 3 (2001).

[16] A. R. Goncharov *et al.*,' cond–mat/0104042 (2001).

[17] Jin–Ho Choy, Soon–Jae Kwon and Gyeong–Su Park, *Science*, **280**, 1589 (1998).

[18] Z.–X. Shen and D. S. Dessau, *Phys. Rep.* **253**, 1 (1995).

[19] Y. Hongjie, M. Zhiqiang, X. Gaojie and Z. Yuheng, *Phys. Rev. B*, **59**, 8459 (1999).
C. J. Hatterer *et al.*, *J. All. and Comp.*, **251**, 103 (1997).

[20] K. A. Müller, *Physica C*, **3**, 185 (1991).

[21] Z. Hiroi, N. Kobayashi and M. Takano, *Nature*, **371**, 139 (1994).

[22] B. E. Warren, *X–ray diffraction*, Dover editions (1990).

[23] A. Lanzara, N. Saini, A. Bianconi, F. Duc and P. Bordet, *Phys. Rev. B* **59**, 3851 (1999).

[24] J. S. Sheir and R. D. Taylor, *Phys. Rev.*, **174**, 346 (1968).

[25] P. Schweiss *et al.*, *Phys. Rev. B*, **49**, 1387 (1994).

[26] S. Aubry, *Physica D*, **103**, 201 (1997).
For a comprehensive review see: S. Flach and C. R. Willis, *Phys. Rep.*, **295**, 181 (1998).

[27] J. L. Marin, C. J. Eilbeck and F. M. Russell, *Phys. Lett. A*, **248**, 225 (1998).

[28] F. M. Russell and D. R. Collins, *Phys. Lett. A*, **216**, 197 (1996).

[29] J. L. Marin, C. J. Eilbeck and F. M. Russell, *Phys. Lett. A*, **281**, 21 (2001).

[30] N. F. Wright and W. H. Butler, *Phys. Rev. B*, **42**, 4219 (1990).

[31] R.M. Hazen, *Crystal Structures of High–Temperature Superconductors*, in *Physical Properties of High Temperature Superconductors II*, ed. by G.M. Ginsberg, World Scientific, Singapore (1990), chapter 3.

[32] See e.g. A. Herpin, *Théorie du Magnétisme*, Presses Universitaires de France, Paris (1968), chapter XII.

[33] N. F. Mott, *Proc. Phys. Soc. London Ser. A*, **62**, 416, (1949),
J. Hubbard, *Proc. Phys. Soc. London Ser. A*, **277**, 237, (1964),
P. W. Anderson, *Prhys. Rev.*, **115**, 2, (1959),
See also e.g. W.A. Harrison, *Solid State Theory* (Dover Publications, New York, 1979), chapter 7.

[34] D.I. Khomskii, *Electronic Phase Transitions and the Problem of Mixed Valence*, in *Quantum Theory of Solids*, ed. by I.M. Lifshits, MIR Publishers, Moscow (1982), chapter 2.

[35] R.J. Cava, *Science*, **vol. 247**, 656 (1990).

[36] G. Calestani, *Chemical and Structural Aspects of High* T_c *Superconductors*, in *High Temperature Superconductivity*, ed. by M. Acquarone, World Scientific, Singapore (1996), pp. 1–40.

[37] G. Burns, *High–Temperature Superconductivity: an Introduction*, (Academic Press, Inc., 1992).

[38] B. Chevalier *et al.*, *Physica C*, **167**, 97 (1990).

[39] A. C. W. P. James, S. M. Zahurak and D. W. Murphy, *Nature*, **338**, 240 (1989).

[40] R.J. Cava, *Physica C*, **282–287**, 27 (1997).

[41] T. Nagata, M. Uehara, J. Goto et al., *Physica C*, **282–287**, 153 (1997).

[42] See e.g. J.B. Ketterson and S.N. Song, *Superconductivity* (Cambridge University Press, 1999), chapter 3 and chapter 9, part I.

[43] Y. Miyazaki *et al.*, *Physica C*, **198**, 7 (1992).

[44] Y. Miyazaki *et al.*, *Physica C*, **230**, 89 (1994).

[45] J. Akimitsu *et al.*, *Physica C*, **201**, 320 (1992).

[46] P. R. Slater, C. Greaves, M. Slaski and C. M. Muirhead, *Physica C*, **208**, 193 (1993).

[47] P. R. Slater, C. Greaves, M. Slaski and C. M. Muirhead, *Physica C*, **213**, 14 (1993).

[48] R. Nagarajan, S. Aygappan and C. N. R. Rao, *Physica C*, **220**, 373 (1994).

[49] H. Ihara *et al.*, *Japan J. Appl. Phys.*, **33**, L300 (1994),
M. A. Alario–Franco *et al.*, *Physica C*, **222**, 52 (1994).

[50] Y. Shimakawa *et al.*, *Phys. Rev. B*, **50**, 16008 (1994).

[51] Y. Matsui *et al.*, *Physica C*, **235–240**, 166 (1994).

[52] D. Pooke *et al.*, *Physica C*, **198**, 349 (1992).

[53] D. N. Argyriou *et al.*, *Phys. Rev. B*, **51**, 8434 (1995).

[54] Y. Zenitani *et al.*, *Physica C*, **248**, 167 (1995).

[55] M. Al–Mamouri, C. Greaves, P. P. Edwards and M. Slaski, *Nature*, **369**, 382 (1994).

[56] R. M. Kadam, B. M. Wani, M. D. Sastry and U. R. K. Rao, *Physica C*, **246**, 262 (1995).

[57] T. Kawashima, Y. Matsui and E. Takayama–Muromaki, *Physica C*, **257**, 313 (1996).

[58] D.M. Ginsberg, *Introduction, History, and Overview of High Temperature Superconductivity*, in *Physical Properties of High Temperature Superconductors I*, ed. by D. M. Ginsberg, World Scientific, Singapore (1989), chapter 1.

[59] A.P. Malozemoff, *Macroscopic Magnetic Properties of High Temperature Superconductors*, in *Physical Properties of High Temperature Superconductors I*, ed. by D.M. Ginsberg, World Scientific, Singapore (1989), chapter 3.

[60] K.A. Müller, *Physica Scripta*, **T35**, 9 (1991).

[61] P.J. Ford and G.A. Saunders, *Contemporary Physics*, **38**, 63 (1997).

[62] S. R. Ovshinsky *et al.*, *Phys. Rev. Lett.*, **58**, 2579 (1986).

[63] M- Xian–Ren *et al.*, *Solid State Commun.*, **64**, 325 (1986).

[64] M. Saiful Islam, M. S. D. Read and S. D'Arco, *Farady Disc.*, **106**, 367 (1997).

[65] M. Z. Hasan *et al.*, *Science*, **288**, 1811 (2000).

[66] See e.g. `http://www.neutron.anl.gov/reference.html`

[67] See e.g. B. Schrader (Ed.), *Infrared and Raman Spectroscopy: Methods and Applications*, Wiley (1995).

[68] R. E. Cohen, W. E. Pickett and H. Krakauer, *Phys. Rev. Lett.*, **62**, 831 (1989);**64**, 2575 (1990),
O. K. Andersen *et al.*, *Physica C*, **185–189**, 147 (1991).

[69] A. D. Kulkarni et al., *Phys. Rev. B*, **43**, 5451 (1991),
E. Rampf et al., *Phys. Rev. B*, **48**, 10143 (1993).

[70] S. L. Chaplot, W. Reichardt, L. Pintschovius and N. Pyka, *Phys. Rev. B*, **52**, 7230 (1995).

[71] B. G. Dick and A. W. Overhauser, *Phys. Rev.*, **112**, 90 (1958).

[72] S. L. Chaplot, *Phys. Rev. B*, **42**, 2149 (1990).

[73] J. D. Fan, G. L. Zhao, T. Edis and Y. M. Malozovsky, *Phys. Rev. B*, **56**, 10747 (1997).

[74] Y. M. Malozovsky and J. D. Fan, *Phys. Rev. B*, **9**, 4334 (1994).

[75] P. Bruesch, *Phonons: theory and experiments I: Lattice dynamics and models of interatomic forces*, Springer (1982).

[76] J. H. R. Clarke, W. Smith and L. W. Woodcock, *J. Chem. Phys.*, **84**, 2290 (1986).

[77] N. F. Wright and W. H. Butler, *Phys. Rev. B*, **42**, 4219 (1990).

[78] R. C. Baetzold, *Phys. Rev. B*, **42**, 56 (1990).

[79] P. A. Deymier, *Phys. Rev. B*, **38**, 6596 (1988).

[80] H. Nozaki and S. Itoh, *Phys. Rev. B*, **48**, 7583 (1993).

[81] S. L. Chaplot, *Phys. Rev. B*, **37**, 7435 (1988).

[82] W. Kress, U. Schröder, J. Prade, A. D. Kulkarni and F. W. de Wette, *Phys. Rev. B*, **38**, 2906 (1988).

[83] V. N. Popov, *J. Phys. C*, **7**, 1625 (1995).

[84] M. S. Islam and L. J. Winch, *Phys. Rev. B*, **52**, 10510 (1995).

[85] S. D'Arco and M. S. Islam, *Phys. Rev. B*, **5**, 3141 (1997).

[86] M. S. Islam, private communication to the author.

[87] J. A. Purton, G. D. Barrera, N. L. Allan and J. D. Blundy, *J. Phys. Chem. B*, **102**, 5202 (1998).

[88] H. Fricke, *Phys. Rev.*, **16**, 202 (1920).

[89] G. Hertz, *Zeit. f. Physik*, **3**, 19 (1920).

[90] R. de L. Kronig, *Zeit. f. Physik*, **70**, 317 (1931).

[91] R. de L. Kronig, *Zeit. f. Physik*, **75**, 468 (1932).

[92] D. E. Sayers, E.A. Stern and F.W. Lytle, *Phys. Rev. Lett.*, **27**, 1204 (1971).

[93] Calculations performed on–line at XCOM: Photon Cross sections Database, web address:
`http://www.physics.nist.gov/PhysRefData/Xcom/Text/XCOM.html`.

J. H Hubbell, W. J Veigele, E. A. Briggs, R. T Brown, D. T Cromer and R. J Howerton, *Atomic Form Factors, Incoherent Scattering Functions, and Photon Scattering Cross Sections*, *J. Phys. Chem. Ref. Data* **4**, 471-538 (1975); erratum in **6**, 615-616 (1977).

J. H Hubbell, and Overbo, *Relativistic Atomic Form Factors and Photon Coherent Scattering Cross Sections*, *J. Phys. Chem. Ref. Data* **8**, 69-105, (1979).

J. H. Scofield, *Theoretical Photoionization Cross Sections from 1 to 1500* keV, Lawrence Livermore National Laboratory Rep. UCRL-51326 (1973).

[94] See e. g. R. D. Evans, *The Atomic Nucleus*, McGraw-Hill, New York (1955), chapter 23.

[95] B. K. Teo, *EXAFS: Basic Principles and Data Analysis*, Springer-Verlag, Berlin (1986).

[96] See e.g. L. I. Schiff, *Quantum Mechanics*, Wiley & sons, New York (1952).

[97] B. H. Bransden and C. J. Joachain, *Physics of Atoms and Molecules*, Longman Scientific & Technical, New York (1983).

[98] See e. g. T. D. Sanders, *Modern Physical Theory : Special Relativity and Quantum Physics*, Addison-Wesley, Reading, (1970), chapter 19.

[99] G. Grosso and G. Pastori Parravicini, *J. Phys. C: Solid St. Phys.*, **13**, L919 (1980).

[100] C. A. Ashley and S. Doniach, *Phys. Rev. B*, **11**, 1279 (1975).

[101] J. J. Boland, S. E. Crane and J. D. Baldeschwieler, *J. Chem. Phys.*, **77**, 142 (1982).

[102] P.A. Lee, *Phys. Rev. B*, **13**, 5261 (1976).

[103] J. J. Sakurai, *Modern Quantum Mechanics*, Addison-Wesley, Reading (1985), chapter 7.

[104] T. A. Carlson, M. O. Krause, *Phys. Rev.*, **137**, A1655 (1965).

[105] T. A. Carlson, M. O. Krause, *Phys. Rev.*, **140**, A1057 (1965).

[106] T. Åberg, *Phys. Rev.*, **156**, 35 (1967).

[107] T. A. Carlson, C. W. Nestor, T. C. Tucker and F. B. Malik, *Phys. Rev.*, **169**, 27 (1968).

[108] P. A. Lee and G. Beni, *Phys. Rev. B*, **15**, 2862 (1977).

[109] K. D. Bomben, M. K. Bahl, J. K. Gimzewski, S. A. Chambers and T. D. Thomas, *Physical Review A*, **20**, 2405 (1979).

[110] P. Fornasini, *Introduzione alla spettroscopia di assorbimento di raggi X*, IV Scuola Nazionale di Luce di Sincrotrone, Santa Margherita di Pula, Cagliari (1997), in italian.

[111] G. F. Knoll, *Radiation Detection and Measurement*, John Wiley & Sons, New York (1979), chapter 1.

[112] B. K. Teo and D. C. Joy, ed., *EXAFS spectroscopy: techniques and applications*, Plenum, New York (1981).

[113] A. A. Maradudin, E. W. Montroll, G. H. Weiss, I. P. Ipatova, *Theory of Lattice Dynamics in the Harmonic Approximation*, Academic Press, New York and London (1971), chapter VII, pp. 304–306.

[114] S. M. Heald and E. A. Stern, *Phys. Rev. B*, **16**, 5549 (1977).

[115] P. A. Lee and J. B. Pendry, *Phys. Rev. B*, **11**, 2795 (1975).

[116] S. J. Gurman and R. F. Pettifer, *Phil. Mag. B*, **40**, 345 (1979).

[117] S. J. Gurman, N. Binsted and I. Ross, *J. Phys. C*, **17**, 143 (1984).

[118] N. Binsted (1998) EXCURV98: CCLRC Daresbury Laboratory computer program. Manual complete of theory an references available on–line at the web address
`http://www.dl.ac.uk/XRS/SRS/`.

[119] P. J. Bryant and K. Johnsen, *The Principles of Circular Accelerators and Storage Rings*, Cambridge University Press, Cambridge, (1993).

[120] J. D. Jackson, *Classical electrodynamics*, Wiley (1984)

[121] P. A Lee, P. H. Citrin, P. E. Eisenberger and B. M. Kincaid, *Rev. Mod. Phys.*, **53**, 769 (1981).

[122] J. Morse, *Detectors for Synchrotron Radiation*, in *Neutron and Synchrotron Radiation for Condensed Matter Studies*, HERCULES, Les Editions de Physique & Springer–Verlag (1993).

[123] January 1996 issue of *Phylosophical Magazine B*, **73**(1) (1996).

[124] E. A. Stern, P. Līvinŝ and Z. Zhang, *Phys. Rev. B*, **43**, 8850 (1991).

[125] In the Einstein model each atom in the crystal is represented by a quantised harmonic oscillator of frequency ω_E. Hence, we can write

$$\langle (r-r_0)^2 \rangle = \sum_{n=0}^{\infty} \langle n|(r-r_0)^2|n\rangle e^{-E_n/k_BT} / \sum_{n=0}^{\infty} e^{-E_n/k_BT} = \left(\frac{\hbar}{2\mu\omega_E}\right) \coth\left(\frac{\hbar\omega_E}{2k_BT}\right) \quad . \quad \text{(D.1)}$$

[126] See for example: C. Chatfield, *Statistics for Technology*, Chapman & Hall, UK (1983).

[127] W. H. Press, S. A. Teukolsky, W. T. Vetterling, and B. P. Flannery, *Numerical Recipes in Fortran 77 – The art of Scientific Computing*, book On-Line at

`http://www.ulib.org/webRoot/Books/Numerical_Recipes/bookfpdf.html`

[128] R. W. Joyner, K. J. Martin and P. Meehan, *J. Phys. C*, **20**, 4005 (1987).

[129] See for example B. P. Roe, *Probability and Statistics in Experimental Physics*, Springer–Verlag, New York (2001).

[130] N. R. Draper and H. Smith, *Applied Regression Analysis*, New York: Wiley (1981).

[131] Detailed information on the GNXAS package can be found on–line at `http://gnxas.unicam.it/`

[132] A. Filipponi, A. Di Cicco and C. R. Natoli, *Phys. Rev. B*, **52**, 15122 (1995),

[133] A. Filipponi and A. Di Cicco, *Phys. Rev. B*, **52**, 15135 (1995),

[134] A. Filipponi, *J. Phys. Cond. Matter* **7**, 9343 (1995).

[135] A. Filipponi and A. Di Cicco, *Task Quarterly*, **4**, 575–669 (2000).

[136] *CERN Program Library Long Writeup D506, MINUIT Reference Manual* (CERN, Geneva, 1992).

[137] E. A. Stern, *Phys. Rev. B*, **48**, 9825 (1993).

[138] G. Bunker, *Nucl. Instrum. Methods*, **207**, 437 (1983).

[139] G. Ruani, C. Taliani, M. Muccini, K. Conder, E. Kaldis, H. Keller, D. Zech and K. A. Müller, *Physica C*, **226**, 101 (1994).

G. Ruani, P. Guptasarma and C. Taliani, *Anomalous Raman Scattering of Apex–Oxygen Related modes in Pr–BCO*, in *Anharmonic Properties of High–T_c Cuprates*, Ed. D. Mihailović, G. Ruani, E. Kaldis and K. A. Müller, World Scientific (1995).

[140] The Nag routines are not free. We have been using the Nag libraries installed on the Unix network of the department. On–line reference information is available at the web–site

`http://www.nag.co.uk/numeric/fl/manual/html/FLlibrarymanual.asp`

[141] The sequential quadratic programming algorithm is a generalization of Newton's method for unconstrained optimization in that it finds a step away from the current point by minimizing a quadratic model of the problem. See e.g.

P. E. Gill, W. Murray and M. H. Wright, *Practical Optimization*, Academic Press(1981).

[142] T. Yokoyama, T. Satsukawa and T. Ohta, *Jap. J. Appl. Phys.*, **28** (10), 1905 (1989).

[143] B. Kolk, *Studies of Dynamical Properties of Solids with the Mössbauer Effect*, in *Dynamical Properties of Solids*, Elsevier (1984).

[144] A. Yoshiasa, K. Koto, F. Kanamaru, S. Emura and H. Horiuchi, *Acta Cryst. B*, **43**, 434 (1987).

[145] G. Dalba, P. Fornasini, F. Rocca and S. Mobilio, *Phys. Rev. B*, **41**, 9668 (1990).

[146] G. Dalba, P. Fornasini and F. Rocca, *Phys. Rev. B*, **47**, 8502 (1993).

[147] A. Yoshiasa and H. Maeda, *Solid State Ionics*, **121**,175 (1999).

[148] J. J. Rehr, J. Mustre de Leon, S. I. Zabinski and R. C. Alberts, *Am. Chem. Soc.*, **113**, 5135 (1991).

[149] We note that, according to the usual theory of elasticity in solids applied to a two–dimensional structure, the ratio $\chi \equiv \theta/\alpha$ equals the ratio $C_{xxyy}/C_{xxxx} \equiv C_{yyyy}/C_{yyyy}$ ($=C_{33}/C_{11}$). The coefficients $C_{\alpha\beta\gamma\delta}$ are the *moduli of elasticity*, which enter the usual stress–strain (T–e) proportionality relation

$$T_{\alpha\beta} = \sum_{\gamma\delta} C_{\alpha\beta\gamma\delta} e_{\gamma\delta} \qquad \alpha,\beta,\gamma,\delta = x,y \quad .$$

[150] See for example: A. K. Ghatak and L. S. Kothari, *An Introduction to Lattice Dynamics*, Addison–Wesley (1972).

[151] S. Nosé , *J. Chem. Phys.*, **81** (1), 511 (1984).

[152] A. J. C. Ladd and W. G. Hoover, *Phys. Rev. B*, **28**, 1756 (1983).

[153] G. P. Tsironis and S. Aubry, *Phys. Rev. Lett.*, **77**, 5225 (1996).

[154] A. Bikaki, N. Voulgarakis, S. Aubry and G. P. Tsironis, *Phys. Rev. E*, **9**, 1234 (1999).

[155] F. Piazza
_____, S. Lepri and R. Livi, *J. Phys. A* **34**, 9803 (2001).

[156] R. Reigada, A. Sarmiento and K. Lindenberg, cond–mat/0108148.

[157] J. L. Marin and S. Aubry, *Nonlinearity*, **9**, 1501 (1996).

For an exhaustive description see also, J. L. Marin, PhD thesis, Paris (1997) (unpublished) and references therein.

For alternative approaches to the study of breather stability see e.g. K. W. Sandusky, J. B. Page and K. E. Schmidt, *Phys. Rev. B*, **46**, 6161 (1992) and references therein.

[158] Z.–P. Shi, G. Huang and R. Tao, *Int. J. Mod. Phys. B*, **5**, 2237 (1991),
Y. S. Kivshar and N. Flytzanis, *Phys. Rev. A*, **46**, 7972 (1992),
O. A. Chubykalo, A. S. Kovalev and O. V. Usatenko, *Phys. Rev. B*, **47**, 3153 (1993),
G. Huang, *Phys. Rev. B*, **51**, 12347 (1995),
M. Aoki and S. Takeno, *J. Phys.Soc. Jpn.*, **64**, 809 (1995),
D. Bonart, A. P. Mayer and U. Schröder, *Phys. Rev. Lett.*, **75**, 870 (1995) and *Phys. Rev. B*, **51**, 13739 (1995),
J. N. Teixeira and A. A. Maradudin, *Phys. Lett. A*, **26**, 349 (1995),
A. Franchini, V. Bortolani and R. F. Wallis, *Phys. Rev. B*, **53**, 5420 (1996),
V. V. Konotop, *Phys. Rev. E*, **53**, 2843 (1996),
S. A. Kiselev and A. J. Sievers, *Phys. Rev. B*, **5**, 5755 (1997).
N. Flytzanis, B. A. Malomed and A. Neuper, *Physica D*, **113**, 191 (1998).

[159] E. Fermi, J. Pasta and S. Ulam, Los Alamos National Laboratory Report No. LA1940, 1955 (unpublished). Also in *Collecetd Papers of Enrico Fermi*, (University of Chicago Press, Chicago, 1962), Vol. 2, p. 978.

[160] T. Cretegny, T. Dauxois, S. Ruffo and A. Torcini, *Physica D*, **121**, 106 (1998),

[161] J. B. Page, *Phys. Rev. B*, **41**, 7835 (1990),
V. M. Burlakov, S. A. Kiselev and V. N. Pyrikov, *Solid State Commun.*, **74**, 327 (1990),
A. J. Sievers and S. Takeno, *Phys. Rev. Lett.*, **61**, 970 (1988).

[162] T. Dauxois, R. Livi and M. Spicci, *Physica D*, **119**, Issues 1–2, 88 (1998).

[163] A. J. Sievers and S. Takeno, *Phys. Rev. Lett.*, **61**, 970 (1988).

[164] F. A. Lindemann, *Phys. Z.* **11**, 609 (1910).
X. H. Zheng and J. C. Earnshaw, *Europhys. Lett.*, **41**, 635 (1998).

[165] F. Piazza, S. Lepri and R. Livi, in preparation.

[166] K. Hori and S. Takeno, *J. Phys. Soc. Jpn.*, **61**, 4263 (1992).

[167] V. M. Burlakov, S. A. Kiselev and V. N. Pyrikov, *Phys. Rev. B*, **42**, 4921 (1990),
K. Hori and S. Takeno, *J. Phys. Soc. Jpn.*, **61**, 4263 (1992),
S. R. Bickham, A. J. Sievers and S. Takeno, *Phys. Rev. B*, **5**, 10344 (1992).
See also the chapter *Moving Breathers* in: T. Cretegny, *PhD thesis*, ENS–Lyon, (1998).

[168] D. Chen, S. Aubry and G. Tsironis, *Phys. Rev. Lett.*, **77**, 4776 (1996).

[169] See G. Huang and B. Hu, *Phys. Rev. B*, **57**, 5746 (1998) and references therein.

[170] K. W. Sandusky and J. B. Page, *Phys. Rev. B*, **50**, 866 (1994),
S. A. Kiselev, S. R. Bickham and A. J. Sievers, *Phys. Rev. B*, **50**, 9135 (1994),
S. A. Kiselev, S. R. Bickham and A. J. Sievers, *Phys. Rev. B*, **48**, 13508 (1993).

[171] S. Flach, K. Kladko and R. S. MacKay, *Phys. Rev. Lett.*, **78**, 1207 (1997),
P. G. Kevrekidis, K. O. Rasmussen and A. R. Bishop, *Phys. Rev. E*, **61**, 4652 (2000),
M. I. Weinstein, *Nonlinearity*, **12**, 673 (1999).

[172] C. P. Poole ed. *Handbook of Superconductivity*, Academic Press, S. Diego (2000).

[173] C. Mealli *et al.*, *J. Chem. Ed.*, **67**, 399 (1990).

[174] See J. H. Ammeter, H. B. Burgi, J. C. Thibeault and R. Hoffmann, *J. Am. Chem. Soc.* , **100**, 3686 (1978),
R. Hoffmann and W. R. Lipscomb, *J. Chem. Phys.*, **36**, 2179, 3489 (1962),
R. Hoffmann, *Journal of Chemical Physics*, **39**, 1397 (1963).